# 'Investigation in the low latitude daytime mesosphere lower thermosphere region'



| | |
|---|---|
| O($^1$D) emission | |
| O($^1$S) emission | |
| OH emission | |

Fountain effect: EIA

Electric field mapping

GLOBAL DYNAMO, EEJ, CEJ

Wave filtering and formation of turbopause height

Wave generation and propagation

dynamical processes over low and equatorial MLTIS

✍ **Alok Taori**

**Ph. D. Thesis**

March 2001
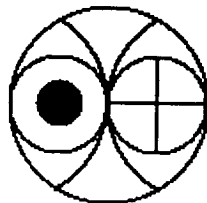
# Investigation in the low latitude daytime mesosphere lower thermosphere region

*Thesis submitted to*

D. A. V. V., University of Indore

*For the degree of*

## Doctor of Philosophy

In

## Physics

By: Alok Khivraj Taori

March 2001

Thesis Supervisor: Prof. R. Sridharan
Physical Research Laboratory, Ahmedabad
Space Physics Laboratory, VSSC, Trivandrum

Thesis Co-Supervisor: Dr. A. K. Dutta
D. A. V. V., Indore.

Physical Research Laboratory
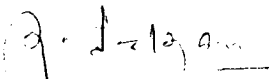Navrangpura, Ahmedabad – 380 009
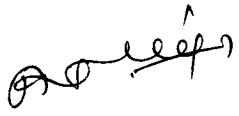Gujrat, INDIA.

Dedicated to



'My Mummy and Papa'

&

*to all my wellwishers...*

# CERTIFICATE

*I hereby declare that the work presented in this thesis was carried out by the author at the PHYSICAL RESEARCH LABORATORY, AHMEDABAD. The results reported herein are original and have not formed the basis for the award of any degree or diploma by any University or Institution.*

*Thesis Supervisor*

(Prof. R. Sridharan)

*Author*

(Alok Taori)

# CONTENTS:

## 3. Emission processes responsible for the OH, O($^1$S) and O($^1$D) dayglow emission   48

## 4. Day- Night measurements of OI 630.0nm airglow emission from low latitudes   73

# Acknowledgements

It is indeed a great pleasure to express my sincere gratitude and indebtedness to the persons who have been instrumental in bringing this work to the present level.

First of all, I express my honest gratitude to my thesis supervisor, Prof. R. Sridharan. It's a sheer delight to work under his kind tutelage. His in-depth understanding of the subject and the associated experimental techniques have always been inspiring. Throughout this period, he always encouraged me in my crisis and I'm fortunate to have him as my guide. He's truly my academic mentor.

I'm grateful to Dr. R. Sekar for the various scintillating academic sessions I had with him. His critical comments and suggestions made me to do things more perfectly.

I want to convey my sincere gratitude to Dr. Harish Chandra, Dr. S. P. Gupta, Dr. H. S. S. Sinha and all the members of the academic committee for their critical assessments and suggestions for the improvement of my work.

I thank Dr. Pallam Raju, Dr. Tarun Pant and Dipu for their invaluable company. It's a delightful experience to have them as my colleagues and get benefited through many informal academic and non-academic discussions. Those discussions supplied the required oxygen to fight adversities. At this juncture, it's also my duty to express my heart-felt gratitude and thanks to Mr. R. Narayanan and Mr. N. K. Modi for the help they provided me. It's always been pleasure to work with them on and off the field stations and the lab. Their informal attitude and spontaneity never made me feel isolated. I've learnt many invaluable lessons from them. For the same reasons, I would like to thank Mr. C. L Piplapure, Mr. Swaroop Banerjee, Mrs. Vijaya Mutagi and Ms. Ranna Patel.

I thank Dr. A. K. Dutta and Dr. K. P. Maheswari, DAVV, Indore for their constant help and encouragement.

# List of scientific publications:

## *Papers:*

₵ 1# `Multiwavelength daytime photometer - a new tool for the investigation of atmospheric processes'.
Sridharan R., N. K. Modi, D. Pallam Raju, R. Narayanan, Tarun Pant, **Alok Taori** and D. Chakrabarty.
Measurement Sci. and Technology (UK), 9, 585 - 591, 1998.

₵ 2# `Imprint of the equatorial electrodynamical processes in the OI 630.0 nm dayglow'.
Sridharan R., D. Pallam Raju, V. V. Somayajulu, **Alok Taori**, D. Chakrabarty and R. Raghavarao.
J. Atmos. Sol. Terr. Physics (UK), 61, 15, 1143 - 1156, 1999.

₵ 3# `First results on daytime mesopause OH rotational temperatures using ground based photometry from equatorial latitudes'.
Sridharan R., **Alok Taori**, S. Gurubaran, R. Rajaram and M. G. Shepherd.
J. Atmos. Sol. Terr. Physics (UK), 61, 15, 1131 - 1142, 1999.

₵ 4# `Effects of 6 January 1997 space weather related processes in the low latitude thermosphere ionosphere system'.
Sridharan R., **Alok Taori**, D. Chakrabarty, H. Chandra, Som kumar Sharma, R. narayanan and N. K. Modi.
J. Atmos. Sol. Terr. Physics (UK), 61, 13, 1101 - 1105, 1999.

₵ 5# ` Coordinated thermospheric Day-Night airglow and ionospheric measurements from low latitudes – First results'.
**Alok Taori**, R. Sridharan, D. Chakrabarty, R. Narayanan, N. K. Modi and P. V. S. Ramarao.
Geophysical Research Letters (USA) 28, 6, 983 – 986, 2001.

₵ 6# `Temporal variabilities in the OH mesopause rotational temperatures over low latitudes'.
**Alok Taori** and R. Sridharan. (under preparation).

₵ 7# `Noontime bite outs in 630.0 nm thermospheric dayglow over an equatorial station in Indian zone'.
**Alok Taori**, R. Sridharan and D. Chakrabarty (under preparation).

₵ 8# `Significant thermospheric contribution in 557.7 nm emission: ground based evidence'.
**Alok Taori**, R. Sridharan, D. Chakrabarty and R. Narayanan (under preparation).

₵ 9# `630.0 nm thermospheric dayglow variabilities under variable electrodynamical forcing: observations from a low latitude station in Indian sector'.
**Alok Taori** and R. Sridharan (under preparation).

## Abstracts presented in national/ international symposia:

1# `Evidence for significant upper thermospheric contribution to O(1s) 557.7 nm dayglow'.
Sridharan R., **Alok Taori**, Tarun Pant, D. Chakrabarty and D. P. Raju.
Presented in IAGA-97, August 1997, Uppsala, Sweden.

2# `Daytime OH rotational temperatures from equatorial latitudes: first results'
Sridharan R., **Alok Taori**, N. K. Modi, R. Narayanan, D. Chakrabarty and M. G. Shepherd.
Presented in NSSS, November 1997, Ahmedabad, India.

3# `Imprint of the equatorial electrodynamical processes in the OI 630.0 nm dayglow'.
Sridharan R., D. Pallam Raju, V. V. Somayajulu, **Alok Taori**, D. Chakrabarty and R. Raghavarao.
Presented in NSSS, November 1997, Ahmedabad, India.

4# `Effects of space weather related processes in the low latitude thermosphere ionosphere system'.
Sridharan R., **Alok Taori**, D. Chakrabarty, H. Chandra, Som kumar Sharma and R. Narayanan.
Presented in NSSS, November 1997, Ahmedabad, India.
Presented in IUGG -99, July 1999, Birmingham, U K.

5# `Daytime mesopause OH rotational temperatures from equatorial and low latitudes using ground based optical methods'.
Sridharan R. and **Alok Taori**.
Presented in IUGG 99, July 1999, Birmingham, U K.

6# `Identification of the dominant short period oscillations in the thermosphere during day and night'.
**Alok Taori**, R. Sridharan, D. Chakrabarty, R. Narayanan, N. K. Modi and P. V. S. Ramarao.
Presented in NSSS 2K, March 2000, Puri, India.

7# ` Daytime mesopause temperature variabilities over low latitude regions'.
**Alok Taori**, R. Sridharan, R. Narayanan and N. K. Modi.
Presented in NSSS 2K, March 2000, Puri, India.

# 1# Introduction

The earth's atmosphere can be treated as a horizontally stratified system to the first order because of the pervasive influence of the gravity. The regions of the neutral atmosphere are named according to different schemes based on temperature variations composition and the state of mixing. Figure 1.1 shows the classification of the atmosphere according to the temperature gradient. The region with negative temperature gradient nearest to the earth's surface is the *troposphere*. The temperature of the troposphere reaches a minimum at the upper boundary called the *tropopause*. The height of the tropopause varies from 15-17 km at low latitudes and 8-10 km at high latitudes. The tropopause temperature is about 210 K. The altitude region from the tropopause to the temperature maximum at 50 km is referred to as the *stratosphere*. The thermal structure of the stratosphere is essentially controlled by the solar UV absorption by ozone and the infrared emission of $CO_2$, water vapour and ozone. From the *stratopause* upward, the temperature gradient becomes negative in the altitude region 50-85 km. This region is called the *mesosphere*. The thermal structure of this region is determined by heating through the absorption of solar U-V radiation by molecular oxygen and ozone and by cooling through the infra red radiation of carbon dioxide. In addition to these, thermal effects due to dynamical motions, such as wave and tidal forces also become very important. The upper boundary of the mesosphere is called the *mesopause*, and is defined by the minimum temperature of about 180K in the earth's atmosphere at a height of about 85 km. Above the mesopause, there exists the *thermosphere*, which encompasses the ionospheric E and F regions. In the thermosphere the temperature increases rapidly with height, with a sharp gradient from 180K - 800K to 1200K at 300 km which is referred to as the *thermopause* or the *exobase*. The high temperature of the thermosphere is caused by the absorption of solar EUV radiation by molecular oxygen at 100-150 km and by the absorption of ionizing EUV radiation above 150 km.

The lower part of the atmosphere is well mixed, and is known as *turbosphere* or *homosphere*. The upper region is the thermosphere where mixing is inhibited by the positive temperature gradient and the various atmosphere constituents may separate under the influence of gravity is known to be the *heterosphere*. The boundary between these two regions, which happen to occur at around 100 km, is
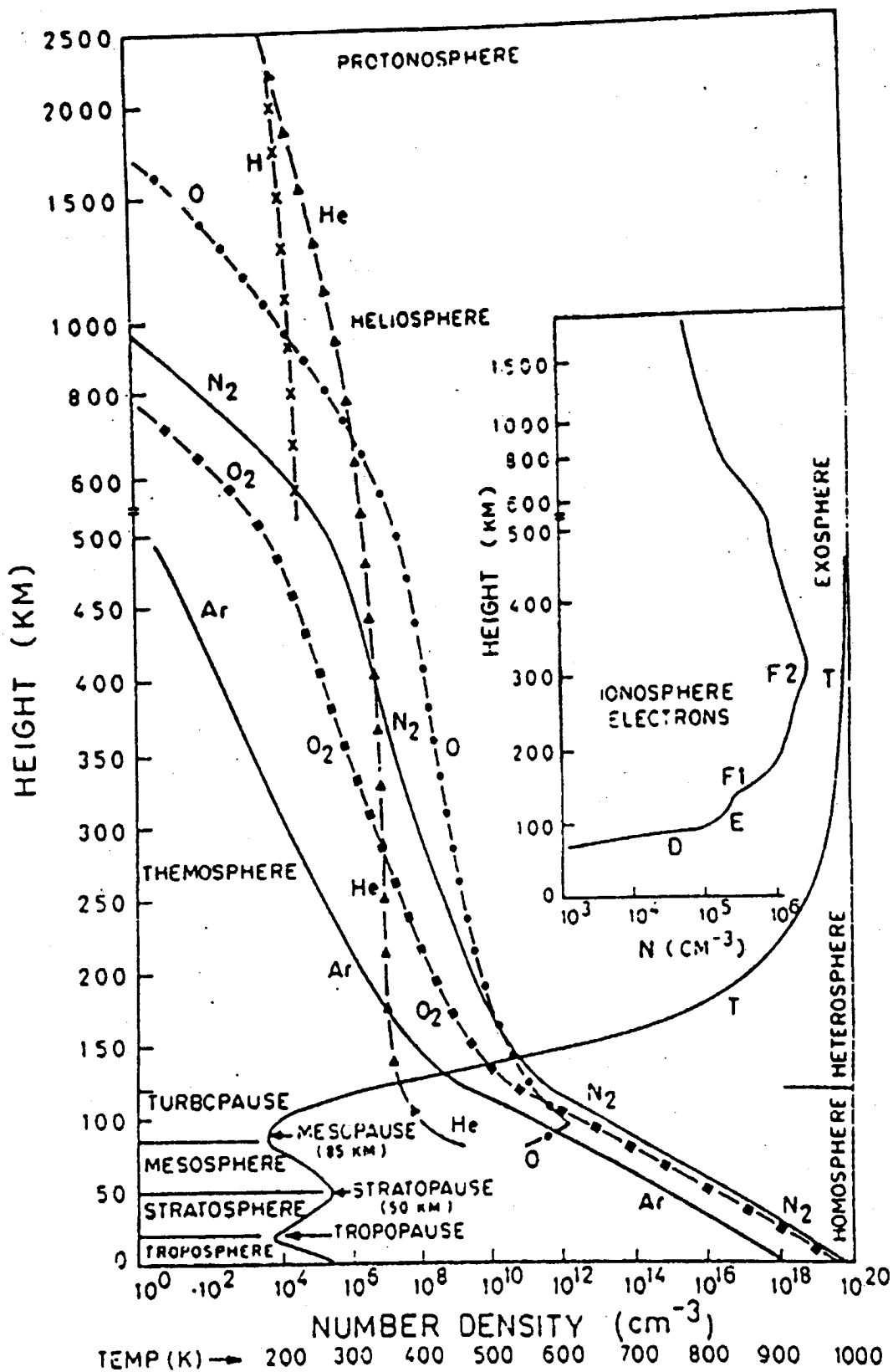
**Figure 1.1.** Thermal and compositional structure of the atmosphere.

referred to as the *turbopause*. Within the heterosphere, the region where the dominant gas is helium or hydrogen, are the *heliosphere* and the *protonosphere* respectively. From the higher levels, above 500 km, individual atoms can escape from the earth's gravitational force, and this region is called the *exosphere*.

The system of mesosphere and thermosphere - ionosphere, ie the upper atmosphere system over equatorial latitudes is the focus of the present thesis and the processes occurring in this region will be dealt with in some detail in the sections to follow.

## 1.1# Structure of the upper atmosphere:

The structure and dynamics of the upper atmosphere is due to the net effect of heat production, loss and transport processes. The upper atmosphere has four channels of heat production.

(1) Absorption of solar UV, EUV and X-ray radiation, causing photodissociation, ionization and consequent reactions that liberate heat.

(2) Energetic charged particles entering the upper atmosphere through the magnetosphere (over high latitudes).

(3) Joule heating by the ionospheric currents, which become important over high latitudes, and

(4) Dissipation of tidal motion and gravity waves due to molecular viscosity and turbulence.

The loss processes are mainly due to the optical and infrared radiations by atomic and molecular species. Another factor in the heat balance is the transport of heat from one level to another. Through molecular conduction, heat is conducted from the thermosphere to the mesosphere. Large thermal conductivity above 200 km, because of low pressure ensures that the thermosphere is isothermal above 300-400 km. Below 100 km, Eddy diffusion is more efficient because of turbulent mixing. Eddies formed due to convection cells transport energy from the thermosphere to the mesosphere. Chemical transport of heat occurs when a specie, created in one place releases its absorbed energy in another place. After recombination of atomic oxygen at thermospheric heights, downward transport of molecular oxygen can heat up the mesospheric region (Fuller Rowell, 1995).

In general, some sort of a balance amongst these processes maintains the structure and dynamics of the upper atmosphere. Among the heat deposition agencies, apart from solar insolation, energetic particle precipitation and heat dissipation due to gravity waves and tides are very important. Occasionally they become very significant when sun becomes highly active and sudden changes in the solar wind and associated enhancements in energetic particle flux occur. These events are currently known as *space-weather* events.

It is believed that waves and tides are crucial in determining the heat balance and short period oscillations in the different atmospheric parameters are often attributed to the processes linked with the wave and tidal dynamics. Most of these forcings experience very strong filtering at mesopause altitudes making this altitude very important with respect to the dynamical coupling between lower and upper atmosphere.

Above 60 km, solar energy causes appreciable ionization. This engenders the partially ionized region in the atmosphere referred to as the *ionosphere*. As the atmospheric composition changes with altitude different chemical reactions dominate the loss processes at different heights. The above processes lead to the formation of D, E and F regions in the ionosphere. The D-region is formed due to ionization of [NO] by solar X - rays and Ly - $\alpha$ radiation. The E-region of the ionosphere, referred to as the dynamo region is formed mainly due to the photoionisation of $N_2$ and $O_2$ by EUV radiation in the wavelength band 80-100nm followed by chemical reactions. Primary ions in the E region are $[O_2^+]$ and $[NO^+]$. In the E region, ions remain tied to the neutral winds while electrons respond to the electromagnetic forcing. In the F region, electric and magnetic fields control the motion of both electron and ion. From 150 to 200 km, a gradual change in the dominant species occurs and $[O^+]$ takes over the $[NO^+]$ and $[O_2^+]$. These changes get reflected in the electron densities, and within this region two different loss mechanisms operate. Below 150 km, the molecular dissociative recombination reaction dominates while at greater heights it is the ion-molecule charge exchange reaction. When this transition region coincides with the level at which the F-region ionization production maximizes, the F region splits into $F_1$ and $F_2$ layers.

Above the $F_2$ layer as the downward diffusion of ions along the geomagnetic field lines is faster than the rate of ionization and recombination, the ion and electron

concentration decrease with altitude. Differential solar energy absorption in the atmosphere with latitude exhibits specific geophysical phenomena.

THE MAJOR ETIS PHENOMENA
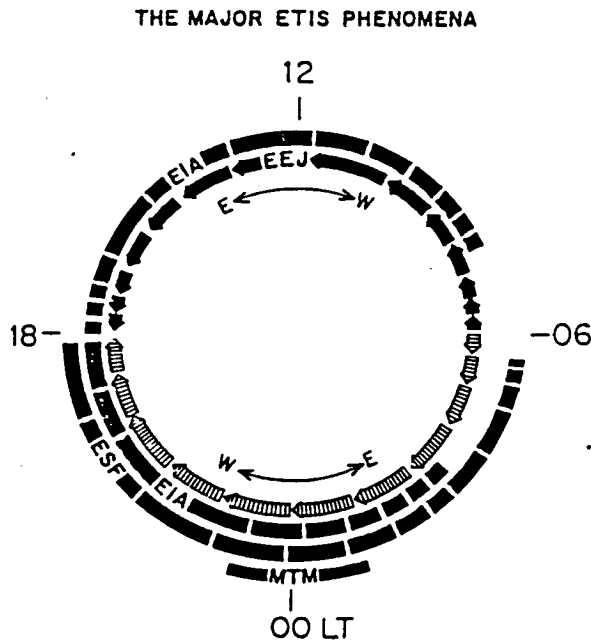


Figure 1.2 Local time dependance of various geophysical processes over low and equatorial latitudes. (After Abdu et al., 1997)

In the following section, a brief discussion on some of the equatorial thermospheric-ionospheric phenomena which forms the base for the present investigation is provided.

# 1.2# Upper atmospheric phenomena over low and equatorial latitudes:

### 1.2.1# Equatorial electrojet:

It is well known now that the effect of global scale tidal wind engenders global dynamo action in the E-region, where maximum polarization takes place because the ions move along with the neutral wind while the motion of electrons is governed by electric and magnetic fields. The orientation of these electric fields over the dip equator is east-west. Over the dip equator, the earth's magnetic field **B** is horizontal and northward. The crossed electric and magnetic fields provide an upward drift velocity $\mathbf{E} \times \mathbf{B}/B^2$ to the ambient plasma and a corresponding Hall current downwards. Because in the E region, larger collision frequencies of ions ensure them to be tied with the neutrals, charge accumulation takes place and an upward Hall

5

polarization electric field gets developed. Further, this Hall polarization electric field is perpendicular to the northward magnetic field and hence another Hall current is impelled in the eastward direction. Due to enhanced Hall conductivity in this region this current is at least 20 times the Pederson current and is referred to as the *equatorial electrojet (EEJ)*. Latitudinal width of this current is ± 3⁰ with respect to the dip equator and is centered around 106 km.
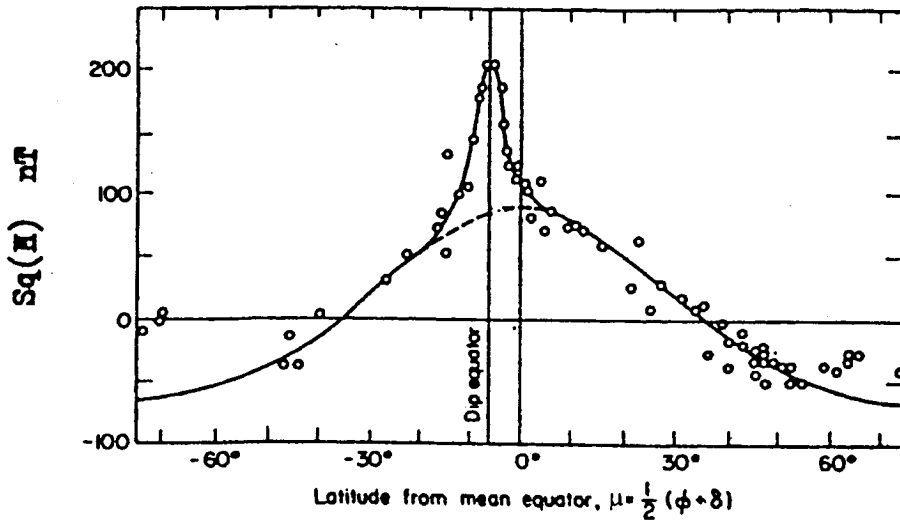


**Figure 1.3.** Latitudinal profile of the daily range, $\Delta H$ nT, of the geomagnetic horizontal field, H, on quiet days; on which the daily range $\Delta H$ nT across the dip equator is superimposed. (After Onwumechili, 1967)

Figure 1.3 shows the variation of the horizontal component of the earth's magnetic field at noon over different latitudes around the same longitude. The excess field (above the dashed line) over the equator is a direct manifestation of the EEJ. In situ measurements by rockets show the height of the peak current density to be around 106 km (Davis et al, 1967; Shuman, 1970; Richmond, 1977; Sampath and Sastri, 1979) and the semithickness to be 6 km. The differences in the instantaneous values of the H component and the average nighttime value from a location over the magnetic equator (for the Indian zone, Trivandrum, $\Delta H_{TRV}$) and another location away from the dip equator (Alibag, $\Delta H_{ABG}$) is usually considered as a measure of the strength of the EEJ. The intensity, height structure, day-to-day variabilities and the latitudinal width of the EEJ have been investigated by earlier investigators (Cahill, 1959; Maynard, 1967; Sastry, 1970; Burrows et al., 1977; Kane and Rastogi, 1977; Reddy and Devasia, 1981). Many Reviews on this subject are available in the

literature (Kane, 1976; Mayaud, 1977; Forbes, 1981; Reddy, 1981). Though several theoretical models of the equatorial electrojet have been developed till now (Untiedt, 1967; Richmond, 1973, a,b; Stenning 1981, 1985; Anandarao and Raghavarao, 1987) and wind effects are also incorporated, many aspects are not yet fully understood. Day to day variations in the peak height and width of the EEJ currents are the most important among them (Stenning, 1985; Reddy, 1989). On some occasions the polarity of the electrojet reverses in the daytime itself for a short duration and this is referred to as the *counter electrojet* (CEJ).

### 1.2.2# Counter Electrojet

One of the enigmatic features in the quiet time magnetic field variations is the phenomenon of 'counter electrojet' (CEJ). CEJ manifests as an abnormally rapid and large post-noon decrease in the field in the electrojet belt such that, $\Delta H$ relative to the steady nighttime level, becomes negative for sometime and recovers to its normal positive value after few hours (Gouin and Mayaud, 1967; Rastogi,1974; Mayaud,1977). This phenomenon typically occurs in the afternoon hours but at times even during morning hours. Sometimes the abnormal decrease and recovery of $\Delta H$ takes place without $\Delta H$ becoming negative and such events are termed as *partial counter electrojet*. It had been shown by means of numerical simulation studies that vertically upward winds are capable of reversing the electrojet. Supporting evidences for the electrojet region to get altered commensurate with the expectations of this hypothesis are available in the literature (Rahgavarao and Anandarao, 1980; Anandarao and Raghavarao, 1987). However, it had been shown recently that some abnormal combination of the global scale winds and tidal oscillations are also linked to CEJ (Somayajulu et al., 1993). They showed experimental evidences for the theoretically predicted distortions in the height structure of the polarization electric fields in the EEJ due to local effects of shearing zonal winds associated with the gravity waves and tides. They showed that on EEJ and CEJ days the mean zonal winds and the amplitude/phase of the tidal components are substantially different. So far, no conclusive causative mechanism could be identified and more comprehensive experimental work needs to be carried out to resolve this problem.

The basic physical mechanism of generation of EEJ has been dealt with in some detail in the chapter dealing with equatorial electrodynamical processes (chapter no. 5).

### 1.2.3# Equatorial-Ionization Anomaly (EIA)

The *equatorial ionization anomaly* (EIA) is one of the most prominent equatorial ionospheric/thermospheric processes and it refers to the development of a double humped structure in the latitudinal profile of the F-region plasma densities during daytime with the crests located at ±15-20° dip latitude and the trough situated over the dip equator. The EIA is formed basically due to the combined effect of charge independent **E×B** drift and subsequent plasma diffusion along the magnetic field lines. Above 150 km both electrons and ions, follow the electromagnetic forcing. They experience maximum **E×B** force over the equator and move upwards. Their diffusion along the magnetic field lines takes the plasma to higher latitudes. This results in an ionization trough over the dip equator and enhanced crests of ionization on either side of the equator. This process is also known as *fountain effect*. One of the classic representations of the EIA has been presented by Croom et al. (1959) wherein they showed the anomalous electron density distribution during noontime at different heights with respect to latitudes along a longitude sector using a chain of ionosondes. In addition to the day to day variabilities, EIA exhibits strong seasonal and solar cycle dependence (Rao and Malhotra, 1964; Sivaraman et al., 1976; Rastogi and Klobuchar, 1990; Walker et al., 1994) as well as longitudinal dependence (Lyon and Thomas, 1963; Walker et al., 1980). This phenomenon is an excellent example of E and F region coupling as the integrated strength of the EEJ shows one to one correlation with the EIA strength (Raghavarao et al., 1978). Earlier investigations were carried out using ionosonde data, TEC measurements and topside sounder data (Anderson, 1973, 1981). Optical techniques using 630.0nm thermospheric emission were used for the study of the retrieval of the EIA (Sridharan et al., 1993). After the development of the dayglow photometer (DGP) (Narayanan et al., 1989; Sridharan et al., 1992a) and Multiwavelength daytime photometer (MWDPM) (Sridharan et al., 1998), the tracking of EIA could be done using optical methods even during daytime (Sridharan et al., 1993a; Pallam Raju et al., 1996). Many reviews on the EIA and associated

features exist in the literature (Moffet, 1960; Raghavarao et al., 1988a; Sastri, 1990; Abdu et al., 1991).

Further relevant details on EIA to the present work have been provided in chapter 5 dealing with the results from coordinated optical and radio probing techniques.

### 1.2.4# Neutral Anomaly (NA)

Using latitudinal distribution of $N_2$ from OGO – 6 satellite data, Hedin and Mayr (1973) showed that there is an enhancement of $N_2$ by ~ 20% at ~18° dip latitude and a trough over the dip equator during 1700 h LT. However, there was a crest over the equator during morning time at ~0600 h LT. This anomalous behaviour of neutrals indicating a geomagnetic control in their latitudinal distribution of neutrals is referred to as *Neutral Anomaly* (NA) (Figure 1.4). The NA was suggested to be due to the ion-drag experienced by the neutrals due to the crest of excess ionization generated as a consequence of the EIA. Higher electron densities at the EIA crests offer larger resistance to the zonal wind motion which is responsible for the transport of neutrals from the day to the night side and hence enable the pile up of neutrals over the crest locations. Thus EIA plays an important role not only in plasma density distribution, but also in the latitudinal distribution of neutrals and hence provides an evidence for the ion - neutral coupling.

### 1.2.5# Equatorial Temperature and Wind Anomaly (ETWA)

After the above plausible explanation of NA to be due to enhanced drag offered by the EIA crests, one would expect to see enhanced neutral temperature at the crest locations and simultaneously reduced zonal winds. The first experimental evidence to this effect was obtained by Raghavarao et al. (1991, 1993) using DE-2 satellite data. This phenomenon referred to, as the *equatorial temperature and wind anomaly* (ETWA) is one of the classical examples of the thermosphere-ionosphere interaction. Simultaneous measurement of plasma densities, neutral zonal winds and neutral temperatures along a given longitude revealed the zonal wind velocity to be maximum at the dip equator collocated with the trough in the plasma densities and a minimum in the zonal winds was seen at the crests of the EIA. Also the neutral temperature enhancements were collocated with the EIA crests and a minimum in zonal wind. ETWA has been suggested to be associated to the frictional force
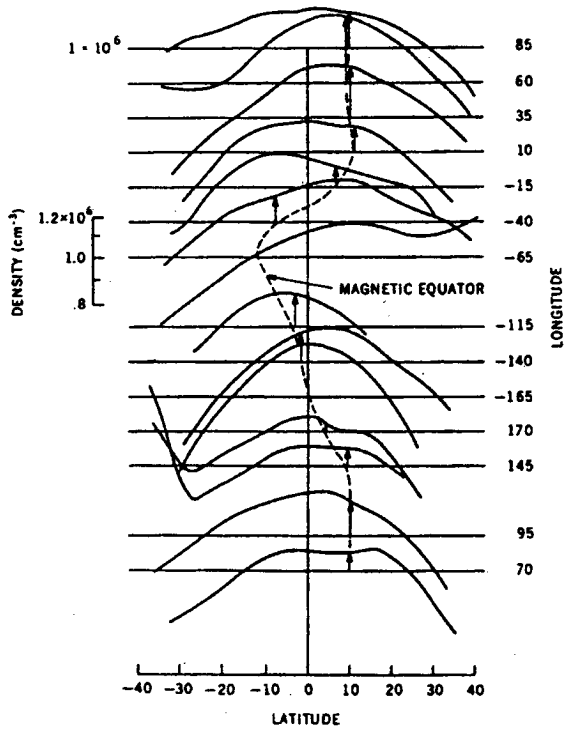
**Figure 1.4** Representation of Neutral anomaly (NA)(After Hedin and Mayr, 1973)
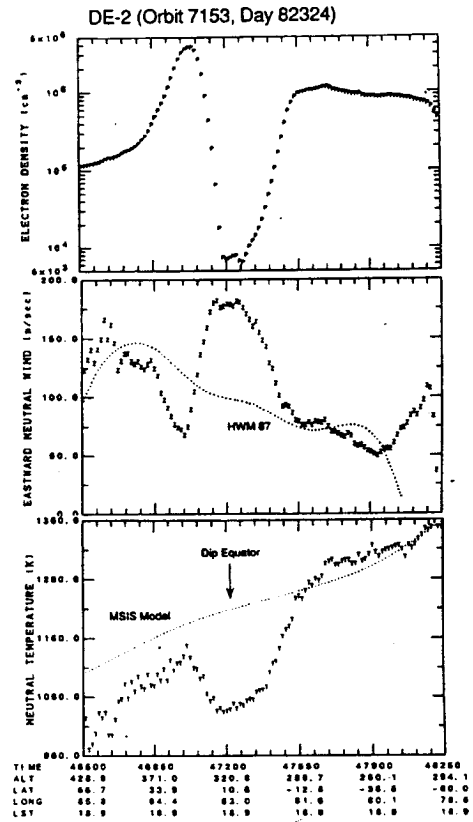
**Figure 1.5.** Representation of equatorial equatorial temperature and wind anomaly (ETWA) (After Raghavarao et al., 1991)

experienced by the neutrals, which in turn is proportional to plasma density. At the trough of the ETWA, less electron densities would offer less drag force and hence the wind magnitudes would be larger when compared with those at the crests. This sort of modulation in the zonal wind motion affects the transfer of heat to other longitudes thereby, resulting in a latitudinally varying temperature profile with a trough over the dip equator and two crests collocated with the EIA crests. In order to find an appropriate mechanism for the generation of ETWA a theoretical simulation using neutral thermospheric model (Fuller Rowell and Rees, 1980; Fuller Rowell et al., 1994) with a parameterized ionospheric model (Daniell and Anderson, 1995; Daniell et al., 1995) was carried out (Fuller Rowell, 1997). The increase in the temperature has been suggested to be due to chemical heating in this study. The above study reproduced the EIA and wind fields similar to that observed by WATS (wind and temperature spectrometer) on board theDE-2 satellite, but was not successful to explain the ETWA completely. Recently Pant (1998)                    with a semi-

empirical approach using MSIS-90 model and DE-2 satellite data, suggested this heating to be a combined effect of ion drag and chemical heating.

So far, our understanding in the ETWA has been limited to the data obtained from WATS on board the DE-2 satellite data during 1981-82 (solar maximum period). Most recently, Raghavarao et al. (2001) analyzed the neutral temperature experiment on board the AE- E data during 1976-77 (solar minimum period). They revealed the presence of temperature anomaly even during that period. Unavailability of the wind parameters restricted them to investigate the wind anomaly and hence they quote this as `equatorial temperature anomaly' (ETA). They showed that like the EIA, the ETA suddenly disappears after 1400 LST, indicating the EIA to be a prerequisite for the ETA formation. However, day to day variation and behaviour of ETWA / ETA under varying geophysical conditions is unknown and need much more investigations.

### 1.2.6# Midnight temperature maximum (MTM)

The maximum in the neutral temperature around midnight hours over low and equatorial latitudes is referred to as the `midnight temperature maximum' (MTM). The first groundbased observations of certain manifestation of the MTM were made by Greenspan (1966) and further by Nelson and Cogger (1971) using 630.0 nm photometers. They reported significant enhancements in the redline intensities. Latter, Behnke and Harper (1973) explained the observed enhancements to be due to the downward movement of F layer associated with the MTM. With NATE experiment in the AE satellite data, characteristics of MTM like latitudinal width, amplitude and time of occurrence are shown to exhibit high degree of variability (Spencer et al., 1977, 1979; Herraro and Spencer, 1982). Over Indian zone, Ranganath Rao and Sastri (1994) reported the MTM associated phenomena using ground based 630.0 nm spectrophotometry. A possible generation of this MTM has been proposed by Mayr et al (1979) to be due to the ion-neutral momentum coupling associated with the diurnal variation in the zonal winds and ion density. It is an example of energy transfer between different tidal modes. The above explanation was later supplemented by Herraro et al (1983). However, simulation studies (Fesen, 1996) using the NCAR - TGCM model could not reproduce the MTM inspite of using realistic solar forcings and ion - neutral momentum coupling in it. But, once the effects of waves of lower atmospheric origin were included, the MTM could be successfully reproduced (Fesen,

11

1996). In fact, because of lack of sufficient investigations MTM could not be understood fully.
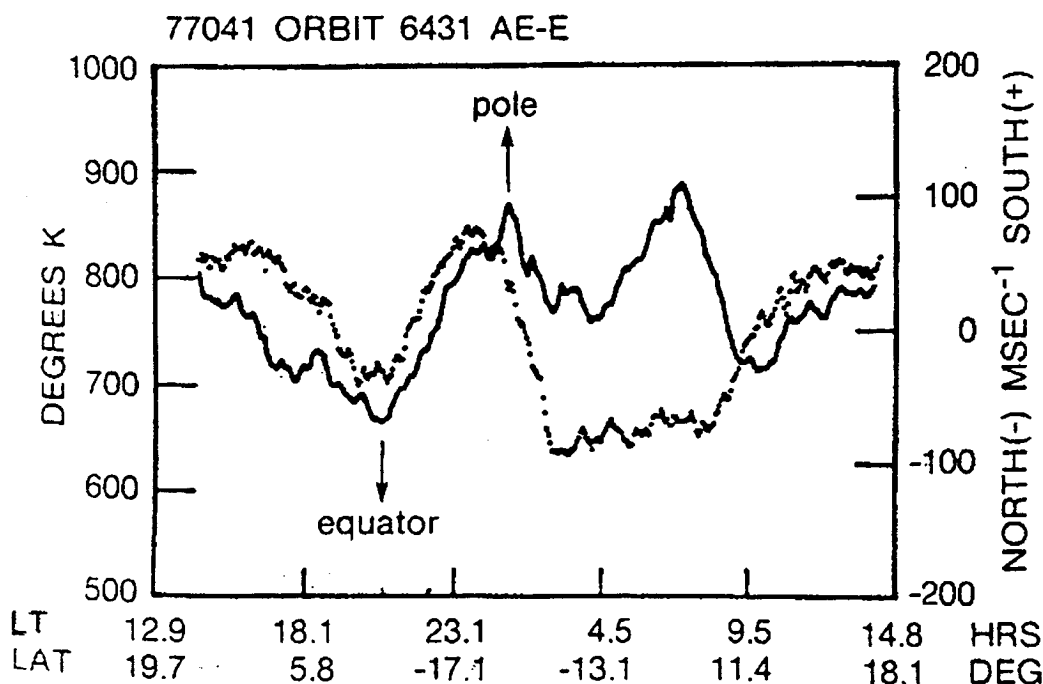


Figure 1.6. Example of measured diurnal exospheric temperature and meridional wind (solid line) showing a large secondary temperature maximum. (After Spencer et al., 1977)

## 1.2.7# Equatorial Spread-F

The other important and probably one the most enigmatic phenomenon of the nighttime equatorial ionosphere is the *equatorial spread-F* (ESF). This refers to one of the turbulent conditions of the nighttime equatorial ionosphere, wherein plasma density irregularities, the scale sizes of which range from a few centimeters to several hundred kilometers, get generated under favourable conditions, mainly due to plasma instabilities within them. ESF manifests itself in a variety of ways. For example, it is seen as 'scattered echoes' in the groundbased ionosondes, 'plumes' in the VHF radars, 'airglow intensity bite outs' in the optical airglow measurements, 'bubbles' in the in-situ satellite measurements, VHF and UHF 'scintillations' in the groundbased beacon receivers.

The Rayleigh Taylor instability is believed to be the primary agency for the development of ESF, which destabilizes the equatorial F-region making the situation conducive for a hierarchy of instabilities to take over (Haerendal, 1974). During post
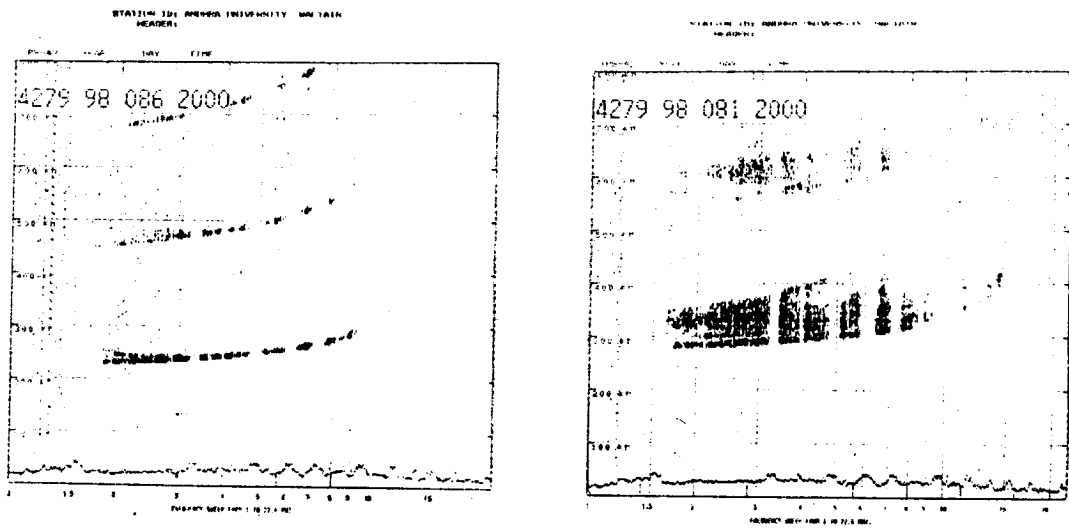
**Figure 1.7.** Example of a non ESF (left) and an ESF (right) day over Waltair as seen in ionograms.

sunset hours over the magnetic equator, the F layer gets lifted to great heights and a steep density gradient in the bottomside gets developed due to the combined action of the uplifting and the chemical recombination in the E and F layers. The situation is similar to the hydrodynamic Rayleigh - Taylor (R-T) instability where lighter fluid supports the heavier fluid (Ossakow, 1981; Mendillo et al., 1992; Sultan, 1996

). Growth and further development of R-T instability depends on the background electron density gradient, electric fields, winds and amplitude of seeding perturbation. These plasma depletions are field aligned and therefore map along the magnetic field lines to even beyond ±15° latitudes. In the zonal direction it may typically extend around 100-200 km and drift towards east with a velocity of 50-150 ms$^{-1}$.

There is a strong longitudinal dependence in the seasonal occurrence pattern of ESF. In the Atlantic region its occurrence is most favoured during winter, in the pacific region during summer and the South American and Asian zone during equinoxial periods (Maruyama and Matuura, 1984; Tsunoda, 1985; Aarons, 1993). Extensive theoretical studies have been carried out towards a comprehensive understanding of ESF (Heelis et al, 1974; Farley et al, 1986). Simulation studies by linear and nonlinear models have brought forward the important aspects related to the ESF (Zalesak and Ossakow, 1982; Sekar and Raghavarao, 1987; 1995; Sekar et al., 1995).

13
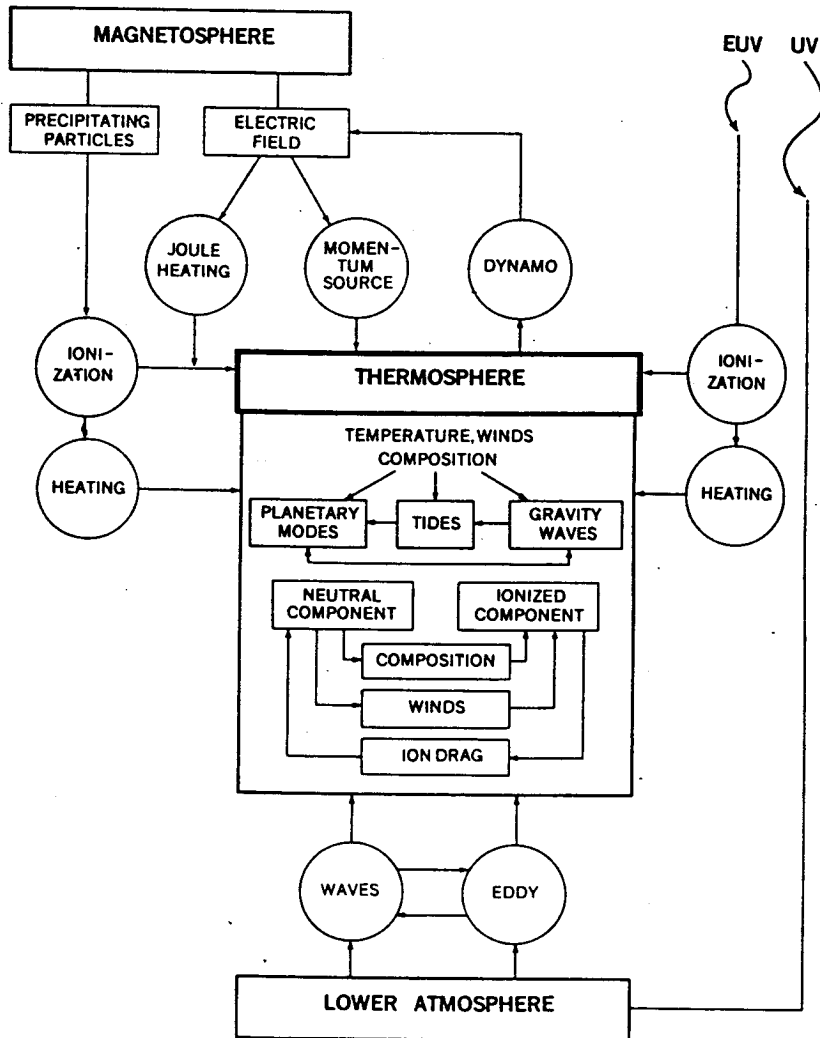
**Figure 1.8.** A schematic diagram for the lower and upper atmosphere coupling mechanisms.

Apart from these processes exhibiting the importance of ionosphere-thermosphere coupling, vertical coupling between different atmospheric regions i.e. the lower, middle and upper atmosphere is very important. A small perturbation originated in the lower atmosphere may reach the upper atmosphere. It may even generate the electric fields (Anandarao et al, 1977) and subsequent electrodynamical effects. Further, in the F region, it may provide a seeding perturbation for the RT instability that may result in the ESF. As a whole, at a given instance, the whole atmosphere behaves as a strongly coupled system. In the next section, a brief discussion on the middle and upper atmosphere coupling is provided.

# 1.3# Middle atmosphere-upper atmosphere-coupling

The atmosphere, with a complex web of processes and phenomena with rather loosely defined boundaries between any two regions, behaves as a strongly coupled system. The coupling between these regions is through neutral as well as electrodynamical process (Hocking, 1996; Wickwar and Carlson, 2000).

As discussed earlier the electrodynamical coupling is essentially through electric and magnetic fields. Electric fields generated in the E-region, due to global polarization between ions and electrons by neutral winds, gets mapped to the F region by means of the conducting geomagnetic field lines. In the E region, these E-W zonal electric fields cross with the N-S magnetic fields giving rise to the EEJ. The same E region electric fields away from the dip equator get mapped to the F region and crossing with the N-S magnetic fields result in the EIA.

Neutral dynamical coupling is through waves and tides. Usually, they have their source in the lower atmosphere and grow in amplitude as they propagate upwards into higher regions of the atmosphere. In the absence of any dissipation, the wave amplitude is expected to grow with increasing altitude. However, as the wave approaches the critical level (where its phase velocity is equal to the background wind velocity) or when the wave amplitude grows sufficiently large, it may break and cause turbulence. In this process the wave looses its energy. These wave breaking/saturation processes occur intermittently in the mesospheric altitudes where the wind reverses its direction resulting in shears. A major consequence of gravity wave saturation in the mesosphere, which has implications to the thermosphere, is the formation of the turbopause. Turbulence is generated through GW breaking, and so will be intermittent both in time and space depending on the characteristics of the gravity waves. The eddy diffusion coefficient depends upon the strength of the turbulence. From theoretical considerations, Lindzen (1981) showed that the eddy diffusion coefficient in the upper mesosphere and lower thermosphere could be drastically different from summer to winter seasons. These results also showed an upward shift in the altitude where molecular diffusion equals eddy diffusion from winter to summer. Above turbopause, the turbulence plays no significant role in the constituent distribution as it is damped by the increasing kinematic viscosity. The constituents are distributed vertically by molecular diffusion according to their respective

are distributed vertically by molecular diffusion according to their respective molecular weights. Hence, the turbopause level is an important factor in determining the concentrations of the constituents at different levels in the upper atmosphere. Chandra and Herman (1969) had shown from theoretical analysis that some of the changes in F region during magnetic storms can be explained by changing the turbopause level and consequent neutral composition (atomic oxygen) higher above. During 6 Jan 1997 space weather event, Sridharan et al. (1999c) reported an enhancement in the 630.0 nm dayglow intensity and a plausible explanation of this is attributed to be due to the variation of turbopause height which redistribute the atomic and molecular species higher above.
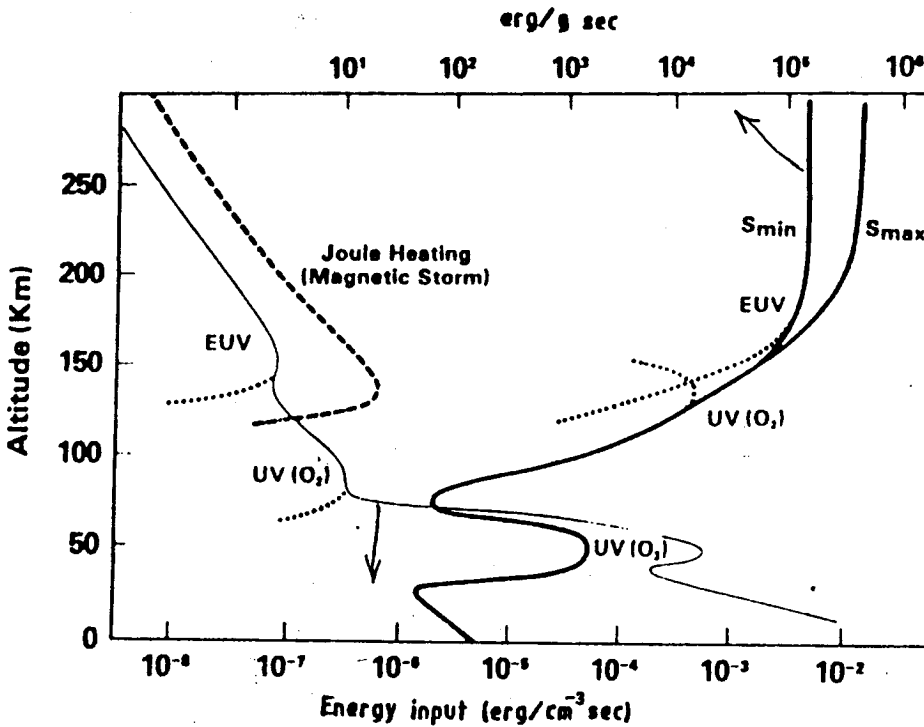


**Figure 1.9.** Schematic of the energies involved in different atmospheric regions.

Apart from the above, energy leakage from the lower atmosphere to the upper atmosphere has its own importance. Whereas, the radiative heat input per unit mass is quite high in the thermosphere compared to that in the middle atmosphere, in absolute terms (input per unit volume) it is quite small in the thermosphere compared to that in the middle atmosphere (Figure 1.9). Thus, in general, energy transfer downwards is insignificant for the energetics of the middle atmosphere. On the other hand, for the same reason, even a small leakage of energy from the middle atmosphere may have profound effects on the thermosphere (Subbaraya, 1994).

# 1.4# Upper atmospheric effects of Gravity waves and tides

The diurnal and semi-diurnal tides excited in the troposphere and stratosphere, grow in amplitude with height and higher above they drive the atmospheric dynamo in the ionospheric E region. Ionospheric phenomena like EEJ and CEJ are still open ended problems and as discussed in the earlier section probably the key lies in the role of waves and tides. Another consequence of gravity waves and tides in the upper atmosphere is the formation of blanketing sporadic E layers at mid latitudes (Whitehead, 1971). Wavelike perturbation in electron densities upto F region have been reported on several occasions (Hines, 1960). For example, for the growth of ESF, the need for a seed perturbations has been suggested to be due to gravity waves (Booker, 1979). Recently, Prakash (1996) invoked a mechanism involving gravity wave winds and the E region electron density irregularities which, in turn make the Pedersen and Hall conductivities non-uniform. The resulting electric field fluctuations in the E region have the potential to get mapped to the F region heights and to act as seed perturbations for the ESF. Meriwether et al. (1997) have shown evidence for the orographic wave heating in the equatorial thermosphere-ionosphere system using Fabry-Perot interferometer observations of 630.0 nm night glow emission.

Apart from this direct manifestation, indirect manifestations may also be of great importance in the lower and upper atmosphere coupling. Wave and tidal energy deposition in the mesopause region is of great significance in this respect. The thermal state of the mesopause, for which waves and tides contribute ~30% of the overall energy budget, is very important and only certain wave modes are allowed to pass to regions higher above. Additional wave and tidal energy budget may affect the eddy diffusion coefficient, which may alter the turbopause altitude, and hence the dynamical processes higher above.

It appears that many of the highly dynamical processes in the mesosphere-thermosphere-ionosphere system have some association with the wave and tidal processes generated in the lower atmosphere. Investigations on these aspects are still in the development stage.

## 1.5# The present work

The present work uses optical instruments like the 'Dayglow photometer', 'Day-Night photometer' and 'Multiwavelength Daytime Photometer', which are unique instruments and has enabled the systematic observations of daytime airglow processes *for the first time*. Focus of the thesis is on the mesosphere-lower thermosphere-ionosphere system, the scope of which is far reaching. For mesospheric and lower thermospheric studies, rotational vibration band of OH (~85 km) and $O(^1S)$ 557.7 nm (~105 and 220 km) emissions were monitored whereas for the thermosphere-ionosphere studies $O(^1D)$ 630.0nm (~220 and 250 km) was used alongwith ionospheric data from VHF backscatter radar and ionosonde. Effects of waves on, the daytime mesospheric temperature and the 630.0nm thermospheric emission were other objectives towards neutral dynamical coupling studies. For electrodynamical coupling, variabilities in the E-region electric fields and the 630.0nm emission have been used. Apart from these aspects, contribution towards the basic understanding of the daytime $O(^1S)$ emission processes, the limitations of its usage for coupling studies and further, the effects of space-weather related issues through a case study addressing to the high latitude – low latitude coupling on low latitude 630.0 nm emission also form a part of the present work.

# 2# Instrumentation

## 2.1# Introduction:

Airglow emissions emanating from different altitudes due to a variety of photochemical processes are also sensitive to the dynamical processes and hence can be used as good tracers for the study of the same. These emissions, in general, had been used widely for the investigation of dynamical and chemical processes in the mesosphere thermosphere-ionosphere region during nighttime conditions. Daytime airglow monitoring had always been a challenge, due to the presence of strong Rayleigh scattered solar background which is more intense by several orders of magnitude. In the past, very few attempts were made to detect and isolate the daytime airglow i.e. the faint dayglow emission from the high solar background with little success, and as a result, the measurements were not done on a regular basis. The present study and the instrumentation is very important and unique in this regard. After a brief introduction of the earlier studies in the daytime detection, details of the instruments used in the present study will be discussed in the sections to follow.

Blamont and Donahue (1961, 1964), were the first to detect NaD dayglow emission using a Zeeman photometer. They used the polarization property of the resonant lines subjected to the Zeeman effect. The principal element of the photometer had been a cell of hot sodium vapour, through which the skylight was passed. Shift in the Zeeman component of the resonant line, was used to detect the dayglow signal (Figure 2.1). Gadsden etal (1966), introduced a correction factor to the observed NaD (sodium) intensities which was called for due to a systematic error in the observed data. However, this method which is rather involved is applicable to the resonant lines only.

Noxon and Goody (1962) and Noxon (1968) made a significant contribution in the detection of 557.7 and 630.0nm dayglow, with a scanning polarimeter. This instrument was designed to respond only to changes in the degree of polarization in the source under study, and was insensitive to variations in the intensity of the source. Rayleigh scattered sunlight which is polarized, alongwith unpolarized dayglow were passed through a rotating slit, half of which was covered with a polarizer and the other half with a compensating attenuator. After the polarizer, the dayglow signals get

modulated significantly. Spectral scanning of both parts of the slit will show the presence of the dayglow signal (Figure 2.2). Though successful, real fluctuations in the polarization and angle dependent background cancellation etc. make the instrument rather involved, and no systematic, continuous observations have been reported in the literature.
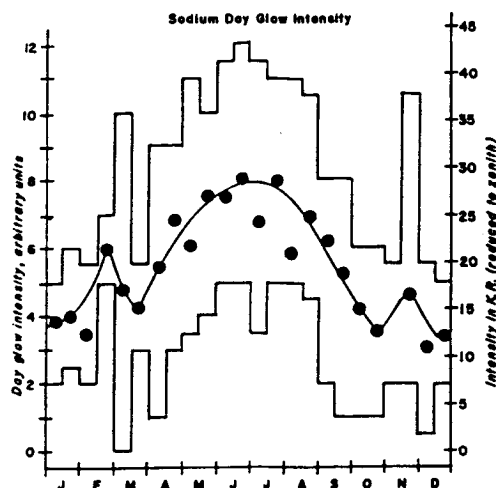


**Figure 2.1.** Sodium day-glow and twilight-glow intensity at Haute Provence (after Blamont and Donahue, 1964)
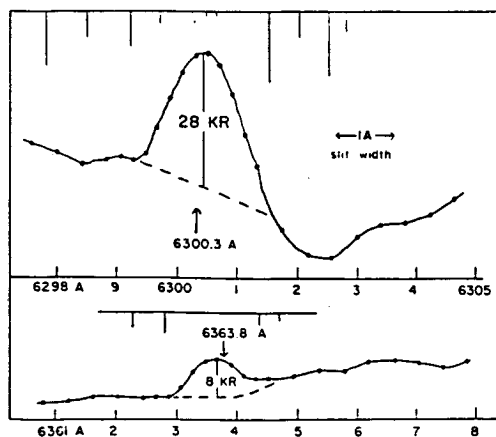


**Figure 2.2.** The 6300 and 6304 A OI lines in the dayglow. Expected line positions are indicated by arrows. Vertical lines at the top of the diagrams are the positions and relative intensities of Fraunhoffer lines in the solar spectrum (after Noxon and Goody, 1962)

Jarret and Hoey (1963) made an attempt to monitor 630.0nm dayglow using a low resolution Fabry Perot and a photographic plate. Ambiguity in the signal separation from Fraunhoffer features did not allow further development, because they too can form fringes at same wavelength region.

Bens et al. (1965) used a polyetalon system for 630.0nm dayglow detection. The system consists of one high order Fabry-Perot etalon made to scan at high

resolution, whereas a second low order etalon is tuned to a fixed wavelength, and this alongwith an interference filter, acted as a monochromator. They reported the thermospheric temperatures to be around 1200°K.
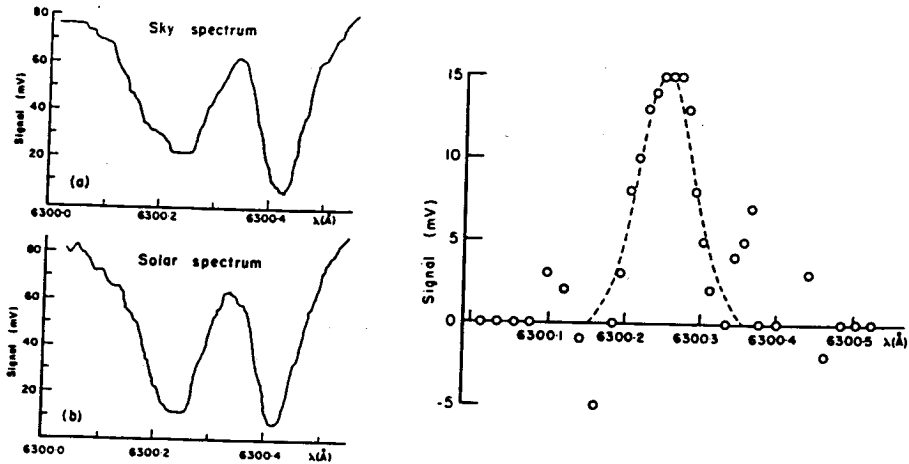


**Figure 2.3.** (Left side) Chart record of the spectrum from the daytime sky(a) and from the sun(b) and on Right side is the result of subtraction the of fig (b) from that of fig (a) (After Bens et al, 1965)

Barmore (1977) reported measurements of OI630.04 nm dayglow emission, using a polyetalon pressure scanning interferometric optical spectrometer (PEPSIOS). They recorded spectra both from the sky and from the sun in a wavelength band of 629.95 to 630.17nm. They concluded that the derived temperatures from the OI 630.04nm dayglow emission were consistent with backscatter radar measurements and differed significantly from model predictions.

With a similar instrument like Bens et al. (1965), Cocks and Jaka (1979) obtained the thermospheric temperatures and wind velocity. A large high resolution Fabry-Perot Interferometer (FPI) and a smaller, low resolution FPI were used in series with an interference filter to obtain spectra of the skylight and direct sunlight over the same spectral interval. The two spectra were normalized at a wavelength representative of the local continuum near 630.03 nm and the emission line then, gets isolated by the subtraction of the normalized sunlight spectrum from the sky light spectrum.
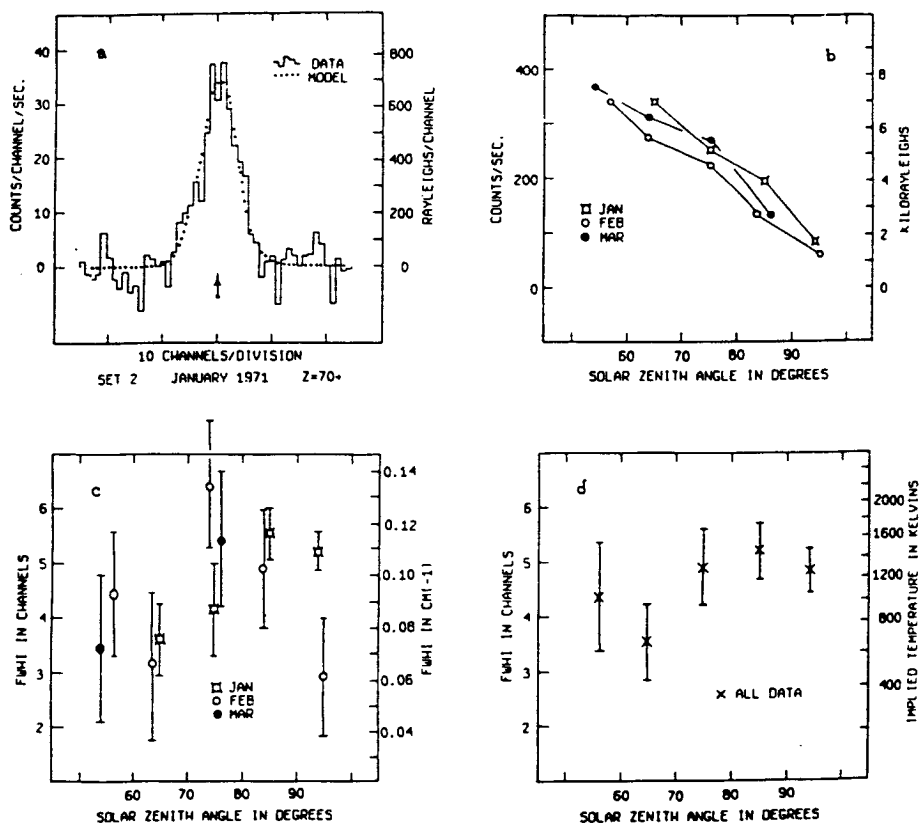
**Figure 2.4.** The 6300 A oxygen emission line obtained by averaging a number of scans of the zenith day sky after subtracting the background of scattered sunlight. The small arrow indicates the expected position of the emission line (a), the integrated count rates of the emission line (b), the widths of the 6300 A emission line (c) and the width of the 6300 A line (average of all data groups). (After Barmore, 1977).
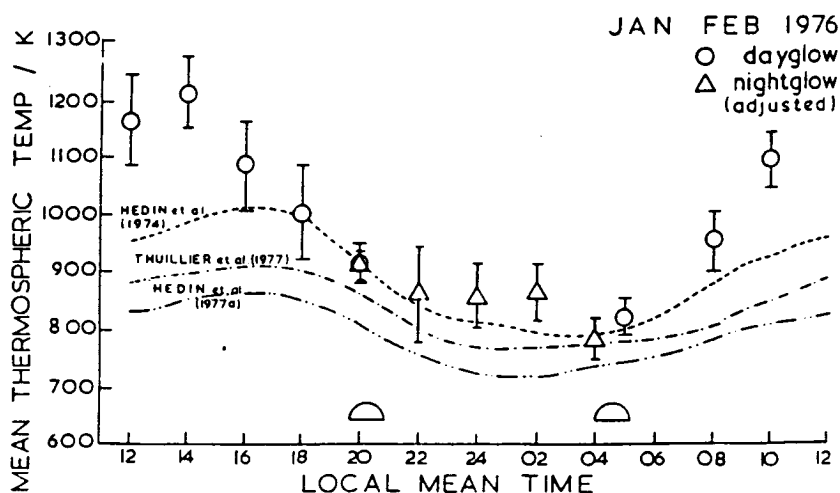


**Figure 2.5.** Mean diurnal variation of thermospheric temperature. The smooth curves illustrate the variations predicted by models of Hedin et al (1974), Thuillier et al.(1977) and Hedin et al (1977). (After Cocks and Jaka, 1979).

The techniques mentioned above are rather involved with each one having its own limitations. The main problem in all the instruments had been the stability and complexity. Techniques involving multiple Fabry Perots were complicated due to the criticality of the optical alignment. These were limited to laboratory conditions and were not ideally suited for field operations. Owing to the above difficulties, the earlier attempts to measure dayglow had been mainly exploratory in nature and only very few reports appear in the literature.

Desai et al (1979) suggested a new photometer with a unique radial chopping mechanism for the detection of resonantly scattered emission from artificially released lithium clouds in the sky so as to track their movement during daytime to infer the atmospheric dynamical parameters. In this technique an untuned broad band interference filter was used. Radial chopping mechanism was not so efficient to separate out the contribution in two zones distinctly and a contribution from one zone into the other zone could not be avoided, and this led to improper background estimation. Narayanan et al. (1989) made a breakthrough in the form of a development of dayglow photometer, using a similar principle for the optics, but with many other improvements both in optics and data handling techniques. Further development was made with an improved and effective mask assembly by Sridharan et al. (1992a). The new method though very effective, was limited to only one wavelength at any given time. Further development of a novel spiral mask (Sridharan et al., 1993) and its use in the multi-wavelength daytime photometer (MWDPM) (Sridharan et al., 1998) enabled simultaneous measurement on multiple wavelengths of interest. In order to investigate the complex processes of the atmosphere that continue to occur during both day and night, round the clock measurements are necessary. Conversion of the dayglow photometer into a day-night photometer (DNP) by suitable diversion of the optical ray path after the filter to the photomultiplier, enabled the detection of relative intensity measurements of 630.0 nm airglow literally round the clock.

The Dayglow Photometer (DGP), Multiwavelength Daytime Photomter (MWDPM) and Day-night Photometer (DNP) are used in the present study and will be discussed in detail in the sections to follow. As these instruments contain critical components like interference filter, Fabry-Perot etalon and a photomultiplier tube, a brief introduction to the various elements will be presented below.

## 2.2# Dayglow Photometer (DGP):

The Dayglow photometer (Narayanan et al., 1989; Sridharan et al., 1992a), which has been used in many of the earlier studies successfully, is one of the instruments used for the investigations carried out and reported in this thesis.
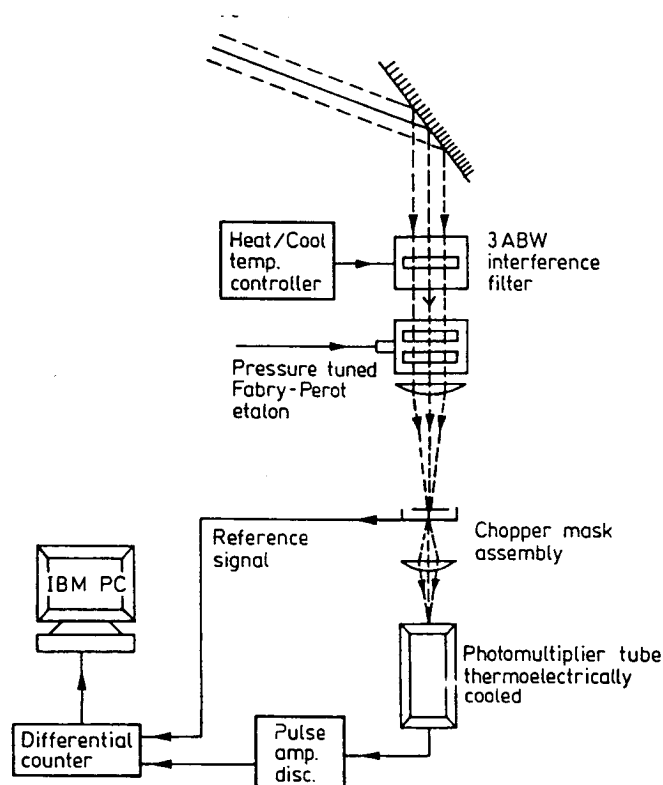


**Figure 2.6.** Schematic diagram of the Dayglow Photometer.

This instrument is capable of retrieving faint emission line intensities embedded in the strong solar background on a single wavelength and is very stable and easy to operate. The dayglow photometer consists of a low resolution Fabry Perot etalon, an interference filter, a chopper mask assembly, photomultiplier, and an in-house developed data acquisition system. The Schematic diagram of the dayglow photometer is shown in the figure 2.6.

## 2.2.1# Instrument Details:

**Interference Filter:**

Interference filters are wavelength selectors that allow transmission of a predetermined wavelength while rejecting or blocking other wavelengths due to constructive and destructive interference taking place at partially reflecting boundaries within the filter. These boundaries are formed by alternating thin layers of dielectric materials with high and low refractive indices. The optical thickness of the dielectric layers is selected so that the wavefronts generated as a result of multiple internal reflections are in phase and reinforce the desired wavelength for constructive interference. Other wavelengths whose wavefronts are out of phase, undergo destructive interference and are not transmitted through the filter. The bandpass selection of an interference filter is made by repetitive vacuum deposition of thin layers of partially reflecting dielectric compounds on a glass substrate. A typical interference filter can have over fifty such layers, each one precisely controlled and evenly deposited over the preceding layer. The thickness of each layer is maintained at $\lambda/4$ of the central wavelength $\lambda$. Alternating layers of dielectric materials with high and low refractive indices make up a stack. A half wave layer ($\lambda/2$) or a multiple thereof, deposited between systematic stacks, forms a spacer layer. The bandwidth of an interference filter is determined by the ratio of the indices of the high and low dielectric materials, the number of layers in a stack and the number of half waves in a spacer. A spacer layer and adjacent stacks form a cavity. The number of cavities in the bandpass selection determines the overall shape of the transmittance curve. Behavior of a filter with the above said background, can be understood from the interference formula -

$$2\mu t \, Cos\theta = n\lambda \qquad (2.1)$$

where '$\mu$' is the refractive index, t is the path length, $\theta$ is the angle of incidence, n is the order of interference and $\lambda$ is the central wavelength. It is clear from equation (1) that any parameter, which can change '$\mu$', 't' or '$\theta$' will shift the central wavelength of the filter. The central wavelength can also change with increasing or decreasing temperature. This effect is due primarily to the expansion or contraction of the spacer layers and the concomitant changes in their refractive indices. With the deviation of

incoming radiation, from normal to the surface of the filter, the central wavelength will shift to a lower wavelength.

In DGP, a narrow band width(0.3 nm FWHM) 50mm diameter filter with a wavelength centered at 630.0 nm is being used. The central wavelength depends on the filter temperature and so it is essential to control the filter temperature. In order to maintain the characteristics of the interference filter all through the period of observations, the interference filter is housed inside a specially fabricated temperature controlled enclosure. The temperature is controlled to better than $1^0C$ which would at the most cause a shift in the central wavelength by 0.025 nm, well within an acceptable limit for photometric use. The temperature control has been accomplished by thermoelectric means using thermoelectric modules, solid state temperature monitoring and closed loop water circulation systems. The calibration of the interference filter, in terms of the central wavelength, bandwidth and temperature coefficient are usually determined beforehand and verified periodically.

## Fabry Perot etalon:

A Fabry-Perot interferometer consists of two glass plates, or fused silica plates, held accurately parallel to each other, at a fixed distance 't'. The spacers are normally made of quartz or invar. These plates are kept in optical contact with the spacers at three points. The facing surfaces of the plates are flat to better than $\lambda/50$ and are coated with metal or dielectric film of high reflectivity (~90%). If the refractive index of the medium between the plates is '$\mu$' and the angle of the incoming radiation with the normal is '$\theta$', then the condition for constructive interference is given by the same formula (2.1).

$$2\mu t \, Cos\theta = n\lambda$$

The distance between two fringes corresponding to '$\lambda$', i.e., the inter fringe distance, better known as the free spectral range (FSR) is given as

$$FSR = \lambda^2/2\mu t \qquad (2.2)$$

For photometric use, a low resolution ($n \approx 10^4$) FP is useful while for line profile determination, i.e. spectroscopic studies, high resolution ($n \gg 10^5$) FP is needed. The maximum Intensity of the central fringe, i.e., $I_{max}$, can be written as

$$I_{max} = I_0 (T/1-R)^2 \tag{2.3}$$

Where, $I_0$ is the incident intensity, 'T' is the transmissivity and 'R' is the reflectivity of the FP plates. For an ideal etalon,

$$T + R = 1 \tag{2.4}$$

The minimum intensity can be written as

$$I_{min} = I_0 (T/1+R)^2 \tag{2.5}$$

and the 'contrast' between of the fringes, represented by 'C' is given by -

$$C = I_{max}/I_{min} \tag{2.6}$$

$$\text{i.e.} \quad C = [(1+R)/(1-R)]^2 \tag{2.7}$$

Ratio of the free spectral range (FSR) to full width at half maximum (FWHM) of the emission profile is the measure of the 'finesse' of the etalon and the coefficient of 'finesse' is defined as

$$F = FSR/FWHM \tag{2.8}$$

It is clear from equation. (2.1), which is the basic equation for a Fabry Perot (FP) that three types of spectral scanning can be done. In the first case by the variation in refractive index 'μ' through a change in the medium between the FP plates or the pressure inside the etalon chamber. In the second case the spacing between the FP plates 't' can be used to scan the order of fringes and usually the variation in 't' is done using peizo electric transducers that change their length due to applied electric potential. In the third case the angle of incidence 'θ' is varied in order to effect a spatial scanning.

A low resolution, 20 mm usable aperture FP etalon is used in the DGP. This etalon is coated for a spectral response (500 – 650 nm) with very high reflectivity (~85%) material and has an air gap of 500 μm. The etalon is kept in a pressure tight brass assembly. The assembly is connected to a foot pump and a pressure gauge to monitor and maintain the pressure of the FP chamber. The free spectral range (FSR) for the 630.0 nm emission comes out to be ~ 0.4 nm. Initially pressure scanning is performed in order to align the fringes over the focal plane with the mask assembly. Pressure scanning, changes the refractive index that ultimately scans the fringe system.

## Mask System:

A variety of spatial scanning mask systems have been employed for the dayglow measurements which incidentally are very crucial. The first version of the mask assembly consists of a semicircular stator and a rotor masks (Figure 2.7) mounted concentrically. A corotating concentric metal disc with a slot which cuts across the opto-coupler, generates reference pulses.



(a)                                                    (b)
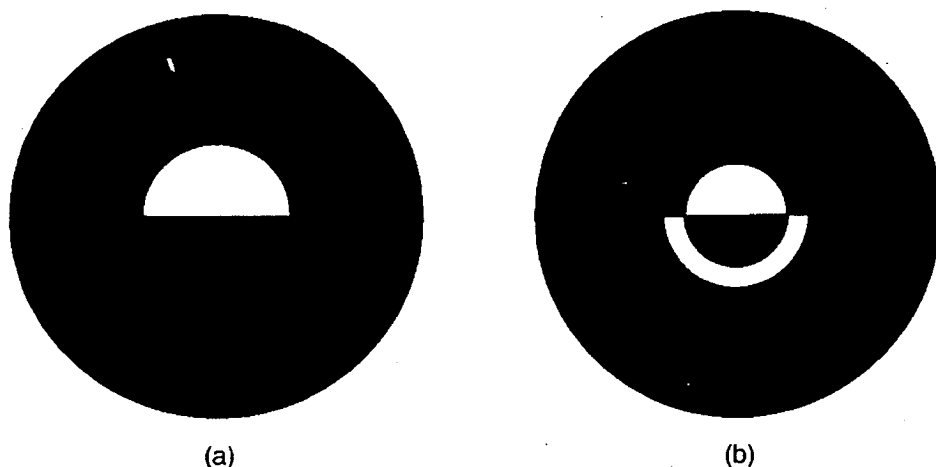
**Figure 2.7.** Semi circular dual mask system (a) the rotor and (b) the stator (After Narayanan et al., 1989).

The stator had two zones, one outer zone and another inner central zone. The outer zone had an outer diameter same as rotor with a semi-circular annular slit. The inner zone was a semicircular slit with radius equal to the inner radius of the outer zone's annular slit. When the masks are concentrically mounted, with the rotation of the rotor, light will be alternately allowed from the inner semi-circular and the outer annular zones. Emission fringes were aligned to fall within either the outer or inner zones of the stator, with the help of pressure scanning. As the rotor rotates at high speed of 1500 rpm, light from both the zones are alternated in quick succession of once in 25 ms. Such fast sampling becomes mandatory in order to overcome the atmospheric scintillation effects, which are normally slower by atleast a factor of two. The up-down counter synchronized with the reference pulses collects the incoming photons on the inner and outer zones separately. Among these one of the zone contains the photons corresponding to emission feature embedded on the solar background while the other zone contains photons of the solar background only in the immediate spectral vicinity. The difference between the signal intensities

corresponding to inner and outer zones represents intensities corresponding to the emission feature. The whole operation is controlled by a menu driven software.

The semicircular mask had certain limitations. When the stator and rotor components are aligned with either the inner or the outer zone, the transmitted signal is uncontaminated and the contribution from the other zone is nil. However, during the transition phase from inner to outer zones and vice versa there is always some contribution from the former. A new improved mask system was designed so as to overcome this problem of overlap between the inner and outer zones. The new mask, which is fabricated to the size as dictated by the optics, is made from high contrast films and the design is depicted in figure 2.8.



Stator                                   Rotor
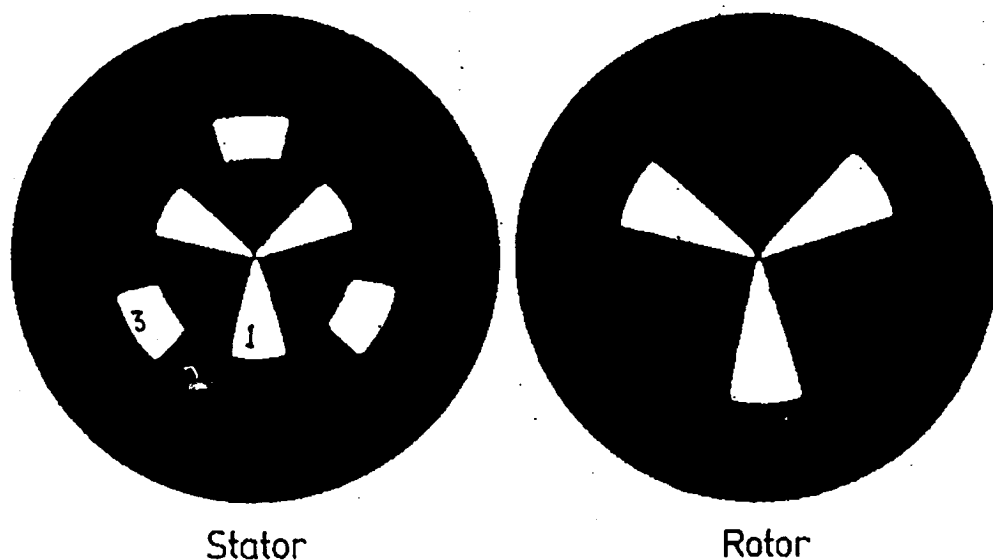
**Figure 2.8.** New mask assembly used in the dayglow photometer (After Sridharan et al., 1992a)

The zones of the stator are sub-divided into twelve sections of equal areas. In a quarter while one section (1) remains transparent, the other two sections (2 and 3) are made completely opaque in the zone area. In the area corresponding to the outer zone, a small section, which is equivalent in area to the section 1 is left transparent and made to match section 3. The rotor mask has sections that are divided in a similar way, but the transparent and opaque sections are extended to cover both the inner and outer zones of the stator. When the transparent portions of the rotor are aligned with those of the inner zone of the stator, light passes only through the inner zone and has the emission feature and contribution of the background continuum. As the rotor moves, it encounters a completely blank area before it starts aligning with the outer zone where only the background contribution is received by the photo-multiplier tube.

As it rotates, once again the rotor encounters a blank area before the inner zone aligns with it. The sequence is repeated. The light that passes through any one of the zones is totally uncontaminated by the light sneaking through the other zone. It is important to state here that the mask covers nearly 0.08nm in the wavelength scale. This allows the solar background and signal to get smoothened. This smoothening becomes very important to make the solar background uniform over the full mask plane, in order to enable proper subtraction of the background. This aspect will be discussed in a separate section.

## Photomultiplier Tube:

Photomultiplier tubes (PMT) are extremely sensitive light detectors providing a current/counts proportional to the incident light intensity. It consists of a photocathode, which emits electrons in response to the incident photons by photoelectric effect. The ratio of the ejected photoelectrons for each incident photon is the quantum efficiency of the photocathode. These photoelectrons are accelerated electrostatically and are focussed onto the first dynode of an electron multiplier. On impact, each electron liberates a number of secondary electrons. These secondary electrons are once again electrostatically accelerated and focussed onto the next dynode. This process is repeated many times, and the secondary electrons from the last dynode are eventually collected at the anode. The ratio of secondary to primary electrons emitted at each dynode depends on the energy of the incident electrons and is controlled by the inter-electrode potentials in addition to the dynode material. By using a variable high voltage supply and a voltage divider network, to provide the inter-electrode voltages, the photomultiplier can be operated over a wide dynamic range. Depending on the coating on the photocathode the wavelength response changes. In the present photometer an extended red sensitive, 14 stage PMT (EMI 9863A) with S-20 cathode of sensitivity $\sim 200\mu A/Lumen$ has been used. It has a quantum efficiency of $\sim 7\%$ for 630.0 nm and a gain of $\sim 10^5$.

## 2.2.2# Setting the DGP for operation:

To ensure the proper detection of the emission line, one has to be careful enough to set the instrumental parameters properly and a standard procedure for this purpose has been evolved:

30

Optical alignment is the first major step. It is accomplished with the help of tiling screws that are placed at 120° separation in the periphery of the FP etalon. The fringes are focussed concentrically onto the mask assembly. Before doing this, one has to ensure that stator and rotor mask too are aligned concentrically and outer and inner zones are getting scanned uniformly. These tests are very crucial for the further operations. The alignment of FP with the mask plane ensures that optical axis is coinciding with the mechanical axis of the DGP at the aperture plane.
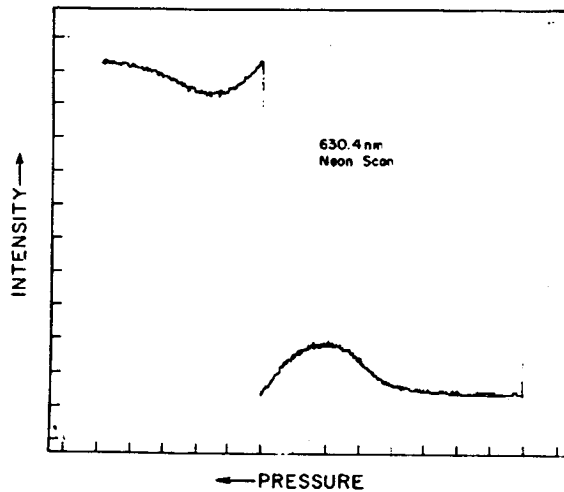


**Figure 2.9.** Pressure scan of Ne- spectral lamp. A nearly symmetrical differential profile about the mean can be observed clearly (After Narayanan et al., 1989).

Once the optical alignment is over, the next step is of electronic gating of the counters and balancing of the gates. It is important to state here that reference pulses from the chopper disc indicate the rate at which the chopping between the areas of the inner and outer zones takes place. The chopper reference pulses are used to fix the time delays and gate-widths for enabling the PMT to accumulate photon counts in a synchronous manner. After the initial time delay $t_{D1}$, for a zone (inner or outer), a gate is opened for a certain duration of time $t_{G1}$, the gate width during which the incident photons are counted by the synchronous counter C1. Similarly the time delay and gate width for the second zone are represented by $t_{D2}$ and $t_{G2}$. These time delays and gate widths can be suitably adjusted so as to account for any dissimilarity in the transparent areas of the masks and to achieve perfect balancing for white light background or for the actual sky conditions. For checking these elements, a pressure scan of a Neon spectral lamp (630.04 nm) is performed. Looking at the bunching of

pulses as seen in a monitoring oscilloscope, typical gate parameters are fixed. A pressure scan of such kind is shown in the Figure 2.9.

As the counts from the outer zones are subtracted from those of the inner zone, it can be seen that the resulting differential counts are negative. Peak differential negative counts are obtained when the fringe completely fills the outer zone. Similarly when the fringe falls over the inner zone, a positive peak is obtained. In between, when light falls equally over both the zones, one obtains zero difference in counts. If this instrumental profile shape is made symmetrical, then one can take that the alignment is proper and if the positive peak and negative peak counts are nearly similar, then it could be construed that the gate balancing is proper.

Once the above tests are over, the DGP has to be optimized for the actual sky signal, i.e. the airglow measurements. The pressure scan has to be performed on airglow emission also. Usually gate parameters set for the laser scan needs only a small correction in photometric applications, because their wavelengths are close by.


## 2.2.3# Critical evaluation of the DGP

After appropriate selection of the instrumental parameters for the emission line, several other tests are performed to make sure that the signal observed by the instrument corresponds only to the airglow emission originating from the atmosphere. At first, a pressure scan of Neon - spectral lamp ($\lambda = 630.4$ nm) is taken and further with the same settings, diffused sunlight was introduced with the spectral source. One can see the diffused light hardly changes the tuning characters of the DGP (Figure 2.10). It should be noted that one of the profiles is deliberately shifted.

Further, pressure scan for the actual 630.0 nm dayglow was performed and one can see the differential profile (figure 2.11), showing the presence of fringes of the dayglow emission clearly.

In order to confirm the emission signatures to be due to dayglow observations, tests were carried out during a severe dust storm (Figure 2.12). The OI 630.0 nm dayglow scan was taken and no feature was obtained. This confirmed the emission feature to be coming from higher altitudes and due to enhanced scattering and poor visibility it could not be detected by the DGP.
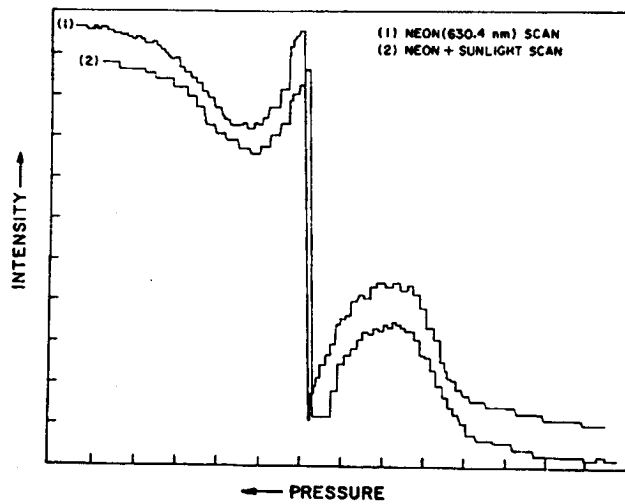
**Figure 2.10.** Performance of the DGP under a test when a scan were taken for sky alone and together with the sunlight reflected on to the front end optics
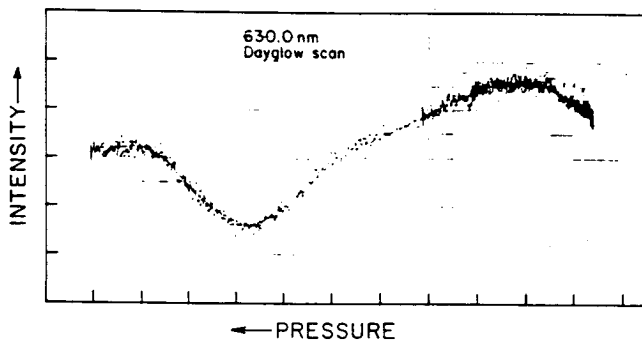
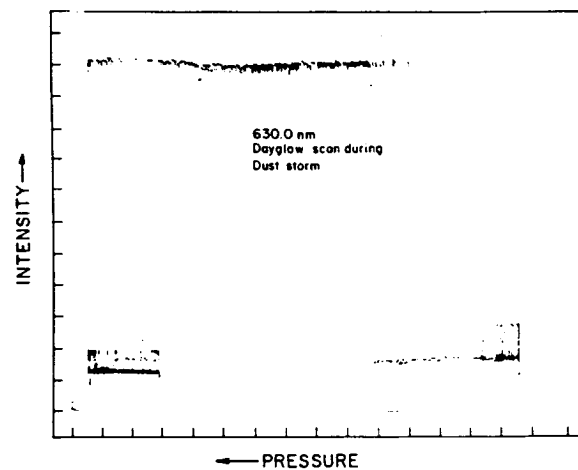

**Figure 2.11.** Actual 630.0 nm dayglow Pressure scan.



**Figure 2.12.** Pressure scan of 630.0nm during a dust storn.

33

After having ascertained about the performance and capability of the dayglow photometer (DGP) in the initial steps of its development, it is now well established for its uniqueness, and has been very well utilized in many investigations of the upper atmospheric phenomena and processes.

## 2.2.4# Effect of spectral smoothening on the solar background:

It was mentioned in the earlier sections that the signals arriving at the mask plane, are smoothed in a wavelength interval of 0.08 – 0.09 nm. This smoothening is very important as it enables unambiguous detection of certain airglow signals during daytime.

It is well known that the solar spectrum reaching the earth's atmosphere contains features of Fraunhoffer and telluric absorption of varying depth and widths. The former due to the elemental presence in the chromosphere of the sun while the later is due to certain specific atmospheric species. Presence of these features at or in nearby wavelengths bands make the detection of any dayglow feature difficult, as absorption features too can produce a fringe pattern in a Fabry Perot. The basic assumption in the present technique of the dayglow photometry is that, the solar background contribution in the wavelength domain separated by 0.08 nm which is a chosen instrumental parameter, is the same. The presence of sharp absorption features in the wavelength domain of interest could make this assumption invalid because, in that case both the gates, one fixed at the emission feature embedded on the solar background and another fixed at solar background will have different solar background contribution within that short wavelength interval, and thus proper background subtraction will not be done. To identify the extent of this ambiguity, a smoothening exercise on the high resolution solar flux data, for the nearby wavelengths of interest was carried out. Results of this analysis revealed that for certain emission wavelengths of interest (557.7 nm, 630.0 nm, 731.6 nm and 740.2 nm), smoothening removes the effect of Fraunhoffer absorption and telluric features from solar background, while for certain emission features (589.6 nm) this is not as effective. The high resolution solar flux data was obtained from Kitt peak observatory, Arizona, using Fourier transform spectrometers. Figure 2.13 a, b, c, d and e show the effect of wavelength smoothening for 557.7, 589.6, 630.0, 731.6 and 740.2 nm wavelength regions. Results of the smoothening exercise indicate that

except for the 589.6 nm, other wavelengths can be detected unambiguously during daytime after the solar background rejection.
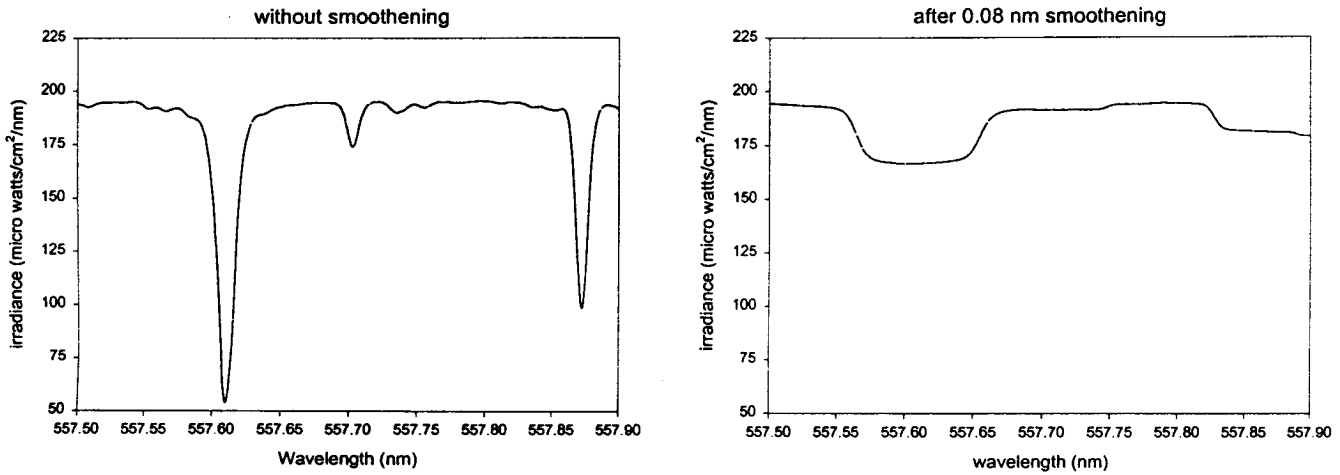


**Figure 2.13a.** Effect of smoothening in the wavelength domain of 557.7 nm , one can clearly notice that sharp features get averaged out after 0.08 nm smoothening.
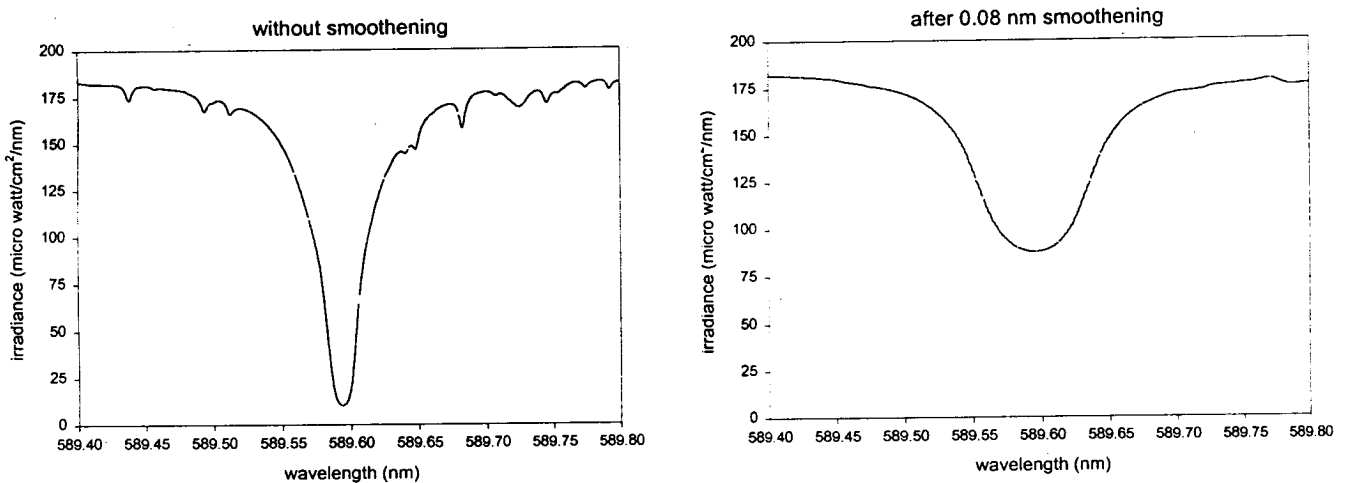


**Figure 2.13b.** Effect of smoothening in wavelength domain near 589.6 nm, sharp features do not allow the solar background to become uniform even after 0.0 8nm smoothening.
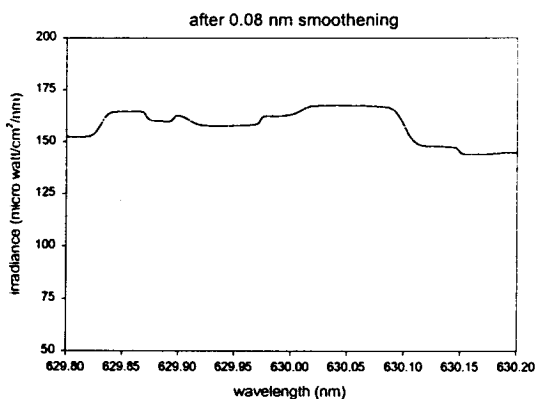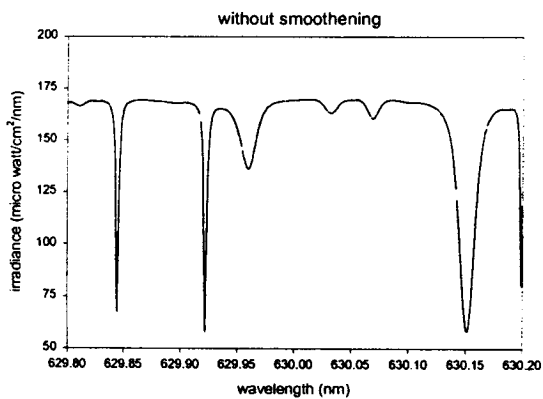
**Figure 2.13c.** 0.08 nm Smoothening effect in the 630.0 nm wavelength domain.
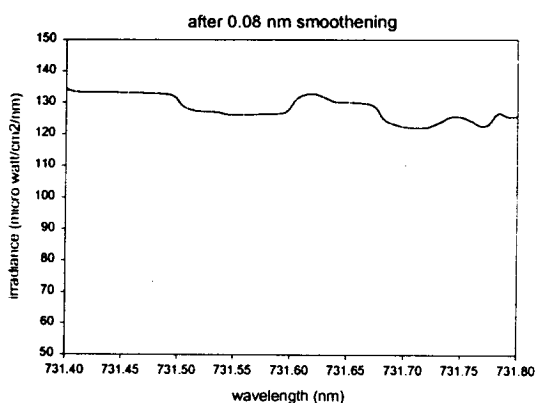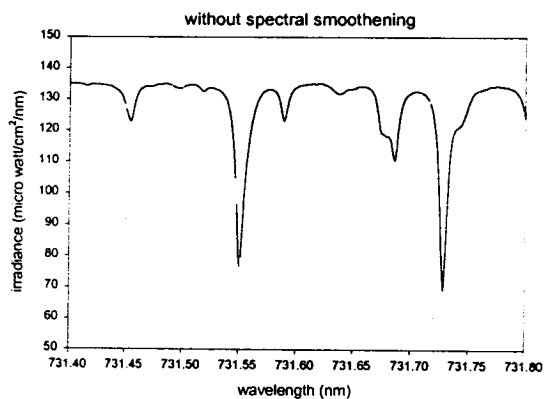


**Figure 2.13d.** same as figure 2.13c, but for 731.6 nm.
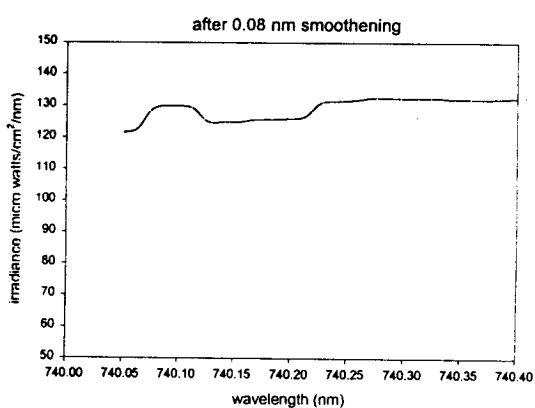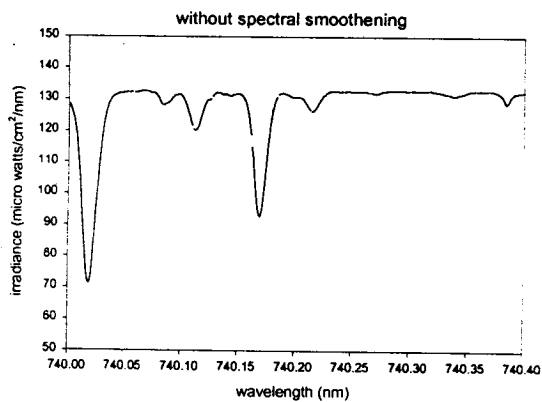


**Figure 2.13e.** same as figure 2.13c, but for 740.2 nm.

36

## 2.3# Daynight Photometer:

The dayglow Photometer which is capable of daytime airglow detection in the presence of high solar background is not directly suited for nightglow measurements, because of the considerably lesser intensities during nighttime. Introduction of a smaller effective aperture Fabry Perot (FP) and mask assembly during daytime reduces these intensities taking it beyond the detection limit. Therefore, round the clock measurements of airglow emissions with a single instrument were not possible because of the requirement of a large dynamic range.
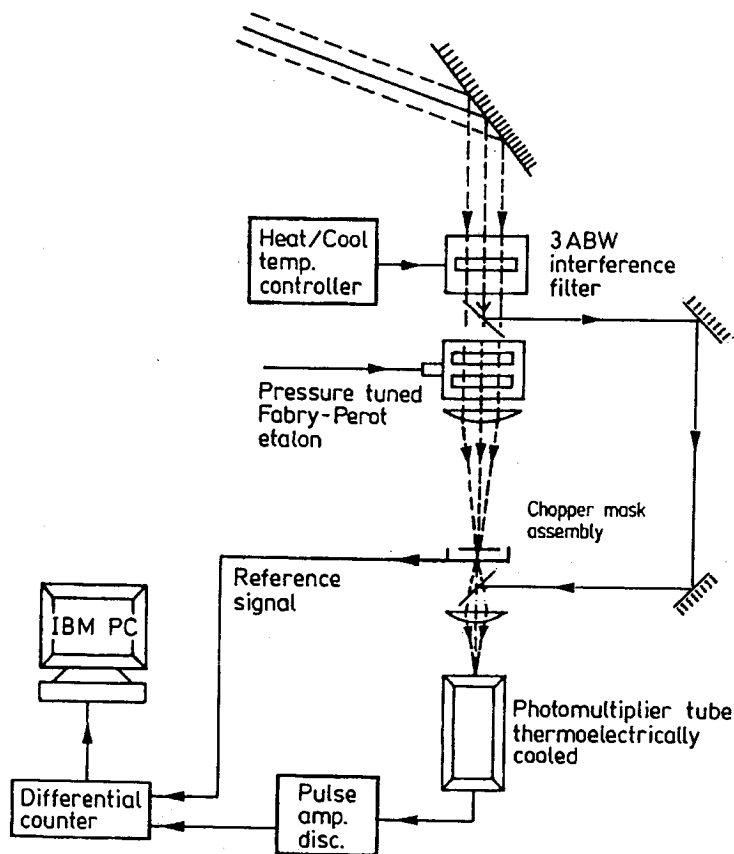
**Figure2.14.**Schematic diagram of the Daynight Photometer.

Continuous measurements are important to study the long period airglow emission variabilities. A simple attachment that would bypass the FP and mask in a DGP, could be used as nighttime photometer (figure 2.14).

Immediately after the front-end interference filter, a periscopic assembly is attached. During daytime, this is disabled so that incoming radiation can pass through FP and mask plane, while during nighttime it is enabled so that incoming radiation passes through filter and then directly to the PMT. This periscopic assembly consists of front silvered good quality mirrors placed at 45° angle in such a way that the incoming radiation after four reflections enters directly to the PMT making nighttime measurements.
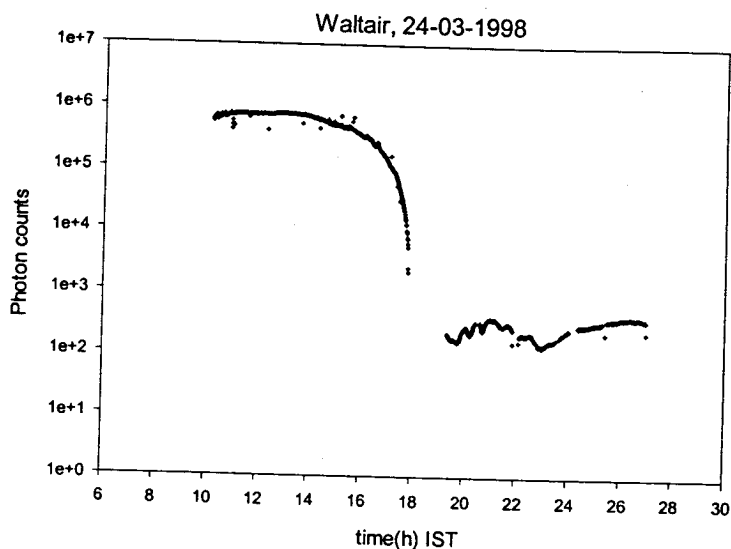


**Figure 2.15.** Day and Night -time intensity variations of 630.0 nm airglow emission as monitored by Day- Night photometer.

## 2.3.1# Data Analysis Procedure

It is well known that there is significant difference in the airglow emission intensities during day and nighttimes. Apart from this, due to different optical components involved in daytime and nighttime detections, there is a systematic bias in the flux which needs to be taken into account while combining the data. The main factor comes from the mask assembly wherein only 8% of the total throughput are allowed under aligned conditions. As the masks are continuously rotating with respect to each other, the effective throughput is ~5.5% only. Further, the finite reflectivity of FP reduces the relative throughput by a factor of 1.14 during daytime. All these factors put together, reveal that the throughput of the DGP would be less by a factor of ~27 and in order to make the day and nighttime intensities comparable, the

nighttime intensity has to be scaled down by the above said factor. On the other hand, dayglow receives its contribution primarily from the photoelectron excitation of atomic oxygen, photo dissociation of molecular oxygen - both contributing to ~70% of the total intensities (Sridharan et al., 1992b). The third process, namely, the dissociative recombination which contributes the rest (while at the same time accounting for 100% of the variabilities), is incidentally solely responsible for the nightglow. Therefore, in order to make the dayglow intensities at par with that of the nighttime, they are uniformly reduced to 30% of the measured values. After inclusion of the above said corrections, the observed day – night variabilities in the 630.0nm airglow emission is depicted in figure 2.15. With the raw data, the comparison and study of variabilities become difficult because of the change in the airglow intensities by several orders of magnitude. As the DGP and DNP are the relative intensity measuring instruments, they are ideally suited for getting the variabilities. In order to study the variabilities and compare them, one needs the intensities to be of the same order. For this purpose the long-term (diurnal) trend was removed from the intensities, and the residuals were obtained, which were normalized to the diurnal trend. Intensities, thus obtained are named as 'fractional intensities' and the analysis is named as 'fractional intensity variation analysis'.
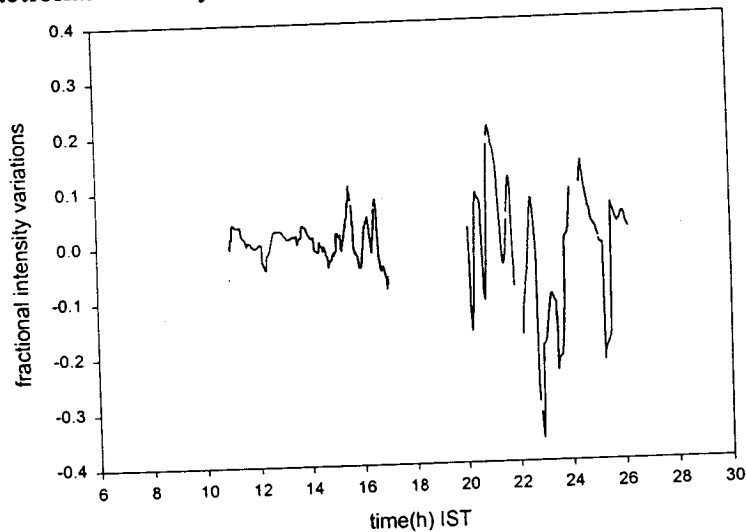


**Figure 2.16.** Temporal variations in the fractional intensities, short time period variations can be noticed clearly.

After this analysis, the variabilities come nearly to the same scale as shown in Figure 2.16. Short period features can now be studied round the clock providing an additional tool for the investigation of geophysical processes.

## 2.4# Multi-Wavelength Daytime Photometer (MWDPM):

In the earlier sections 'Dayglow photometer' and 'Day – Night photometer' were described. In the DGP, pressure tuning of the etalon was used to bring the emission feature to the central maximum. If the same instrument is to be used for the measurements of other wavelengths, then one has to change the interference filter at the front end of the DGP and the FP pressure has to be readjusted to bring the new emission feature to the central maxima. This becomes cumbersome if one needs nearly simultaneous measurements at different wavelengths. Such needs of multiple wavelength detection had always been in demand for atmospheric studies especially in those pertaining to the coupling processes, rotational temperature measurements, and wave propagation and associated studies. In order to overcome these difficulties and to allow the photometer to detect different wavelengths nearly simultaneously, a novel spiral mask assembly was designed paving the way for Multi - Wavelength Dayglow Photometry. Using this mask assembly alongwith the several proper combination of optics, the MWDPM with unique features has been developed and the chief elements are discussed below:



**Figure 2.17.** Schematic diagram of Multiwavelength Daytime Photometer. (After Sridharan et al., 1998)

## 2.4.1# Interference Filter:

The interference filters used in the MWDPM have narrow bandwidths (FWHM) ranging from 0.3 nm, centered at the wavelength of interest. For the present study, interference filters with central wavelength 630.0 nm, 557.7 nm, 731.6 nm, 740.2 nm and 589.0 nm are used depending upon the type of investigation. Similar to the DGP, the filters are maintained at temperatures better than $1^0$C using bipolar temperature controllers.

## 2.4.2# Fabry-Perot etalon:

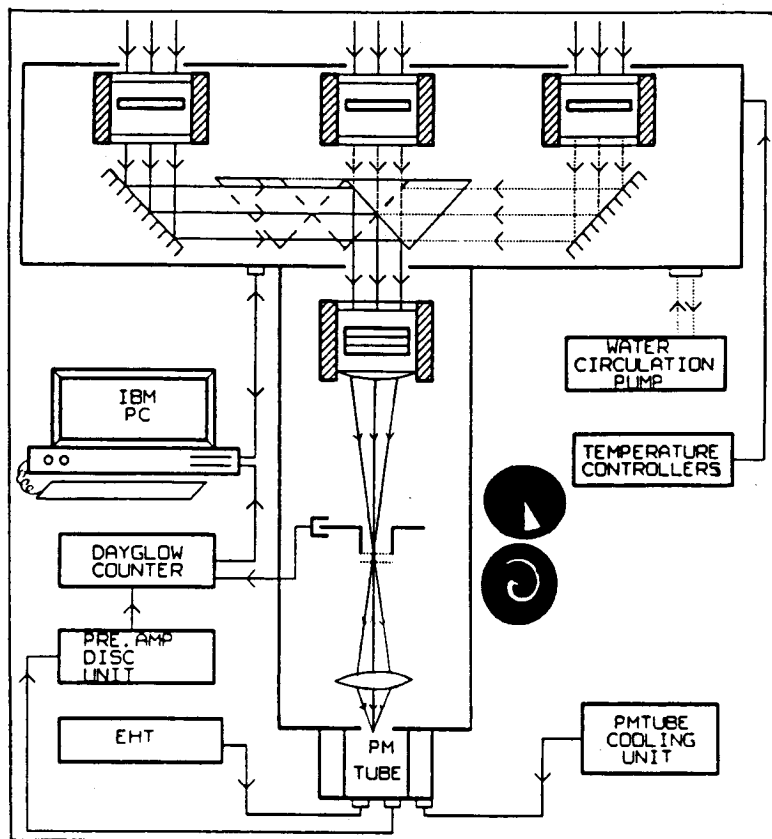The special Fabry-Perot used in the MWDPM is a low - resolution optically contacted air gap (~300 $\mu$m), broad - band (400-800 nm) etalon. For multi-wavelength selection the FP fringes are adjusted by pressure scanning in such a way that all the wavelengths of interest fall under the spectral range of the aperture (here mask plane). In other words, a common pressure position is fixed where all the fringes (in this case three) are formed on the mask plane at different radial distances. The FP is kept inside a pressure tight brass housing. This brass housing is attached to a foot-pump and to a pressure gauge, which can be used to adjust the pressure inside the FP chamber. After the identification of the pressure position suitable for the multi-wavelength detection, the pressure is kept fixed at this level throughout the operation of the MWDPM.

## 2.4.3# The Mask Assembly:

The mask for multi-wavelength detection consists of a transparent spiral mask as a stator spiraling outwards i.e. the radial vector is drawn away from the center when the concentric rotor with 30° triangular transparent zone starts rotating. The fringe diameters at the image plane for different angles of incidence are calculated. The image plane is divided into 12 segments of $30^0$ each. The inner points of the fringe at the beginning of each sector provide the inner spiral, while that of the outermost point at each sector boundary provides the outer spiral. With this arrangement, $1/r^2$ dependence of the fringe diameters has automatically been taken into account. The wavelength span of the spiral covers atleast one FSR of the shortest wavelength of interest. The rotor mask has 30° transparent zone that extends to the outermost diameter of the spiral.

The rotor is concentrically mounted to the static spiral mask. With the rotation of the rotor, a complete blank zone is encountered once in every rotation, which is used for the generation of the reference signal. A reference plate with a small cutout and an opto coupler mounted to match the cutout is aligned with the blank area in the spiral mask. The rotation of the rotor mask over the opto coupler provides reference pulses that coincide with the beginning of the innermost spiral. When the rotor position completely overlpas the region of the spiral mask containing the emission feature of interest, at the time of appearance of the fringes thus is used in fixing up the



(a)                                          (b)
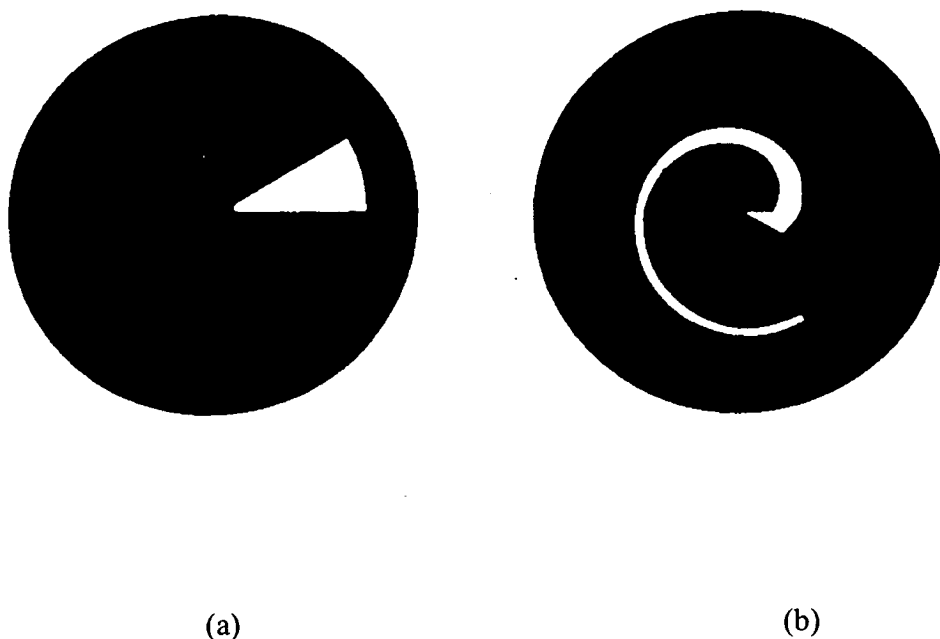
Figure 2.18. Novel mask design for MWDPM (a) Spiral stator mask that separates different wavelengths at different times in an FP fringe system. (b) Rotor with a $30^0$ transparent segment that selects wavelength of interest at specified time intervals. (After Sridharan et al., 1993)

radial position of the fringe. The operation sequence is shown in the figure 2.19 and can be explained as follows. In this, stator is shown with the interference fringes as dashed concentric circles. In reality, only one fringe at a time, which is selected by front-end filter, would be present over the mask. Fringes of different wavelengths of interest will appear at different portions of the spiral.
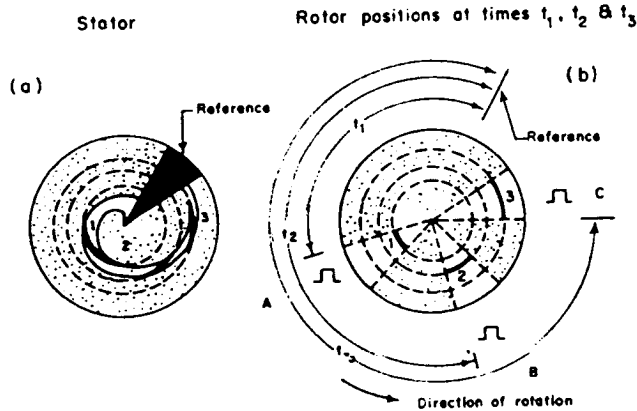
**Figure 2.19.** (a) Interference fringes (dashed concentric circles 1,2 and 3 representing different wavelengths). The continuous thick parts present the portion of the fringes seen through the spiral stator. The $30^0$ segment represents the reference. (b) Net effect of the rotor mounted concentrically with the stator. The corresponding fringes 1, 2 and 3 seen through the rotor at interval $t_1$, $t_2$ and $t_3$ with respect to the reference represent the fringes resulting from each wavelength of interest. The gate pulses for the PMT are also depicted. (After Sridharan et al., 1993).

The segment of the fringes, which will be seen due to rotation of transparent triangular rotor is denoted as 1, 2 and 3 in the figure 2.19b. The first segment of fringe 1 will be let through both the masks at a time interval of $t_1$ after the reference pulse. Likewise fringe segment 2 and 3 will be let through at times $t_2$ and $t_3$ respectively. The selection of the desired fringe can be done now electronically by appropriately gating the PMT at the correct time interval, by enabling the photon counters at times $t_1$, $t_2$ and $t_3$ respectively. Thus the spatial information of the fringe position is now transformed into time domain, and different emission features will appear at different times enabling their detection. An equal area immediately after the emission feature lets in the contribution due only to the background.

## 2.4.4# Functional details of the MWDPM

It is clear from the schematic of the MWDPM (figure 2.18) that the front end of the MWDPM contains three interference filters. These interference filters are housed in separate enclosures and are temperature controlled with the help of Peltier elements and bipolar temperature controllers. Right after the filters, front silvered mirrors are kept below the left and right end filters. In between these mirrors a right-

angled prism, with both the adjacent faces front silvered, is mounted on a rail. One face of the prism and one of the mirrors would now form a periscopic combination. Depending upon the position of the prism, only one emission line is allowed. The positions are being sensed by means of opto couplers and the prism movement is controlled by a stepper motor which in turn is controlled by a computer. The emission feature is then passed through the FP etalon, which forms circular fringes of the corresponding emission feature. These fringes are then focussed onto the mask plane, that differentiates the combined intensities of emission feature and the background, and, the background alone separately, but near simultaneously. Corresponding fringe segments are then re-focused on photomultiplier tube and the collected photon counts are sent to the synchronous gated photon counter units and are displayed on the monitor, after a preset integration time.

In the above, it is essential that the optical axis be aligned to the mechanical axis of the instrument. For that, the center of the fringe system formed on the mask plane should coincide with the center of the rotor mask that can be accomplished with the help of FP tilting screws. This in turn has to be concentric with the stator mask. Finally they should get focused on to the PMT photocathode. This is checked with gate and pressure scan of a He − Ne laser (632.8 nm). A symmetrical differential gate scan ($D_1$ scan; in which the fringe is being scanned with the scanning of the dual gates corresponding to signal + background and background alone) testifies a proper alignment. In a differential scan (figure 2.19) positive maximum is achieved when $G_2$ is positioned over the emission fringes (signal embedded on the solar background) while the $G_1$ is still far from the emission fringes representing the solar background. The difference $G_2$-$G_1$ yields the representative emission intensity, which is shown in the figure.
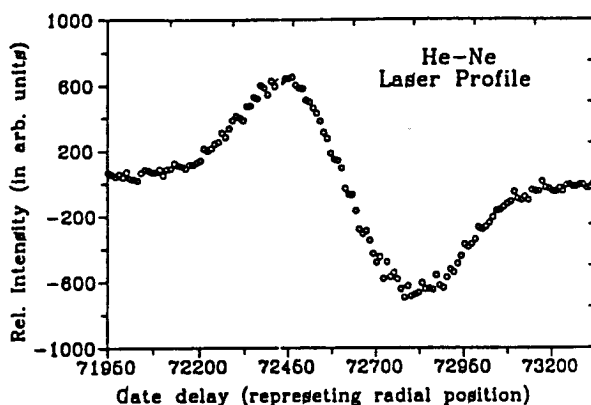


Figure 2.19. The relative intensity of the laser beam obtained with the dual gate scanning.

When both the gates see nearly same emission intensities then difference is zero and when $G_1$ covers the emission feature and $G_2$ is away, then maximum negative difference counts are obtained. Asymmetry in the laser profile means gate settings and this has to be removed with a proper adjustment in the gate parameters.

### 2.4.5# Critical evaluation of the MWDPM

One has to be very careful while detecting the dayglow emission the intensity of which is less than a few percent of the scattered solar background. One could be assured of proper solar background rejection and unambiguous detection as the incoming radiation on the aperture plane (mask) is being smoothed over the spectral window of 0.08nm, which averages out most of the sharp features, if any. Another critical test was done with the help of the pressure scan of the sky signal for 557.7 nm emission line and a clear cut differential profile was obtained (Figures 2.20). Now keeping rest of the instrumental parameters the same, sunlight was reflected into the system. Care is taken not to saturate the photomultiplier tube by appropriately diffusing the sunlight ensuring that the full spectrum of sunlight is allowed to enter. A repeat pressure scan is taken and is depicted in Figure 2.21. One could see that the finer features of the solar spectrum had been completely integrated out and pressure scan yields a nearly flat profile.
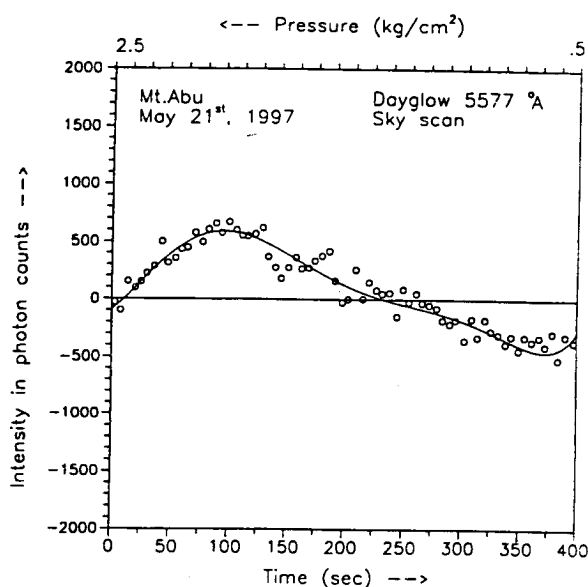


**Figure 2.20.** A typical pressure scan of the day sky and the differential profile of O($^1$S) 557.7 nm dayglow with 1 second integration of the datum point.
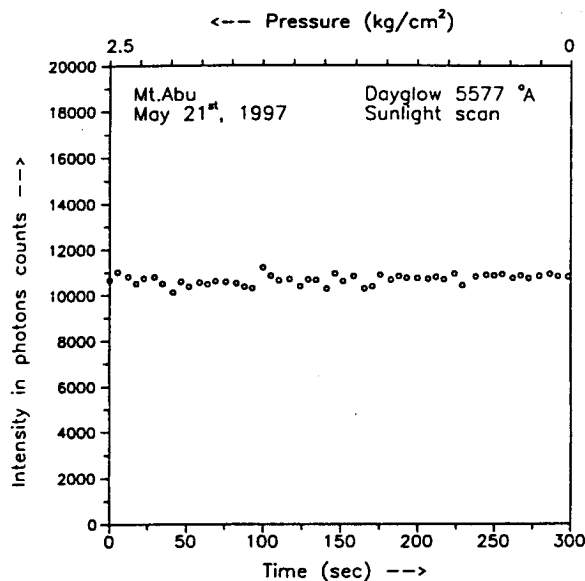
**Figure 2.21.** A pressure scan of the direct solar spectrum in differential scanning mode.

Similar to the DGP, another test was performed with a polarizer. Due to its unpolarized nature, the dayglow signal was not affected with the rotation of the polarizer, while the solar background being polarized in nature was found to get modulated.

As a final step, MWDPM was kept alongwith the DGP at the same place to monitor 630.0 nm thermospheric dayglow. The similar features observed in both the MWDPM and DGP are shown in Figure 2.22 confirming the capabilities of the -
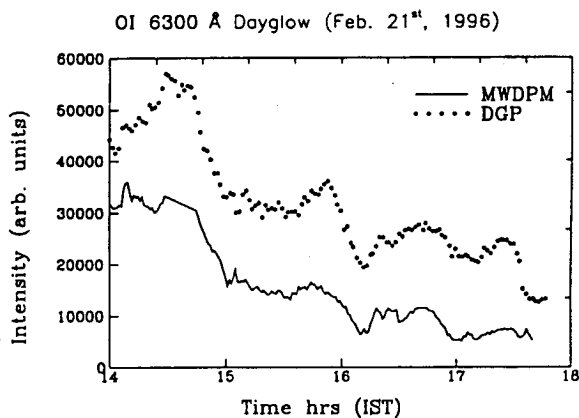


**Figure 2.22.** The similar variation of OI 630.0 nm dayglow intensity seen both by the MWDPM and by the DGP, validating the performance of the MWDPM.

latter to monitor different dayglow emission signals, even in the presence of high solar background unambiguously.

Results from all the three instruments form the basis of the chapters to follow.

# 3# Emission processes responsible for the OH, O($^1$S) and O($^1$D) dayglow.

Absorption of solar energy by atomic and molecular species at different altitudes leads them to take part in various chemical and physical processes. Excitation of atomic and molecular species to higher energy levels, their de-excitation and the resultant emission of radiation known as 'airglow' are an outcome of these physical and chemical processes. In this chapter we discuss about the optical and near infrared radiations that result from the de-excitation of OH radicals, O($^1$S) and O($^1$D) atomic species. These emissions have been used extensively for the investigation of the mesosphere-thermosphere-ionosphere system. It is well known that allowed transitions of atoms from the excited state to the ground state by the spectroscopic selection rules via direct transition occur typically within $10^{-8}$ seconds. Certain species de-excite to ground state via an intermediate (metastable) state. Their direct transitions to these metastable states violate the spectroscopic selection rules for the dipole transition. These are called the forbidden transitions. Emissions like OH Meinel band, O($^1$S) and O($^1$D) used for the study of the atmospheric processes, are forbidden transitions in nature. These metastable states have longer life time which allows them to get locally thermalised in the atmosphere. Thus monitoring of these lines provides an information on the ambient atmospheric conditions including the dynamics and chemistry of the ambient. Processes responsible for their excitation and for the subsequent emission are discussed briefly in the following sections.

## 3.1# Hydroxyl 'OH' Meinel band emission:

All the identified hydroxyl bands in the airglow are radiated from the transition of vibrational level (v') ≤9. Although many extensive experimental and theoretical investigations have been carried out since its discovery, a complete understanding of the excitation mechanism of the OH menial bands has still not been achieved. The possible production mechanism can be stated as the following:

The most widely accepted mechanism for the production of OH radicals in the mesopause region is the exothermic reaction in which ozone reacts with the insitu generated 'H' producing the OH radicals in the excited vibrational levels:

$$O + O_2 + M \xrightarrow{K_1} O_3 + M \qquad\qquad M = N_2, O_2, O$$

$$O_3 + H \xrightarrow{K_2} OH^*(\upsilon \le g) + O_2 + 3.34eV \qquad (3.1)$$
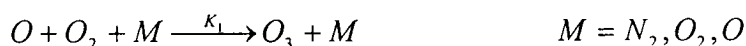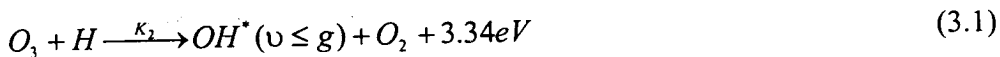
The excess energy is channeled into different vibrational levels of OH upto $\upsilon$ = 9 (Bates and Nicolet, 1950). Though this mechanism is accepted as the major source of the mesopause $OH^*$, yet no consensus has emerged on the exact distribution of these metastable radicals among their vibrational levels (Golden, 1997). Another exothermic perhydroxyl-oxygen reaction has been proposed by (Nicolet, 1950; Krassovsky, 1972).

$$H + O_2 + M \xrightarrow{K_3} HO_2 + M$$
$$O_3 + H \xrightarrow{K_2} OH^*(\upsilon \le 9) + O_2 + 3.34eV \qquad (3.2)$$
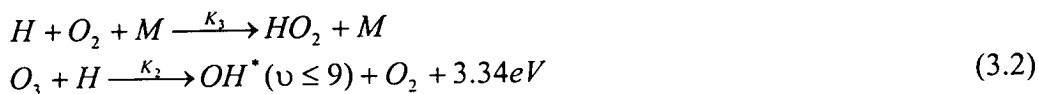
Dick (1977), Takahashi and Batista (1981) and Sivjee and Hammway (1987) investigated this emission process as a probable source of OH radicals.

Another probable mechanism was proposed by Krassovksy (1963), which includes molecular oxygen

$$O + O + M + M \xrightarrow{K_4} O_2^* + M \qquad (3.3)$$
$$O_2^* + H \xrightarrow{K_5} OH^*(\upsilon') + O \qquad (3.4)$$

And this reaction was studied by Takuechi (1981). It is generally believed that the contribution of this mechanism to the OH emission is very small in comparison to the Bates-Nicolet's ozone mechanism. Another mechanism proposed by Street and Johnson (1976) suggests that the OH radicals may even deexcite to lower vibration levels in a step like process:

$$OH^*(v) + M \xrightarrow{K5} OH^*(v-1) + M \qquad (3.5)$$

While McDade and Llewellyn (1987, 1988) suggested a 'sudden death' type process which lead the decay of vibrationally excited OH radicals to the ground state

$$OH^*(v) + M \xrightarrow{K6} OH^*(v = 0) + M \qquad (3.6)$$

49
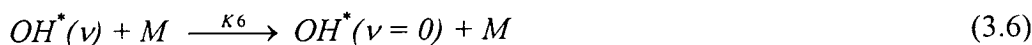
Apart from these sources, during daytime three additional sources are likely to be present. One among them is the photo dissociation of $H_2O_2$.

(i) $$H_2O_2 \xrightarrow{h\upsilon} 2OH \qquad (3.7)$$

(ii) due to photodissociation of water vapour.

$$H_2O + h\nu \rightarrow H + OH \qquad (3.8)$$

and     (iii) dissociative recombination of $H_2$ and O.

$$H_2 + O(^1D) \rightarrow OH \qquad (3.9)$$

Though there are distinct possibilities for the above reaction (3.7), (3.8) and (3.9) experimental confirmations are not cited in the literature.

Apart from the processes responsible for the OH emission the altitude profile of the OH volume emission rates have also been studied extensively. Rocket measurements of the altitude profile of OH emission show different vibrationally excited OH radicals to peak at different altitude regions. Rogers et al. (1973) showed two classes of OH radicals to peak at around 83 and 85 km (figure 3.1). The altitude difference can be taken as indicative of the different quenching mechanisms to dominate at different altitudes. He showed that OH emissions peak near to the mesopause and with a half width from 8 to 10 kms, and almost all the time is fairly coincident with the mesopause altitude. Further, Lopet-Moreno et al. (1987) with rocket experiment and model calculation showed the altitude profile of volume emission rates, for different vibrationally excited OH radicals. McDade and Llewellyn (1987) devised two models to study the collisional dynamics of the deactivation of $OH^*$ by M. These were referred to as the collisional cascading and the sudden death models. With ETON-5 rocket borne observations of the integrated column emission rate of the OH (8-3) band and simultaneous observations of O enabled them to simulate their models. They showed OH (8-3) band to peak near 87 km (McDade et al., 1987a). Most recently, Golden (1997) discussed about the altitude distribution of vibrationally excited OH radicals. The altitude of peak OH ($v^1$) concentrations and hence the emission altitude is given approximately by the expression

$$H_{peak} = (83 + 0.7 \, v^{'}) \, km$$
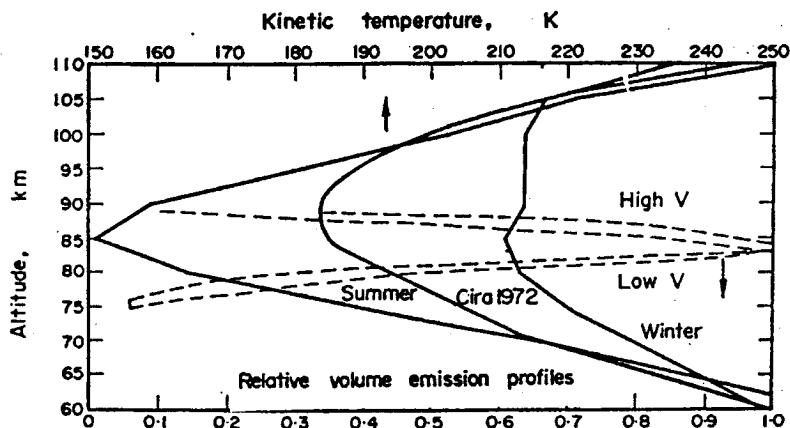
**Figure 3.1.** Kinetic temperature profiles (solid lines) and relative volume emission profiles of high and low vibrational OH sequences (broken lines) (After Meriweather, 1973).
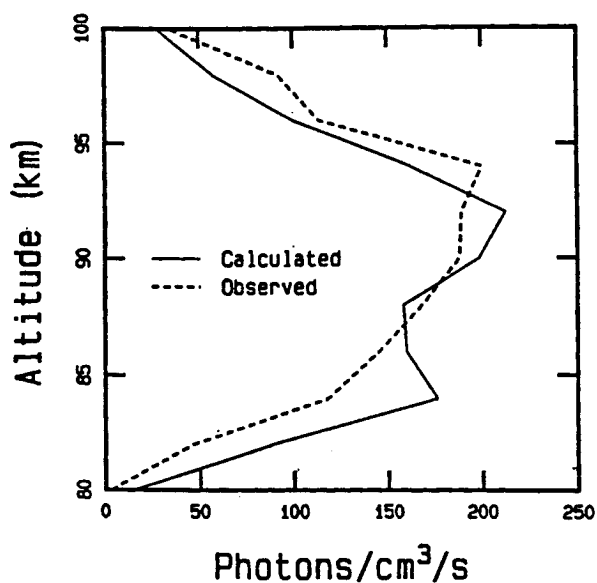


**Figure 3.2.** Simulation of the OH (8,3) band profile from the ETON experiment (After Golden, 1997)

Figure 3.2 shows the altitude profile, which is a fairly good average representation of available measurements from rocket experiments. Recently, using WINDII instrument onboard the UARS satellite, Lowe et al.(1996) showed a volume emission rate profile of $P_1(3)$ line of OH (8, 3) band over 40°N and 40°S. They showed the emission layer peaks near 88 km during most of the time, with a half width of 6-8 km during spring equinox.

From the above, it is clear that OH emissions peak near the mesopause region, and have different photochemical sources. Further, nighttime OH intensities depend mostly on the ozone and so the OH emission variabilities can be used to infer the ozone concentration. To some extent insitu generated hydrogen concentration also can be inferred. Using nighttime photometric observations of OH (9, 3) Meinel band,

51

bands are excited primarily by the reaction between ozone and atomic hydrogen and their variations are believed to be driven essentially by the variability of the mixing ratio of atomic oxygen in 85-90 km regions, which inurn is controlled by the transport processes. At low and mid-latitudes, vertical diffusion due to small scale gravity wave breaking dominates the transport of odd oxygen resulting in the semiannual oscillations noticed in the OH band emissions.

In addition to obtaining information on some of the important minor constituents, one of the most potential applications of 'OH' emission measurements is the possibility of inferring the neutral temperatures of the mesopause region, the region which otherwise is not easily accessible. The OH radicals have their lifetime ranging from few milliseconds to ~ 65 milliseconds, decreasing from vibrational levels $v = 9$ to $v = 0$ (Llewellyn and Long, 1978). Inter collision time at mesopause altitude is typically of the order of 0.1 ms. This fact, added with the available larger collisional cross section of OH radicals lead the vibrationally excited OH radicals to attain local thermodynamical equilibrium. As a consequence the OH rotational temperatures and their variabilities, can be treated to be the same as the ambient temperatures. Meriwether (1975) showed that any seasonal variation in the emission processes may not affect the temperature estimates by more than 5 to 10K. The derivation of the rotational temperatures from the relative intensity variabilities is dealt in detail in the chapter dealing with the daytime mesopause temperature and its variabilities.

Using nighttime photometric observations of OH (9, 3) Meinel band, Texier et al. (1987), presented seasonal variabilities. They argued that the OH bands are excited primarily by the reaction between ozone and atomic hydrogen and their variations are believed to be driven by the variability of the mixing ratio of atomic oxygen in 85-90 km regions, which inurn is controlled by transport processes. At low and mid-latitudes, vertical diffusion due to small scale gravity wave breaking dominates the transport of odd oxygen that lead OH band to a semi-annual oscillations.

Apart from seasonal variations, short period features in the OH emissions had been of great interest. These small-scale oscillatory features are often attributed to the passage of gravity waves, which are believed to be the most important coupling agents in the different atmospheric regions. In one such study on the identification of

wavelike structures, Taylor et al. (1991) reported simultaneous intensity, temperature and imaging measurements of short period wave structures in the OH nightglow emissions. With the oscillatory features, they deduced the 'η' parameter, which suggested a possible ratio to exist between intensity and temperature variations, in case of the passage of gravity waves:

$$\eta = \frac{\nabla I / \bar{I}}{\nabla T / \bar{T}}$$

where $\nabla I$ is the change in the intensity, $\bar{I}$ is time averaged intensity, $\nabla T$ is the change in the temperatures and $\bar{T}$ is time averaged temperature. With model calculations of Walterschid et al (1987) (which infer the possible 'η' values for different periodicities of the waves), Taylor et al. (1991) showed the observed 'η' values to fall under the gravity wave category as its values were nearly 6 -7 for small period gravity waves.

In recent times, the WINDII instrument onboard the UARS satellite provided volume emission rate profiles with high altitude resolution. Melo et al. (2000) showed the OH emission rate profile to have a double peak on several occasions separated by 4 to 6 km. Their theoretical exercise showed this to be due to complex processes, which could be caused by gravity waves for small-scale events and temperature inversion and turbulent mixing for large horizontal scale/ long duration events. However, groundbased photometric measurements are always preferred for such studies wherever temporal resolution is needed. So far, groundbased studies were limited only to the moonless nighttime conditions only. Development of a Dayglow Photometer (DGP) and Multi Wavelength Daytime Photometer (MWDPM) made the daytime airglow measurements possible (Narayanan et al, 1989; Sridharan et al, 1992a, 1998). The MWDPM was operated from Kolhapur to monitor OH 731.6 nm line of (8, 3) band on a trial basis and four days of data could be collected. Figure 3.3 shows the observed intensity variabilities in OH emission line during the observational period. Large day to day variation and wavelike oscillatory features are evident in the variabilities.
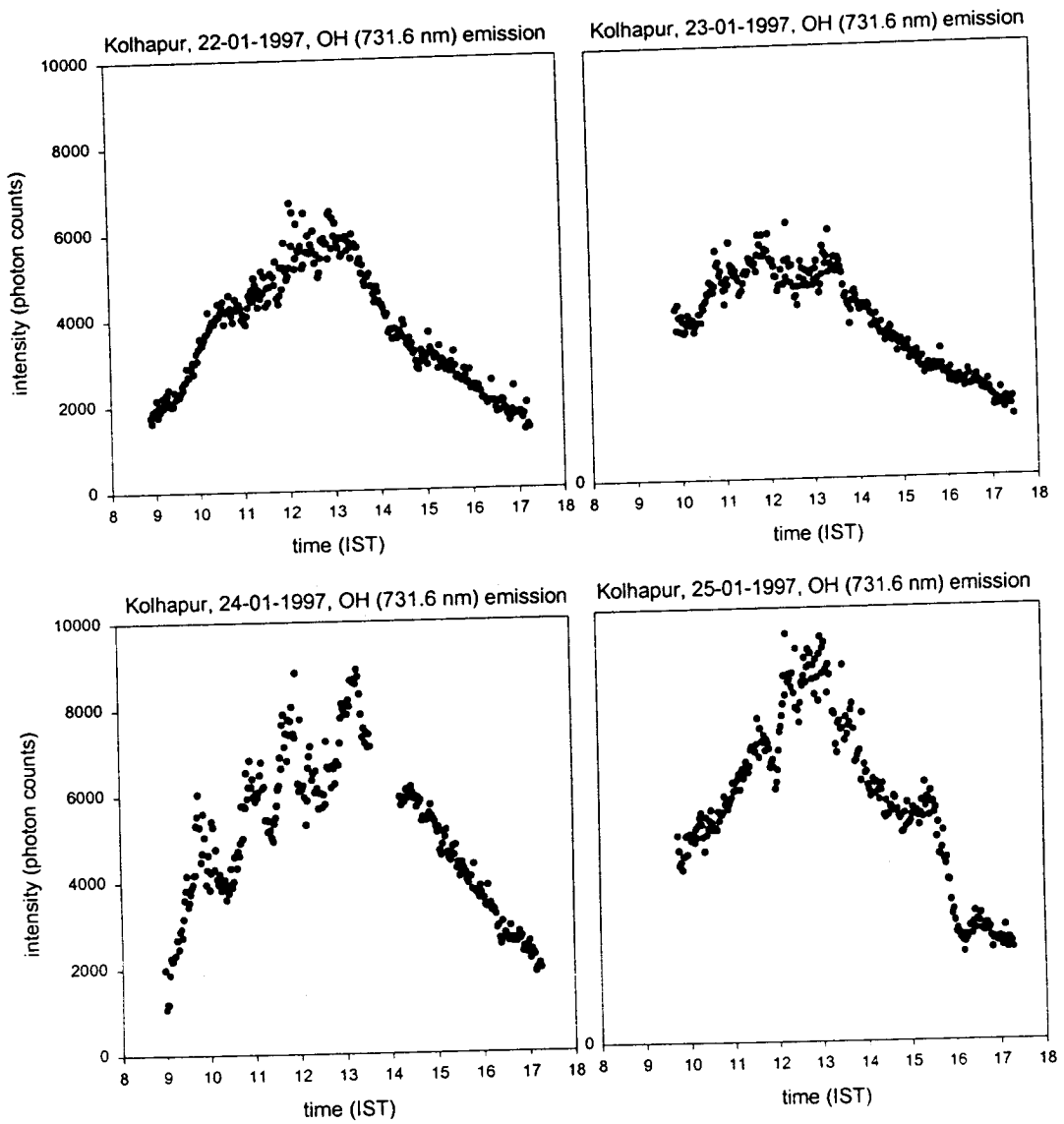
**Figure 3.3** Observed intensity variabilities in daytime OH emission line over Kolhapur during 1997.

54

# 3.2# O($^1$S) 557.7 nm green line airglow emission:

The oxygen greenline O($^1$S) 557.7 nm emission is an outcome of deexcitation of atomic oxygen from $^1$S to $^1$D state. The greenline has been studied extensively with photometers, spectrometers and interferometers from ground during nighttime conditions. Earlier than the present study, for the daytime conditions only rocket and satellite borne measurements were capable of giving information on this emission.

Rocketborne airglow measurements played an important role in the study of greenline chemistry and also attitudinal distribution of multiple in situ measurements of other pertinent parameters (Wallace and McElroy, 1966; Hays and Sharp, 1973; Kulkarni, 1976; Cogger and Murphy, 1980; Yee and Abreu, 1987). It is well accepted that O($^1$S) emission has two source regions. One of the sources is situated at lower thermospheric heights (~97 km) while the other is situated near upper thermospheric altitudes centered ~220 km. Half width of the lower source is nearly 10 km, while the upper source has a half width of ~50 km.

## 3.2.1# Chemical origin of O($^1$S) 557.7 nm.

The chemical origin of the greenline in the mesospheric/lower thermospheric altitudes was first thought to be due to three body recombination reaction known as `Chapman mechanism' -

$$O + O + O \rightarrow O_2 + O(^1S) \qquad\qquad (3.10)[1]$$

Barth and Hiddebrandt (1961) discussed about the rate coefficients of the Chapman mechanism calculated from their laboratory experiments and showed that the rate coefficients ($8 \times 10^{-38}$ cm$^1$s$^{-1}$) are three orders smaller than what is required to produce the observed greenline intensities. Barth (1964) proposed another possible mechanism -

$$O + O + M \xrightarrow{K_1} O_2^* + M \qquad\qquad (3.11a)[2]$$

$$O_2 + O \xrightarrow{K_2} O_2^* + O(^1S) \qquad\qquad (3.11b)$$

where $O_2^*$ refers to the possible excited states of molecular oxygen and M is the ambient species. $K_1 = 1.8 \times 10^{-33} \left(\dfrac{300}{T}\right)^2$ cm$^6$ S$^{-1}$ and $K_2 = 2.5 \times 10^{-12}$ cm$^3$ s$^{-1}$ (Bates, 1992).

After a series of experiments on the rate coefficient of the probable mechanism (Donahue et al., 1973; Slanger and Black, 1977; Bates 1981; McDade and Llewellyn, 1986), the Barth mechanism is now widely accepted as the most important source of $O(^1S)$ 557.7 nm emission in the lower thermospheric layer.

On the otherhand for the upper atmospheric emission of 557.7 nm it was first proposed by Nicolet (1954) that dissociative recombination of $O_2$ is the main source. This process involves molecular oxygen ions and electrons.

$$O_2^+ + e \xrightarrow{\alpha} O(^1S) + O \qquad\qquad (3.12)^3$$
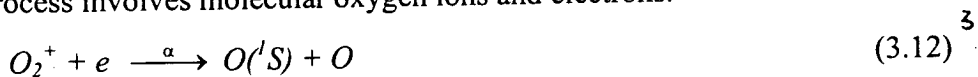
The quantum yield of $O(^1S)$ from the above reaction has been the subject of many theoretical (Guberman, 1987), Laboratory (Bates and Zipf, 1980; Zipf, 1988; Queffelec et. al., 1989), and in situ studies (Hernandez, 1971; Hays and Sharp 1973; McDade et al., 1984; Yee and Killeen, 1986; Yee and Abreu 1987; Takahashi et al., 1990). These studies have discussed the contribution of dissociative recombination process in the total $O(^1S)$ 557.7 nm emission.

Other possible sources of $O(^1S)$ emission are the photodissociation of molecular oxygen and photoelectron impact excitation of atomic oxygen.

$$O_2 + h\nu \rightarrow O(^1S) + O \qquad\qquad (3.13)^4$$
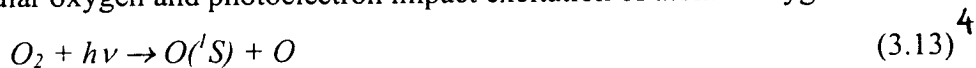
The production of $O(^1S)$ by photodissociation was discussed by Bates and Dalgarno (1954); Walker (1965); Lawrence and McEwan (1973). The photoelectron excitation is given by the reaction below -

$$O + e^* \rightarrow O(^1S) + e^* \qquad\qquad (3.14)$$

and this mechanism was discussed by Wallace and McElroy (1966); Feldman and Doering (1971) and Hays and Sharp (1973).

During nighttime the thermospheric sources remain very less with a contribution < 20% to the total volume emission rates of 557.7 nm emission, while during daytime they are expected to become very significant (Wallace and McElroy 1966; Hays and Sharp, 1973; Shepherd et al., 1997) raising their contribution to ≥70% in the total volume emission rates (figure 3. 4).
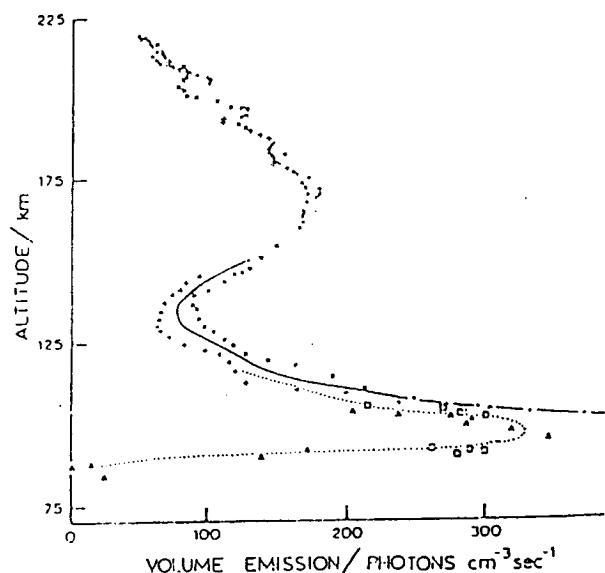
**Figure 3.4 a** Observed 558 nm dayglow emission Rates (After Wallace and McElroy, 1966)
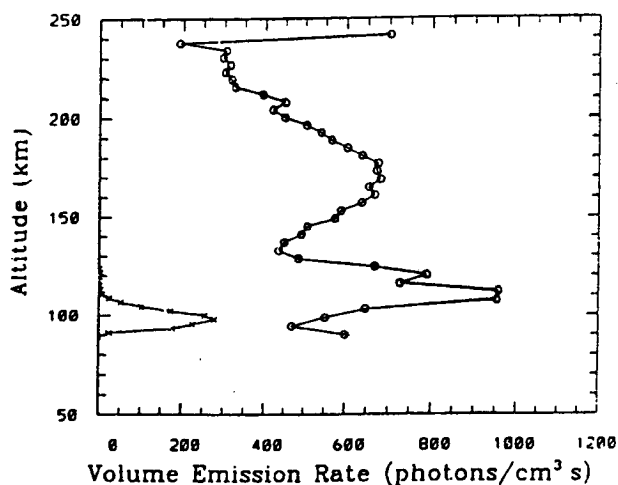
**Figure3.4 b** Greenline daytime (circle) and nighttime (crosses) volume emission rate profiles derived from the inversion of WINDII data.(After Shepherd et al, 1995)
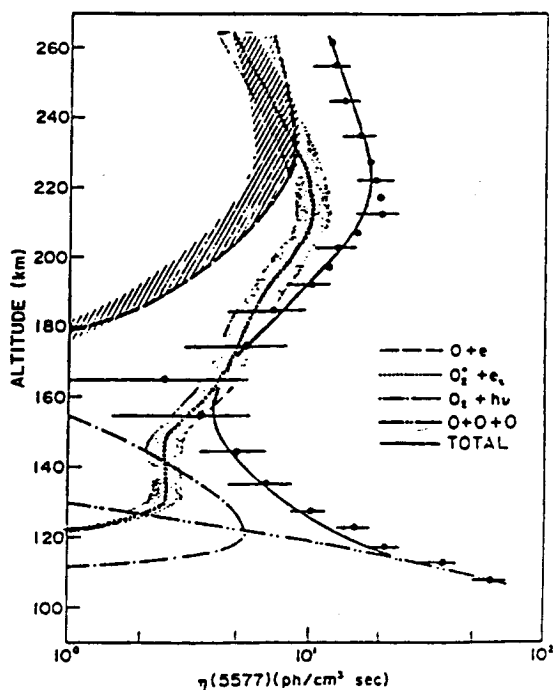


**Figure3.5** Composite picture of 557.7 nm emission processes and their altitudinal importance (After Hays and Sharp, 1973)

Hays and Sharp (1973) showed that reaction (1) and (2) are dominant below 120 km, reaction (3) is significant above 120 km and is dominant between 160-220 km, reaction (4) is dominant between 120-160 km and reaction (7) is important only above 190 km. They discussed the composite effect of these sources and showed that

57

the lower thermospheric layer (lower thermospheric) peaks near 97 km while the upper thermospheric layer peaks near 180-240 km altitudes (figure 3.5).

Systematic groundbased photometric studies of 557.7 nm were limited to only nighttime conditions until the present study. Most of the earlier investigations emphasized seasonal, solar cycle and short period oscillations as well (Fukuyama, 1976, 1977; Misawa and Takeuchi, 1978; Petitdidear and Teitelbaum 1977; Takahashi et al., 1977, 1984, 1985; Taylor et al., 1987). Daytime detection of 557.7 nm was difficult due to presence of very high solar background. The isolation, detection and systematic measurements of the dayglow emission feature became possible only after the development of Dayglow Photometer (Narayanan et al., 1989; Sridharan et al., 1992a) and a Multi Wavelength Daytime Photometer (Sridharan et al., 1998). Results obtained on daytime 557.7nm emission intensity and its utility for the investigation of the atmospheric processes will be discussed in a later section of this chapter.

## 3.3#  Processes responsible for $O(^1D)$ 630.0 nm emission

Since its identification in the nightglow spectrum by Cabannes (1935), the 630.0nm emission has been investigated most widely. From theoretical calculations, Bates and Dalgarno (1954) showed OI 630.0 nm to be one of the strongest features in the dayglow spectrum. Chamberlain (1958) showed that 630.0 nm emission originates in the region between 140-300 km. Extensive reviews of the earlier work on this emission are available in the literature (Chamberlain, 1961; Bates, 1978; Hays et al., 1978; Torr and Torr, 1982).

630.0 nm emission is an outcome of the deexcitation of oxygen atom from the $^1D$ excited state to $^3P$ ground state. Figure 3.6 shows the energy level diagram of the excited state $^1D$ and $^1S$ excited state of the oxygen atom. The principal thermospheric source of $O(^1D)$ atoms are collisions between ground state oxygen $O(^3P)$ and photoelectrons (Dalgarno and Walker, 1964; Wallace and McElroy, 1966), dissociative recombination of the molecular oxygen ion (Bates 1946; Peterson et al., 1966) and photodissociation of molecular oxygen in the Schuman-Runge Continuum (Barbier 1959; Noxon and Johnson 1972). These processes can be explained in the following subsections.

### 3.3.1# Electron impact –

Ground state atomic oxygen O($^3$P), may be excited to the $^1$D state during a collision with electrons of energy greater than 1.96 eV.

$$O(^3P) + e\ (E > 1.96\ eV) \rightarrow O(^1D) + e \tag{3.15}$$
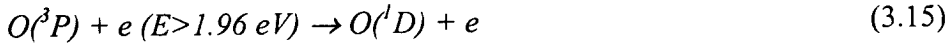
The production rate of this process is given by.

$$P_e(Z) = n[o] \int_{E_{th}} \sigma^{1D}(E)\phi(E, Z)dE \tag{3.16}$$

Where $P_e$ is the production rate, n[O] is the ground state oxygen density, $\phi(E, Z)$ is the electron flux at energy E and at an altitude Z and $\sigma_{1D}(E)$ is the excitation cross section.

### 3.3.2# Dissociative Recombination –

This process has been accepted as the primary source of O($^1$D) during nighttime (Bates, 1946).

$$O_2^+ + e \rightarrow O(^1D) + O \tag{3.17}$$

Out of the several combinations a fraction results in the creation of a metastable oxygen O($^1$D) atom. The rate of production of O($^1$D) by dissociative recombination is

$$P_{DR}(Z) = B_{1_D} B_{o_2} \eta[O_2^+]\eta_e \tag{3.18}$$

$P_{DR}$ is the production rate, $B_{1_D}$ is the efficiency for the production of O($^1$D) atoms, $\beta o_2^+$ is the total recombination rate n[$O_2^+$] is the molecular oxygen ion number density and $n_e$ is the electron density.

### 3.3.3# Photodissociation -

Neutral molecular oxygen gets dissociated by the Schumann - Runge continuum (125-175 nm) (Brandt, 1958).

$$O_2 + h\nu \rightarrow O(^1D) + O(3P) \tag{3.19}$$

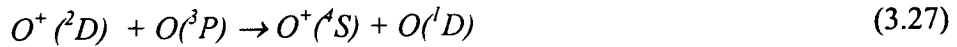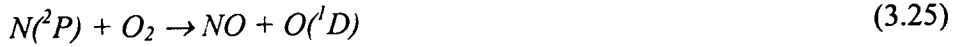and for a given solar flux the rate of production of O($^1$D) is given as

$$P_{PD}(z) = n[O_2]\int_\lambda \sigma_{SR}(\lambda)F_\infty(\lambda)\sigma^{-\sum_i \sigma_i N_i} d\lambda \tag{3.20}$$

where $P_{SR}$ is the O($^1$D) production rate, n[$O_2$] the molecular oxygen density, $F_\infty(\lambda)$ the unattenuated solar flux, $\sigma_{SR}(\lambda)$ the Schumann Runge cross section, $\sigma_i$ the

absorption cross section of the $i^{th}$ atmospheric species and $N_i$ the column density of the $i^{th}$ species.

Apart from the above processes for $O(^1D)$ formation, there are other sources, which contribute to its production (Solomon and Abreu, 1989). These are listed below :

$$O(^1S) \rightarrow O(^1D) + h\nu \ (557.7 \ nm) \tag{3.21}$$

$$N(^2D) + O_2 \rightarrow NO + O(^1D) \tag{3.22}$$

$$N + O_2 \rightarrow NO^- + O(^1D) \tag{3.23}$$

$$N(^2D) + O \rightarrow N(^4S) + O(^1D) \tag{3.24}$$

$$N(^2P) + O_2 \rightarrow NO + O(^1D) \tag{3.25}$$

$$N(^2P) + O \rightarrow N(^4S) + O(^1D) \tag{3.26}$$

$$O^+ \ (^2D) + O(^3P) \rightarrow O^+(^4S) + O(^1D) \tag{3.27}$$

$$e^* + O_2 \rightarrow e^* + O + O(^1D) \tag{3.28}$$

### 3.3.4# Radiation quenching of $O(^1D)$ atoms :

The oxygen $O(^1D)$, metstable state is destroyed both by radiation and by collisional quenching:

$$O(^1D) \rightarrow O(^3P) + h\nu \ (630.0nm) \tag{3.29}$$

$$O(^1D) + O_2 \rightarrow O(^3P) + O_2 \tag{3.30}$$

$$O(^1D) + N_2 \rightarrow O(^3P) + N_2 \tag{3.31}$$

Under photo-chemical equilibrium, the number of $O(^1D)$ atoms produced at any altitude is given by

$$[O(^1D)^{(2)}] = \frac{P_e(Z) + P_{DR}(Z) + P_{PD}(Z)}{A_{1_D} + K_{N_2}[N_2(Z)] + K_{O_2}[O_2(Z)] + K_O[O(Z)]} \tag{3.32}$$

where $K_{N_2}, K_{O_2}$ and $K_O$ are the quenching rates due to $N_2$, $O_2$ and $O$ respectively. $A_{1_D}$ is the Einstein's transition probability. The volume emission rate $N_{630.0}$ for 630.0 nm photon is given as

$$N_{630.0}(Z) = A_{630.0} \ [O(^1D)(Z)] \tag{3.33}$$

where $A_{630.0}$ is the transition probability which accounts for the branching.
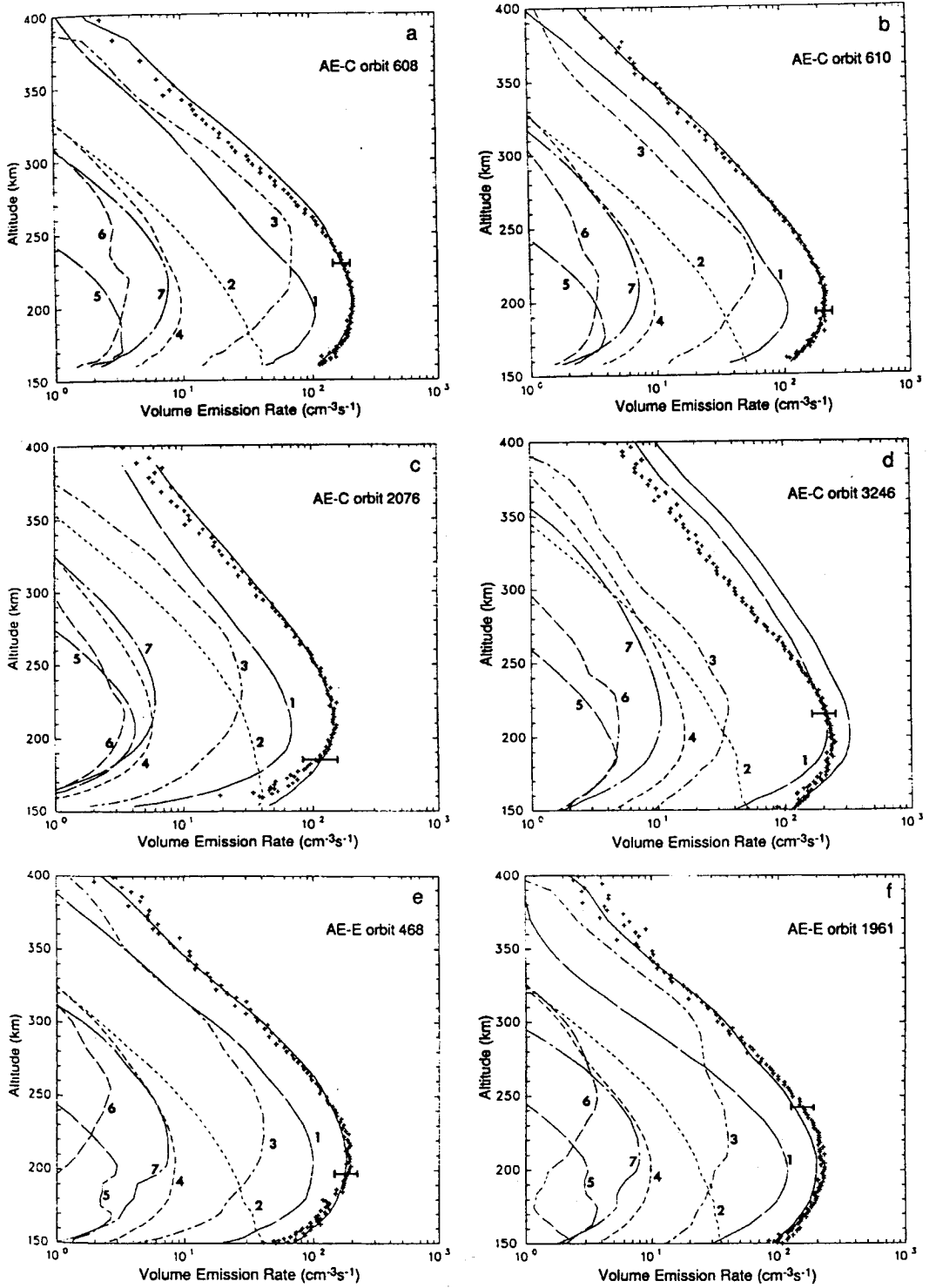
**Figure 3.7.** Measured and modeled 630 nm volumeemission rate profiles. Inverted measurements from the VAE experiment are represented with pluses. Total modeled emission is shown with a solid line. Contribution sources (1)e*+O; (2) hv+$O_2$; (3) $O_2^+$ +e; (4) O($^1$S); (5)N($^2$D)+$O_2$; (6)N$^+$+$O_2$ ;(7)N($^2$D)+O. (After Solomon and Abreue, 1989)

As stated earlier, there had been only a few attempts to measure the daytime emission by ground based techniques and hence very few estimates of the volume emission rates are available. Among the few studies, one of the most comprehensive studies by Hays (1978) and Solomon and Abreu (1989) have used the data from the Visible Airglow Experiment (VAE) onboard the Atmospheric Explorer (AE) Satellite. They showed that photoelectron excitation, photodissociation and dissociate recombination are sufficient to explain the measured 630.0 nm dayglow and that photoelectron contribution to the dayglow is the most significant, followed by the photodissociation and the dissociative recombination in descending order of significance. Figure 3.7 shows their calculations on the 630.0 nm emission.

Solomon and Abreu (1989) also showed large spatial variabilities to prevail in the 630.0 nm dayglow. As mentioned earlier, during nighttime it is the dissociative recombination (DR) process that is believed to be responsible for the 630.0nm emission. This process depends on the available electron densities at the emission altitudes and hence the electron density variabilities would get reflected in the 630.0nm variabilities. Using the above argument 630.0nm emission has been used extensively for the study of electrodynamical aspects of the equatorial upper atmosphere (ionosphere). Day to day variations in the ionospheric processes and the resultant changes in the emission (Pal and Kulkarni, 1973; Sahai et al., 1987), retrieval of equatorial ionization anomaly (Chandra et al., 1973; Sridharan et al 1993), plasma depletion and equatorial spread F (Mendillo et al., 1985; Meriweather et al., 1985; Mendillo et al., 1992) are some of the important studies carried out using 630.0nm emission in the recent times. With the new Dayglow Photometers some very interesting reports on the use of 630.0 nm dayglow emission for equatorial F region processes have also been reported (Sridharan et al, 1994; Pallam Raju and Sridharan, 1996; Sridharan et al, 1999a,b,c).

## 3.4#  Results from low latitude stations on 630.0 nm and 557.7 nm dayglow emission variabilities.

As we discussed in the instrumentation chapter, the aim of the development of the MWDPM was to study the coupling processes in the mesosphere-lower thermosphere region and for this, initially three emissions Na 589.0, $O(^1S)$ 557.7nm and $O(^1D)$ 630.0nm were selected. NaD emission is representative of ~92 km altitude

while O($^1$S) and O($^1$D) are expected to represent lower and upper thermospheric regions respectively. As the resonantly scattered sodium lines are situated very close to strong Fraunhoffer absorption features, it has been found experimentally that this line may not be suitable for our studies. When the data obtained for 557.7 nm and 630.0 nm were analyzed, few important observations were made. It was seen that there existed (1) large day to day variabilities, (2) variability in the occurrence time of noontime maximum and (3) on most of the occasions the 557.7nm emission variabilities had one to one correspondence with the 630.0 nm emission variations indicating the importance and potential of the common source. The following sections describe some of the new results from the near simultaneous measurements of the O($^1$S) greenline and O(1D) redline, made with a view to investigate the relative importance of the various excitation processes during daytime, in comparison with nighttimes and also to study the coupling of the different atmospheric regions.

### 3.4.1# Examples of observed variabilities in the daytime 630.0 and 557.7 nm emission intensities: New results:

26$^{th}$ January 1996 was one the among few days when the new MWDPM was operated on 630.0 nm O($^1$D) and 557.7 nm O($^1$S) emissions from Mt. Abu (24.6N, 73.7E), a low latitude station in the Indian zone. This is a location up to which the crest of the Equatorial Ionization Anomaly could extend on days of strong zonal electric fields over the dip equator. The observed intensity variabilities of both the emissions are depicted in Figure 3.9a. Similar diurnal behavior in both the emissions could be clearly seen. Apart from this all small - scale features like small hump, dip, kinks in their variabilities have one to one correspondence too. In short, variabilities in one emission have their image in the other emission.

Another interesting day with clear sky conditions from Mt Abu was 4$^{th}$ April 1996, when the data could be collected from 0800 IST – 1730 IST. This day was different from other days with regard to the diurnal behavior of both the emissions. Figure 3.9b shows the intensity variabilities of both the emissions. One can notice that instead of a usual noon time peak, a steady level in both the emissions was observed for an extended period. With similar, short as well as long period features in both the emissions after 1600 IST there had been a steady and slow decreasing trend.

Further investigations in the same operational mode of MWDPM were carried out from another low latitude station Kolhapur (16.8 N, 74.2 E), in the Indian zone

during February 1997 and few more days of long time series data could be obtained when clear sky conditions were present. Figure 3.9c depicts the results corresponding to 4th February 1997. With a noontime peak in both the emissions around ~1300 IST, they followed a decreasing trend during later hours. A steep decay of the intensity was observed ~1400 IST for a short time duration, which was followed by an increase at ~1420 IST, raising the intensity levels to the average values. After this a monotonous decreasing trend could be seen clearly in both the wavelengths.

Figure 3.9d presents the observed intensity variabilities on 6th February 1997 over Kolhapur. On this day data could be collected from 0900 IST to 1730 IST. A double hump diurnal maximum could be clearly observed. One of the peaks occurred at ~ 1100 IST while the other occurred at ~1245 IST. Overall short period as well as long period variabilities in both the emissions i.e. the 557.7 nm and 630.0 nm dayglow emissions, were strikingly similar.

9th February 1997 was another interesting day showing similar intensity variations in both the green and red line emissions (Figure 3.9e). One could see the count levels to be lesser on this day. Smooth long period (~ 6 hrs) oscillatory feature in both 557.7 nm and 630.0 nm intensity variations could be clearly observed. Peak intensity occurred at ~1200 IST. Many shorter period oscillatory features in both the dayglow emissions show one to one correspondence.

Interesting intensity variabilities shown in Figure 3.9f were observed on 11th February 1997. A steady rise in the emission intensities up to ~1200 IST could be seen clearly. The oscillatory features in both the emissions were strikingly similar.

Figure 3.9g and 3.9h depict the intensity variabilities, observed on 12th and 13th February 1997 from Kolhapur confirming the earlier observations

Apart from the days when 557.7 nm $O(^1S)$ and 630.0 nm $O(^1D)$ emissions show one to one resemblance, there were occasions when they did not show similarities. 1st February and 2nd February 1997 were among those few days when intensity variabilities of 557.7 nm and 630.0 nm emissions did not reveal the similarities usually observe in them. The intensity variabilities on this day are shown in figure 3.10a. On 1st February 1997, 557.7 nm and the 630.0 nm intensities showed totally different behaviour. Long period oscillations in both showed different behaviour while the short period variabilities in both the emissions had close correspondence.
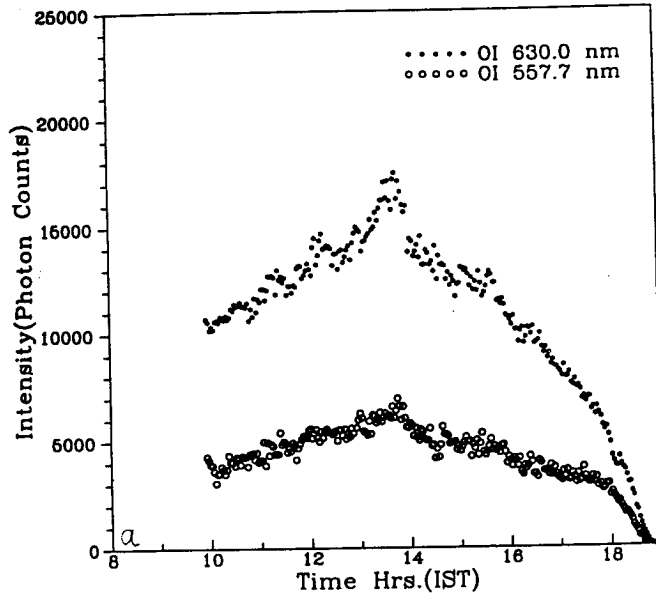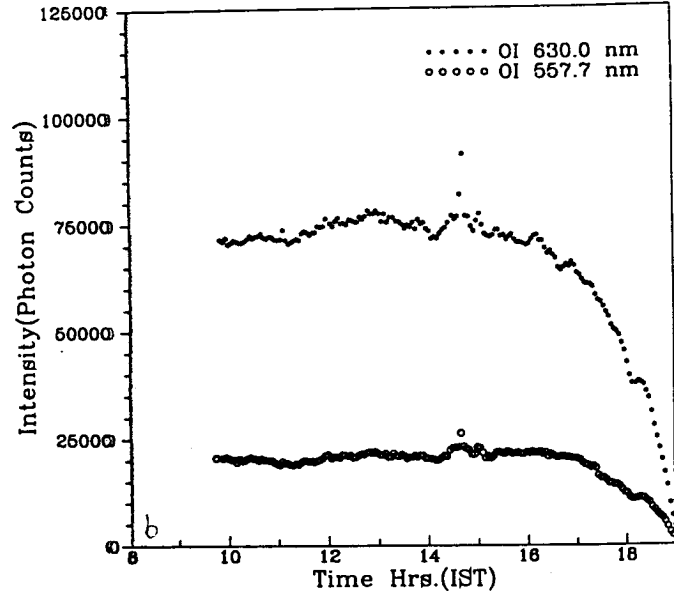
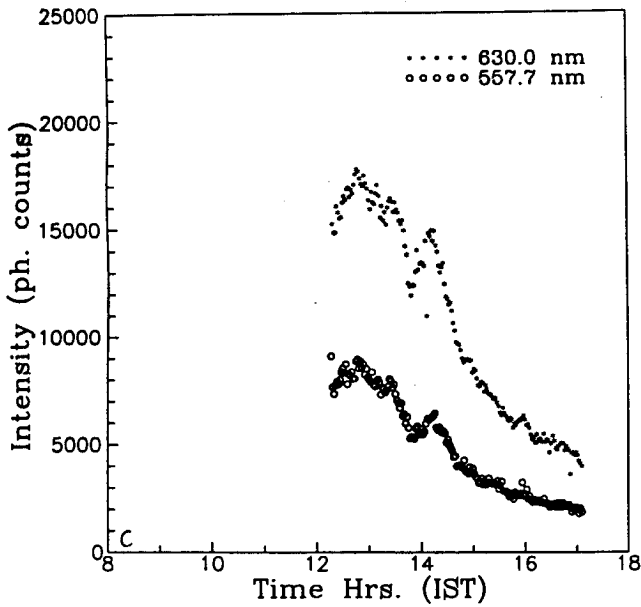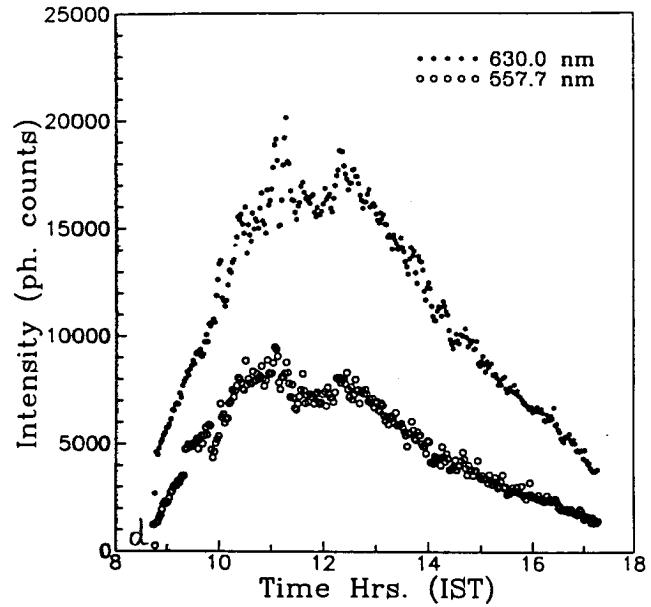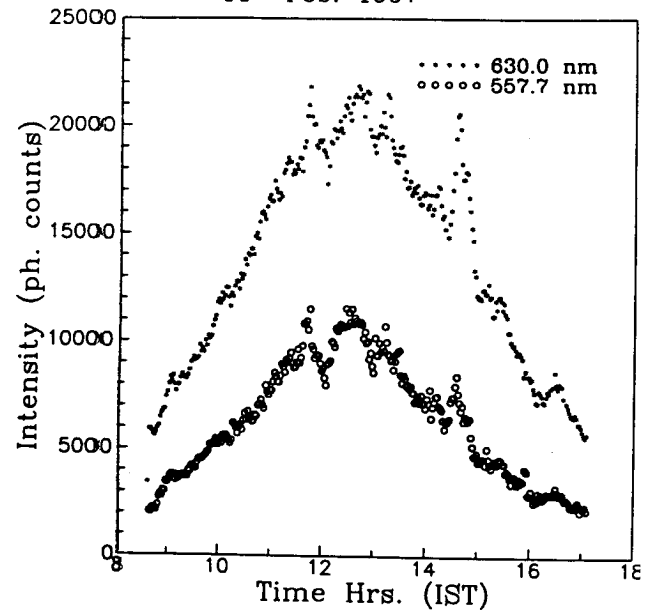**Figures 3.9(a,b.c,d)** Observed intensity variabilities of 557.7 nm lower thermospheric and 630.0 nm upper thermospheric emission.

65
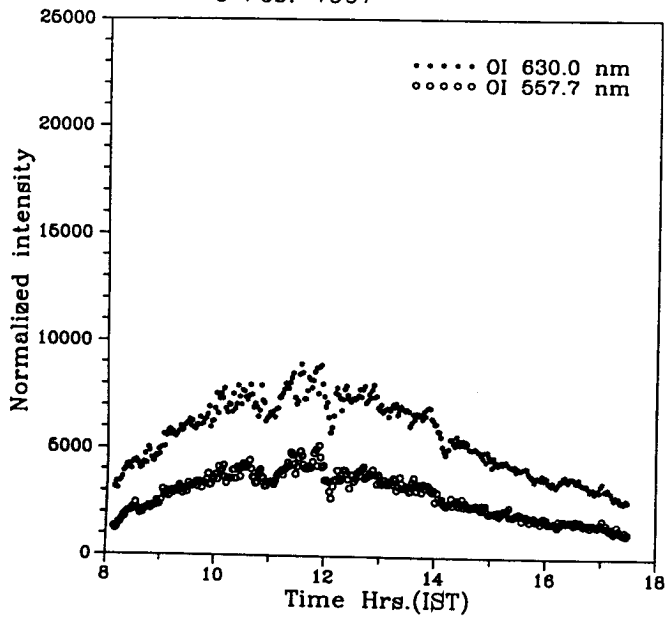
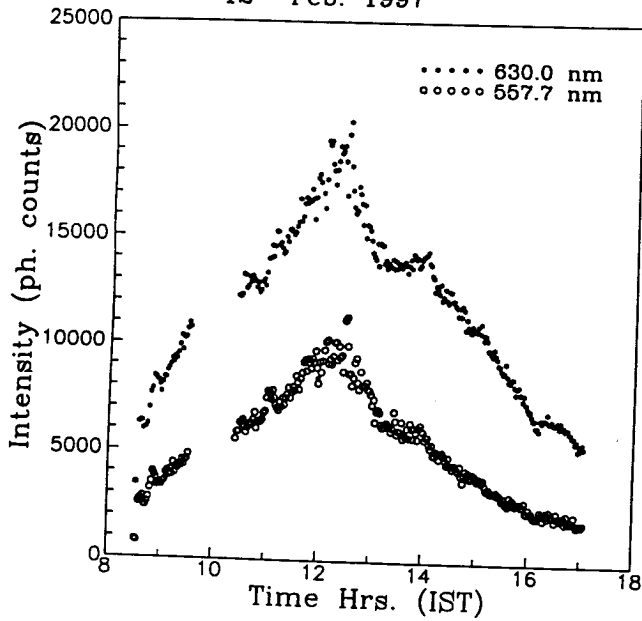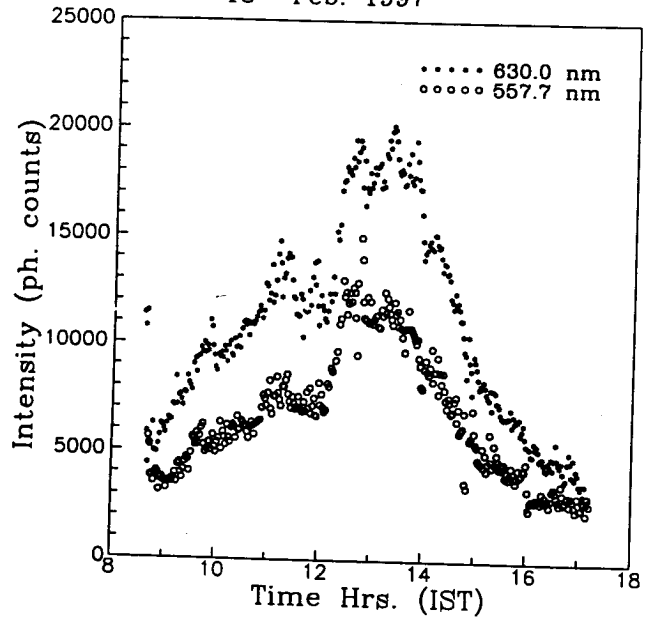**Figures 3.9(e, f, g, h)** Observed intensity variabilities of 557.7 nm lower thermospheric and 630.0 nm upper thermospheric emission.
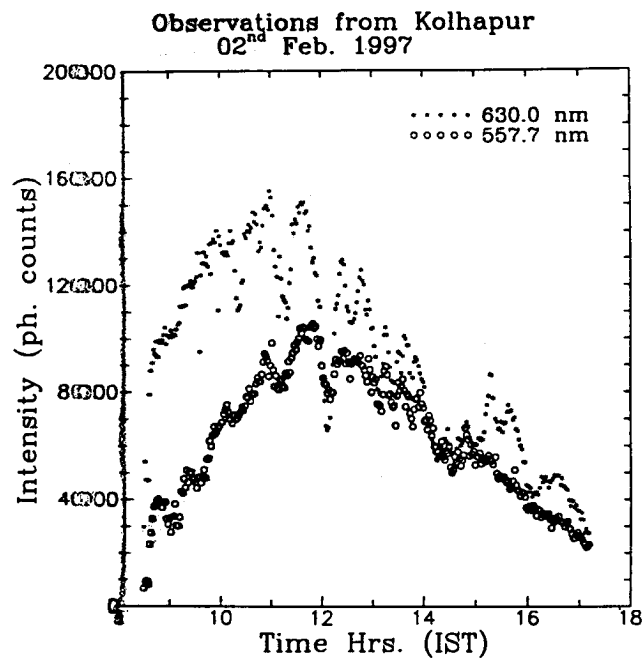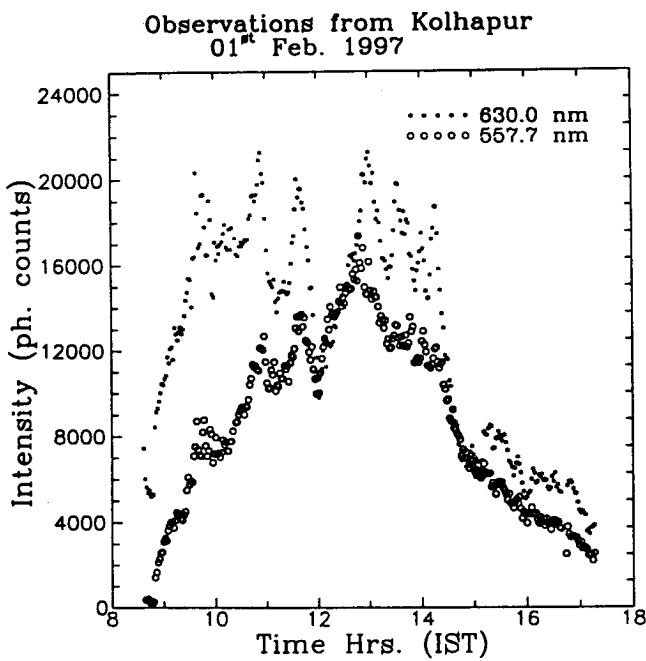
**Figures 3.10(a,b)** Observed non-similar behavior of 57.7 nm lower thermospheric and 630.0 nm upper thermospheric emission.

On 2$^{nd}$ February (figure 3.10b) the 557.7nm emission reached the peak values around 1200 h while the 630.0 nm emission had maximum value around ~1100 IST. Asymmetric temporal evolution of the 630.0nm intensities in comparison to 557.7 nm emission intensities was observed. Despite long period features being different, one can see that from ~1000 IST to ~1500 IST, shorter period oscillatory feature do have resemblance in both the emission variabilities. These results have important repercussions.

### 3.4.2# Discussion –

In the light of the above discussed results one could conclude that except on some occasions, the 557.7 nm emission variability has one to one correspondence with the 630.0nm intensity variations. The resemblance indicates towards the dominance of F region contribution in 557.7nm emission. In order to check the same, an exercise was carried out to see the relative contribution of the thermospheric source (i.e. the F region contribution) in 557.7 nm emission. For this, published data of 557.7nm volume emission rates for different solar zenith angles (Vir Singh et al., 1997), using WINDII (wind imaging interferometer), on board the UARS satellite was considered. In this exercise integrated volume emission rates have been estimated. Contributions from lower thermospheric source is referred to as E region contribution while the upper thermospheric source is referred to as F region

69

contribution. The exercise showed that for all the solar zenith angles the F region contribution to the total volume emission rate remains nearly 70% (Table 1). The reason for the dominance of F region contribution could be found in the study of Hays and Sharp (1973). They showed that dissociative recombination becomes very significant for the thermospheric (F region) contribution in 557.7 nm emission. The dissociative recombination process depends on the available electron densities at those altitude regions. Peak emission altitude of 630.0 nm emission and thermospheric peak of 557.7 nm emission are not far from each other and so the electron density variabilities through dissociative recombination channel would affect both the emissions. Thus, both the emissions showing similar variabilities throughout the day is considered very important providing experimental confirmation to the model calculations and hence revealing that, the upper thermospheric source has dominance over the lower thermospheric source of 557.7 nm emission, throughout the day. These results are the *first ground - based evidence* for the significant upper thermospheric contribution to the 557.7 nm emission during the day which has conventionally been thought to be a lower thermospheric / upper mesospheric tracer. Occasional differential, diurnal nature of 557.7nm and 630.0nm emission intensities, emphasis towards the possible role of other dynamical processes the effect of which surpass the photochemical processes. Strong tidal influences in 557.7nm emission have been reported in the literature (Shepherd et al., 1995; Zang and Shepherd, 1999). How much these tidal forcing could dominate and change the relative contribution of both the sources in 557.7 nm emission is pending for the further possible investigations.

Apart from the above, one could also see large day to day variations in both the emission intensities. As mentioned earlier while presenting the data, variation in the occurrence time of the noontime maximum can be noticed on some days. Because the noontime maximum in the intensities, is solar controlled the above said variation suggests strong influences of dynamical forcing on the emissions. Presence of short period oscillatory features in the intensities are believed to be due to gravity wave associated processes. These processes are very important and proper understanding of their effects on the system, demand for a larger database and supporting evidences.

| Integrated Volume emission rate (VER) calculations for 557.7 nm O($^1$S) dayglow | | | | |
|---|---|---|---|---|
| Solar zenith angle | $17^0$ | $30^0$ | $50^0$ | $80^0$ |
| E – region contribution (lower layer) | 15200 | 13800 | 12000 | 6300 |
| F – region contribution (upper layer) | 42600 | 34400 | 32000 | 12600 |
| Total VER | 57800 | 48200 | 44000 | 18900 |
| % F – region contribution (upper layer) | 73 | 71 | 72 | 68 |

**Table 3.1.** E and F region contribution to the 557.7 nm Volume emission rate for different solar zenith angles (data base from Singh et al 1997).

## 3.5# Conclusions:

The results discussed in this chapter show strikingly similar variabilities in 557.7 nm and 630.0 nm emissions and are first to provide ground - based evidence for the significant thermospheric contribution in the 557.7 nm dayglow emission all through the day. As a consequence it can be concluded that 557.7 nm emission can not be used as a tracer for the upper mesospheric lower thermospheric processes during daytime. The complex behavior of 557.7nm emission occasionally, when its variations do not have resemblance with 630.0 nm emission, and the large variabilities in both the emissions needs further coordinated in depth investigations, with emphasis on the dynamical forcings.

# 4# Day- Night measurements of OI 630.0 nm airglow emission from low latitudes.

## 4.1#Introduction:

The low and equatorial thermosphere-ionosphere system (TIS) is well known to exhibit a variety of large and small-scale dynamical processes. Large-scale processes (both spatial and temporal) like Equatorial Electrojet (EEJ), Equatorial Ionization Anomaly (EIA), Neutral Anomaly (NA), Equatorial Temperature and Wind Anomaly (ETWA), Equatorial Spread-F (ESF) and Midnight Temperature Maximum (MTM) are well known and have been investigated widely. A brief description of these equatorial phenomena has been given in the introduction chapter of this thesis. Many studies bringing out the key features in these processes have been reviewed in the literature ( Raghavarao et al., 1988; Abdu et al., 1999 and references cited therein). Presence of short period oscillatory and irregular structures in the upper atmosphere have been detected by several techniques and had been a puzzle for a long time. Hines (1960) interpreted these irregular variations to a single physical process viz. the internal atmospheric gravity waves. Since then, gravity waves and associated phenomena had been one of the most important aspects in the upper atmospheric investigations and most of the times, oscillatory features in almost all the TIS parameters are attributed to them. However, so far, the investigations on the presence and persistence of these gravity waves in the thermosphere-ionosphere system are rather scanty. The gravity waves, usually generated in the lower atmosphere, propagate upwards, with their amplitudes increasing in order to conserve their energy due to the negative density gradients. Their interaction with other waves, tides and mean winds, lead them to significantly modify the energetics and dynamics of the ambient medium (Murata, 1974; Lindzen, 1981; Garcia and Solomon, 1985; Liu and Hagan, 1998). They act as a means of transport of heat and momentum from one region to another and are well appreciated to be the agents for the lower and upper atmosphere coupling (Hocking 1996; Wickwar and Carlson, 1999).

These gravity waves deposit significant amount of heat and momentum to the different altitude regions as they propagate upwards. The most important filtering process occurs at the mesopause region. Once the wave penetrates this region, it might affect the upper atmosphere (Murata, 1974; Fritts 1984; Killeen and Johnson, 1995; Hocking 1996). So far, the detection of short period oscillatory features in the

upper atmosphere had been rather difficult, and for the daytime conditions, these problems are even more severe. Usually the methods opted for these studies can be categorized under radio and optical airglow measurement techniques. Abdu et al. (1982) had shown the presence of gravity waves in the thermosphere ionosphere system through the ionograms. In their study, with the observed oscillatory features in $h_pF_2$ and $f_oF_2$, a first order speculation of these features to be due to the wave associated process was envisaged. Further, with the help of true height electron density profiles they deduced the height time cross section of the iso – electron density values. Figure 4.1 shows the result of their analysis wherein the downward phase propagation, characteristic of internal atmospheric gravity waves could be seen clearly. They deduced the intrinsic wave parameters also with the help of the above analysis.
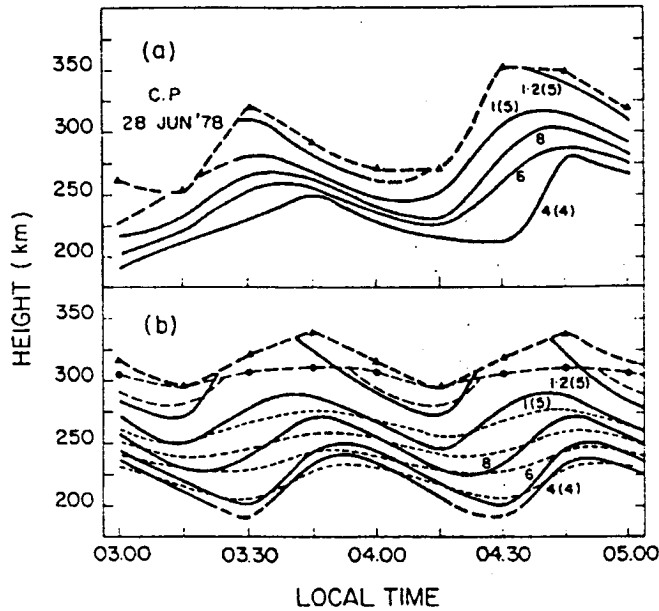


**Figure 4.1.** (a) True height-time cross section of the electron iso-density contours and (b) height-time cross section of electron iso-density contours (after Abdu et al, 1982).

To find out the disturbed component of the $F_2$ layer critical frequencies, Mishin et al. (1991) calculated the values of $\Delta fo = f_oF_2 - \mathbf{f_oF_2}$ , where $\mathbf{f_oF_2}$ are the averages over 13 five minute values. To obtain the periods of the oscillatory features ($\Delta fo$), the residue was subjected to spectral analysis. With the help of the ionosonde chain, the direction of wave propagation was determined. They found periodicities of 27 minutes to 96 minutes to be dominant in the ionosphere (Figure 4.2).

**Figure 4.2** foF2 time variation (a) at Moscow (b) at Dushanbe (After Mishin et al, 1991)

There are few other studies also using radio probing, wherein oscillatory features had been discussed in the context of gravity waves (Huang and Cheng, 1991; Mishin et al., 1991). Airglow photometry is always preferred for such studies due to their better temporal resolution. The most widely used tracer for the thermosphe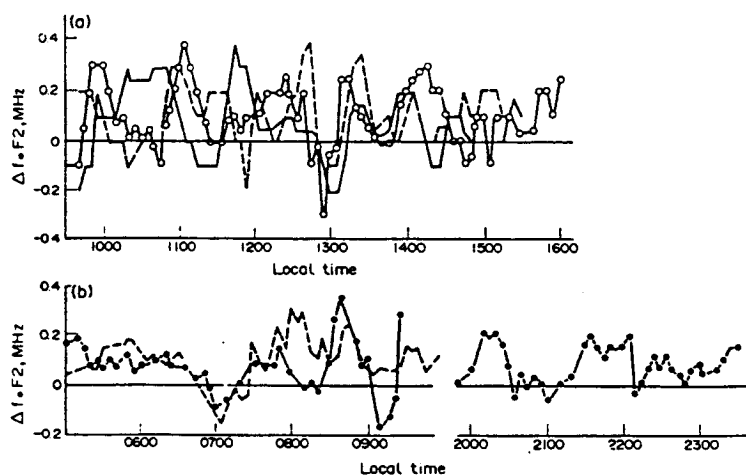re-ionosphere system is the 630.0 nm ($O^1D$) emission, which centers around 220 km during daytime and ~250 km during nighttime with a layer of typical semi-thickness of ~75 Km.. Photometric studies on 630.0 nm emission have revealed the presence of short period oscillatory features in the thermosphere-ionosphere system (TIS) (Takahashi et al., 1989; Sobral et al., 1997).

Sobral et al (1997) identified the gravity waves manifesting themselves as perturbations in the 630.0nm nightglow emission intensities measured with a scanning photometer over low latitudes in the south American sector. Disturbances travelling from south to north were recorded as moving depletion or valleys. Their appearance during the post sunset period were taken as indication that solar terminator may be the source of the wave generation. A sample of their observations is shown in figure 4.3.
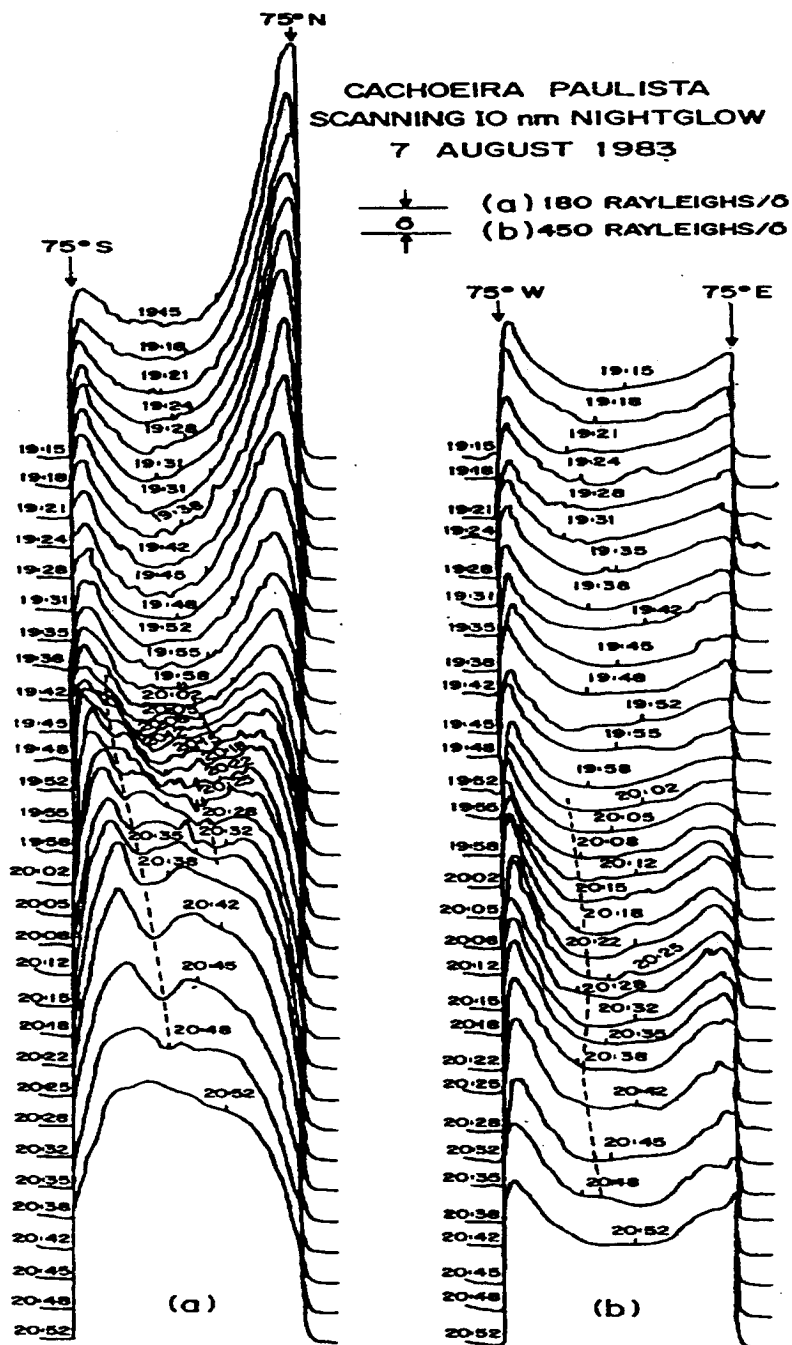
74

**Figure 4.3.** Sequence of meridional profiles of the OI 630.0 nm airglow intensity. The patches of south to noth propagating events are indicated by dashed lines (after Sobral et al, 1997).

Interferometric studies at 630.0 nm over the equatorial region sometimes show the enhancement in the thermospheric temperatures (Meriwether et al., 1997). These enhancements were hypothesized to be due to the penetration of the gravity wave energy from the surface to the thermosphere where viscous dissipation could cause the heating.

As mentioned in the chapter 2 (instrumentation), until the development of the Dayglow Photometer (DGP) (Narayanan et al., 1989; Sridharan et al., 1992a), photometric studies on 630.0 nm airglow emission were generally restricted to moonless nighttime conditions only. Presence of high solar background during daytime, which was the constraint, was effectively overcome by the virtue of a unique mask assembly in combination with an appropriate Fabry Perot etalon. After its development, the DGP has been used extensively for the investigation on the TIS processes.

It was shown from the observations of 630.0 nm dayglow, that the F − region electron densities play crucial role in the dayglow and contribute nearly 100% in the temporal variabilities through the dissociative recombination process (Sridharan et al., 1992b). Further, the DGP was successfully used to provide a precursor to the equatorial spread-F using its bi-directional mirror scanning option from a low latitude station Waltair (Sridharan et al., 1994). Tracking of equatorial ionization anomaly was also done using the mirror scanning option of the DGP (Pallam Raju et al., 1996) (Figure 4.4).
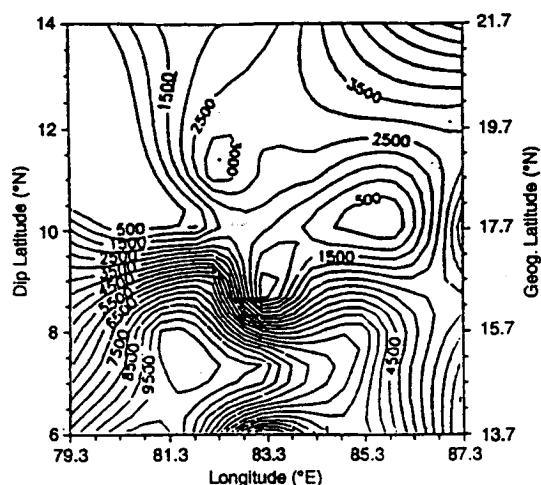


**Figure 4.4.** A 2D map obtained from Waltair on 11February 1995 at 1730 h. Wavelike features with scale size ranging ~800 km in the north-estern direction could be clearly seen. (after Pallam Raju and Sridharan, 1996)

Further, it is well appreciated that at a given instance, the atmosphere behaves as a strongly coupled system and gravity wave modes are some of the most important coupling agents. On the basis of the above, one may suggest some wave modes to be present in the TIS (thermosphere ionosphere system) during most of the times, irrespective of day or nighttime conditions. In case, these periodicities could be identified one could get some clues on the preferable modes of the gravity waves responsible for the lower and upper atmosphere coupling.

## 4.2# Present investigation

In order to investigate the above possibility, 'round the clock' observations are essential, and the **Daynight Photometer** described in the instrumentation chapter was effectively used and the results obtained from these studies form the subject matter of this chapter.

The stated aims of the investigations are, (1) identification of the persistent wave modes in the TIS and (2) behavior of the TIS as a whole. The Day –Night Photometer was operated from Waltair ($17.7^0$ N, $83.3^0$ E, dip latitude 10.09 N), a low latitude station in the Indian zone during March 1998 as a part of the Indian Solar Terrestrial Energy Program (ISTEP) campaign. The first results on the day – night 'round the clock' variations in the 630.0nm thermospheric emission intensities and coordinated ionosonde observations are presented and discussed in the following sections.

## 4.2# Airglow observations and corresponding ionospheric data:

21st March 1998 ($A_p$=33) happened to be the first day when data for long time duration could be collected (Figure 4.5). There had been a steep rise by at least two orders of magnitude in the intensity level from the typical nighttime levels by 0700 h. Wavelike oscillatory features could be seen at least up to 1500 h. The intensity level remained more or less steady from 1000 h to 1400 h. The fluctuations seen ~1300 h is believed to be due to extraneous reasons. Beyond 1500 h a gradual decrease in intensities is noticed till 1800 h when usually the dayglow mode of observation ceases. The nightglow mode of observation could be started only from ~2000 h due to the drastic changes in the intensity levels during twilight times. The wavelike

oscillatory features persisted throughout the night though better perceived than the daytime conditions, essentially due to the prevailing low level background intensities.
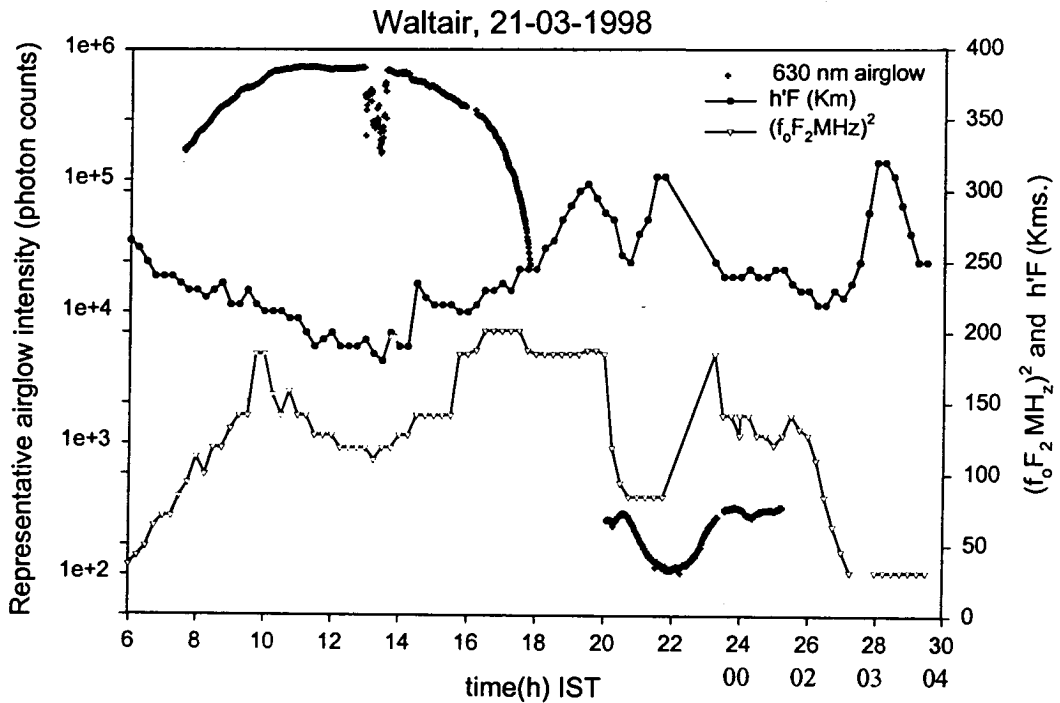


**Figure 4.5.** Simultaneous observations of 630.0 nm airglow and ionospheric parameters on $21^{st}$ March 1998

With regard to the ionospheric data from the same location the variations of h'F (the base height of the F - region) and the $f_oF_2^2$ which is a proportional quantity to $N_{max}$ (the maximum F region electron density) on $21^{st}$ March are also depicted in figure 4.5. The $f_oF_2^2$ registered a linear increase from 0600 - 1000 h followed by a noontime bite - out. From 1600 - 2000 h the density levels remained the same, following which a steep bite out lasting for 2.5 h occurred, centered at 2100 h. Beyond midnight there had been a steady decrease. Wavelike perturbations are seen both in $f_oF_2^2$ and in h'F (figure 4.5). The h'F variations ranged from ~190 km to 300 km during the course of the day. The possible relation between the ionospheric parameters during daytime to the dayglow variations would be discussed later.

**Figure 4.6.** Simultaneous observations of 630.0 nm airglow and ionospheric parameters on $22^{nd}$ March 1998

Figure 4.6 represents the dayglow variabilities on $22^{nd}$ March 1998 ($A_p$=11). The daytime intensity levels had been similar to that on $21^{st}$ March. The solar zenith angle control is clearly depicted. However, during late evening and night hours there are distinct differences. One could notice an enhancement in intensity maximizing ~2100 h instead of a bite out. These are manifestations of the changes occurring in the F - region electron densities. The h'F and $f_oF_2^2$ data for the same day are depicted in figure 4.6. Large-scale variability are present on this day too, more so in the h'F than in the $f_oF_2^2$. The consequences of these variations are discussed later.

The third day of day-night observations had been on $23^{rd}$ March 1998 ($A_p$=05) (Figure 4.7). The day started off like the previous two days till ~1500 h. The consistent feature on all the days is the flat top from 1000 h to 1400 h with no major variations. On this day, large oscillations got triggered ~1500 h with periods of ~30 min till the end of the day and later during night too systematic oscillatory features were recorded with a period of ~1 h. When one looks at the ionospheric data for the same day as depicted in figure 4.7, the variabilities had been more or less similar to the earlier two days with $f_oF_2^2$ showing some similarity in terms of the variations with the dayglow intensities. Such nighttime intensity variability is believed to have important consequences with regard to the development of plumes of irregularities during the phenomenon of equatorial spread F.

79

**Figure 4.7.** Simultaneous observations of 630.0 nm airglow and ionospheric parameters on 23$^{rd}$ march 1998.



**Figure 4.8.** Simultaneous observations of 630.0 nm airglow and ionospheric parameters on 24$^{st}$ March 1998

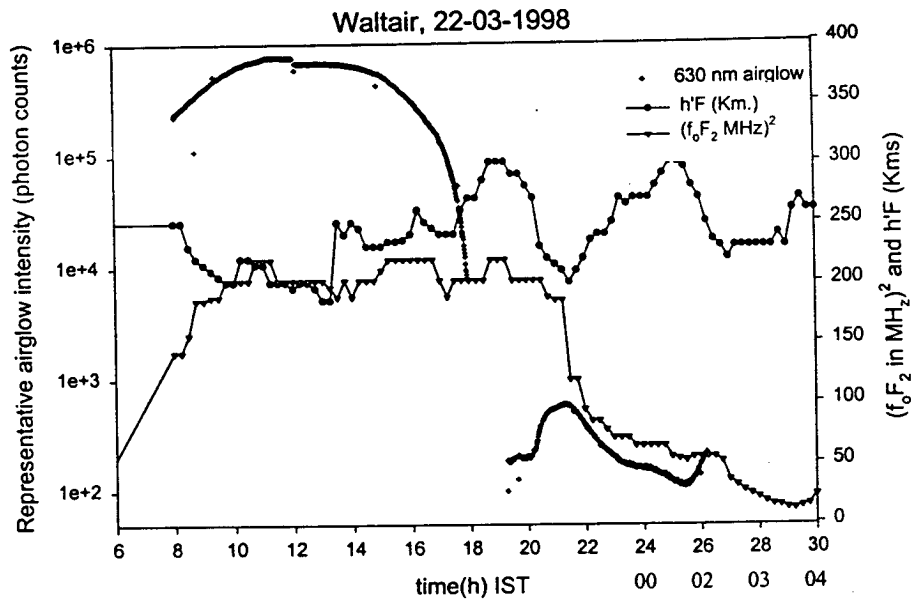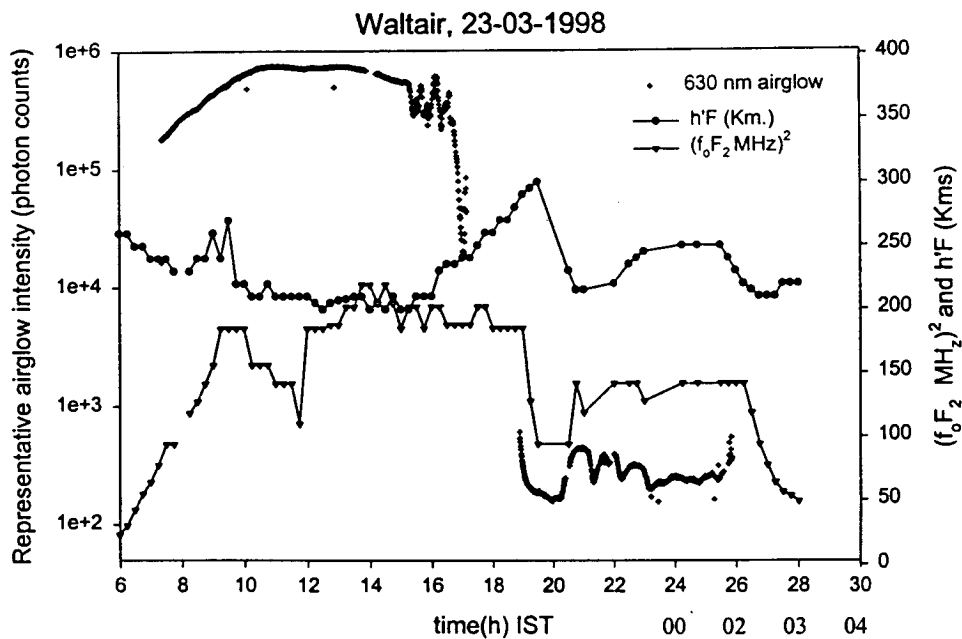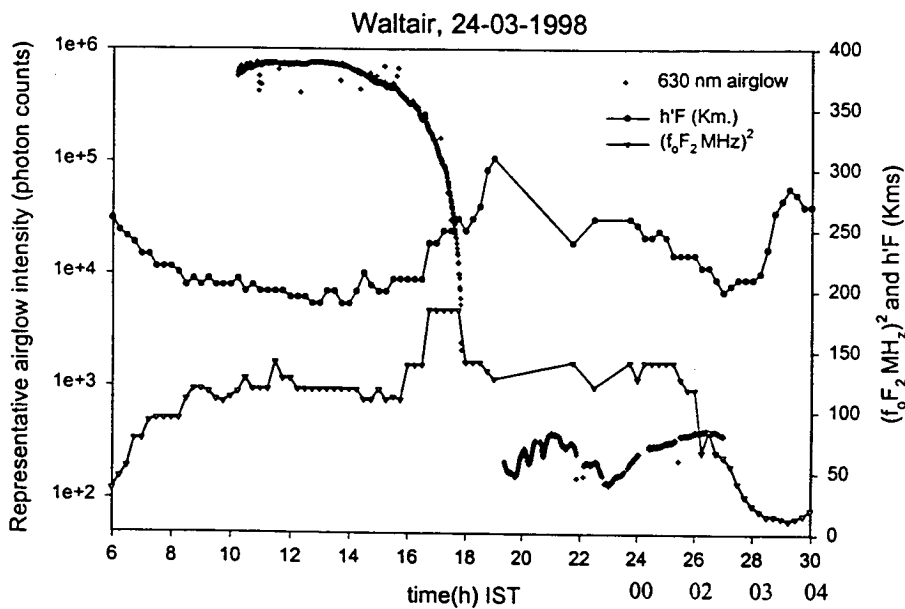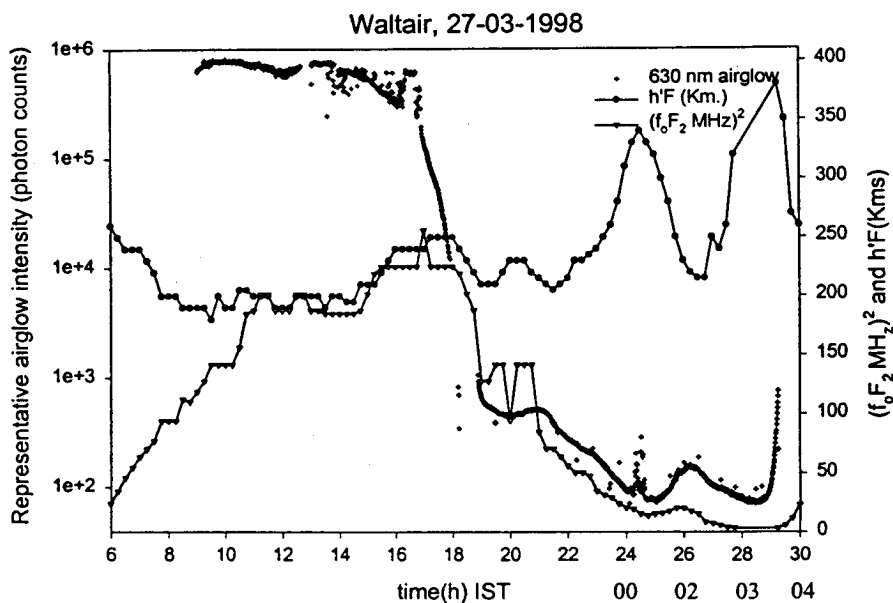**Figure 4.9.** Simultaneous observations of 630.0 nm airglow and ionospheric parameters on 27th March 1998

The data for 24th March 1998($A_p$=07) is depicted in figure 4.8. The dayglow intensities had been responding smoothly to the solar zenith angle variation while during evening hours a burst of oscillatory features were recorded with periods ~25 min to ~3 h. Unfortunately, there is a gap in the ionospheric data during 1900-2200h (figure 4.8).

27th March 1998 ($A_p$=13) had been distinctly different as compared to all the other four days, with a modulation by a 4 h period oscillation (figure 4.9), the presence of which had been felt all through the night. The ionospheric data especially h'F too registered the presence of such oscillations. These aspects will be discussed later.

## 4.3# Discussion:

### 4.3.1# F - region behavior during daytime

The simultaneous measurements of F - region ionospheric parameters and the 630.0 nm thermospheric airglow continuously during day and nighttimes enable one to investigate one of the fundamental aspects viz., chemical-dynamical coupling between the ionosphere and thermosphere. This statement gets vindicated when we carefully examine the h'F values and the dayglow intensity levels during the course of the day. Both the parameters are anti-correlated irrespective of the time of the day

81

though the sensitivity factor is different. This observation is consistent on all the days. As mentioned earlier, the F - region electron densities though contribute only 30% to the total dayglow intensity through dissociative recombination, nearly all the variabilities could be explained on the basis of the electron density variations in the emission region (Sridharan et al., 1992b). The other two major contributors viz., the photoelectron excitation of atomic oxygen and photo dissociation of molecular oxygen by the Schumann - Runge continuum, though account of 70% of the intensity, hardly vary with time, especially during the time interval of 0900 - 1600h. This conclusion was based on measured electron densities. The above arguments only imply that the F layer had been maintaining its layer shape over Waltair even during daytime and any movement in the base height causes the whole layer to be moved, essentially altering the chemical coupling conditions and hence the emission of 630.0 nm dayglow. Figure 4.10 depicts the possible relation of h'F and the average dayglow counts from 0800 to 1600 h, when the solar zenith angle effects associated with the dominant processes are considerably reduced and only the chemical recombination dictates the variabilities. The negative correlation is striking and more or less similar to the nighttime conditions.
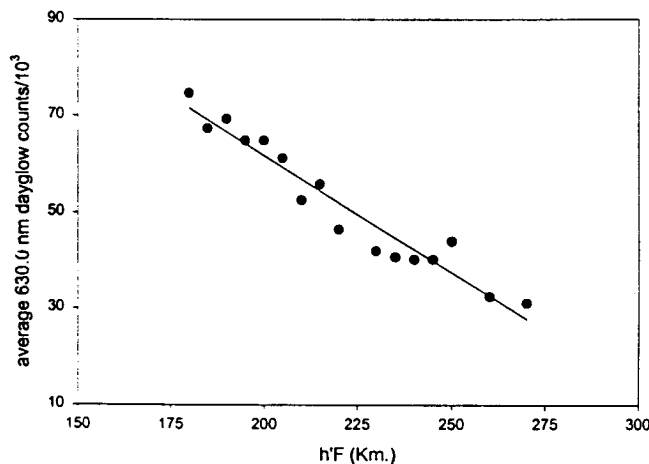


**Figure 4.10.** Observed inverse relation between dayglow counts and h'F over Waltair during March 1998.

The above result improves our basic understanding in the ionospheric dynamics because of the following. During nighttime F layer height (h'F) is well known to affect the 630.0 nm nightglow intensities via corresponding changes in the available electron densities at the emission altitudes. The variations in the h'F is equivalent to a physical displacement of the F layer. Thus it is inferred that the F layer

maintains its layer shape during nighttime and any variation in the base height will be able to affect the available electron densities at 250 km (the emission altitude of 630.0 nm nightglow). However, during daytime there is continuous production of electrons and hence the situation becomes complex. Hence, it was taken for granted in the earlier studies that the availability of electrons at emission altitudes to be more important rather than the variation in the base height itself. In the above context the present results showing the anti-correlation between base height of F region and dayglow, similar to the nighttime conditions is very important and fundamental.

Once such a relation between h'F and the dayglow intensities gets established and the inference being that it is linked through the electron density distribution in the emitting region centered around 220 km, it is logical to explore the possibility of establishing an empirical formula linking h'F and the $f_oF_2{}^2$ in the same fashion as had been shown by Barbier (1959) for nighttime conditions. The relationship comes out
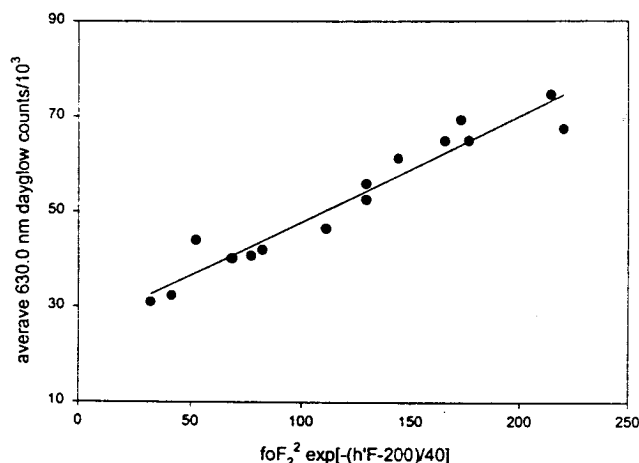


**Figure 4.11.** Relation between dayglow counts and Barbier type formula linking the ionospheric parameters with the 630.0 nm dayglow emission.

strikingly (figure 4.11) relating the instantaneous intensity to the maximum electron density and the base height of the F – region as given below-

$$Q_{6300} = A + B \ (f_oF_2)^2 \ \exp[-(h'F-200)/40] \qquad \qquad -----(1)$$

Where, $Q_{6300}$ denotes the dayglow intensity and A and B are constants. Difference between this formula and that of the Barbier is that, in place of $h_pF_2$ , h'F, and in taking H, the scale height, an average scale height of 40 km is used. Fresults are considered fundamental and extend the concepts, which are usually applicable for nighttime conditions, to daytime conditions as well.

### 4.3.2# Persistence of specific periodicities in the TIS

The second aspect of the present study attempts to investigate the dominant periodicities during day and nighttime conditions, as these waves are in general the coupling agents. One can see that there is more than an order of magnitude difference in the daytime and nighttime 630.0 nm emission intensity levels. In order to investigate the wave features associated in them and their relative importance, these intensities have to be in the same scale. For this purpose, the fractional intensity variation analysis (FIA) was carried out. In FIA, the intensity data (I) was detrended from the long period variation. Long period variations in the intensity ($I_0$) were obtained by taking a running average of I for 1.0 hour. The residuals obtained ($I - I_0$) were then normalized to the $I_0$ and are called as the corresponding fractional intensity. The data had been treated alike for both day and nighttime conditions. The residual counts were then normalized to the long period trend ($I_0$). The ratio ($I-I_0$)/$I_0$ then represents the fractional intensity and this step gives due weighting for both the night and dayglow intensities. The observed variabilities are now depicted in different panels in figure 4.12 (a,b,c,d,e). One common element that seems to emerge is that the variabilities are significantly less pronounced during sunlit hours than during nighttime. This is understandably so as the centroid of dayglow emission region is not far from the region of maximum production of ionization. Inspite of this limitation, periodicities ranging from 1 - 2 h do show their presence. During night hours, large relative amplitude variations with periods ranging as small as 30 min to 2h could be seen on different days and at different times. Fourier analysis of the day and nighttime fractional intensities was carried out to obtain the dominant periodicities in the 630.0 nm intensity variabilities. The analysis revealed the presence of 0.2 − 3 hours periodicities most of the times. It is evident from the figures 4.13 (a −e) that nearly 0.3, 0.5 and 1 hour periods have significant spectral contribution in the variabilities during most of the time irrespective of day or nighttime conditions. These fall under the class of gravity waves, presumably transporting energy and momentum
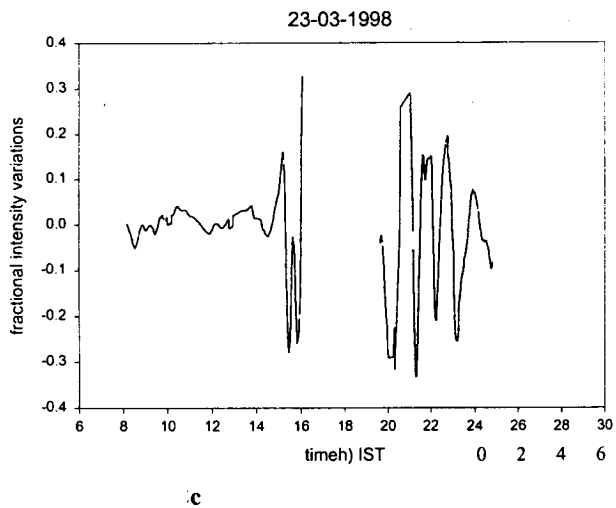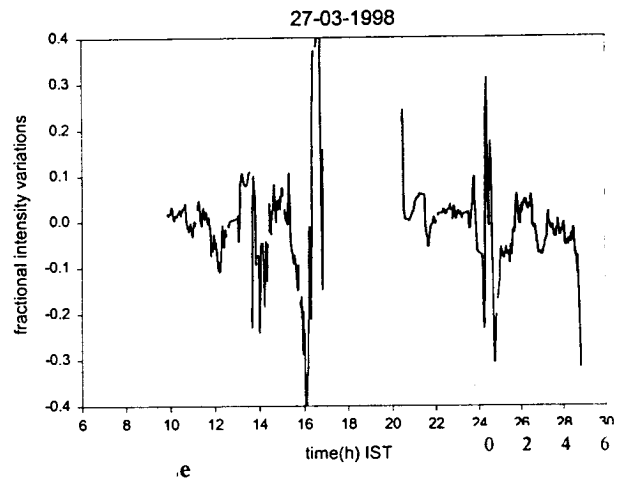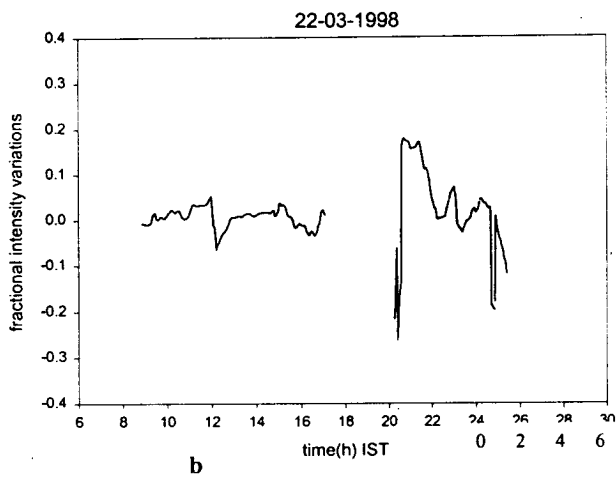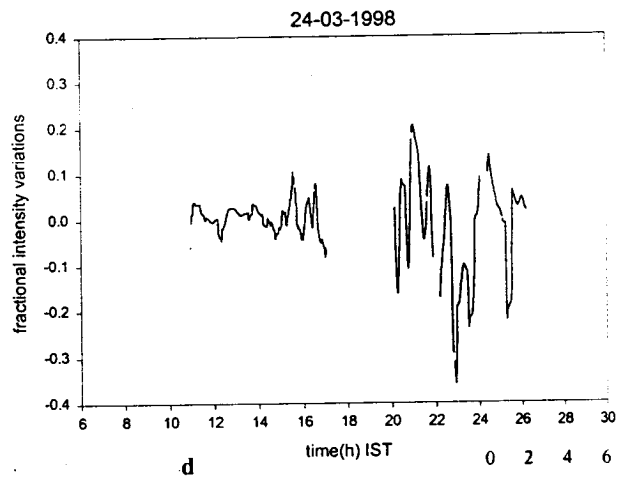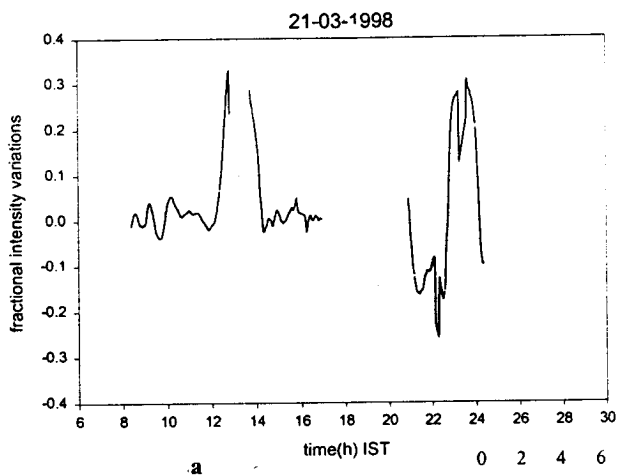
**Figure 4.12 (a,b,c,d,e)** Fractional intensity variations on $21^{st}$,$22^{nd}$,$23^{rd}$,$24^{th}$ and $27^{th}$ March 1998.
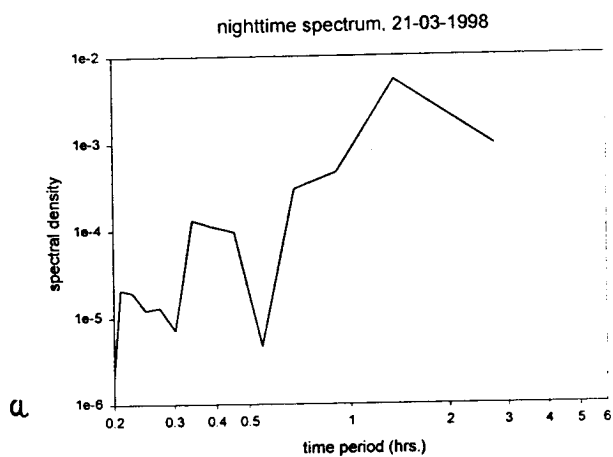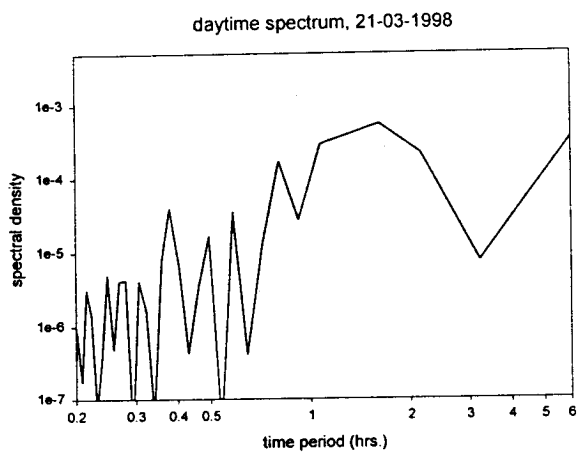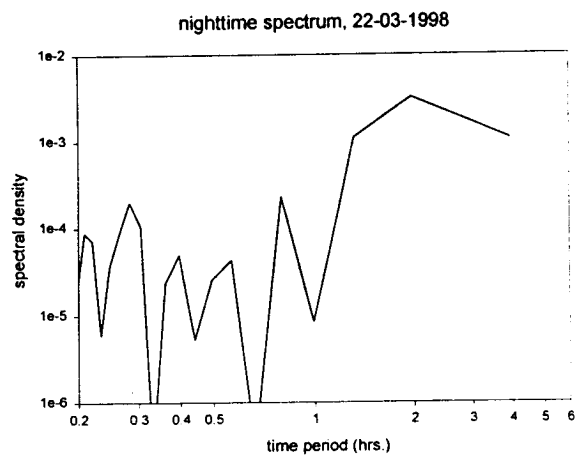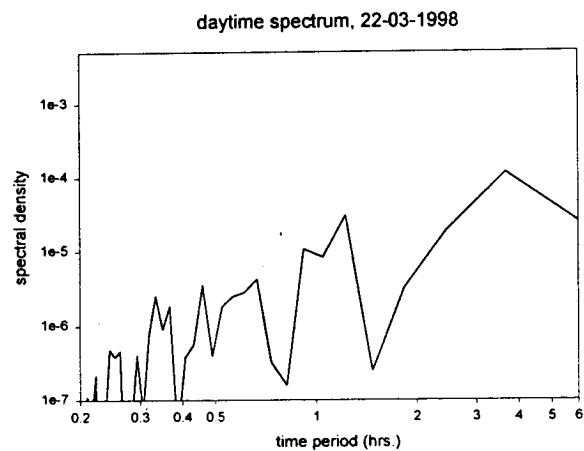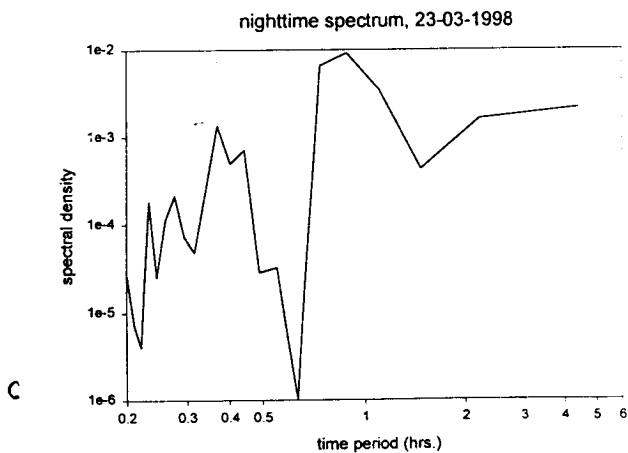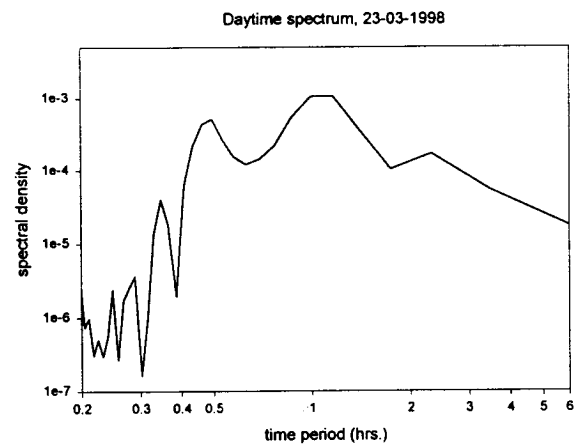
**Figure 4.13 (a,b,c)** Fourier analysis of the Fractional intensity variations on 21st,22nd,23rd March 1998.
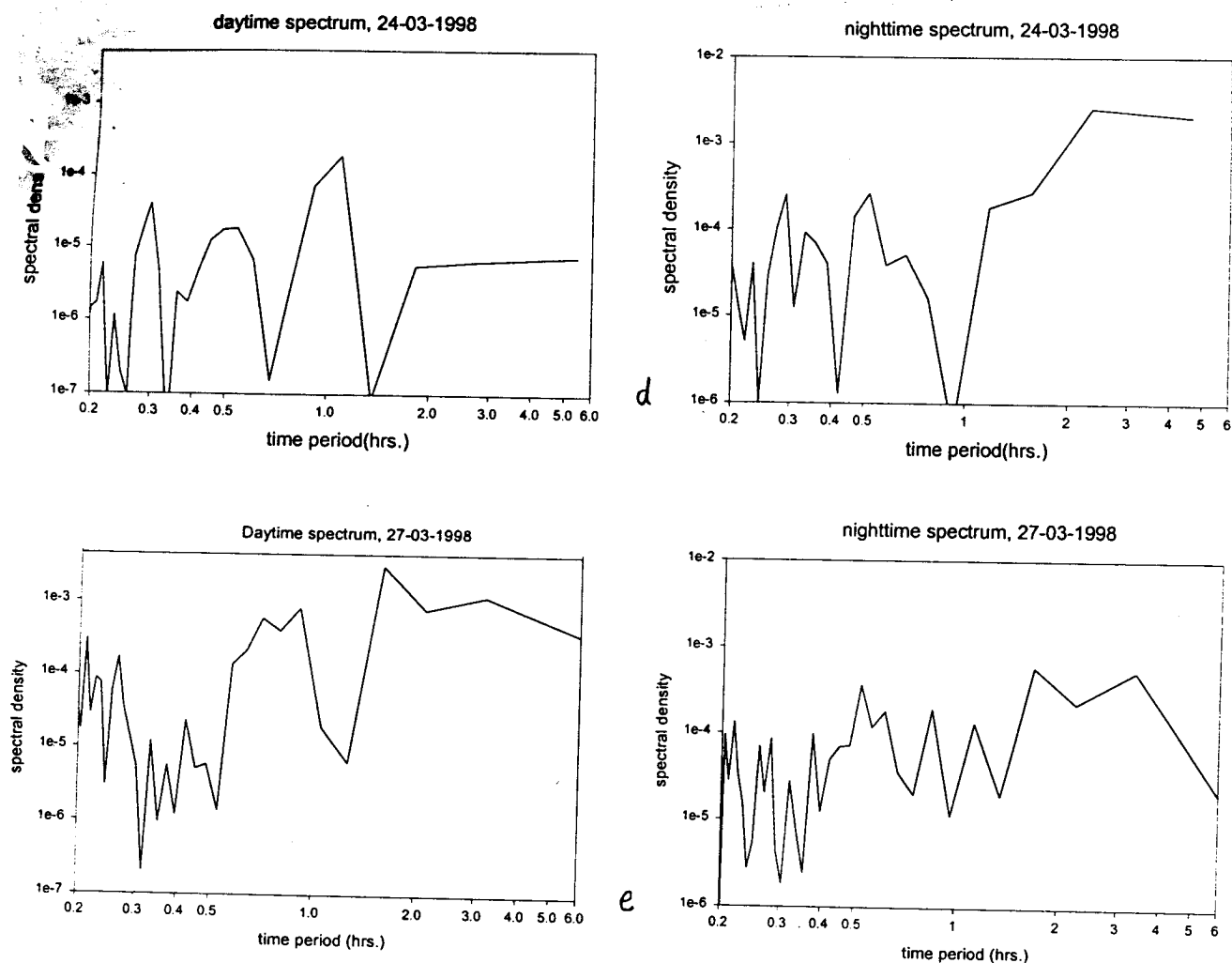
**Figure 4.13 (d,e)** Fourier analysis of the Fractional intensity variations on 24th and 27th March 1998.

from one region to the other. From the measurements representing a particular region, it is difficult to infer anything about the source region. It becomes critical when the period under consideration is a magnetically disturbed one when large-scale wave activities get triggered in the thermosphere. The present results represent moderately disturbed conditions with a slow recovery towards 27th March. Interestingly the wave activities seem to be of comparable magnitude both during day and nighttime conditions on this day, while on all the other days nighttime activities are significantly higher. These aspects call for further detailed study.

## 4.4# Conclusions:

It is demonstrated that the dayglow intensity levels are governed both by the location of the base of the F - region and the maximum electron density. An empirical

formula similar to the one by Barbier for nightglow intensities has been worked out and found applicable to dayglow intensities as well, vindicating the earlier results on 630.0 nm dayglow that the F- region electron densities essentially decide the dayglow variabilities. Persisting wave activities both during day and nighttimes indicate their significance as potential coupling agents. More detailed studies are being planned in the near future.

# 5# Daytime mesopause OH - rotational temperature: estimation and variabilities:

The mesopause region typically located around 85 Km is known to be the coldest region of the upper atmosphere, with the temperatures ranging from $140-220$ K, from summer to winter. This region is one of the least explored regions in the Earth's atmosphere because of its relative inaccessibility. It may well be termed as a 'transition' or the 'boundary' region in many respects. This is the transition zone between those dominated by photochemical processes (lower atmosphere) and transport processes (upper atmosphere). While the turbulent mixing dominates the lower region ensuring homogeneous composition, the atmospheric constituents are in diffusive equilibrium above 110km altitude. Further, it acts as a filter to the spectrum of the waves that get originated at lower altitudes, and as a consequence the thermal state of this region becomes very important in the lower and upper atmosphere coupling processes. In short, the mesopause region is said to set the lower boundary conditions to the thermosphere higher above. Figure 5.1 is a schematic of the physical processes, which affect or occur in the mesopause region.
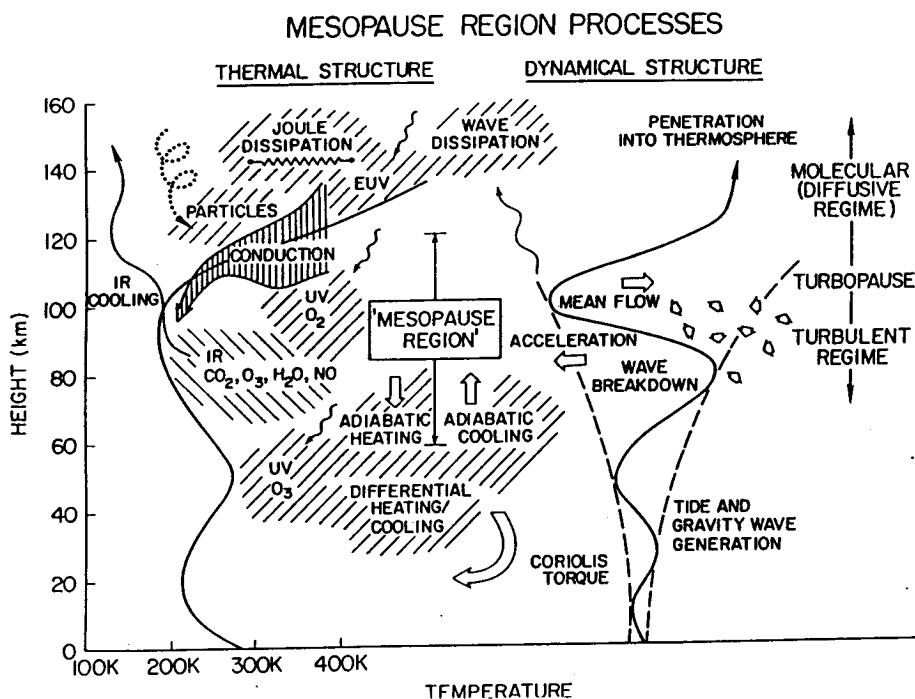


Figure 5.1. Schematic of physical processes which affect and/or occur in the mesopause region.

The primary sources of heat for this region include (1) EUV and UV solar absorption, (2) Joule dissipation of the atmospheric currents (high latitudes) (3) Particle precipitation (high latitude) and (4) dissipation of wave and turbulence energy. The Primary heat sink between 100 and 140 km is downward heat conduction. Below 100 km the loss due to infrared radiation becomes important in determining the thermal structure. Among the heat inputs to the mesopause region, waves and tides contribute nearly 30% of the total heat budget (Subbaraya, 1994). Due to the highly variable nature of waves, the thermal state of the mesopause region also gets affected. These waves and tides, which are believed to originate mainly from the lower atmospheric sources, propagate upward. They grow in their amplitude due to the prevailing negative density gradient, in order to conserve their energy. They encounter linear and nonlinear filtering processes. This results in the transfer of heat and momentum to the ambient, and thus modify the background conditions (Fritts, 1984, Garcia and Solomon, 1985, Forbes et al., 1988). The most significant filtering process occurs at the mesopause altitudes which in turn decides the turbulent energy inputs to the higher altitudes (Fuller-Rowell, 1995). The changes in the turbulent energy inputs alter the turbulent eddy diffusion. As a result, the equilibrium position of the molecular diffusion and eddy diffusion, better known as 'turbopause' gets altered. The turbopause height is usually taken as the base of the thermosphere and higher above. So, the thermal state of the mesopause region essentially defines the lower boundary conditions to the thermosphere and through that the exosphere higher above. Mesopause region, not being far from the dynamo region would become extremely important in the electrodynamical processes also (Murata, 1974). Due to the above reasons, study of the mesopause temperatures and their variabilities becomes very important.

## 5.1# Wave filtering processes:

Filtering processes, also known as saturation or dissipation processes of waves can be linear or nonlinear. Linear wave saturation processes involve generation of Kelvin-Helmholtz instability, convective instability and wave mean flow interaction etc., while the nonlinear processes include wave and wave-tidal interactions. Wave propagation would modify the ambient and they give an acceleration or deceleration to the mean motion. This may give rise to velocity shears in the adjacent regions.

The velocity shear within two adjacent layers may give rise to the Kelvin-Helmholtz (K-H) instability. Growth of K-H instability further would form billows, which may result in small scale eddies and finally their energy would ultimately be dissipated in the medium. These waves, when propagate upwards, after interaction with the medium, may introduce a region of temperature gradient which would form a localized circulation cell, and a flow from hotter to cooler region would get initiated. This kind of an unstable condition is nothing but a convective instability. The circulation ultimately would lead the waves to dissipate their energy and momentum to the ambient by the remixing processes.

Further, the wave-mean flow interaction plays a very important role in the growth of the wave. As the period of the wave is affected due to background wind, higher heights would experience a Doppler shifted time period of the wave. Which can be written as

$$T' = (V_p/V_p\text{-}V)\ T \qquad\qquad (5.1)$$

Where T' is Doppler shifted time period of the wave, T is the actual time period, V is the mean wind velocity and $V_p$ is phase velocity of the wave. Thus the wave period becomes infinite when $V_p \approx V$, and so the wave gets infinite time to interact with the ambient. Because of this, the wave would dump its energy and momentum at these altitude regions. This layer, where $V_p \approx V$ is known as the critical layer. As a consequence, this wave will not be allowed to pass through this region. Nonlinear interaction includes wave-wave and wave-tidal interactions, where inter-modulation among them lead to the dissipation of significant amount of energy and momentum to the ambient. These processes become very important in the mesopause altitudes, as this is the transition region where wind direction and thermal gradients change their signs and so the study of the thermal behaviour of the mesopause becomes very important. Therefore, by monitoring the mesospheric temperature and their fluctuations, which may be of the order of a few degrees in magnitude with periodicities ranging from few minutes to several hours, one would be able to investigate mesospheric dynamics better.

# 5.2# Methods of measurement:

When it comes to measurements, conventional in-situ methods lack the required precision and are also unsuitable for the study of temporal variabilities. Remote sensing methods are simpler and more reliable with the required temporal resolution. Sodium lidar and passive airglow monitoring are the most widely used ground-based remote sensing methods.
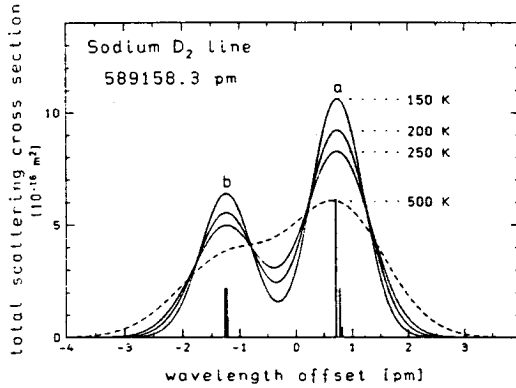


**Figure 5.2.** Variation of the total scattering cross section in the Na hyperfine structure of the D2 resonance transition with atmospheric temperature. (After Fricke and Von Zahn, 1985)
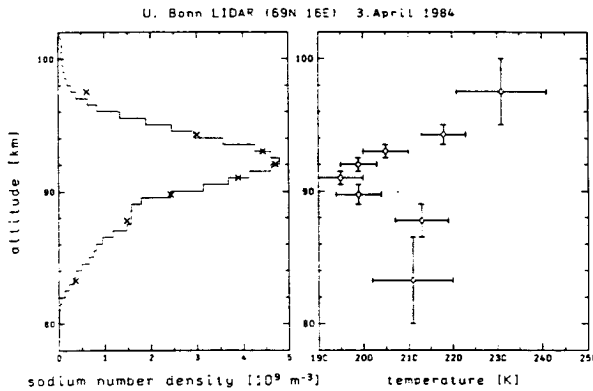


**Figure 5.3.** Results obtained for 3 April 1984 at Andoya (69N,16E) (a) sodium number densities normalized to the sodium density around 91 Km slice (b) mesospheric temperature profile. (After Fricke and Von Zahn, 1985)

Sodium Lidar uses active probing of the Doppler broadening of the hyperfine structures of sodium $D_2$ line by a narrow band lidar. Basic principle behind the temperature derivation is as following. Atomic sodium is present in the terrestrial atmosphere in the altitude range from about 80 to 100 km, with a peak density of $\sim 10^9$

atoms m$^{-3}$. The sodium $D_2$ resonance line consists of six hyperfine transitions. At atmospheric temperatures, these six lines blend into two components referred to as $D_{2a}$ and $D_{2b}$, which are separated by about 2 picometer (or .002 nm). At a representative temperature of 200K, the Doppler broadening will produce, a full width at half maximum (FWHM) of 0.0012 nm, and thus the two components $D_{2a}$ and $D_{2b}$ are still resolved (Figure 5.2). The minimum between them will be filled in only for temperatures in excess of 500K. Given a narrow band, sufficiently powerful laser and a sensitive, high speed detection system, one may probe this Doppler broadened hyperfine structures of the $D_2$ line at several altitudes in the atmospheric sodium layer and thus derive height resolved temperatures between approximately 80 and 100 km (Figure 5.3). This method was further utilized in many investigations and some of the interesting aspects of the dynamics in the mesopause region are discussed in the literature. Occasional Bimodel behaviour of mesopause altitude (VonZahn et al., 1996), sudden temperature enhancements (Huang et al., 1998) are a few among them. However, for better temporal resolution, photometric observations have their own advantage. Most widely used airglow emissions for the study of the mesopause region are the OH meinel bands, $O_2$ atmospheric band and NaD emission. Mienel band of hydroxyl molecular emission is the preferred one among them. It was discussed in chapter3, that the OH Meinel band peaks around the mesopause region near 85 km, with a half width of about 6 to 8 km (Lopez Moreno et al., 1987; McDade et al., 1987). They encounter sufficient collisions with the ambient atoms and molecules and so are in thermodynamical equilibrium and therefore the rotational temperatures deduced from the ratio of the two suitable rotational line intensities can be taken as the mesopause temperature itself (Sivjee, 1992).

### 5.2.1# Method for OH rotational temperature estimation:

With a tacit assumption that OH radicals are in local thermal equilibrium with the ambient, a general formation of the relation between the intensities of the two rotational lines of the same vibrational band and the rotational temperature, i.e. the mesopause temperatures can be obtained as shown below:

Integrated volume emission rate or the intensity of a line can be expressed as

$$I(j''\upsilon'', j'\upsilon) = N(j'\upsilon')A(j''\upsilon'', j'\upsilon') \qquad ---(5.2)$$

Where $j''v''$ is rotational and vibrational quantum number of the upper state, $j'v'$ is rotational and vibrational quantum number for the lower state. $A$ represents the Einstein's transition probability for the spontaneous transition and $N$ is the number density of OH radicals in the excited state. Assuming the OH radicals to follow a Maxwell Boltzman distribution, one can state –

$$N(j'v') = c(2j'+1)\exp[-fv'(j')\frac{hc}{KT_R}] \qquad ---(5.3)$$

Where $c$ is a constant $(2j' + 1)$ represents the statistical weight of the state and $f_v \cdot$ is the rotational term difference between the initial and final states. And so the intensity of one line can be written as-

$$I(j''v'', j'v') = c(2j'+1)A(j''v'', j'v')\exp[-fv'(j')\frac{hc}{KT_R}] \qquad ---(5.4)$$

For two rotational lines in the same vibrational band, this expression can be written as

$$I_1 = c(2j_1'+1)A_1\exp[-f_v(j_1)\frac{hc}{KT_R}] \qquad ---(5.5)$$

and

$$I_2 = c(2j_2'+1)A_2\exp[-f_v(j_2)\frac{hc}{KT_R}] \qquad ---(5.6)$$

Further, the ratio of the two lines can be written as -

$$\frac{I_1}{I_2} = \frac{(2j_1'+1)}{(2j_2'+1)}\frac{A_1}{A_2}\exp[\frac{\{f_v(j_2)-f_v(j_1)\}hc}{KT_R}] \qquad ---(5.7)$$

which can be written as -

$$T_R = \frac{\frac{hc}{K}[fv(j_2)-fv(j_1)]}{\ln[\frac{I_1}{I_2}\frac{(2j_2+1)}{(2j_1+1)}\frac{A_2}{A_1}]} \qquad ---(5.8)$$

With the selection of 731.6 nm and 740.2 nm lines of OH (8,3) band, the above expression reduces to-

$$T_r = \frac{362}{\ln[3.44 \times \frac{I_1}{I_2}]} \qquad ---(5.9)$$

## Mesopause OH rotational temperatures:

Earlier studies on the mesopause temperatures were limited to nighttime conditions only wherein solar cycle, seasonal and day to day variabilities have been studied and have been reviewed in the literature (Sivjee et al, 1972). With the low-resolution spectra of the R and Q branches of OH (7-2) band by airborne measurements and by ground based measurements of (8-3) band, Sivjee et al(1972), presented latitudinal and temporal variations in the OH rotational temperatures. While discussing the observed temperature variations ranging from 150K to 270K, they stated that the observed variations imply either an increase in the altitude of the OH emitting region from 85 km to about 100 km or a fall to 75 km. However, these measurements suffered poor temporal resolution and contained large errors. Assuming a stationary mesopause and a corresponding temperature profile of the atmospheric temperatures, the cause of rotational temperature variations were thought of as either due to (i) mesopause dynamics or (ii) nonthermal equilibrium of excited species or (iii) the existence of several competing mechanisms for OH production at different altitudes. Further investigations and consistent results reported by Takahashi et al (1981, 1983) and their good agreement between Doppler temperatures and rotational temperatures led the investigators to believe that the OH radicals are indeed in local thermodynamical equilibrium, at mesospheric altitudes.

Another interesting report by Meriwether (1975) was dedicated for the short period fluctuations in the OH rotational temperatures. He used a tilting filter photometer. With a sampling rate of one per minute and with a precision of ±5K, fine structure variations in the OH (8-3) rotational temperatures were brought out (Figure 5.4). These micro-fluctuations were attributed to be due to the density modulations originating from internal gravity waves present in the high latitude winter mesosphere.
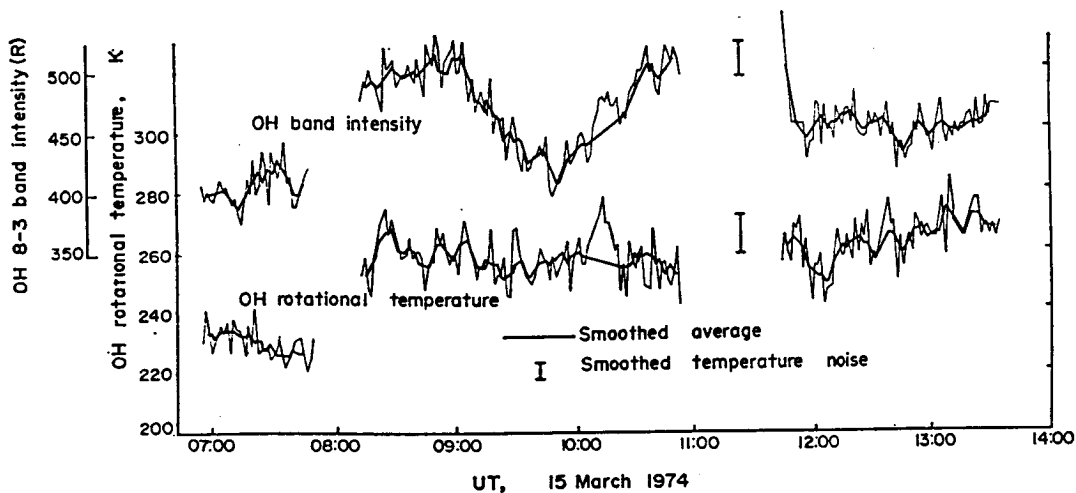
**Figure 5.4.** OH rotational temperature and intensity of the OH (8, 3) band. (After Meriwether, 1973)

Majmudar and Kulkarni (1979) used OH (7-2) band for the rotational temperature estimation, from Mt. Abu (24.6°N, 72.7°E). Their photometric observations on seasonal and nocturnal variation of temperature revealed (i) maximum temperature during winter months and minimum in summer, (ii) larger scatter in the temperatures in the month of November and (iii) significant day to day variations. The large scatter in the temperatures during winter was ascribed to the enhanced turbulence from winter to summer.

The other important aspects on the gravity wave propagation were also investigated with the help of OH rotational temperatures and emission intensities. Using OH emission alongwith the other mesospheric emissions (557.7 nm, Na and $O_2$ Atmospheric) one can get a fairly good idea about the gravity wave characteristics. Cogger et al. (1988) were among those investigators who used OH rotational temperatures and 557.7 nm intensities from 51°N using tilting filter photometer for wave studies. Negative correlation between temperature and 557.7 nm intensities were taken as an indication of two regions being linked through wave activities. Spatial scan of different regions of the sky was performed to obtain the wave parameters, in their study. They deduced the horizontal wavelength to vary from 5 to 100 kms and the vertical wavelength from 0.7 to 8 km.

Elphinstone et al. (1988) analyzed the moving thermal structures near the mesopause region with the help of OH (8,3) rotational temperatures. Their objective was to determine the velocities, wavelengths and periods associated with the moving structures. Velocities of the structures in the meridional direction were found to be

96
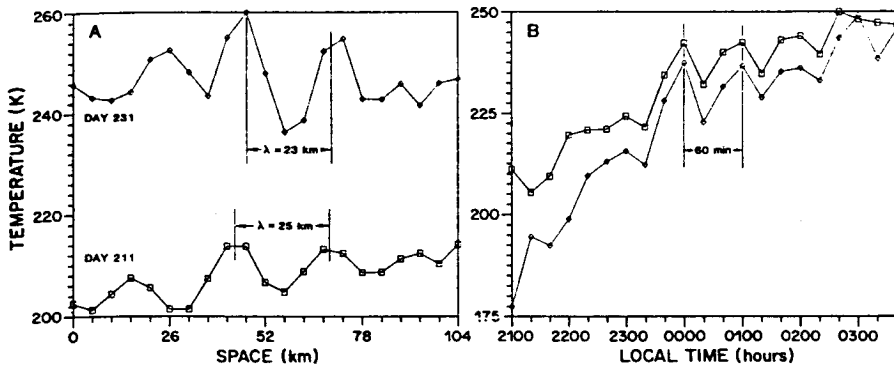
Figure 5.5: moving structures in the mesopause temperatures (After Elphinstone et al., 1988)

poleward. Corresponding bulk wind velocities measured near the 95 km height region were equatorward indicating the presence of filtering of internal gravity wave by the background wind. A sample figure indicating the horizontal wavelength and time period is shown in Figure 5.5. One can notice a temperature variation of 75K within 4 hrs.

Simultaneous ground based measurements of multiple atmospheric airglow emissions like OI557.7, 630.0, 777.4, NaD and lines of OH (9,4) and $O_2$ atmospheric (0,1) band are also reported in the literature (Takahashi et al., 1989). For this purpose, a multichannel tilting filter photometer was used. With the ratio of the selected lines hydroxyl rotational temperatures in the range of 190 to 210K were obtained. Wavelike oscillations were also observed. With the same instrument, Clemesha et al. (1990) reported mesopause temperatures from Cachoria Paulista (23°S) during 1983 to 1986, and showed the annual mean to be ~193K, with ~2.3K oscillation amplitude. In a report by Takahashi et al. (1994) seasonal variation in the mesopause temperatures observed at equatorial (Fortaleza, 4°S) and low latitudes (Cachoria. Paulista, 23°S) were presented. They showed that the semiannual oscillation is predominant in both the places. Seasonal variation in the equatorial region was found larger than that over that at low latitudes (Figure 5.6). These seasonal variations were suggested to be due to vertical turbulent mixing being stronger over the equatorial region than at low latitudes.
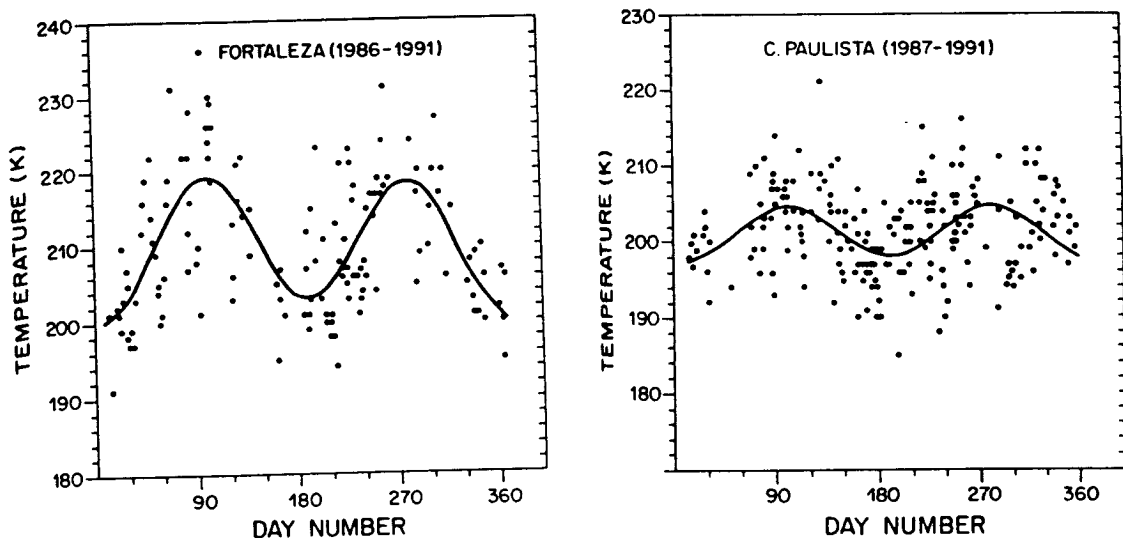
**Figure 5.6.** Seasonal variation in the OH rotational temperatures over equatorial (left) and low latitude station (right). (After Takahashi et al., 1994)

Taylor et al. (1991) reported simultaneous intensity, temperature and imaging observations of short period wave structures in the OH nightglow emission with a low light level TV camera co-aligned with a narrow field of view Michelson interferometer from 32°N. A coherent wave like pattern of horizontal wavelenth 23±1 km moving with a velocity of 28±2 ms$^{-1}$ with an apparent period 13.7±1.2 minutes was obtained. The induced intensity and temperature perturbations too were found to exhibit wavelike behavior apart from the imaging observations. Intensity variations upto 30% were also noticed. They showed that the brightest wave forms were ≤10K hotter than the adjacent dark regions. The amplitude of the intensity fluctuations were ~8 times more than the temperature variations. Large-scale structures in the hydroxyl rotational temperatures are also available in the literature (Scheer et al., 1994). Their results showed significant deviation from CIRA 86 model values and also a preferential horizontal gradient in the temperature with significant amplitude of 2, 11 and 28 day periods.

All the above said groundbased observations were limited to the nighttime, moonless conditions only. Presence of high solar background continuum disabled the daytime investigations in the mesospheric OH temperatures. This scenario was changed recently with the development of multi-wavelength daytime photometer (MWDPM) (Sridharan et al., 1998) and its deployment to monitor the rotational lines of OH (8,3) band. These results will be discussed in the following sections.

## 5.2.2# First results on daytime OH-rotational temperatures from equatorial latitudes:

**Validation of the technique:**

The MWDPM was operated from Tirunelveli (8.7°N, 77.8°E. 0.5 dip latitude), an equatorial station in the Indian zone. Two rotational lines 731.6 nm and 740.2 nm of OH (8-3) band were monitored during daytime and the ratio of these lines were made use in formula 5.9 in order to estimate the daytime rotational temperatures. On a couple of days when simultaneous measurements were available in the vicinity of the experimental site, the estimated temperatures were compared with those measurements by the Wind Imaging Interferometer (WINDII) onboard the Upper Atmosphere Research Satellite (UARS). Intercomparison of these results has been taken as the validation of the method adopted in the present case. A brief account of this method for the estimation of lower atmospheric temperature from the WINDII data is provided in the next section, while the WINDII measurements themselves are shown in figures 5.7a and b.

Rotational temperatures were estimated from the relative intensity measurements for about two hours in the mornings of 19th and 21st April 1997. Bad sky conditions prevented continuous operation of the MWDPM. The UARS was crossing the same latitudinal zone in the near vicinity and provided an opportunity for a unique set of observations to validate the technique and results.
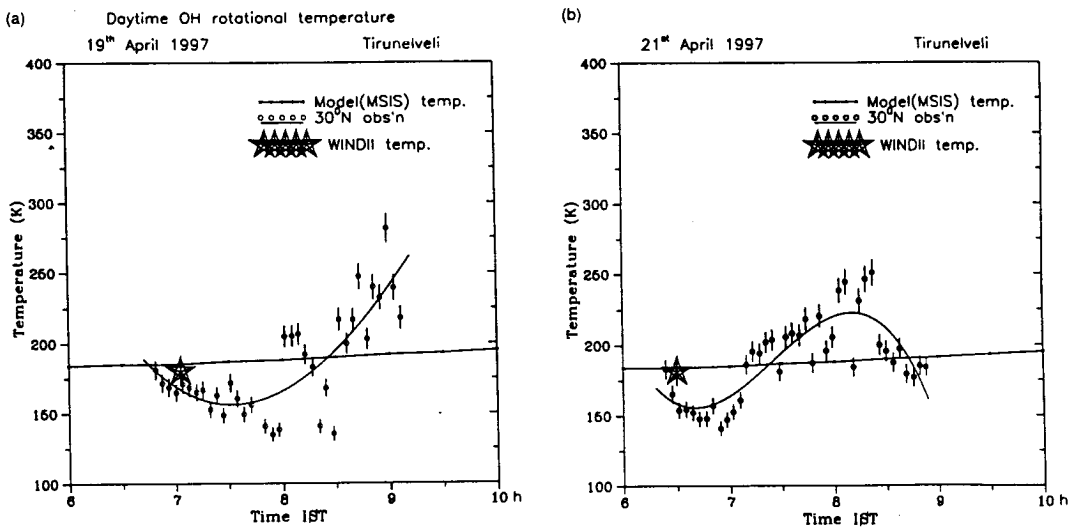


**Figure 5.7.** Observed Daytime mesopause OH rotational temperature variabilities from an equatorial station, Tirunelveli **(a)** on 19th April 1997 (left) and **(b)** on 21st April 1997 (right).

Figure 5.7a depicts the estimated temperature variabilities based on the raw data along the 30° look angle of the photometer, pointing northwards on 19th April, 1997. On that day, the observations were made starting from 0645 hrs. At that time the estimated temperatures were close to the MSIS-90 model (which is the updated version of MSIS-86 extended by using a lower atmosphere model, namely CIRA-86, Hedin, 1991) prediction for that day. The maximum deviation from the model was as high as 40-50K. The uncertainties in the temperature estimates do not exceed ± 7.5%. The WINDII estimated temperatures corresponding to the OH emission height of 85 km is depicted by a star. The uncertainties in the WINDII estimates do not exceed ± 5%. These temperature estimates and that from the relative intensities of OH rotational lines appear to be in broad agreement.

The results obtained from the MWDPM observations of 21st April are depicted in Figure 5.7b. They show distinctly different variabilities with regard to the phase of the variation, i.e. they are opposite in phase when compared with the 19th April results. The model value remains fairly steady around 188K. With a maximum deviation of ± 40K from the model, the results from two days, though extend hardly for two hours duration on each day, are important, as nearly simultaneous satellite based measurements were available, enabling the independent validation of the ground based daytime optical technique.

## 5.2.3# Temperature estimations by WINDII instrument onboard the UARS:

Before one critically assesses the variabilities, as these measurements happen to be first of their kind, validation of the method becomes important. This is so as the MWDPM measures relative intensities of the selected emission lines. Though extreme care is taken while removing the background continuum contribution, as the continuum intensities are typically two orders of magnitude larger than the emission line intensities, any imbalance in the continuum rejection in any one of the wavelengths monitored will lead to large errors. As mentioned above, in the present case comparisons have been made with the WINDII estimates nearly at the same time and in the nearby locations.

The WINDII measures the 553.0 nm as background for the 557.7 nm $O(^1S)$ emission intensities. For the daytime conditions the observed background in the altitude region of 70 – 100 Km is dominated by Rayleigh scattering, which is proportional to the total molecular density integrated along the line of sight. The

scattered intensities are used to derive a density profile from which the altitude profile of the temperature is derived under hydrostatic equilibrium assumptions (Chanin and Hauchecorne, 1984). A density scale height $H(z)$ is determined for each height $z$ by fitting $I(Z)$ as :

$$\frac{-1}{I(z)}\frac{dI(z)}{dz} = H(z) \qquad ---(5.10)$$

Air pressure $P(z)$, density $n(z)$ and temperature $T(z)$ are related by the gas law-

$$P(z) = R\, n(z)\, T(z)\, /\, m \qquad ---(5.11)$$

$$\frac{dP(z)}{P(z)} = \frac{mg(z)}{RT(z)}dz = d[\log P(z)] \qquad ---(5.12)$$

Where m is the mean molecular mass and R is the universal gas constant.

If $g$ and the temperature are assumed to be constant in the $i^{th}$ layer, then the pressure at the bottom and top of the layer are related by -

$$\frac{P(z_i - \Delta z/2)}{P(z_i + \Delta z/2)} = \exp[\frac{mg(z_i)}{RT(z_i)}\Delta z] \qquad ---(5.13)$$

Thus, the temperature can be expressed as following:

$$T(z_i) = \frac{mg(z_i)\Delta z_i}{R\ln[\dfrac{P(z_i - \Delta z/2)}{P(z_i + \Delta z/2)}]} \qquad ---(5.14)$$

Density profiles calculated by eqn. (5.10) are used to obtain pressure values using the MSIS model, and their substitution into the eqn. (5.14) will yield the temperature. (Chanin and Hauchecorne, 1984). One of the assumptions is that the temperatures at 110 km is ~230K for the MSIS model. This assumption and the method of the temperatures have been validated by Shepherd et al. (1997) by comparing the same with a variety of groundbased and spaceborne techniques.

The mean temperature profiles obtained for 19$^{th}$ and 21$^{st}$ April, 1997 are given in Figures 5.8a and 5.8b, alongwith the geographical coordinates to the

measurements. While, on 19th April, the latitude was close to that of the groundbased observations, the satellite
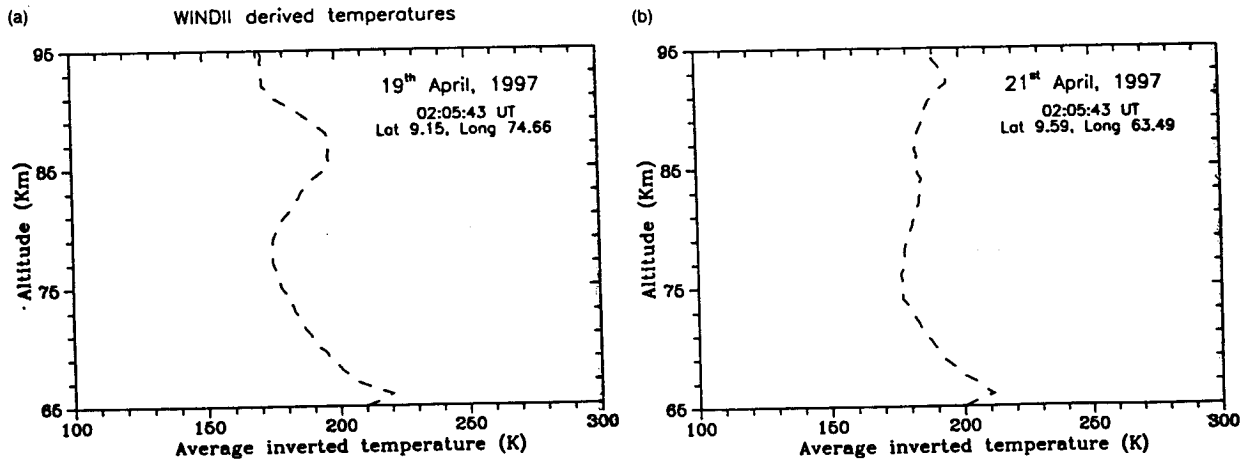


Figure 5.8. WINDII derived mesospheric temperatures on (a)19th and (b) 21st April 1997.

measurements correspond to ~4° west of the ground site. On 21st April, it was to the west of the observation site by 15°, though at around the same latitude. One can see that on both the days, the nature of the temperature variations at ~85 km with respect to the mean profile is opposite.

## 5.2.4# Mesospheric wind data :

A Partial Reflection (PR) radar at 1.98 MHz was operated from Tirunelveli, from where the groundbased optical measurements were carried out. The PR radar makes use of the spaced antenna technique, and samples the horizontal winds in the 60 to 98 km altitude region. Full correlation analysis (Briggs, 1984) has been carried out to deduce the wind components following standard procedures (Rajaram and Gurubaran, 1998). In the present study, radar data corresponding to 84 km height on both 19th and 21st April, 1997 are utilized to examine the short period wind fields. Figures 5.9a and 5.9b depict the nature of the variabilities in the wind components on those days. The data points were smoothed by taking a five point running average. Short period ~45 min. fluctuations were quite prominent on 19th April, while these fluctuations were absent on 21st April. On 19th April, meridional wind reached a maximum of ~40 ms$^{-1}$ at around 0730 hrs IST and was equatorward, while on 21st

April it was poleward with a magnitude of ~18 ms$^{-1}$. It should be noted that the zonal wind magnitude remained close to zero from 0700 hrs to 0830 hrs on 21$^{st}$ April. It is interesting to note that the variabilities of both the meridional component of the neutral winds and the rotational temperatures were similar, indicating a possible link mainly through wave activity in the mesosphere.
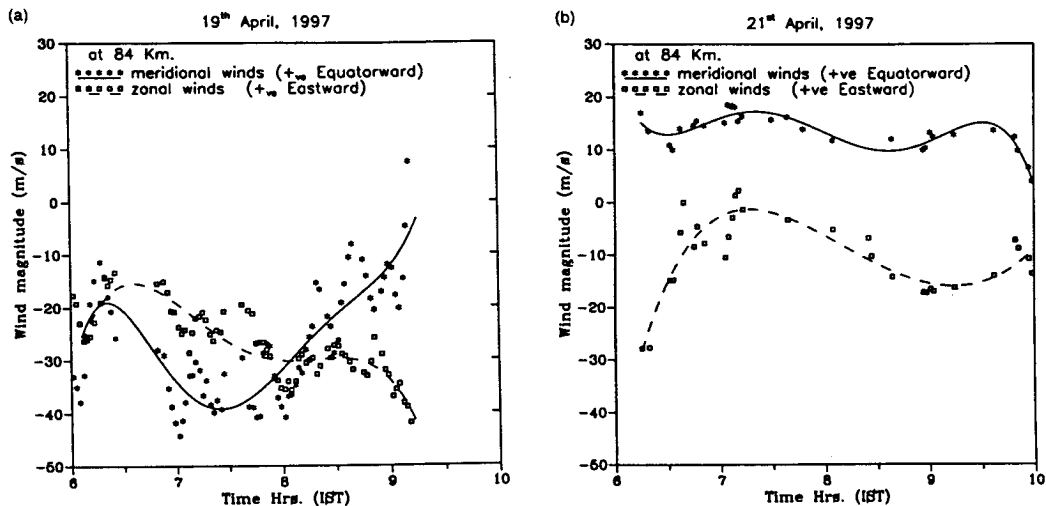


Figure 5.9. Observed Wind variabilities over the same location, Tirunelveli on (a) 19$^{th}$ and (b) 21$^{st}$ April 1997.

Detailed study on this aspect could not be carried out further due to lack of simultaneous coordinated measurements.

## 5.3# Further results on mesopause temperatures:

After having validated the technique of retrieval of the OH rotational temperatures, the MWDPM was operated during the next year, i.e. 1998 from the same location to collect more data. During March 1998, data for few more days could be collected and out of which four days of data are taken for further studies. In spite of the limited data, large day to day variabilities and periodicities of small-scale oscillatory features ranging from 0.5 to 6 h could easily be seen on all the days in the mesopause temperature. Figure 5.10d depicts the inferred mesopause temperatures on 23$^{rd}$ March, 1998. Though initially upto 0800 h the measurements agreed very well with the model, later they began to deviate from it, and by 1000 h IST the difference reached as high as 30 K with the observed values being less than the model values. From 1000 to ~1500 h the trends were very similar in both the model and

measurements. Beyond 1500 h the measurements showed an increasing trend, while the model predicted an asymptotic decrease. One could clearly see a dominant 6 h period in the variabilities.



**Figure 5.10.** Observed temperature variabilities over Tirunelveli during March 1998.

Figure 5.10a depicts the temperature data corresponding to 8th March, 1998. On this day no data could be collected during 1200-1400 h due to the presence of cloud patches in the field of view. The measurements were centered with respect to

the model values. The temperature deviations, if any, was only marginal upto 1400 h. Beyond 1500 h the measurements were higher by 20K, and a steep decrease was observed beyond 1730 h.

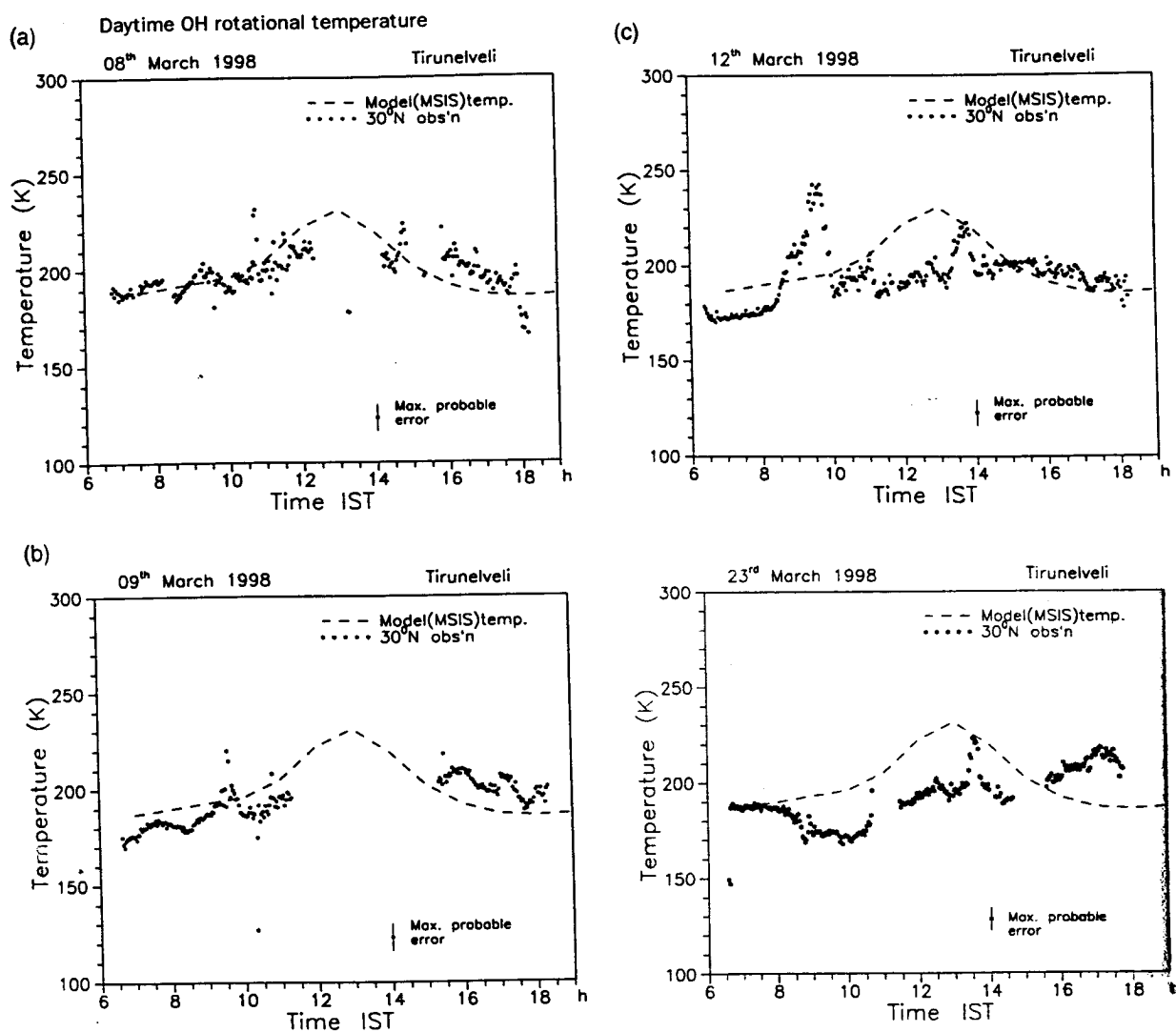Figure 5.10b shows the temperature variabilities as observed on 9th March, 1998. On this day too no data could be collected during 1100 h to 1500 h due to poor viewing conditions. In the morning hours the measured temperatures turned out to be less than the model values, while during afternoon they were higher than the model. Very clear oscillatory features with periods ranging from 1 to 1.5 h were present.

Next clear day, when measurements could be made was 12th March 1998 (figure 5.10c) Unlike the earlier days, continuous data could be obtained from the morning 0630 h to 1745 h IST. The measurements were deviating from model values, significantly upto ~1400 h IST. The mesopause temperatures registered a steep increase at 0815 h by ~25K. Small scale fluctuations were recorded all through the day, with periods ranging from 0.5 to 2 h. The mean of the observed temperatures were centered near 185 K.

The observed mesopause OH rotational temperatures over the equatorial latitudes bring out clearly the large day to day variabilities. The detected variability based on the periodicities indicates that these oscillations could be due to the modulation of the temperatures by the passage of gravity waves in these regions. These sorts of wave like disturbances could originate from below, in the tropospheric and stratospheric regions. It is well known that, inspite of the stratosphere acting as a filter, disturbances of extremely small amplitudes originating in the lower atmosphere would become large enough to modulate the densities and temperatures at mesospheric altitudes. Another possible mode for the presence of waves is through ducted waves and their horizontal propagation around the mesopause altitudes. These results are the *first of their kind* made *during daytime* conditions. The experimental uncertainties do not exceed ±7.5K. Often large variabilities around the model temperatures, with periodicities ranging from 0.5 to 6 h have been noticed. The comparison of the estimated OH rotational temperatures with the UARS data could be treated only as an order of magnitude comparison since the UARS measurements corresponded to geographical locations separated by 4° to 15° in longitude on 19th and 21st April, 1997. Inspite of this, the MWDPM results presented are of the same magnitude as the values deduced from the WINDII data which in turn, have been

20K from the model predictions. A steep increase of ~30K within a short duration of 15 minutes, overshooting the model values, is noticed at ~1200 h. As a whole, one could clearly see the superposition of different periods in the temperature variabilities.

The temperature variabilities were subjected to Fourier analysis to obtain the dominant periods. It is seen that periods of about 15 min, 45 min, 1 h and 1.5 h (figure 5.11b) were present, which is more or less similar to 22nd January. These periods fall under the category of the gravity waves permissible in the mesopause region.

Figure 5.11c depicts another data set representing 24th January, 1997, revealing many interesting features. On this day, very large amplitude oscillations were noticed. The difference between the maximum and minimum temperatures was nearly 60K, and the maximum amplitude of the oscillations was ~30 - 40K, which is nearly 20% of the steady state values. During the initial hours, the measured temperatures were lower than the model values by 30 K. After 1000 h, the temperatures followed an increasing trend upto ~1300 h. Large oscillatory features with periodicity being nearly 30 - 45 min. were present. A gap in the data around 1400 h for 15 minutes was encountered due to power failure. The Fourier analysis of the temperature variabilities revealed that nearly 15, 30 , 40, 50 min, 1.2 h and 1.8 h periodicities to be present (figure 5.11c).

When compared with the remaining days, 25th January was the most interesting day during the observational period. A dc shift in the temperature levels by 20 - 25K from the model values could be noticed in figure 5.11d. Subdued nature of the wave activities could also be seen. Initially the temperatures remained steady upto ~1100 h and then a slow and steady increase upto ~1300 h was observed. Amplitude of the wave activities was not more than 10K, which incidentally is the least during the four days of observations. With a noontime maximum around 1300 h, the temperatures followed a decreasing trend with oscillatory features embedded in them. Though of lesser spectral densities, periods nearly of 15, 25, 45 min and 1.5 h were found to be present in the variabilities (figure 5.11d).
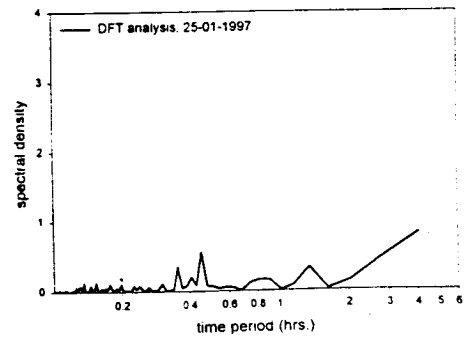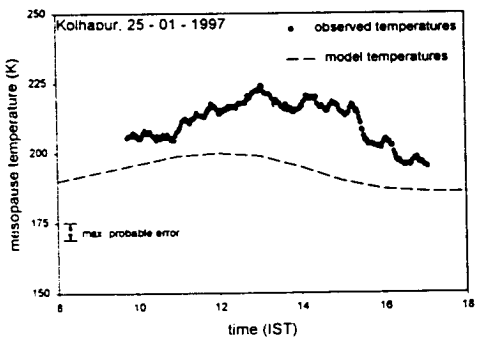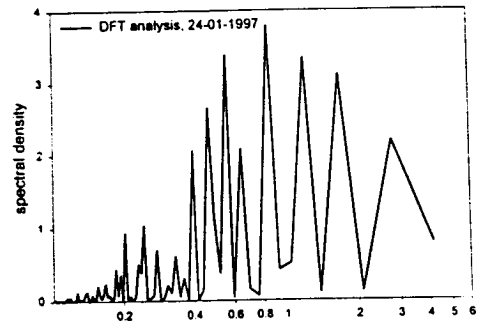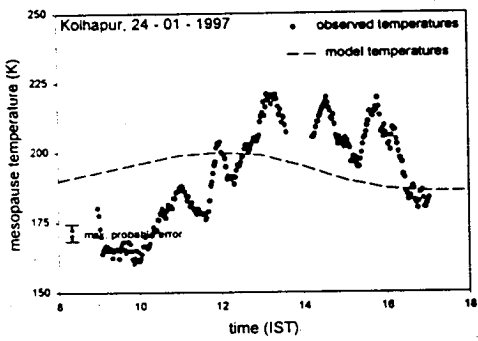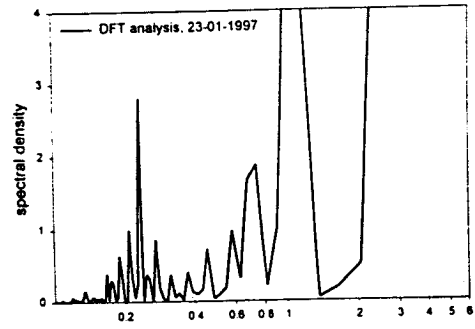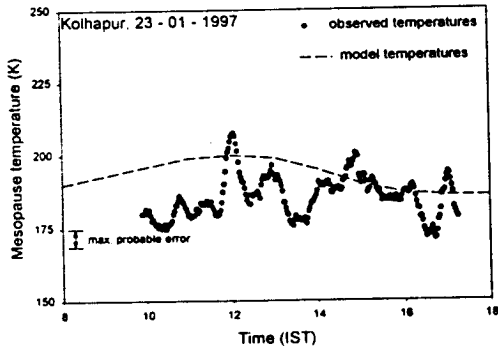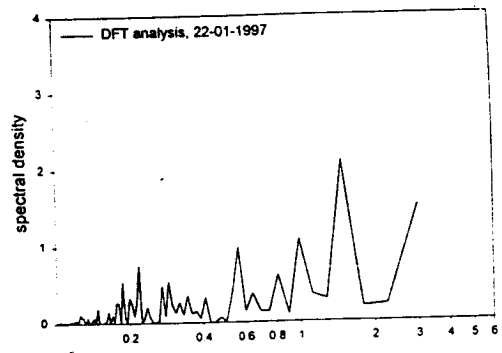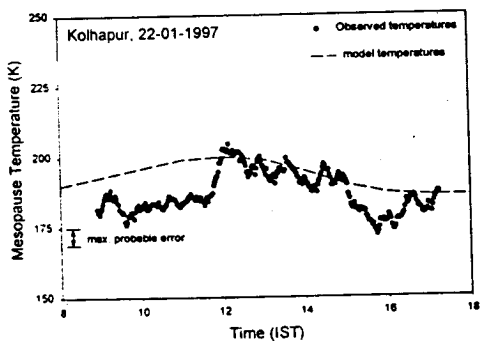
**Figure 5.11.** Observed temperature variabilities over Kolhapur (left) and their DFT analysis.

## 5.5# Discussion:

Most of the earlier studies on the mesopause OH rotational temperatures were restricted only to the night time conditions and focussed on the variabilities and on the identification of the short period oscillatory features that could be attributed to gravity waves. The present results are some of the `first of their kind' to report the daytime temperature variabilities. The observed periodicities were within the range, which are already reported in the literature to be present in those altitudes. Their periods are well above the natural period (Brunt - Vaisalla period) at mesopause altitudes and so they are believed to fall under the internal gravity wave category. These gravity waves are some of the most important coupling agents between lower and upper atmosphere and hence presence of specific periods in the mesopause altitude is important.

A large amplitude oscillation for significant time duration in the mesopause temperatures is an interesting observation. Occasionally this amplitude is as high as 50K, which is ~30% of the steady level. Effects of these oscillations on the atmospheric system are not yet quantified, though one could speculate that they would have very important repercussions. First of all, these temperature changes would alter the atmospheric scale height, which in turn would modify the distribution of atomic and molecular species higher above triggering chain reactions on the ambient electron densities and the ion - neutral interactive processes. An indication of this process to be active was observed during the January 1997 campaign from 22$^{nd}$ to 25$^{th}$ January, from a low latitude station Kolhapur, when 630.0 nm thermospheric emission was also monitored together with the 731.6 and 740.2 nm OH emission to deduce the mesospheric temperatures. There were corresponding enhancements in the 630.0nm intensities together with the mean mesopause OH rotational temperature increase (figure 5.12). The observed features could be due to either an overall increase in the scale height H, caused by the temperature increase and that would have affected the distribution of atomic and molecular species higher above, thus affecting the rate of emission of the 630.0 nm dayglow. The other possibility can be due to the change in the incoming turbulent energy flux at mesospheric heights, which would have changed the mesopause temperatures and further would have affected the turbopause height, which is the height where eddy diffusion and molecular diffusion become equal. The change in the turbopause height will affect the distribution of the atomic

**Figure 5.12.** Simultaneous measurements of mesopause temperatures and thermospheric 630.0 nm emission.
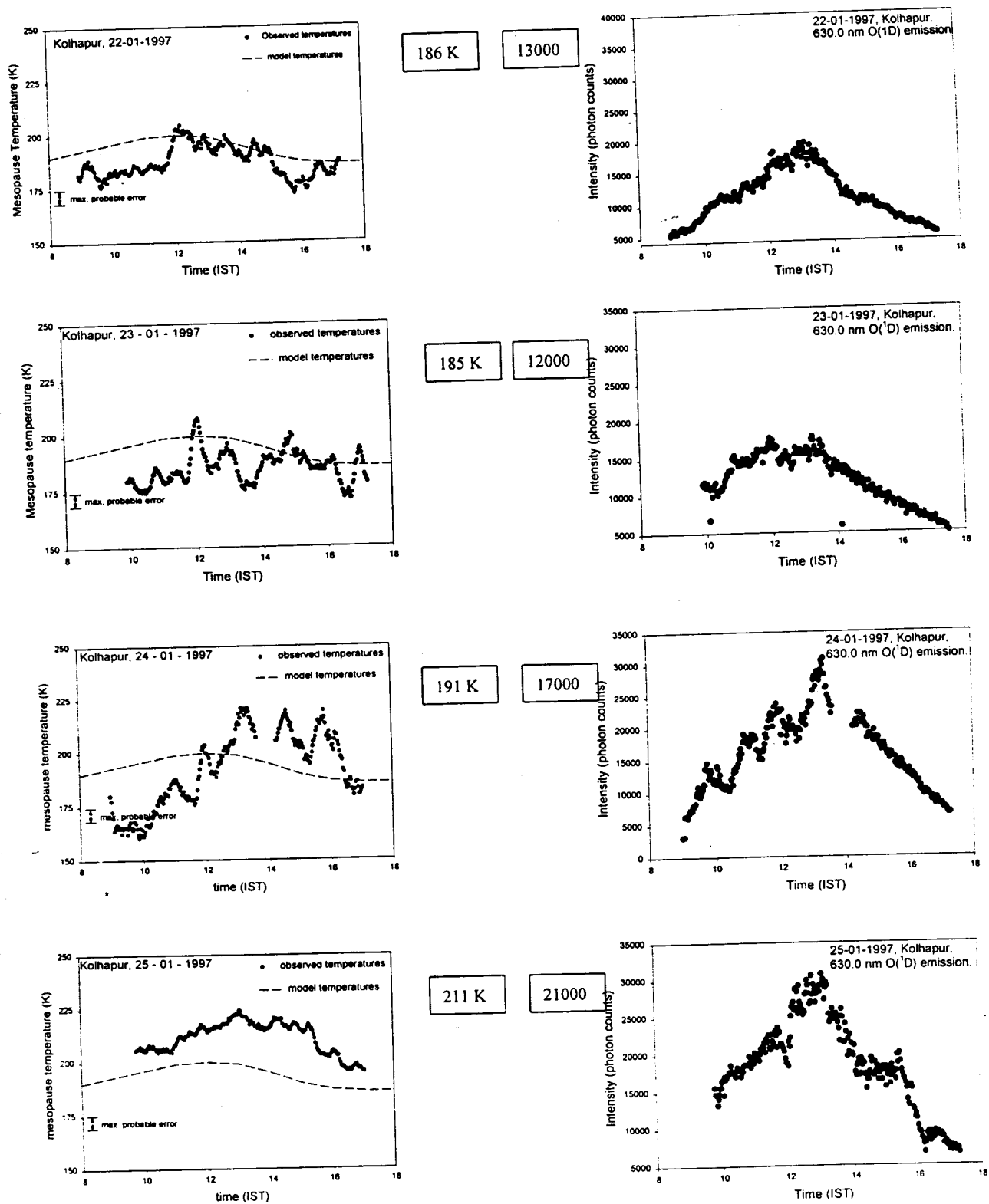
and molecular species higher above resulting in the enhanced 630.0 nm dayglow emission.

As said earlier, changes in the temperature in the base of the thermosphere can alter the atomic and molecular distribution higher above which may affect the available electron densities (Rishbeth, 1973; Stenning, 1981). Electron density changes would in turn affect the wind driven electrodynamical processes like the global scale dynamo. The electrodynamical aspects will be much more important over the equatorial region, where the phenomenon of equatorial electrojet is critically dependent on the ion neutral collision frequencies. Stenning (1981, 1985) has critically discussed the consequences of changes in the neutral and electron densities in the context of the equatorial electrojet. Further, the mesopause temperature variabilities may also affect the mesospheric chemistry via changes in the temperature dependent rate coefficients. All the above call for a detailed study.

Steep temperature enhancements on occasions, within a short time interval of few minutes is important while studying the coupled dynamics of the mesospheric region. There had been few reports on the sudden mesopause temperature enhancements using potassium Lidar (Huang et al., 1998) and by optical observations (Taylor et al., 1995, Hecht et al., 1995). These have been described as due to spectacular gravity wave events, which are thought to be either due to wave - critical layer interaction or due to wave - tidal linear and nonlinear interactions. The present observations of steep temperature enhancements could be either both or due to one of these processes. Due to lack of simultaneous coordinated observations it could not be conclusively proven till now.

Large temperature oscillations on 24th January and then subdued wave activities on 25th January with an upliftment in the temperature levels is yet another interesting observation. It appears that significant amount of energy got deposited into the system on 24th January and the after effect of the deposition would be the increase in the temperature levels. It should be noted here that a space weather event was in progress during 20 - 26th January. There were significant particle precipitation on 24th January over high latitudes. Whether the observed features of 24th and 25th January are due to the modified global circulation, the mechanism of deposition of additional energy at mesopause altitudes is yet a question that remains to be answered. Apart from this, in a recent study, Goldberg et al. (1995) showed that events of this type may change the mesospheric chemistry over high latitudes. It is unlikely that the

same process might be active over low latitudes also. In short, more systematic observations are called for, in order to be able to explain these results.

## 5.6# Conclusions:

At present, inferences made are more suggestive than conclusive. With the data set reported in the present study on the mesopause temperatures, one can suggest that-

1) The thermal state of the mesopause region is highly dynamic. Daytime mesopause temperatures exhibit large day to day and significant temporal variabilities.

2) Significant deviations from MSIS-90 model values could be clearly noticed. Occasionally these deviations become as high as 25% of the steady level values.

3) Steep enhancements in the mesopause temperatures within a short time interval of <0.5 h emphasize the presence of strong dynamical dissipative process.

4) Presence of specific periods in the mesopause temperature variabilities on most of the days provide an important clue for the lower and upper atmospheric coupling studies.

# 6# Optical investigations of the daytime equatorial electrodynamical processes

Equatorial electrodynamical processes had been dealt with elaborately in the introduction chapter. The E and F regions of the equatorial ionosphere are known to be controlled by electrodynamical forcings. During daytime mainly the E region dynamo electric fields are responsible for the electrodynamical forcing while during nighttime the F region dynamo takes over. In the case of the global scale atmospheric dynamo, the mechanical force is provided by the tidal winds which drag the conducting ionosphere across the geomagnetic fields generating electric fields and setting up associated currents (Ratcliffe, 1970; Hargreaves, 1995).

## 6.1#  E- region dynamo:

The dynamo theory explains the production of dynamo electric fields and currents in the E - region by the separation of ions and electrons, which could be understood by considering the forces that affect the ion and electron motions given by

$$dV_i/dt = eE/m_i + \omega_i (V_i \times B) + \nu_{in}(U-V_i) \tag{6.1}$$

$$dV_e/dt = eE/m_e + \omega_e(V_e \times B) + \nu_{en}(U-V_e) \tag{6.2}$$

Where $V_{i,e}$ are the ion and electron drifts respectively, e is the particle charge, E is the electric field vector, B is the magnetic field vector, m is the particle mass, U the neutral wind velocity, $\nu_{i,e}$ are the collision frequencies and $\omega_{i,e}$ the gyrofrequencies. Right hand side (RHS) includes the two basic tendencies of motion of ions and electrons. First, the presence of electric and magnetic field causes ions and electrons to gyrate along the earth's magnetic field lines. They do so with frequencies of gyration $\omega$ given by $\omega = eB/m$. Second, there is a tendency to maintain the mean velocity of the surrounding fluid (i.e. tidal motion) which consists primarily of neutrals. This tendency is directly proportional to the particle collision frequency $\nu$ given by

$$\nu_{(i,e)-n} \sim n\sigma \tag{6.3}$$

Where n is the particle number density and $\sigma$ is the collision cross section.
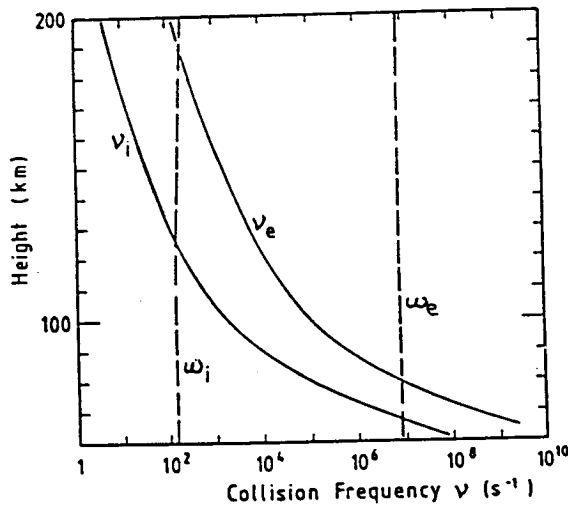
**Figure 6.1.** Typical height profiles of collision frequencies and gyro frequencies (After Volland, 1984)

These two forcing mechanisms, which tend to carry the ions and electrons in different directions, compete with one another, each dominating at different altitudes (Volland, 1984). The gyrating motion of the charged particles is independent of altitude (Figure 6.1) since it is determined only by the constant parameters, mass, charge, and magnetic field strength. The effect of collision increases exponentially with decreasing altitudes in proportion to the number density. For the electrons and ions there are critical transition altitudes below which the collisional forces overtake the electromagnetic forces. In the region between the two transition altitudes, referred to as the 'dynamo region', the electron motions are dominated by the electromagnetic forces while the heavier, slower ion motions are dominated by collisional forces, resulting in charge separation (figure 6.2).

This separation of charges produces an electric field, which in turn would produce currents. Magnetic field lines act as a highly conducting electric wires between E and F regions, and thus E-region electric fields from adjacent latitudes get mapped to F region altitudes over the dip equator. An analogous electric circuit is shown schematically in figure 6.3. These electric fields in the E and F regions are responsible for a variety of equatorial ionospheric processes like the equatorial electrojet, counter electrojet and the equatorial ionization anomaly. These phenomena will be explained briefly in the next section.

114
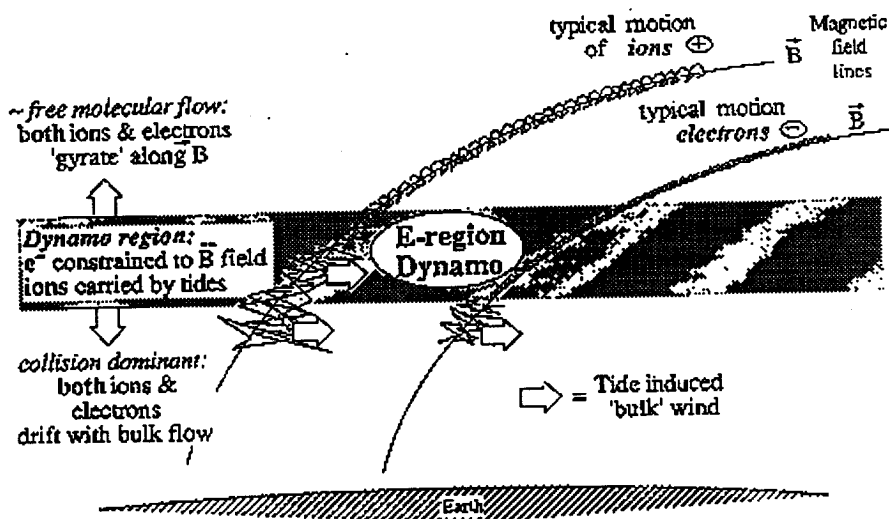
**Figure 6.2.** This schematic representation shows that in the dynamo region, the ions are collision dominated while the electrons tend to gyrate around magnetic field lines. A separation of charges may result from the disproportionate influence of tidal motion on the ions in the dynamo region. Induced electric fields produce currents which then give rise to the Sq – magnetic variation.
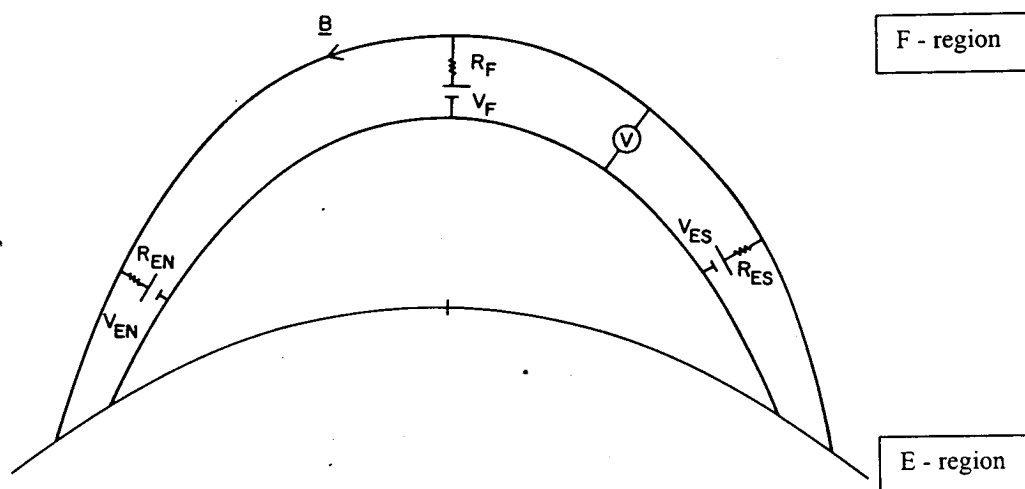


**Figure 6.3.** Analogous electric circuit for the E region electric field mapping to the F region.

Some of the relevant equatorial processes pertaining to the present thesis are discussed below and the new results highlighted.

115

# 6.2# Daytime equatorial electrodynamical processes:

## 6.2.1# Equatorial Electrojet:

The global scale dynamo action would manifest as zonal electric fields over the dip equator. This east - west electric field crosses with the north – south geomagnetic field resulting in the separation of ions and electrons which gives rise to vertical Hall polarization electric field. This vertical field in turn would cross the magnetic field and would enhance the zonal current flow, which is nothing but the **equatorial electrojet** (EEJ). Typical ion density profiles and the conductivity profiles in addition to the conceptual slab geometry diagram explaining the EEJ are given in figure 6.4.

Vertical profiles of daytime composition and plasma density (left) and conductivities (right) for average solar conditions.
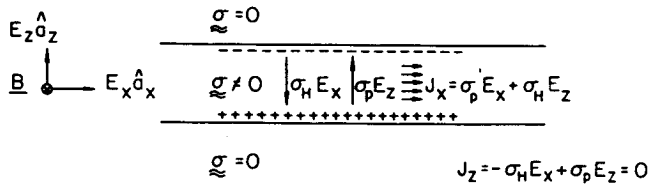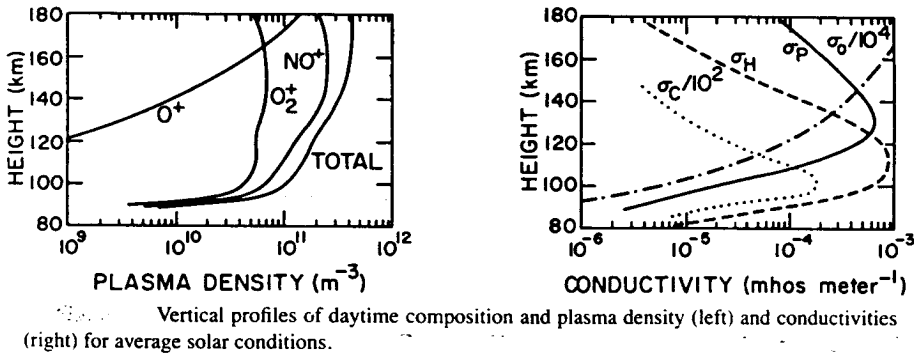
**Figure 6.4.** Slab geometry of the equatorial electrojet formation (After Kelly, 1995).

The formation of electrojet could be understood mathematically from Maxwell's equations which expect the curl free behavior of the electric fields -

From $\nabla \times \mathbf{E} = 0$, one can deduce:

$$\partial \mathbf{E_x}/\partial Z = \partial \mathbf{E_Z}/\partial x$$

$$\partial \mathbf{E_x} = (\partial \mathbf{E_Z}/\partial x)\, \partial Z$$

In fact, horizontal scale size ($\partial x$) of conductivity variations is 100 times that of the vertical ($\partial Z$) variations of conductivity, and as experiments indicate $E_z$ to be 10-20 times of the $E_x$. Clubbing the above statements together, one can say that the zonal electric field can change only slightly in the E region itself, and so we shall assume the conductivity gradients rather than the variations in $E_x$ to dominate the divergence of the vertical Hall current. The Hall current can not flow across the boundary and a charge layer builds up resulting in an upward directed electric field. In a steady state in this simplified slab model, no vertical current may flow and the vertical pedersen current must exactly cancel the Hall current. This would imply that

$$\sigma_H E_x = \sigma_P E_Z$$

and hence

$$E_Z = (\sigma_H/\sigma_P)E_x$$

Since $\sigma_H > \sigma_P$, the vertical electric field component exceeds zonal electric field component. One can see that

$$J_x = \sigma_H E_Z + \sigma_P E_x$$

$$J_x = [\sigma_H \cdot (\sigma_H/\sigma_P) \, Ex + \sigma_P E_x]$$

$$J_x = (\sigma_H^2/\sigma_P^2 + 1) \, \sigma_P \, E_x = \sigma_c E_x$$

Where $\sigma_c$ is the *Cowling conductivity*. Therefore the enhanced zonal conductivities lead an intense jet of current to flow over the magnetic equator in the east-west direction which is usually measured in terms of the ground magnetic field variation. The EEJ is centered around 106 km and has a latitudinal extent of around ±3°, centered around the dip equator (Onwumechilli, 1967). The electrojet strength is usually inferred from the differences in $\Delta H$ which itself is the difference between the average nighttime value and the instantaneous daytime value of the horizontal component of the geomagnetic field ($\Delta H$) from two stations, one over the dip equator and another well away from the EEJ belt. For the Indian zone, Trivandrum (0.3°N., dip lat.) and Alibag (13.2°N dip lat.) are usually considered and $\Delta H_{TRD} - \Delta H_{ABG}$ is taken to be a measure of the intensity of the EEJ at any instant (Rastogi and Patil, 1986). On some occasions during the day the ($\Delta H_{TRD} - \Delta H_{ABG}$) EEJ values may go below the average nighttime values and this is referred to as the counter electrojet (CEJ), when the primary electrojet current is believed to change its direction from eastward to westward (Rastogi, 1973) or as a partial CEJ when the electrojet intensity

decreases for sometime before reverting back, not necessarily going below the nighttime values. The exact causative mechanism of the CEJ is still a topic of research though there are hypothesis linking it to the neutral dynamics (Raghavarao and Anandarao, 1980; Somayajulu et al., 1993).
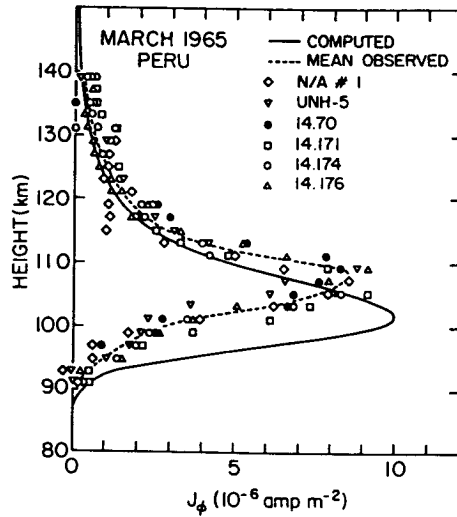


**Figure 6.5.** Observed and computed eastward current density profile near noon at the dip equator (After Kelly, 1995).

## 6.2.2# Equatorial ionization anomaly:

Equatorial ionization anomaly refers to the double humped structure in the latitudinal profile of the F region ionization density at low geomagnetic latitudes, with a trough centered around the dip equator and two crests on either side of it around 20° dip latitude. Since the time of its discovery by Appeleton (1946), this anomaly has been the theme of many theoretical and experimental investigations. EIA is a unique geophysical phenomenon that demonstrates the dominance of electrodynamical processes over the photochemical ones. E region dynamo electric field, driven by tidal winds, gets mapped to the F region along the highly conducting magnetic field lines. This electric field crossing with the magnetic field lines gives rise to a vertical plasma drift, with a velocity, $V_d = E \times B/B^2$. Besides, as the ion gyro-frequency is much higher than the ion-neutral collision frequency at F region altitudes, the plasma once lifted upwards can diffuse along the field lines under the influence of gravitation and pressure gradient forces. This diffusion of plasma along the magnetic field lines transports the plasma away from the equator, i.e. to low latitudes, forming crests of

ionization. These important and unique facts of the equatorial F region dynamics were recognized and advocated by Mitra (1946) and Martyn (1947). Mitra suggested that field aligned diffusion of ionization from equator could be responsible for the formation of the anomaly, but Martyn included vertical drift of ionization near the equator alongwith the subsequent diffusion to higher latitudes, a mechanism that has come to be known as the 'fountain effect'. Croom et al (1959) provided the first results on the latitudinal distribution of ionization at noon at different altitudes by making use of data from a chain of ionosondes.
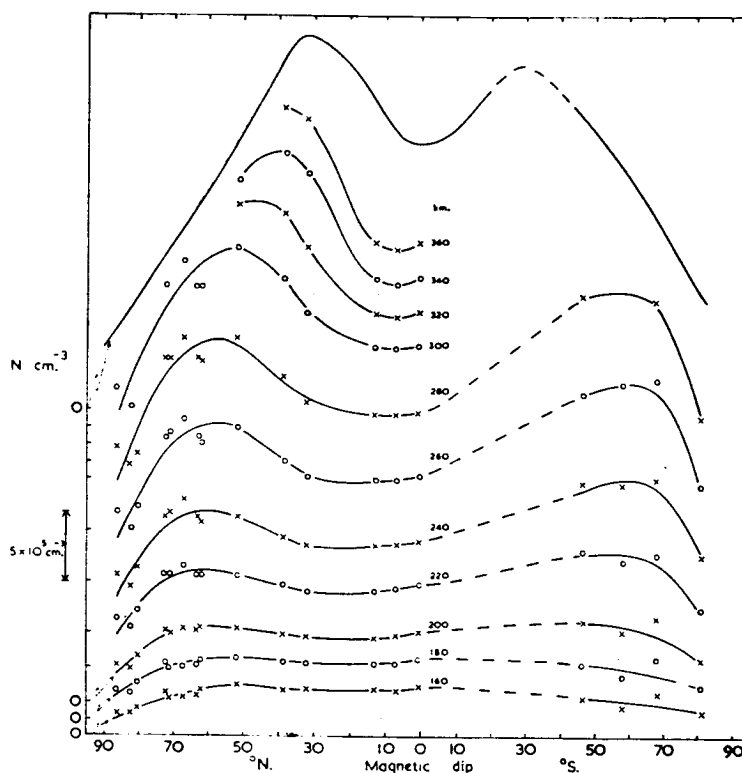


**Figure 6. 6.**Equatorial ionization anomaly as observed in the latitudinal chain of Ionosondes. (After croom et al.1959).

Anderson (1981) performed a theoretical study and showed the combined effect of vertical drift and field aligned plasma diffusion to be responsible for the equatorial ionization anomaly (figure 6.7). The development of the anomaly exhibits a diurnal pattern that is dependent on the phase of the solar activity. Crest to trough ratio of the ionization is usually taken as the anomaly strength (Rush and Richmond, 1973). This strength is larger in low solar activity and the latitudinal extent of the crests are narrower than what one observes during high solar activity period. Larger

winter crest and asymmetry in the anomaly are dealt in detail by many investigators highlighting the role of cross equatorial winds (Walker et al., 1981; Rao and Malhotra, 1964,).
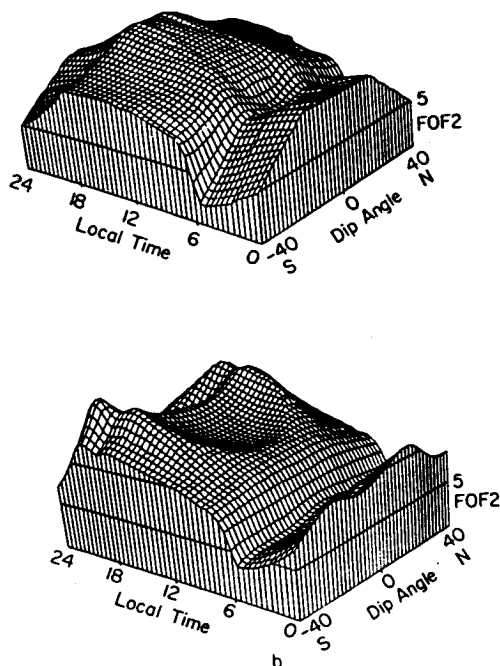


**Figure 6.7.** Dip angle variation of foF2 as a function of local time obtained from numerical solution of plasma continuity equation (a) F region vertical plasma drift neglected and (b) vertical plasma drift included. (After Anderson, 1981)

In another critical study on the EIA, it was unambiguously demonstrated that the strength of the EIA directly depends on the integrated strength of the EEJ as perceived from ground magnetic data (Raghavarao et al, 1978).

## 6.3# Use of OI 630.0 nm emission for the study of electrodynamical processes

In the earlier chapters the processes responsible for the dayglow emissions of interest were presented. The three most important processes for the 630.0 nm thermospheric emission (that has peak emission altitude ~220 kms) (Solomon and Abreu, 1989) are-

(i)     Photoelectron excitation of 'O':

$$O(^3P) + e \rightarrow O(^1D) + e$$

(ii)     Photodissociation of $O_2$:

$$O_2 + h\nu \rightarrow O(^1D) + O(^3P) \quad \text{and}$$

(iii)    Dissociative recombination of $O_2^+$ ions:

$$O_2^+ + e \rightarrow O(^1D) + O(^3P)$$
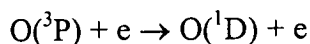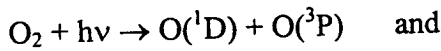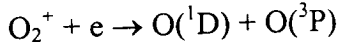
Transition of $O(^1D)$ to $O(^3P)$ gives an emission at 630.0 nm. Hays et al. (1978) showed that the photoelectron contribution to the 630.0 nm dayglow is the largest followed by the photodissociation and dissociative recombination. The dissociative recombination the dominant nighttime source, contributes only by 20-30% of the overall 630.0 nm daytime intensities.

It was earlier shown that the temporal variabilities in the 630.0 nm dayglow intensities are essentially determined by the F region electron densities and the consequent dissociative recombination of $O_2^+$ with the ambient electrons (Sridharan et al., 1991, 1992b). Once the above process is understood, the dayglow photometer was effectively used in the investigation of the electrodynamical processes of the equatorial ionosphere. The photometer was successfully used to monitor the evolution of the EIA by operating it in a meridional scanning mode from different geographical locations. The latitudinal gradient in the dayglow intensity and its variations were ascribed to the movement of the crest of EIA during its evolution (Pallam Raju et al, 1996) (Figure 6.8). It had also been used from Waltair, a strategic location in a bi-directional north and zenith pointing mode in order to infer the strength of the EIA and to arrive at a precursor for the nighttime equatorial spread F (ESF), well in advance (Sridharan et al., 1994).
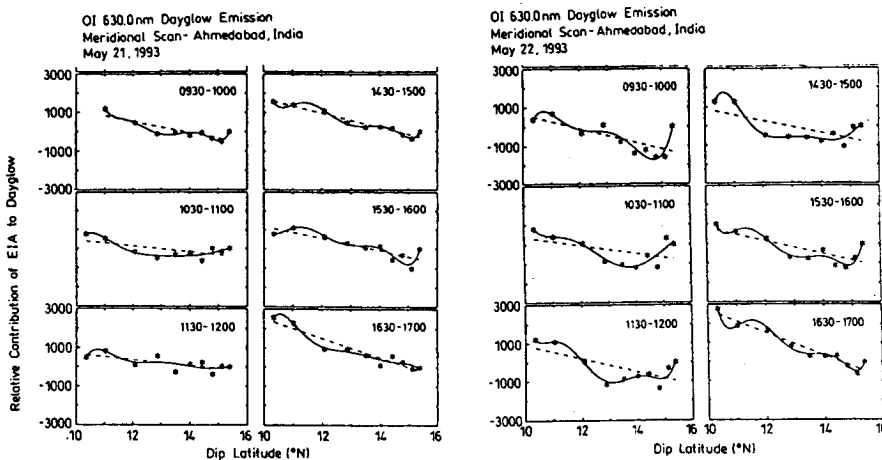


**Figure 6.8.** Hourly plots of EIA contribution to dayglow at different dip latitudes (After Pallam Raju et al, 1996).

In the present study, further campaigns were carried out to investigate the electrodynamical processes and on the response of the 630.0 nm dayglow to the same. Results from a campaign, carried out from Kolhapur during 1997 with the help of meridional scanning of MWDPM, clearly showed the anomaly development and its movement while in another campaign from Waltair during March 1998, steep noontime bite outs on 630.0 nm were observed, once again emphasizing the significance of the electrodynamical control on the dayglow emission. Further, a study on the overhead E and F region electrodynamical coupling over the dip equator was successfully carried out from a multi – instrumented campaign of which the DGP was a part, during 1991. These results will be discussed in the sections to follow.

## 6.4# Response of 630.0 nm emission to the electrodynamical processes : Results from Kolhapur (16.8$^0$ N, 74.2$^0$ E, 13 N dip latitude)

Once it is understood that the F – region electron densities through the dissociative recombination are responsible for the temporal variabilities in the 630.0 nm dayglow, the electrodynamical forcing which affects the electron density distribution are expected to get reflected in it. As discussed above, the most important electrodynamical process at F-region heights is the development of the Equatorial Ionization Anomaly (EIA) which transports plasma from the dip equator to low latitudes due to ExB drift. By monitoring the spatial variability of F region plasma through 630.0nm dayglow with time, one would be able to track the movement of the EIA crests.

With this idea in the background, the MWDPM was made to look at different elevations by means of a mirror, during a campaign, conducted from Kolhapur (16.8N, 74.2E) during January - February 1997 when the solar activity was significantly low. The photometer collected data from zenith, 30°N elevation corresponding to ~380 km and 20°N elevation corresponding to ~604 km separation from zenith for an emission centered at ~220 km. It is assumed that, within this short latitude separation of ~6°, the solar zenith angle corrections may not be very important and only a systematic bias in the data would be present. Day to day variations in the evolution and strength of the anomaly were clearly noticed.

Figures 6.9 (a-d) show the observed intensity variations for the three look angles of 0$^0$, 30° and 20°N elevation (top panel). When ratio of the intensities of 30°

and 20°N to the zenith intensities is taken, one can clearly see the development of an inverted 'bow shape' in the ratios with time. A decrease upto local noon and then an increase in the ratio can be linked with the movements of the crest of EIA. At $30^0$ and $20^0$ elevation angle the photometer looks through a larger column of dayglow emission layer as compared to zenith for a stratified emission layer. There will be a gradual decrease in intensity as one moves from lower elevation towards zenith. This could be seen on all the days depicted in figure 6.9. With the progression of time, the EIA develops with the formation of the crests of ionization at latitudes close to the equator, which later starts moving to higher latitudes and getting intensified while doing so. The crest would be encountered overhead Kolhapur when the dayglow intensities would increase significantly. This is typically seen to occur around 1000 – 1100 h. The time would critically depend on the primary driving force namely the zonal electric field intensity over the dip equator. Later, in the afternoon and evening hours, the EIA crest would retrace back to the equator. The whole process is confined to daytime during the low solar activity period while during high solar activity, the EIA crests may persist to late hours in the night and on some days may seen during pre sunrise hours too. From the figures the movement of the EIA crest would be perceived well if we consider the ratio of instantaneous dayglow intensity at the three look angles. The variations of $I(30)/I(z)$ and $I(20)/I(z)$ clearly indicate the strength of the crest and its possible latitudinal range. When the ratio of intensities reaches its lowest value would be the time of the crossing of the EIA crest over Kolhapur. As the crest moves northwards the ratio would start increasing and if it is more than the morning value it would mean that the crest either has crossed midway between the zenith and low elevation location or at the most has reached overhead there. This mode of operation can be thought of as a means of studying the EIA crest dynamics within a latitude zone of $6^0$. The day to day variability in the EIA could also be studied using this method. The data from Kolhapur for the month of February 1997 represents days of varying electrojet strength and with several days of Counter electrojet too. As mentioned earlier the integrated strength of EEJ had been shown to have an excellent correlation with the strength of the EIA which is given by the relative intensity of the crest to trough ratio and also the latitudinal location of the crests (Raghavarao et al 1978). During counter electrojet (CEJ) events one would expect a proportional impact on the development of EIA (Rastogi and Klobucher,
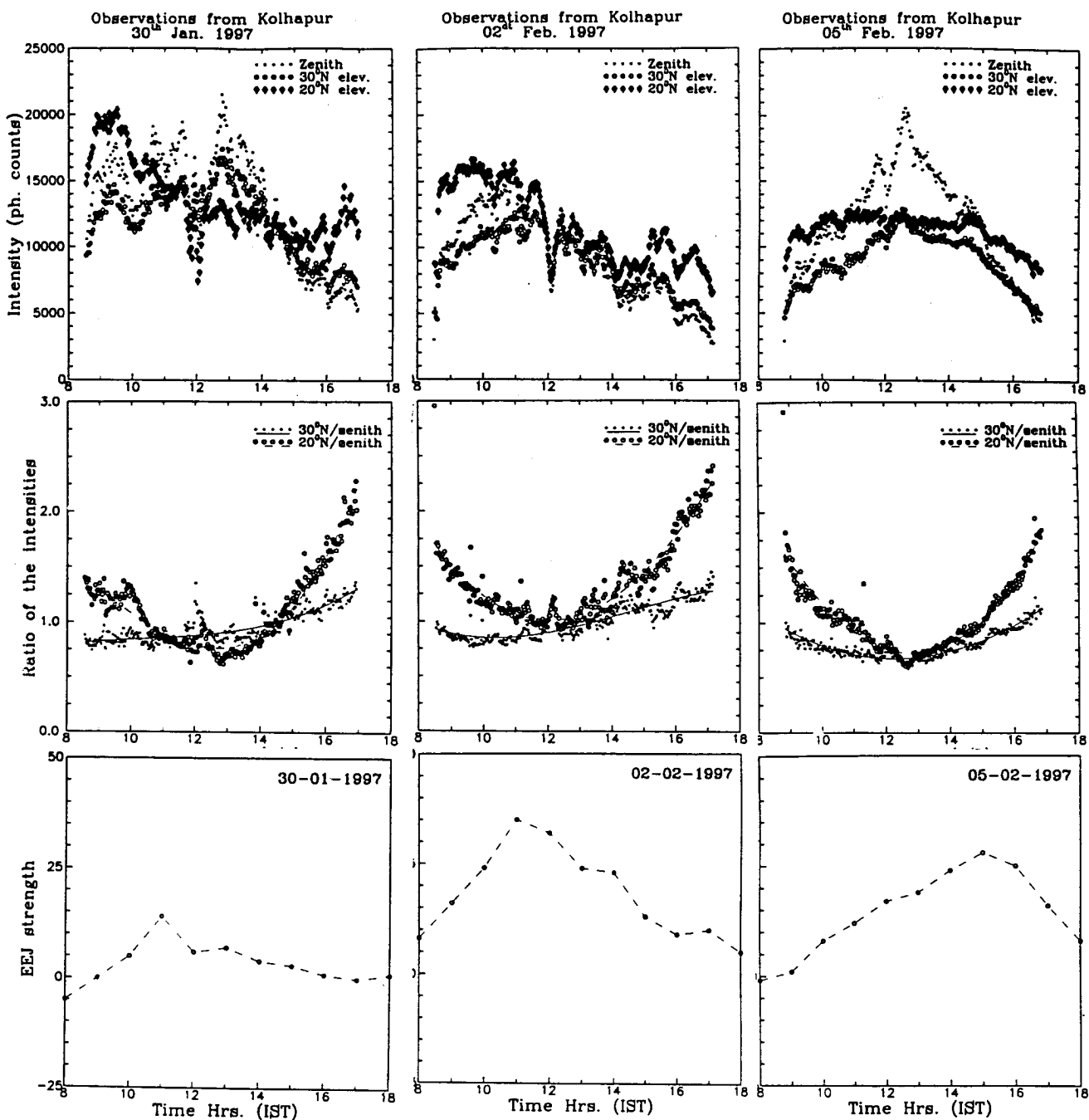
**Figure 6.9a.** Evolution of EIA as seen in the 630.0 nm intensities on 30$^{th}$ January, 2$^{nd}$ February and 5$^{th}$ February 1997. Top panel show the intensity variation over zenith, 30$^{0}$N and 20$^{0}$N, middle panel show the variation in the ratio of 30$^{0}$N intensity and 20$^{0}$N intensity to the zenithal intensities. Bottom panel show the electrojet strength on that day.
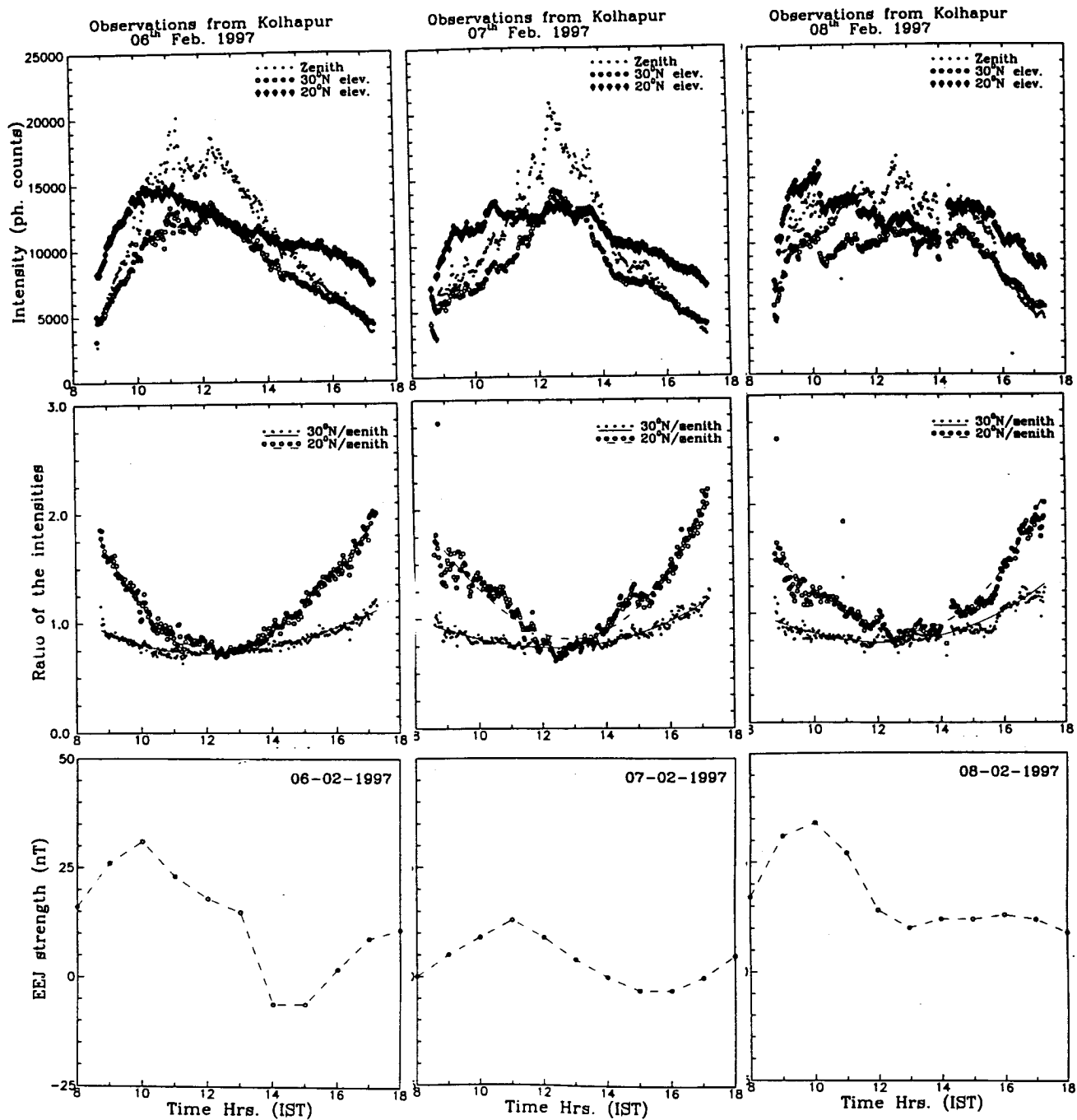
**Figure 6.9b.** Same as figure 6.9a . but for the days 6th, 7th and 8th February 1997.

125
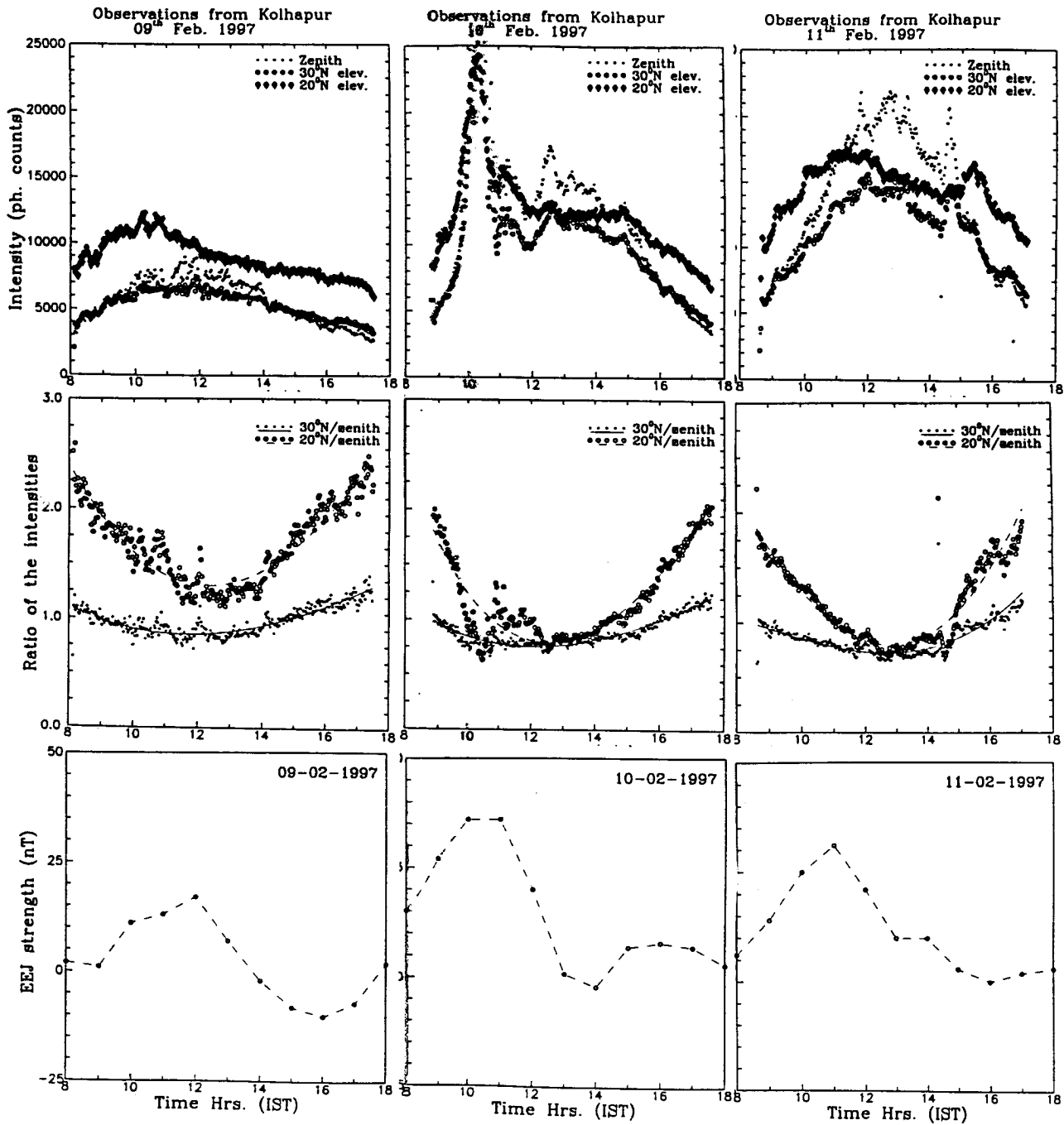
**Figure 6.9c.** Same as figure 6.9a, but for 9th, 10th and 11th February 1997.
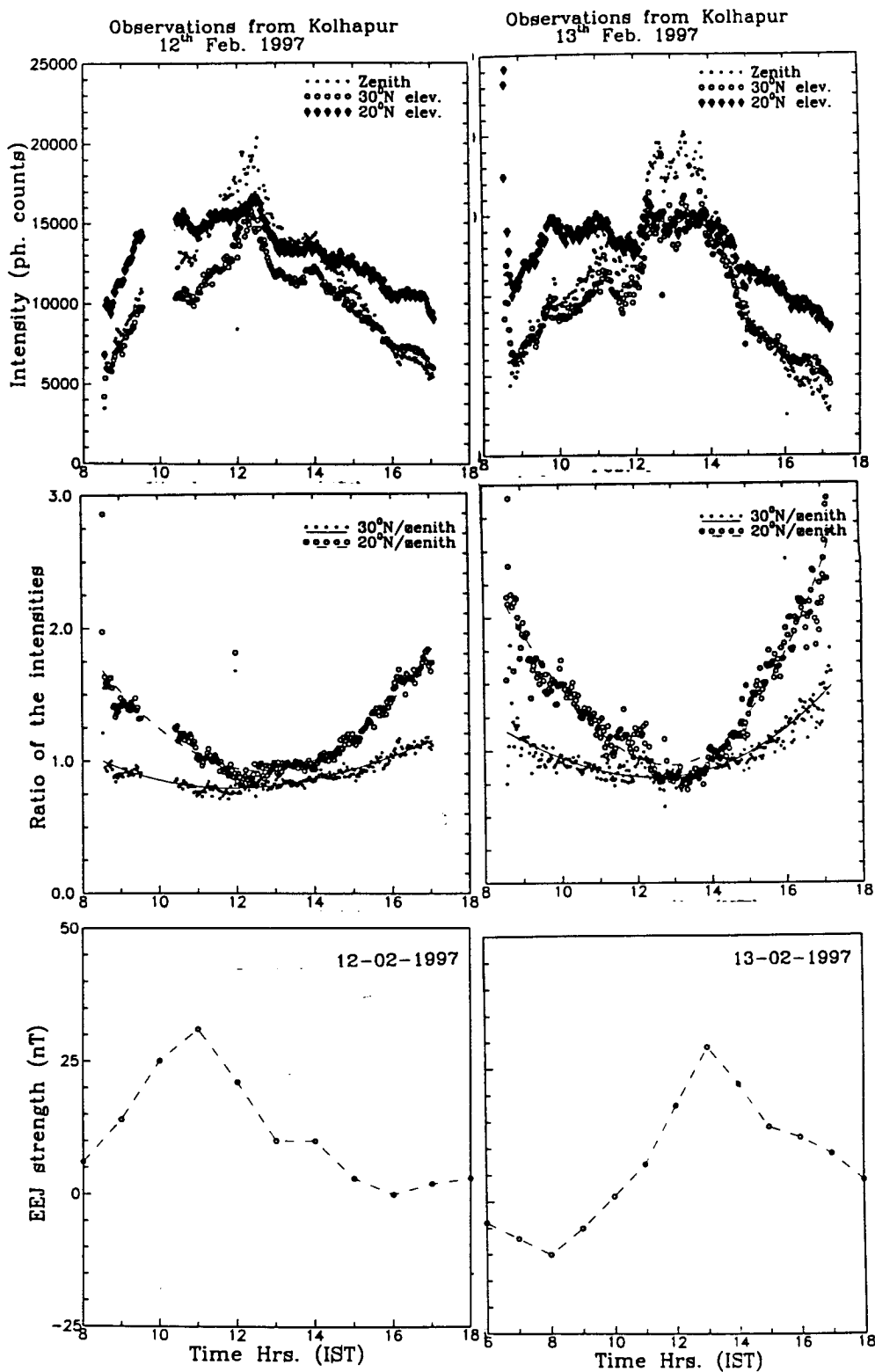
**Figure 6.9d.** Same as figure 6.9a, but for 12th and 13th February 1997.

127

1990). In the examples presented herein, the EEJ strength had been moderate on 5th Feb 97 and as a consequence, the effects of the EIA crests probably did not cross much beyond Kolhapur latitudes. On the other hand, though the EEJ strength had been rather low on 30th Jan the crest seems to have come closer to $16^0$ N dip latitude. From 6th Feb onwards one encounters a series of CEJ days, both partial and full CEJs. A unique example of a morning CEJ is also seen on 13th Feb. From the slopes in the morning and afternoon hours it could be inferred that the EIA crest had crossed Kolhapur on 6th Feb and come to midway of the two representative locations i.e. upto $\sim13^0$ N dip latitude, while on 7th it had relatively moved further north. The situation on 8th is somewhat analogous to 7th Feb with a partial CEJ. 9th Feb depicts a classical CEJ and the temporal variation of the intensity ratio shows a perfect symmetry. There had been a partial CEJ on 10th Feb and a moderate EEJ strength on 11th and 12th Feb, showing relatively weak EIA. On 13th February 1997 one encounters a morning CEJ followed by a weak EEJ, with ratios exceeding the typical values both in the forenoon and afternoon hours.

## 6.5# Electrodynamical coupling of E and F region over dip equator - An investigation:

As had been discussed in the earlier chapters, the F-region of the ionosphere is essentially controlled by the transport processes while the production, due to photo-ionization peaks well below the F peak and the equatorial F-region is dominated by the electrodynamical processes. Due to the resultant generation of electric fields because of the dynamo action, while in the E - region it is the generation of the EEJ, in the F – region it would be the fountain effect and the consequent development of EIA. Ionization only beyond 150 km could participate in the development of the EIA as, only here the electron and ion gyro-frequencies are significantly larger than their respective collision frequencies with the neutrals and the plasma would experience a charge independent **EXB Drift**. Under such conditions the F – region plasma would get lifted up physically to greater heights only to diffuse along the geomagnetic field lines to latitudes away from the dip equator. The propelling force is due to the zonal electric fields only. Therefore the height region of 150 km could be considered as the source region of F - region plasma. If at any particular height region over the equator

could be monitored, the plasma fountain could be inferred and the electrodynamical coupling of the equatorial ionospheric region investigated.

The DGP operating on OI 630.0 nm thermospheric dayglow, the 50 MHz VHF radar providing the zonal electric field data in the electrojet region and ground based magnetometers were operated in a campaign mode from Thumba, Trivandrum and the first signatures for the imprint of the equatorial electrodynamical processes in the thermospheric dayglow were obtained unambiguously.

Figure 6.10a,b,c,d and e depict the OI 630.0 nm dayglow variations alongwith the Doppler frequency of the backscattered echoes and the groundbased magnetic data representing the electrojet strength during those days. The thin dashed line in all the figures represents the five point running average of the measured Doppler frequency, while the dotted line corresponds to the dayglow intensity at the corresponding times. The prominent spikes in the dayglow intensity beyond 1300 hrs IST on 12th February are an artifact due to the passage of clouds within the field of view of the dayglow photometer. Only long period trends were considered for the further analysis. Overall features in the 630.0 nm dayglow variabilities and VHF radar data on a given day reveal that, there are similarities in the temporal variations in them, but with a time lag. Variations in the dayglow intensity followed the VHF radar estimated velocities. The latter is directly proportional to the zonal electric fields. Nearly all the features like steep increase, broad peak, bite outs and small structures in the VHF radar data are seem to get reproduced in the dayglow data.

A detailed cross correlation analysis was performed on the variabilities with the cross correlation coefficients being estimated for time delays ranging from 0 to 8 hours. From the best-fit curve of the coefficients, the time delay that has to be introduced in the Doppler frequency curve, in order to have a correlation coefficient $\geq 0.9$ is estimated.

Table 6.1 gives the details of the derived time delays, the cross correlation coefficient, alongwith the measured Doppler frequency. The thin continuous curve in the top panel in all the figures represents the Doppler frequency data, but time shifted, based on the above cross correlation analaysis. The diamonds joined by the dashed line in all the figures represent the electrojet strength as inferred from the ground magnetic data shifted by the same duration as that of the VHF radar derived Doppler frequency.

| Date | Peak Doppler Freq. (-ve) Hz | Derived time delay (hrs.) | Overall correlation coefficient |
|---|---|---|---|
| 12th February 1991 | 60 | 3.14 | 0.87 |
| 14th February 1991 | 90 | 2.08 | 0.92 |
| 15th February 1991 | 100 | 2.00 | 0.91 |
| 16th February 1991 | 110 | 1.17 | 0.82 |
| 20th February 1991 | 120 | 1.20 | 0.94 |

**Table 6.1.** Overall correlation coefficients and derived time delays for the days under consideration.

The electric field fluctuations represented by the variations in the Doppler frequency which are much above the uncertainties reveal very good correlation (correlation coefficient $\geq 0.9$) with the 630.0 nm dayglow variations. A critical look at the gross features of both the Doppler frequency and the dayglow intensity reveals that, invariably on all the days under consideration the dayglow intensity maximized at ~1300 h IST, unlike the time of maximum of Doppler frequency which could be anywhere between 1000-1300 h. This is essentially due to the solar insolation control of the former, while the latter is being dictated by the combined effect of neutral winds and the electron density at any instant. In the present exercise, importance is given to shorter period variabilities only, so as to highlight the electrodynamical coupling of the E and F-regions. In order to accomplish this, one hour running average of both the airglow and the VHF radar data were taken and the actual data were detrended by smoothing and the difference would now represent shorter period variations.

The data for all the days under consideration were treated alike and are depicted in separate panels of Figures from 6.10a to 10e.

It could be seen that 12th and 14th February, 1991 were Counter Electrojet days, with the electrojet current reversal occurring at 1300 h on 12th February and at 1430 h on 14th February. The Doppler frequency curve showed zero, as the Esq irregularities which are used as tracers for inferring them are known to disappear during CEJ periods ( ; Krishnamurthy and Sengupta, 1972). The backscatter echoes reappeared with the return of the normal electrojet. Further, on 12th and 14th
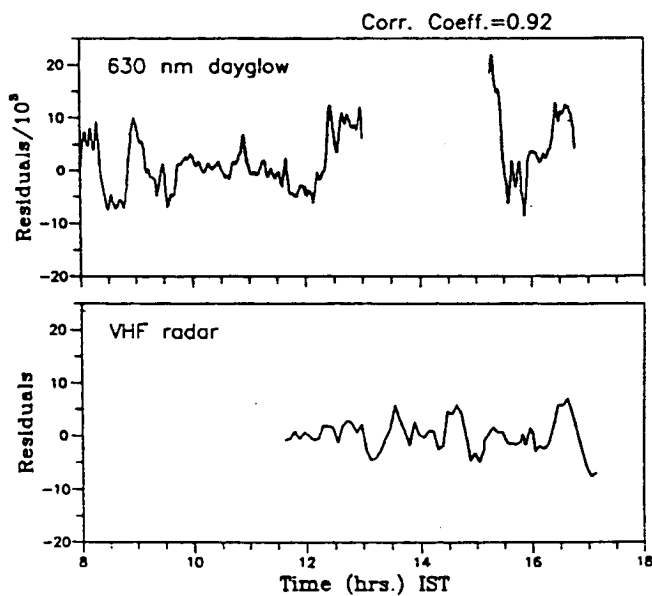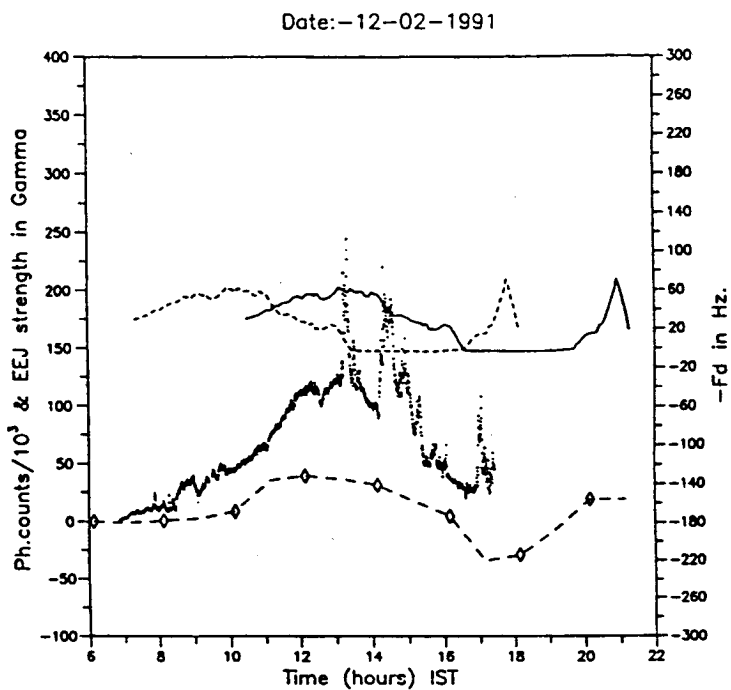
**Figure 6.10a.** (Top Panel) The temporal variability exhibited by OI 630nm dayglow emission (…) from Thumba, alongwith the actual Doppler frequency measured by the VHF backscatter radar (dashed) and the time shifter (by 3.14 h) Doppler frequency (continuous). The EEJ values are also shifted by 3.14 h (diamonds). (mid and bottom panels) The residual variabilities in 630nm dayglow and Doppler frequency after removing the long period trend On 12th February 1991.

**Figure 6.10b.** (Top) Same as figure 6.10a, but, with the time shift for the Doppler frequency and the EEJ strength being 2.08 h for 14th February 1991 (mid and bottom) residual variabilities for the same day.

February, electric field magnitude remained rather low, as it is very clear from the magnetic and backscater data. On 14th February, large scale modulation of the electric fields could be inferred from the backscatter data. Though there are indications for similar modulations in the dayglow too, the effects are not pronounced to the same extent. This could be due to the peculiar behaviour of the electric field on

this day. As mentioned earlier, the lower panels of Figures 6.10a to e represent only the smaller period variations both in dayglow and VHF radar data, after removing the slow varying component. Since the dayglow data on 12th February for the duration 1300-1500 h was corrupted due to passage of clouds, this part of the variations was not considsered for the cross correlation analysis.

The data stretch on 14th February is slightly longer, and with a higher correlation coefficient of 0.95. The close similarity in the time shifted ground magnetic data could be clearly seen in Figure 6.10b. These results alongwith the ones depicted in Figures 6.10c to 6.10e for the remaining three days clearly bring out, that on all the days including the CEJ days, there existed a good correlation between the Doppler frequency and the OI 630.0 nm dayglow data.

15th, 16th and 20th February provide examples of very good correlation with the time shifted Doppler frequency variations at 101.4 km and the dayglow variabilities centred at 220 km. Similar to the earlier figures, the residuals in the dayglow and the electric field are depicted in the lower panels.

Further, it has been observed that larger the Doppler frequency, or the electrojet strength, the time delay is smaller and also the 630.0 nm peak intensity had been smaller. The examples of the counter electrojet days are very striking, as during these days when the primary electric field was considerably reduced, it was reflected in the time delays. For example, the driving electric field strength on 12th Feb. was only 30% of that on 16th February, and so the deduced time delay is 3.14 hours in comparison to the 1.17 hours on 16th February. The important conclusion being arrived at is the reduced magnitude of the zonal electric fields, causes the E x B drift velocities to be lesser and it would manifest in the time delays. Few more days when the VHF radar data were not available also show that there is close correspondence between the dayglow and magnetic data and they do fall under the same lines as discussed above.
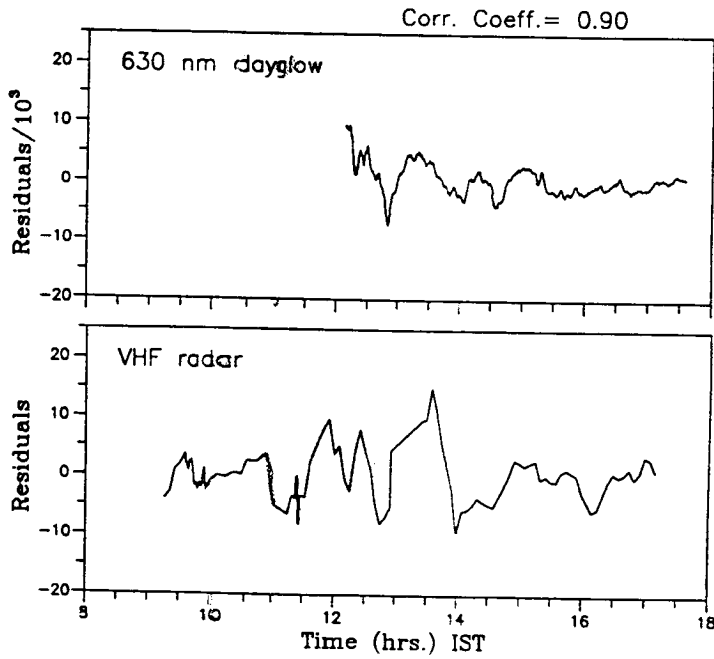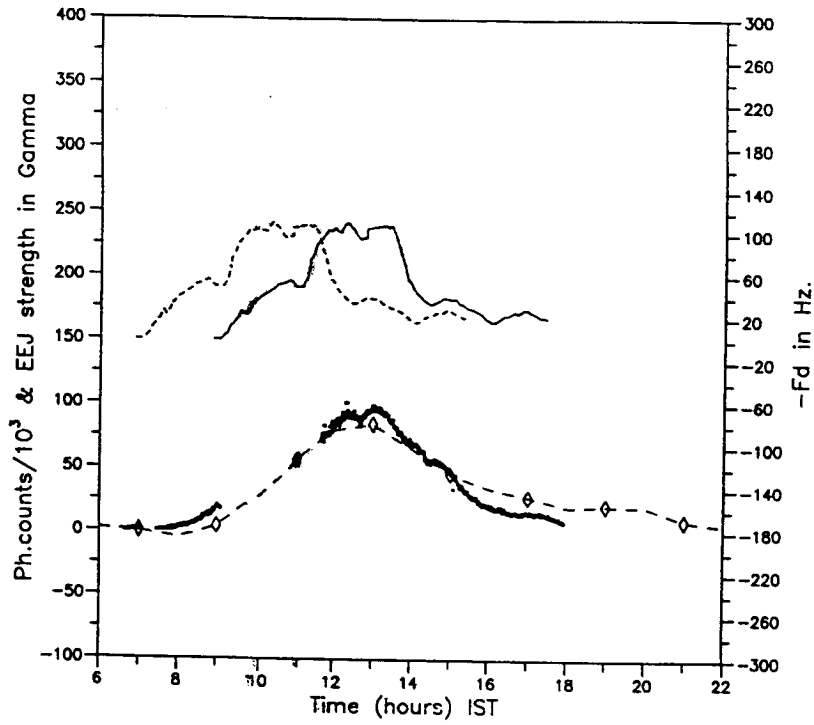
**Figure 6.10c.** Same as figure 6.10b, but, with the time shift for the Doppler frequency and the EEJ strength being 2.00 h for 15th February 1991.
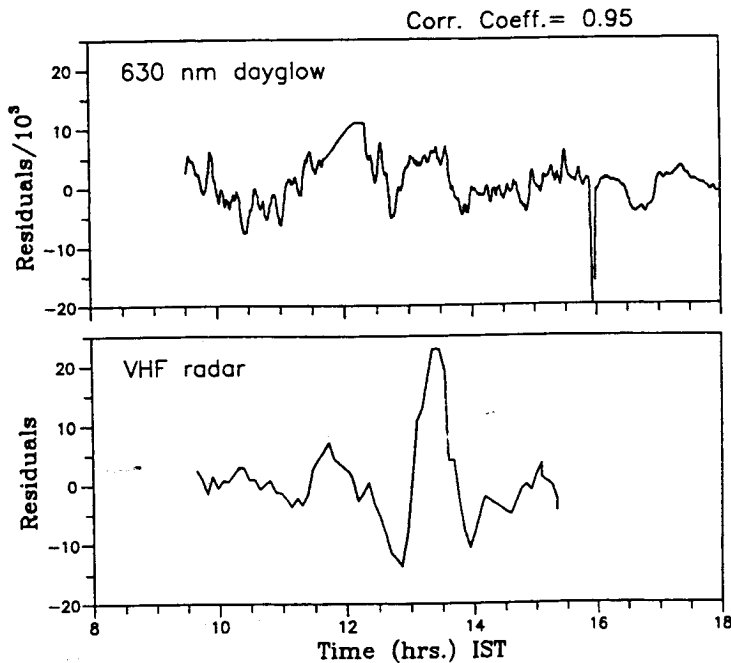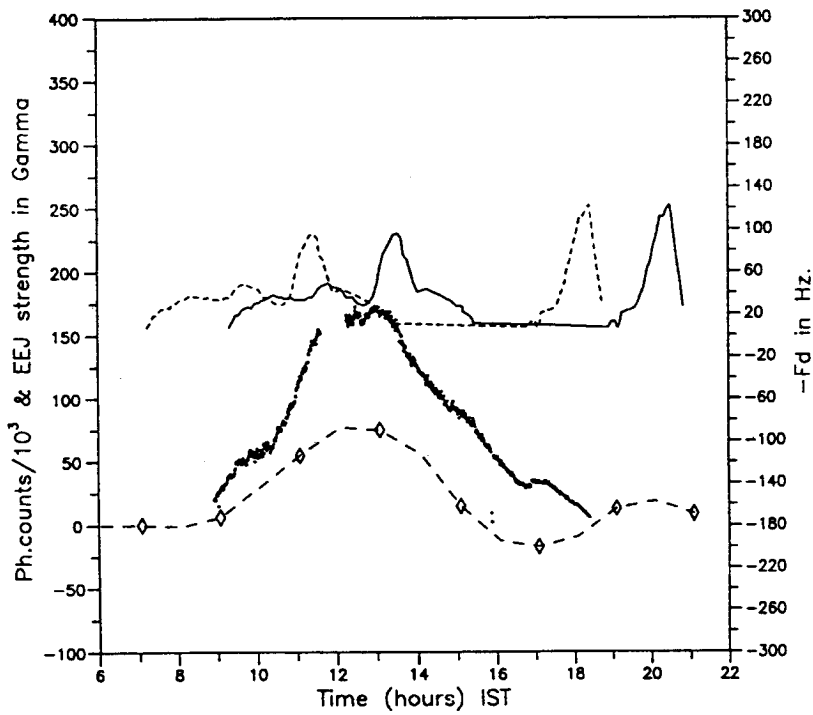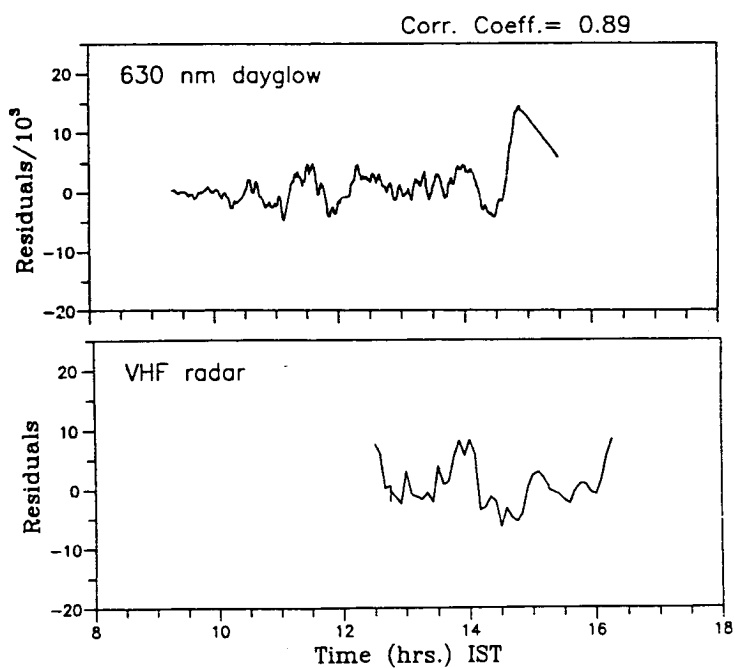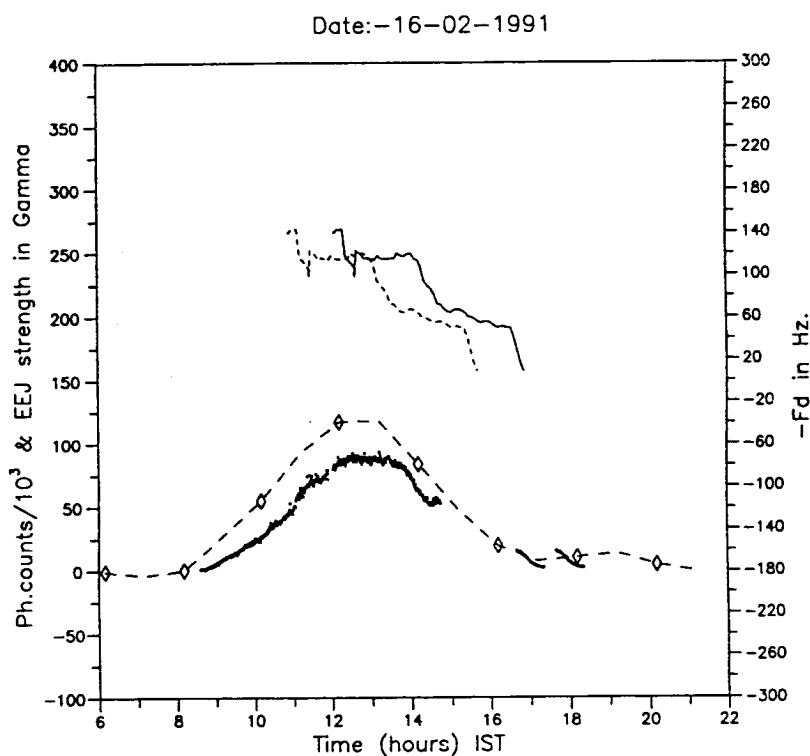
**Figure 6.10d.** (Top) Same as figure 6.10a, but, with the time shift for the Doppler frequency and the EEJ strength being 2.08 h for 16th February 199.

Date:-20-02-1991



Corr. Coeff.= 0.92
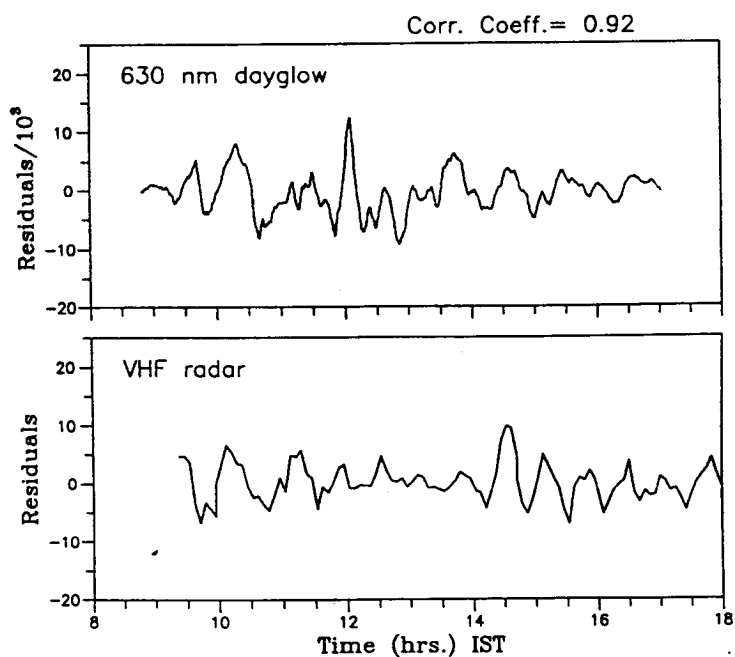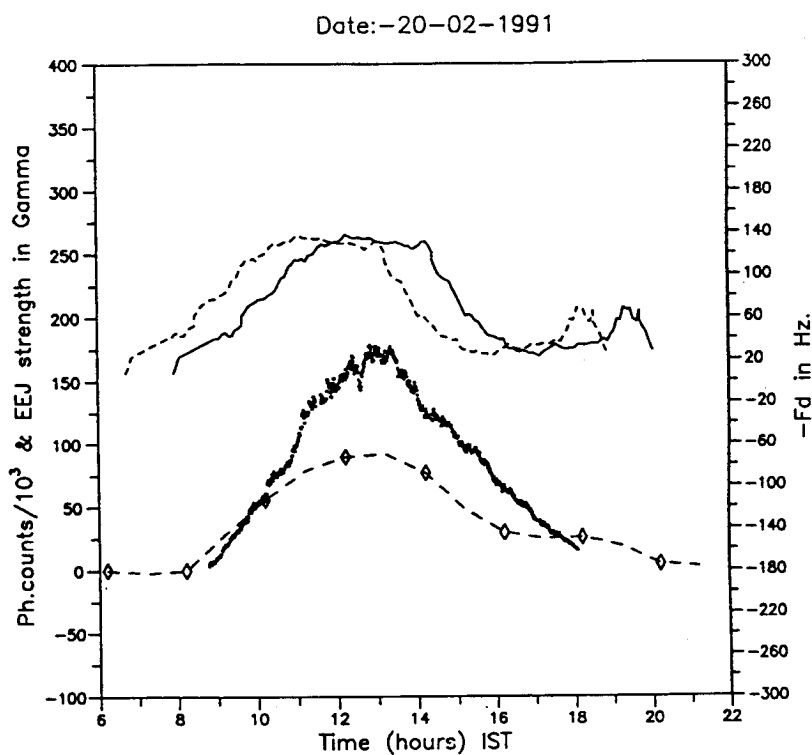
**Figure 6.10e.** Same as figure 6.10a, but, with the time shift for the Doppler frequency and the EEJ strength being 2.08 h for 14th February 1991 (mid and bottom) residual variabilities for the same day.

As the next step, the relation between the integrated strength of EEJ as obtained from the time integrated Doppler frequency/groundbased magnetic data (depending on the data availability) and the peak dayglow intensity were studied, because it is the time integrated plasma transport to the peak dayglow emission region that modulates the altitude integrated dayglow at any instance. The electrojet strength was integrated from 0800 h to the time, accounting for the delay from the time of peak dayglow intensity, i.e. if the peak of the dayglow occurred at 1300 h and time delay inferred from cross correlation analysis is 1 hour, then the representative EEJ strength is obtained by integrating it from 0800 h to 1200 h. In order to vindicate the results obtained from the optical and radar data, the ground based magnetic data for the remaining days were treated similarly to deduce the integrated electrojet strength. The rationale for doing so is supported by the earlier work of Rastogi and Patil (1986), who found very good similarities between EEJ strength ($\Delta H_{TRD}$-$\Delta H_{ABG}$) and the Doppler frequency $f_D$ measured by the VHF radar. The comparison of simultaneous magnetic data and the VHF radar data revealed a scaling factor of 1.5 for the EEJ strength to be brought on par with the VHF radar frequencies. Both these estimates are plotted in figure 6.11. The inverse trend between the EEJ strength and the peak dayglow intensity seems to be very clear.
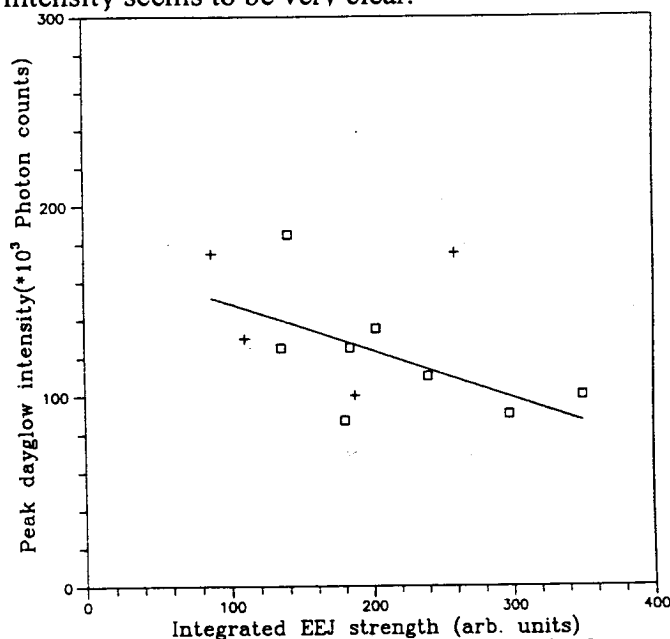


**Figure 6.11.** The negative correlation between the time integrated Doppler frequency (crosses) and the ground magnetic data (unfilled squares)

Therefore, the present study is considered to provide the *first direct experimental confirmation* for the zonal electric field as the driving agency, with the

F-region responding to its variabilities with a time delay. This time delay will be the time taken for the plasma transport from 150 km to the 220 km (peak emission altitude of 630.0 nm dayglow). Observed anti-correlation between the peak counts of 630.0 nm dayglow and electrojet strength could be explained as due to the plasma transport to higher altitudes, leaving lesser ionization at the peak emission altitude (~220 km) of 630.0nm. As the E region electric field is the primary driving force, stronger the electric field, more effective and faster would be the transport of plasma to higher altitudes.

Apart from this, on consecutive days in any epoch during quiet times, one does not envisage any significant difference in the production of ionization and therefore the day to day variability in the peak electrojet intensity would be a direct measure of the electric field variability itself. It should be noted that the temporal variations in the electrojet current intensity is essentially controlled by the electron density and the neutral winds, while the former depends on the solar zenith angle, the latter does not. As a consequence, the maximum of electrojet current intensity might show day to day variability, while in the case of dayglow, the dominant part is solar dependent and therefore the maximum occurs nearly at the same time.

Even though the dominant processes being different for EEJ and the dayglow, the observed overall correlation in the temporal variations and in the short period oscillations (residual) is striking and very important. These results are the first groundbased experimental evidence for the electrodynamical coupling of the E and F regions and plasma transport processes.

# 7# Effects of space weather related processes on thermospheric OI 630.0 nm emission over low latitudes

## 7.1# Introduction:

Space weather refers to the dynamic, highly variable conditions in the geospace environment including those on the sun, in the interplanetary medium and in the magnetosphere-ionosphere-thermosphere system. Adverse changes in the near earth space environment have significant implication in the earth's atmospheric system. Most important near earth space is solar-terrestrial environment. It has been realized that the sun, in addition to the electromagnetic radiation, is also a source of hot plasma in the form of solar wind. These plasma emissions are capable of influencing significantly the Solar-Terrestrial environment (Tinsley, 1994; Baker, 1996; Luhman, 2000). These influences generate disturbances known as 'geomagnetic storms' in the earth's magnetosphere-ionosphere system. Solar wind carries interplanetary magnetic field alongwith them. Interaction of this IMF with the earth's magnetic field gives rise to variety of processes and any deviation in these parameters significantly affects the atmospheric processes. These aspects are discussed in further section.

## 7.2# Solar wind interaction with the Earth's magnetosphere:

The Earth's magnetosphere is a vast magnetic cavity within which the earth resides. Source of the earth's dipole magnetic field is believed to be a giant dynamo, set up by the ponderous flow of matter inside the core of the earth. The dipole field, which behaves as a compressible fluid, on interaction with the solar wind, gets distorted, compressing the geomagnetic field to $\sim 10\,R_E$ in the dayside and extending it to several hundred $R_E$ in the nightside. Boundary of the earth's magnetic cavity better known as the magnetopause is in dynamical equilibrium and is highly variable depending on the dynamic pressure exerted by the solar wind. Inside the magnetopause, is the region called the magnetosphere. The highly energetic solar wind plasma being unable to directly penetrate deep into the magnetosphere through magnetopause, sweeps around the earth surrounding the cavity and drags the field along the anti-sunward side resulting in a long and active tail structure, called the

'magneto-tail'. Figure 7.1 schematically illustrates the interaction of solar wind with the earth's atmosphere.
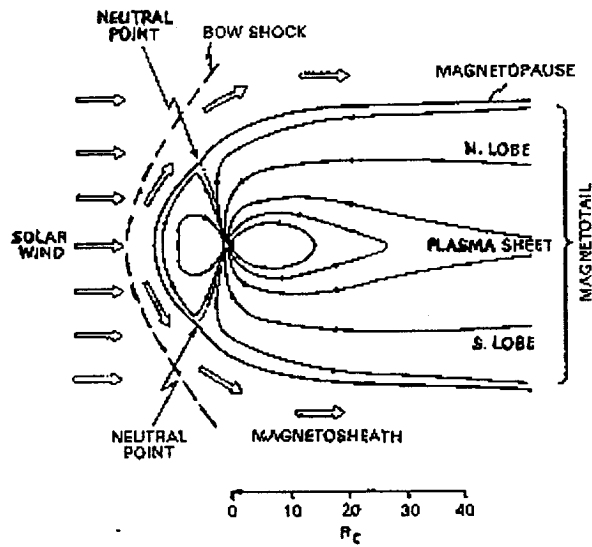


**Figure 7.1** Cross section of the geomagnetic cavity and external plasma flow, showing the magnetopause and the shock.

During the solar wind magnetospheric interaction, a preferential flow of plasma, energy and momentum takes place from the solar wind to the magnetosphere. Viscous interaction (Axford and Hines 1963) and magnetic reconnection or flux transfer events (Dungey, 1961) are the two fundamental processes for this energy transformation. Magnetic reconnection is thought to be the most effective mechanism for the energy exchange between the solar wind plasma and the terrestrial atmosphere.

Magnetic reconnection processes are essentially the magneto-hydrodynamic interaction between the magnetic field associated with the solar wind plasma and the geomagnetic field. As the incoming solar wind plasma impinges on the magnetosphere and compresses it, in some regions the solar wind associated IMF and magnetospheric field become so close that the geomagnetic field diffuses through the solar wind plasma and gets connected with the IMF (Bz component). The newly connected field lines move away from each other, joining the general solar wind flow and thus allowing the solar wind plasma to enter into the magnetosphere and to the ionosphere lower below.

These reconnected field lines are swept back into the geomagnetic tail, where a second reconnection process takes place, producing field lines, which are closed

again. This accelerates the plasma or the flux associated with the closed field lines towards earth. These processes are depicted in figure 7.2 in a simplistic way.
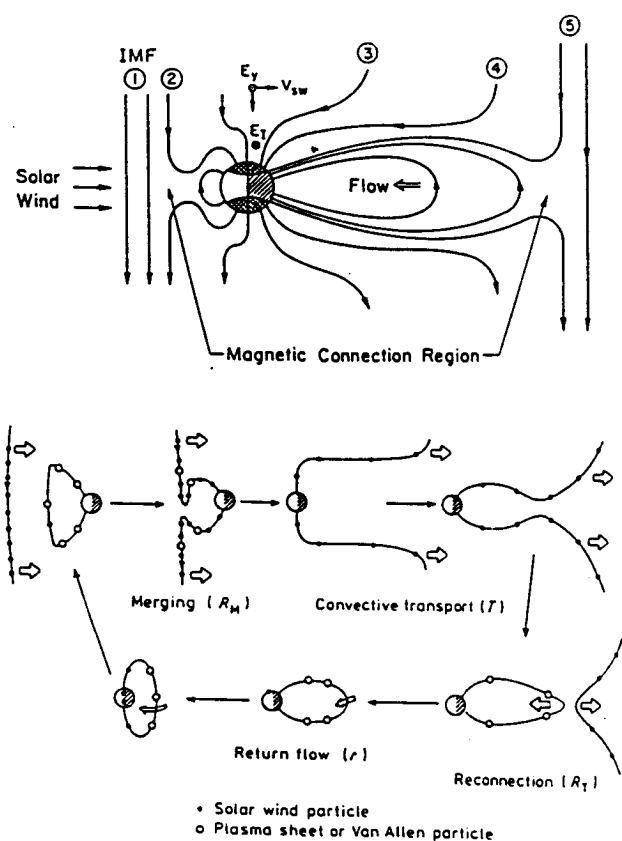


**Figure 7.2** Process of magnetic connection and reconnection (After Axford and Hines1963)

During space-weather events large amount of momentum and energy is being exchanged from solar wind plasma to the terrestrial system. Some of the energy is directly transferred to the ionosphere over polar latitudes through cusp regions and also via field aligned currents. Another major part of the solar energy, stored in the magneto-tail region in the form of kinetic and thermal plasma energy as well as magnetic field energy is transferred to inner magnetospheric ring current, direct particle precipitation and a complex web of other currents and associated processes. This additional energy, as a consequence of `space-weather' related processes modify the circulation cells and affect the terrestrial environment globally rather than locally.

# 7.3# 6th January, 1997 Space Weather Event

The 6th January, 1997 'space - weather' event has the distinction of being the first such event to have been monitored from start to finish. The magnetic cloud that left the sun in the form of a Coronal Mass Ejection (CME) was detected on 6 January at 1730 hrs UT and its evolution was monitored by Solar Heliospheric Observatory (SOHO) spacecraft, and substantial changes in the density, temperature and velocity of the solar wind were detected. The WIND spacecraft initially observed that the magnetic field within the cloud was strongly southward and turned northward within 12 hours. With the arrival of the magnetic clouds at the magnetosphere, strong reaction in the auroral zones were noticed, with the peak of the aurorae occurring on 10th January at 100 hrs UT, and with the activity spreading to as low as 55° latitude in both the hemispheres. The charged particle fluxes have been reported to be larger by a factor of 100 than the previous levels with an associated impulsive heating and sub-storm activity, alongwith moderate spacecraft changing, and intense upward flowing auroral ions. Further, on 11th January, extremely strong pressure pulses were detected in the solar wind, with plasma densities increasing by a factor of 30. As the increased pressure reached the earth, the magnetopause was compressed to $<6R_E$ (Carlowicz, 1997). The first terrestrial effect observed as a consequence of this geomagnetic storm was a communication blackout at Halley Bay station in Antarctica.

One of the most significant visible impacts of these events is the development and enhancement in the auroral activities. McEven et al. (1999) observed an active red aurora (OI 630.0 nm emission) at Eureka, Canada (88.9°N magnetic) and F.E. Smith (67.8°N mag.) at 0220 hrs. UT on 10th January which continued upto about 1500 hrs UT on 11th January. They reported the enhanced OI630.0 nm polar F region emission throughout this period (Figure 7.3).

Variation of IMF $B_z$ was compared with the onset of these emission features. When $B_z$ was positive, continuous polar arcs and when $B_z$ turned negative F layer, patches were noticed. With Meridional Scanning Photometer (MSP), they presented the dusk-dawn scans from 0230 hrs to 0730 hrs UT on 11th January, with an average of 6 min. for a plot. Significantly enhanced emission of 630.0 nm polar aurora could be clearly noticed. At around 0315 hrs and 0650 hrs UT sudden enhancement in the $H_\beta$ 428 nm emission, was observed which is indicative of more excitation due to

energetic electron. Motion of the precipitation source from dust to dawn also could be seen in Figure 7.4.
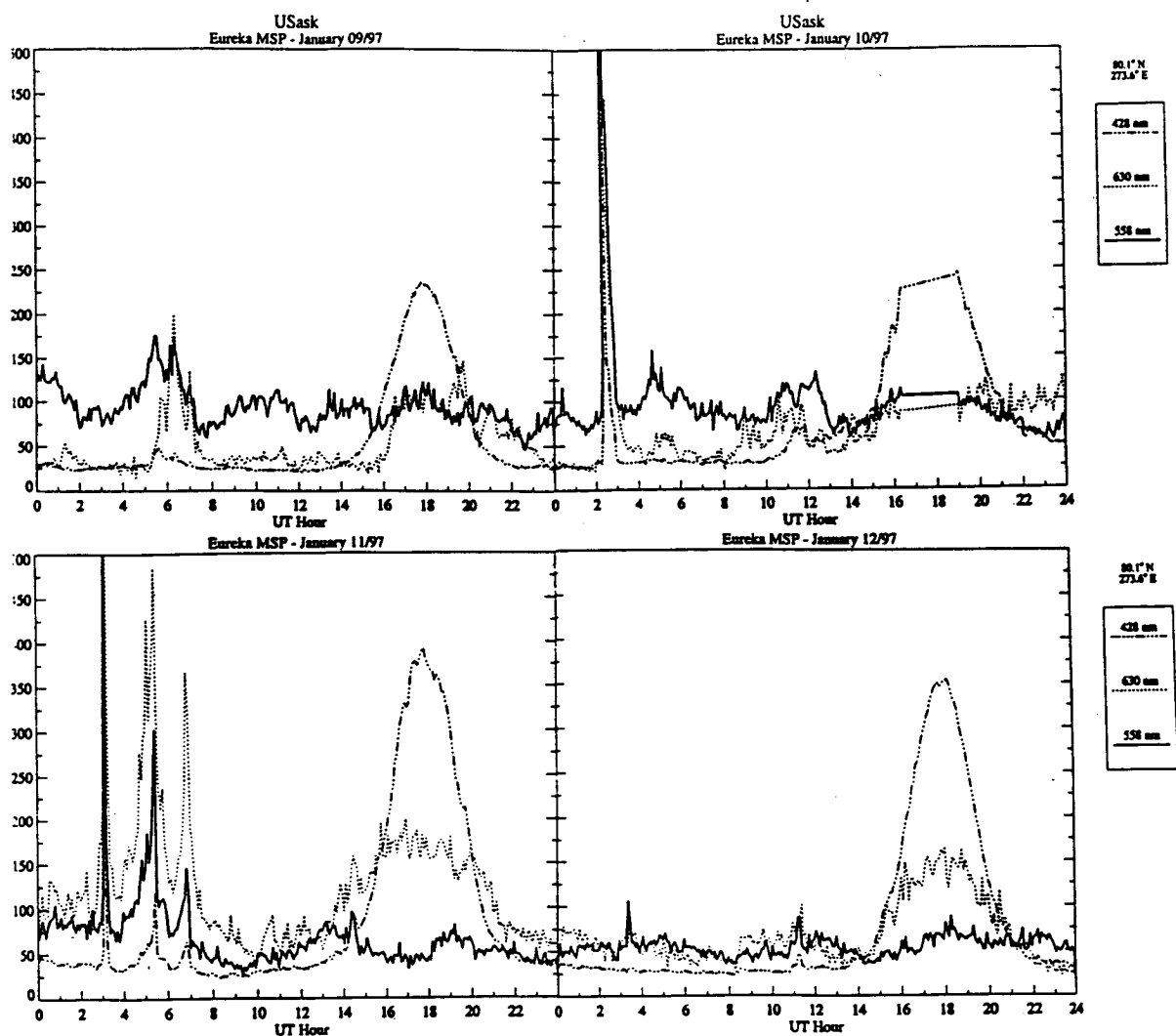


**Figure 7.3.** Observed behavior of airglow emissions during 6th January 1997 space weather event over high latitudes (After McEwen et al., 1999)

This has been one of the important reports on the response of ionosphere-thermosphere system to the 6 January, 1997 'space weather' event, using 630.0 nm emission. There had been no reports on the low latitude TIS response to this event. This gap was filled up by Sridharan et al. (1999) and this forms a part of this thesis. These results are discussed in the next section.
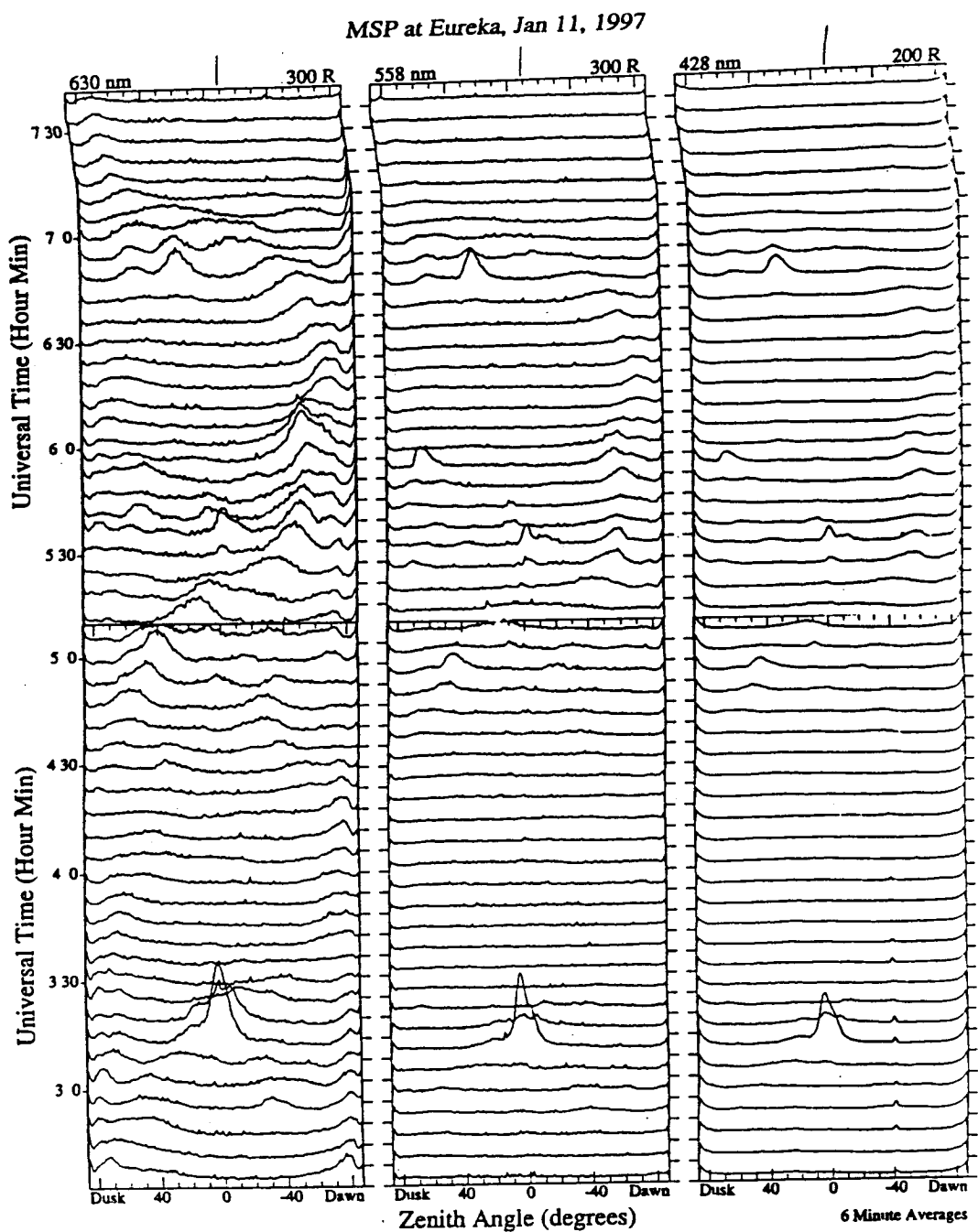
**Figure 7.4.** Observed movement of disturbances on 11th January 1997, enhanced activity in 630nm could be seen clearly (After McEwen et al, 1999)

144

## 7.4# Results from a low latitude station Mt. Abu during 6th January 1997 Space Weather Event

### 7.4.1# Observation:

The unique Dayglow Photometer (DGP) capable of retrieving very faint emission features that are < 0.5% of the background continuum was operational from Mt. Abu (24.6°N, 73.7°E) during January 1997. Details of the DGP have already been discussed in the chapter dealing with the instrumentation. Dayglow data on 630.0 nm emission variabilities were available on 9th, 11th and 12th January 1997 during this space-weather event.
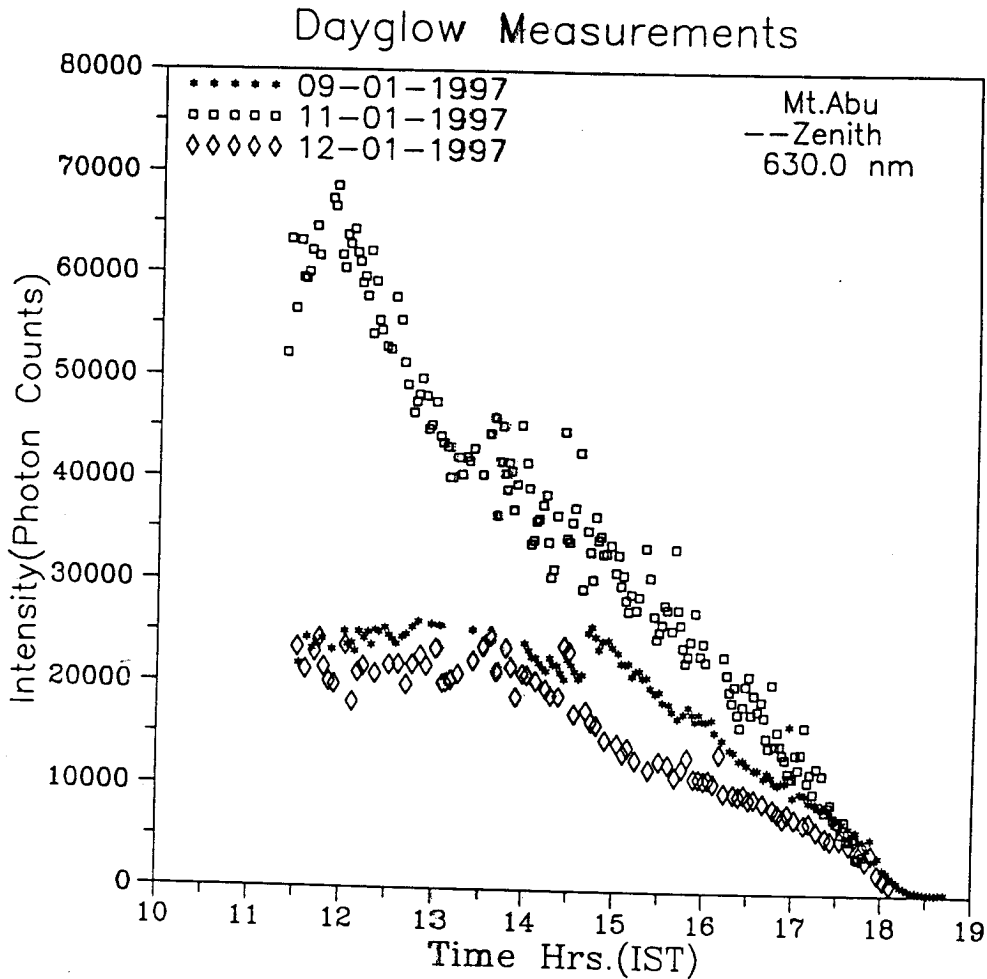


**Figure 7.5.** Behavior of 630.0 nm dayglow over Mt. Abu during 6th January 1997 space weather event. (After Sridharan et al., 1999c)

The 9th and 12th January data revealed nearly similar variations, with a flat region within the time domain of 1130 hrs to 1430 hrs, before monotonically decreasing to intensity levels below the detection limit of the DGP by 1800 hrs.

Figure 7.5 shows the relative intensity variabilities on these days. Large period (1-2 hrs.) oscillatory features could be deciphered from the intensity variations, and are typical of non-storm days. However, on $11^{th}$ January, the relative intensities were larger atleast by a factor of 2.5 around 1130 hrs and overall intensity levels were much higher than that of on $9^{th}$ and $12^{th}$ January. After 1130 hrs, intensities further decreased steeply to typical evening levels by 1700 hrs. Large-scale modulation due to wave activities can also be seen prominently in the raw data presented in the Figure 7.5.

To see the overall behaviour of thermosphere-ionosphere system, ionospheric data from Ahmedabad (23°N, 72.6°E) on those days were scrutinized. Variabilities in the ionospheric parameters (h'F and $f_oF_2$) is presented in Figure 7.6. Though prominent, large scale wave activities were present during this period, while the results reveal no such enhancements or significant changes in the electron densities similar to and commensurate with the dayglow intensities. It can be seen that the $f_oF_2$ values on $9^{th}$ and $11^{th}$ January are quite comparable and that there was a marginal increase on $12^{th}$ January when $f_oF_2$ reached ~9 MHz around noontime. Further, in order to investigate whether there had been any change in the electron densities, representative ionograms were reduced to N (h) profiles and it was found that there were no significant changes in the nature of the electron density profiles.

## 7.4.2# Discussion

The steady behaviour of the F region of the low latitude ionosphere against the highly varying behaviour of 630.0 thermospheric emission is an important result. During quiet times, it has been conclusively shown by means of coordinated measurements that the dissociative recombination which follows the charge exchange reaction of $O^+$ with $O_2$ contributes nearly 30% of the total intensity in the absolute sense and at the same time it accounts for nearly 100% of the variabilities (Sridharan et al., 1992b). The other two major contributors to the 630.0 nm dayglow are photoelectron excitation of O and photodissociation of $O_2$. These two contributors remain fairly steady throughout most of the day, except during short intervals at sunrise and sunset.
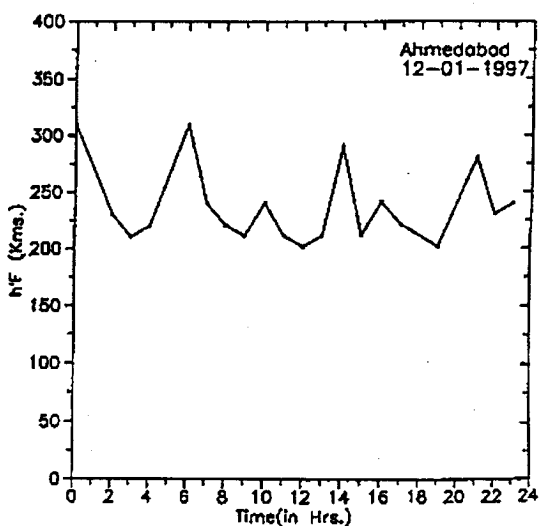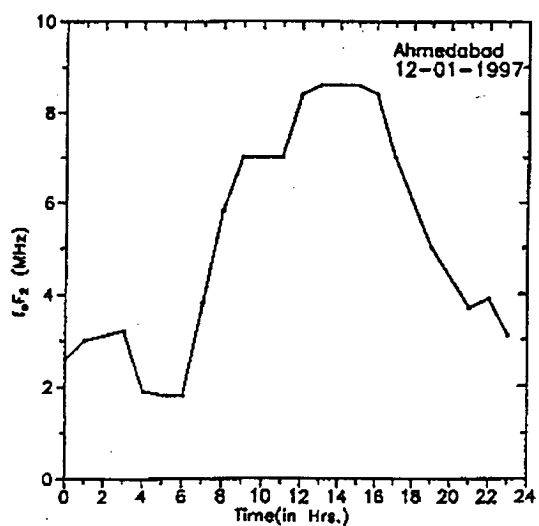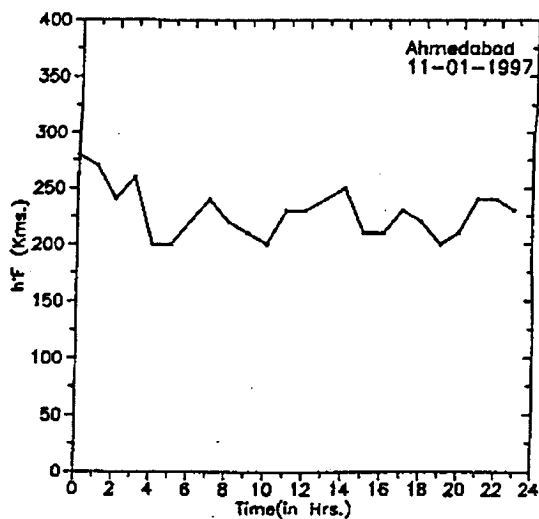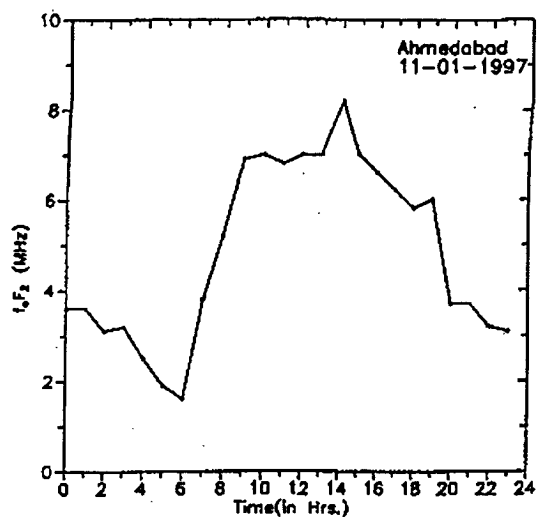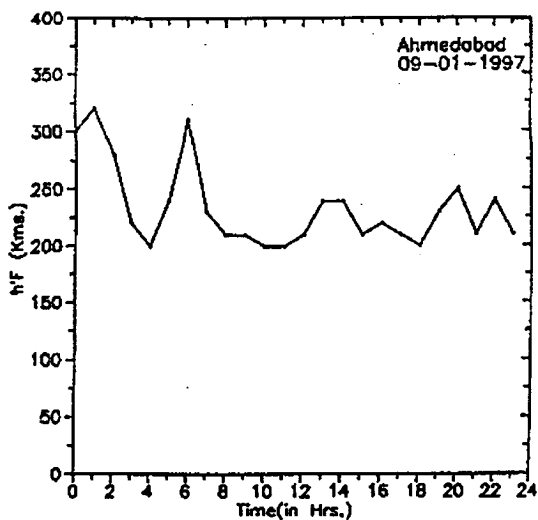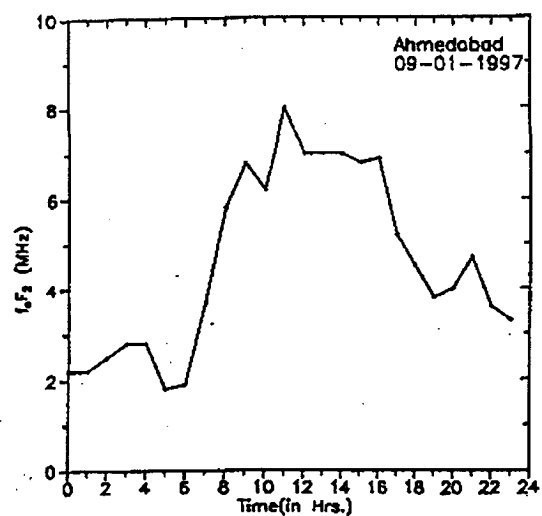
**Figure 7.6.** Variation in the ionospheric parameters over Ahmedabad during the observation period (After Sridharan et al., 1999c)

147

These initial results through a case study has been further vindicated through the results discussed in chapter 4 of this thesis wherein the control of h'F and $f_oF_2$ have been unambiguously shown and a Barbier type empirical relation has been worked out. These are applicable for normal conditions. During the `space – weather' events under discussion, the steady level of the F region electron densities during this period, indicates that there was no significant change in the UV flux. This means the contribution to OI 630.0 nm dayglow by the photoelectron excitation of O also should have remained, comparable on all the three days under consideration. Having ascertained from the ionospheric data that no such dramatic changes were present on 11th January when compared with 9th and 12th January, other possibilities need to be explored.

One of the possibilities is the energetic neutral atom precipitation, resulting from the resonant charge exchange from the Earth's ring current, which essentially acts as a store house of energy during the main phase of a geomagnetic storm only to release it into the terrestrial atmosphere during the recovery phase (Tinsley, 1981; Lui et al., 1996). The energies of the neutrals range from that of the thermal plasma in to the MeV range. The range 1-100 keV includes the carriers of the major part of the ring current energy. The energetic neutrals are created by the transfer of an electron to the ion from a thermal neutral and travel on essentially straight line trajectories with the velocity of the ion before neutralization. While most will escape into space, a fraction will lose their energy in the thermosphere. Because the neutrals have no affinity towards the magnetic field lines, they have a free to access to the equatorial thermosphere.

Figure 7.8 indicates schematically some trajectories of energetic neutral atoms. When an atom reaches the denser thermosphere, it may be re-ionized, depending on species and energy, and then be trapped by the magnetic field again. The energetic particles can go through many such cycles of being neutralized by charge exchange and ionized and getting trapped and untrapped, before most of their kinetic energy is consumed/dissipated. Usually such Energetic Neutral Atom (ENA) precipitation resulting in a low latitude aurora, is short lived lasting for an hour (Tinsley, 1986). Further, on several occasions, satellite measurements have revealed an increase in flux (by an order of magnitude) during storm time with the energy getting pumped into the atmosphere and becoming comparable to the solar EUV input (Ishimoto et al., 1992). There is invariably an ionospheric response associated with

the same. In the light of the above and observed ionospheric parameters, it appears that the present observations may not be due to ENA.

Large changes in the electron temperatures may alter the chemical reaction rates, responsible for the 630.0 nm O($^1$D) dayglow emission can be yet another possibility. However, enhancement in the dayglow intensities by a factor of 2.5 is unlikely to be due to this process. The unusual penetration of lower atmospheric tides to the upper atmosphere causing changes in the neutral composition and temperature thus affecting the chemical reactions, and finally culminating in the enhanced dayglow intensities, is yet another possibility. But, some effect must be seen in the F region electron densities as well. However, this possibility cannot be completely ruled out at this stage.
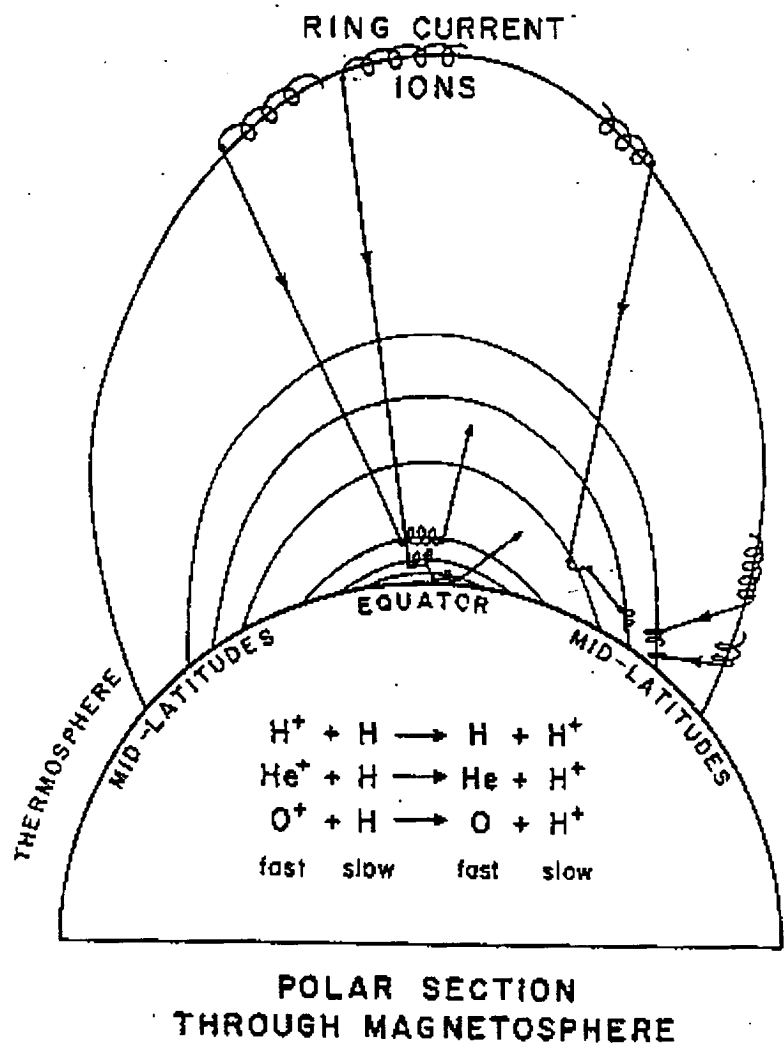


Figure 7.8. schematic of trajectories of the energetic neutral atoms

Another possibility is the enhancement in the population of thermal electron flux in the low latitude thermosphere ionosphere system. As the excitation threshold of $O(^1D)$ state is just 1.96 eV, one might feel that the electron excitation can still take place without changing the total ion density, thus satisfying one of the important observations with regard to the F region ionospheric parameters. However, there are no corroborative measurements of the thermal electron fluxes in the F region, though the 2 MeV electron flux on GOES did register a three orders of magnitude increase on $10^{th}$ January. On $11^{th}$ January, the magnetopause was compressed to $\sim 6$ $R_E$, and auroral particle precipitation was centred over $\sim 56^o$ geomagnetic latitudes. Mt. Abu, being at $17^oN$ geomagnetic is very far and is not observing enhanced airglow associated with a rare low latitude aurora, or the mid-latitude sub-visual red arc at the foot of the magnetic field lines passing through the plasma pause. Apart from these dynamical process, other process is the chemical reaction followed by dissociative recombination, involving $O^+$ ions ($[O^+]\sim Ne$ in the F region) and the $O_2$ molecules with ambient electrons, i.e.

$$O^+ + O_2 \rightarrow \quad O_2^+ + O$$
$$O_2^+ + e \rightarrow \quad O^* + O^*$$
$$O^* \rightarrow \quad O + h\nu \,(630.0 \,nm)$$
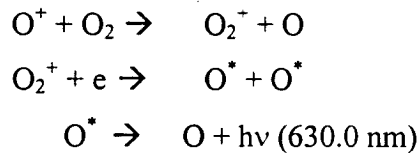
In the above scheme (Solomon and Abreu, 1989), the dayglow intensity could be enhanced either by increasing $N_e$ or by increasing the $O_2$ densities. Since there is no conspicuous change in the F region plasma densities, if at all the chemical processes cause enhanced dayglow that could only be through changes in $O_2$. Upto certain levels any enhancement in $O_2$ would result in enhanced airglow both due to dissociative recombination (DR) and photo-dissociation (PD), beyond which, due to a web of processes F region electron densities would also be altered significantly.

The composition change at any given altitude could be brought about by neutral dynamics, i.e. by means of global circulation changes associated with the geomagnetic storm and the energy inputs at high latitudes. Some of the recent results from low latitudes have clearly brought out the time-delayed response of the low latitude thermosphere-ionosphere system (Pant and Sridharan, 1998) as possibly due to the global circulation. The time delay between the energy deposition as indicated

through the recovery phase of $D_{ST}$ index and the low latitude effect (which is clearly indicated in February 97 event) has been shown to be 14-16 hr. (figure 7.9), which fits with the present observations. But usually these changes would also be reflected in the [O]/[N₂] ratio in the F region, which is known to be a direct measure of the F-region electron densities. Positive and negative ionospheric storms have generally been understood based on such composition changes.
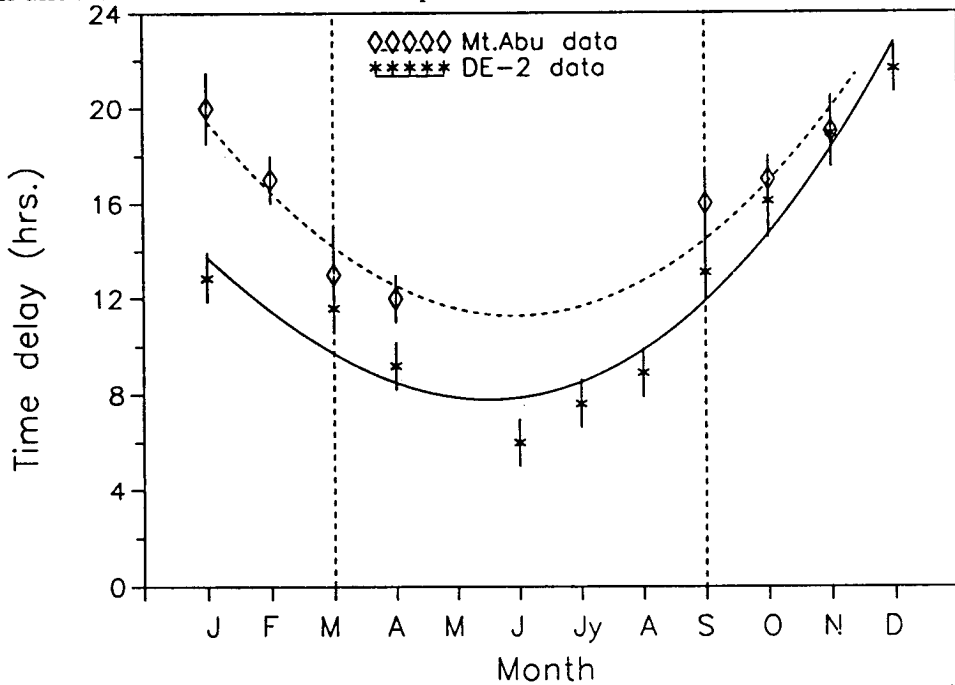


**Figure 7.9.** Time delayed response of low latitude TIS to the storm time index (Dst) using ground based and satellite observations. (After Pant and Sridharan, 1998)

Further, as mentioned earlier, there were no significant deviations in the electron densities negating the point that electron densities would have been enhanced due to the circulation and resulted in the observed airglow intensity enhancement. Thus one may need to look at further possibility.

An enhancement of O over low latitudes due to equatorward transport associated with high latitude auroral heating would result in the simultaneous enhancement of O, O₂ and N₂. This may increase photoionization which will be balanced by the faster chemical recombination due to increased molecular densities, thus maintaining nearly the same F region electron densities while increasing the airglow intensities. Another possible mechanism may be due to significant change in the turbopause altitudes, from where onwards atomic and molecular species follow their own scale height distribution. Any change in the turbopause height redistributes the atomic and molecular densities, without affecting the total content. There had

been evidences in the past for unusual change in the turbopause level. Control of turbopause level on the atomic and molecular densities is also investigated in the literature (Sridharan and Raghavarao, 1984).
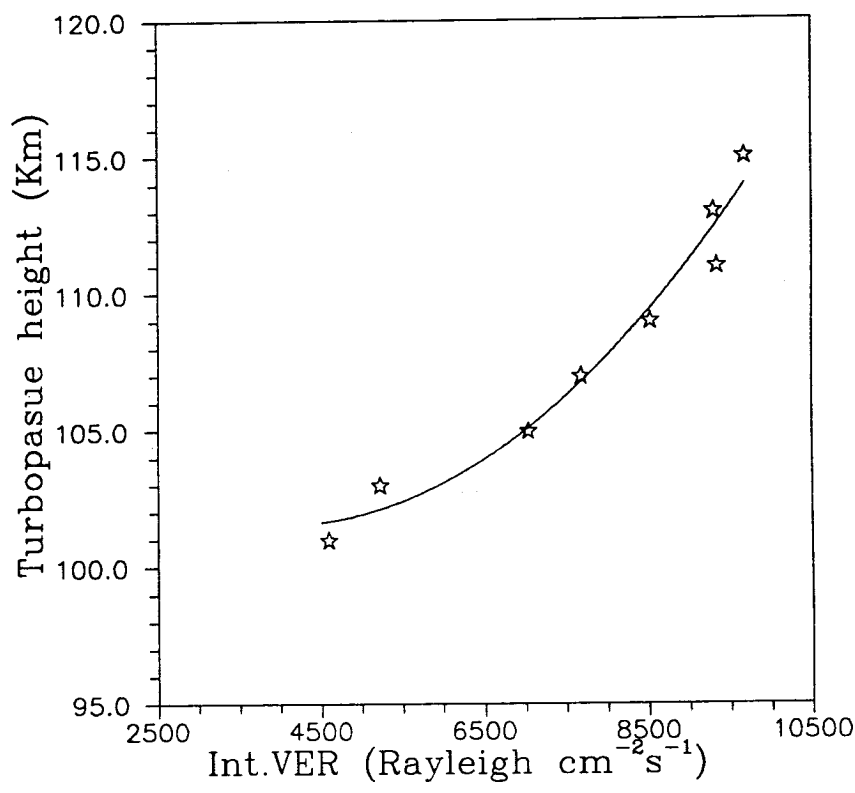


**Figure 7.10.** Effect of turbopause height variation on the 630.0 nm volume emission rates.

In the light of the above, a model simulation exercise was carried out. With change in the turbopause height from ~100 km to ~115 km, changes in molecular oxygen and atomic oxygen concentration (taken from MSIS model) was obtained. Effect of these changes on the volume emission rates of 630.0 nm emission through photodissociation and dissociative recombination, for the observed electron densities were calculated. Result of this model simulation exercise is presented in Figure 7.10. It is clear in this that a change in turbopause height from 105 km to 115 km can bring a change in the 630.0 nm dayglow by about a factor of 2. It can be suggested that this process, alongwith the contribution from other processes could be responsible for the observed feature in the dayglow during 6th January 1997 space weather event. However, there is no direct experimental verification supporting this scheme. Since

any observation on the turbopause level is extremely difficult, this suggestion turns out to be speculative, pending experimental verification. However, if this mechanism has to play a significant role, then one would expect to see the opposite behaviour in the compositions at low/equatorial latitudes and mid/high latitudes. This suggestion is based on the experimental results on the turbopause level using in-situ rocketborne composition measurements by Danilov et al., 1979 from mid latitudes and its dependence on the geomagnetic activity. They showed that turbopause height shows opposite behavior with respect to the $A_p$ values for high and low latitudes. The 'space weather' events affect the auroral extent, which may be critical to decide the relative classification of a station as mid and high latitude station. As a consequence, one would expect a different behaviour in airglow intensities too, and this demands for the measurements from equatorial - low – mid and high latitudes simultaneously.

## 7.5# Results from another low latitude station, Kolhapur

### 7.5.1# Observation:

Another space weather event of nearly similar magnitude as 6th January 1997 occurred during 6th-12th February 1997. During this period the MWDPM was operational from Kolhapur, and continuous data for this event could be monitored on 630.0 nm dayglow.
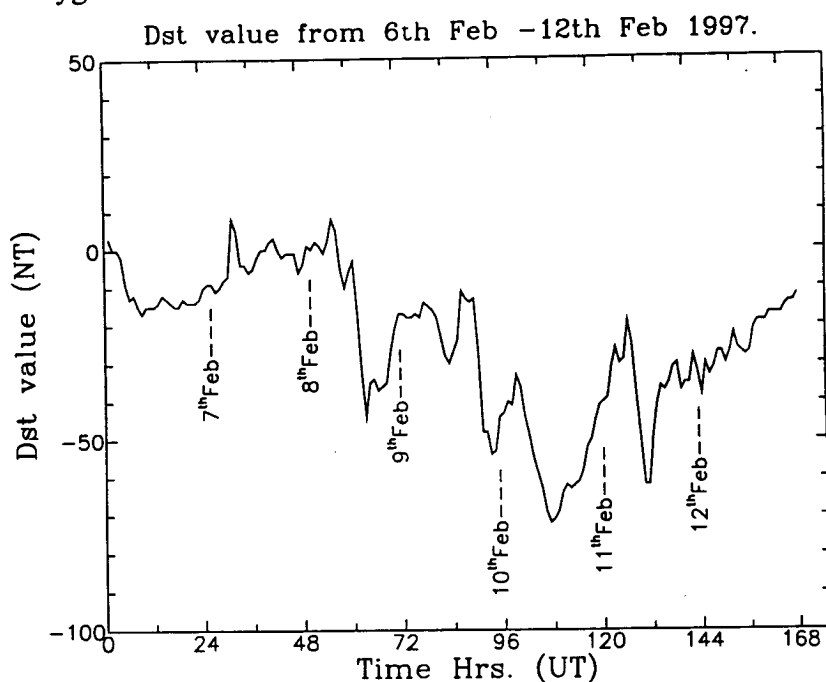


Figure 7.11. Sequence of Dst variations from 6th to 12th February 1997.

$6^{th}$ February was a quiet day with moderate activities. It was $7^{th}$ February when activities were triggered. This can be seen clearly in the development of the $D_{st}$, the storm time index which is representative of the solar wind-magnetosphere-ionosphere interaction processes. A build up in the $D_{st}$ index could be noticed. $8^{th}$ February happened to be the day from where onwards a complex web of processes started and $D_{st}$ values started decreasing sharply, with the difference in the maximum and minimum values being nearly 60 nT. On this day, particle precipitation over high latitudes were enhanced very significantly. It was an event of a recurrent storm and even on $12^{th}$ it was just recovering. The full stretch of this event is shown in Figure 7.11.
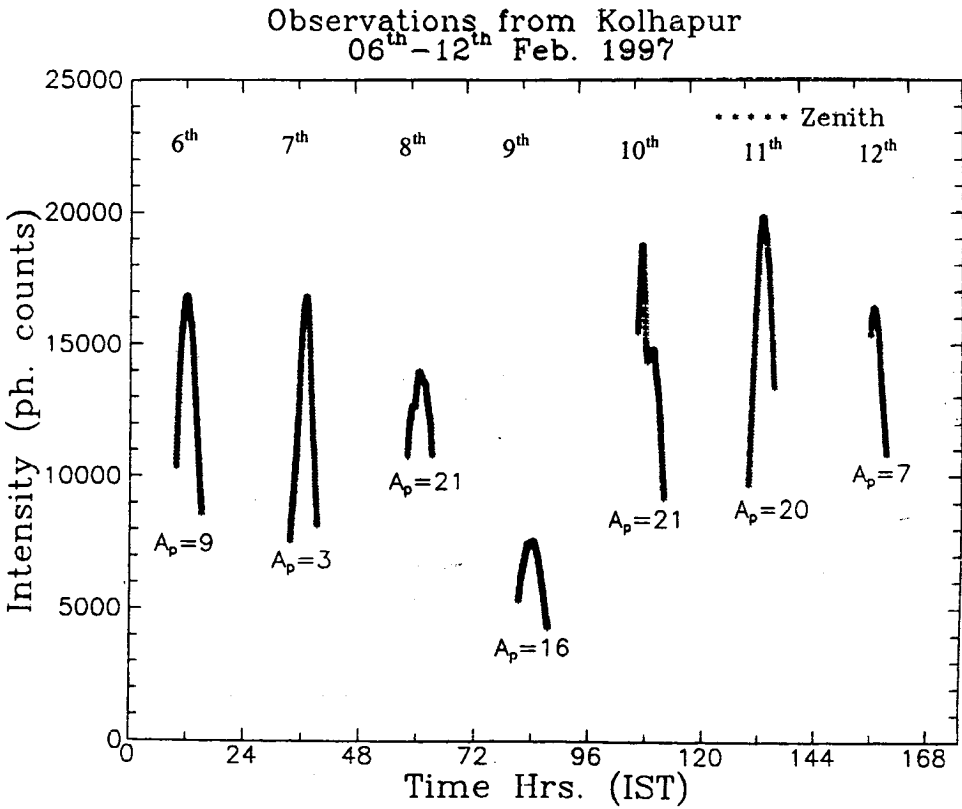


**Figure 7.12.** Full stretch of the 630.0 nm dayglow intensity variabilities from $6^{th}$-$12^{th}$ February 1997.

During this period, dayglow intensities showed very interesting features. Intensity variabilities in full stretch during this period is shown in figure7.12. Figure

7.13 represents the day to day variations in the intensities. On 6th Febuary, a double hump noontime maximum around 1100-1300 hrs was recorded in the dayglow intensity. A usual smooth decrease could be seen clearly in the Figure 7.13 in the afternoon hours. On 7th with a usual day to day variabilities in the build up of the temporal profile, intensities registered a noontime peak at about 1300 hrs. Oscillatory features too were noticed (Figure 7.13). 8th Feb. showed a different nature in the temporal variabilities. On that day prominent oscillatory features with periodicities ranging from 0.5 hr to 2 hrs are clearly visible. Peak count level was lower than the earlier days i.e. 6th and 7th February. There was a remarkable difference on 9th Feb. intensity variabilities. The intensity levels were nearly 2.5 times smaller than that of 7th February. Short period oscillatory features were enhanced and large period (>1 hr.) were subdued on that day. 10th February was another interesting day. A steep increase in the intensities at about ~1000 hrs IST was noticed. Intensities came down to normal values by 1200 hrs IST. With large oscillatory features the intensity then decreased to typical evening levels. On 11th with many oscillatory features the intensities registered a noontime peak and later decreased to the evening time level. Similarly on the 12th, with oscillatory features embedded, intensities were at their peak levels about ~1300 hrs IST and then they decreased slowly to below the detection level by the end of the day. One could clearly see that with a delay of nearly 16 hours the overall pattern of 630.0nm intensity levels follow the pattern that of the Dst variation. The observed delay fall well within the current understanding of the transport that may be carried from high latitudes to the low latitudes due to the modified global circulation cells. Day to day variabilities on these days (6th – 11th February) is shown in Figure 7.13.

## 7.5.2# Discussion:

It is interesting to note that the observed decrease in the intensities is opposite behaviour of 630.0 nm intensities when compared to the earlier observation of the intensity enhancement from Mt. Abu. Difference in these two observations was only the location i.e. Mt. Abu is $\sim24^0$ N while the Kolhapur is situated at $\sim17^0$ N, as there was not much difference in the impact and the intensity of these two events, namely the 6th Jan.1997 and 8th Feb., 1997 event.
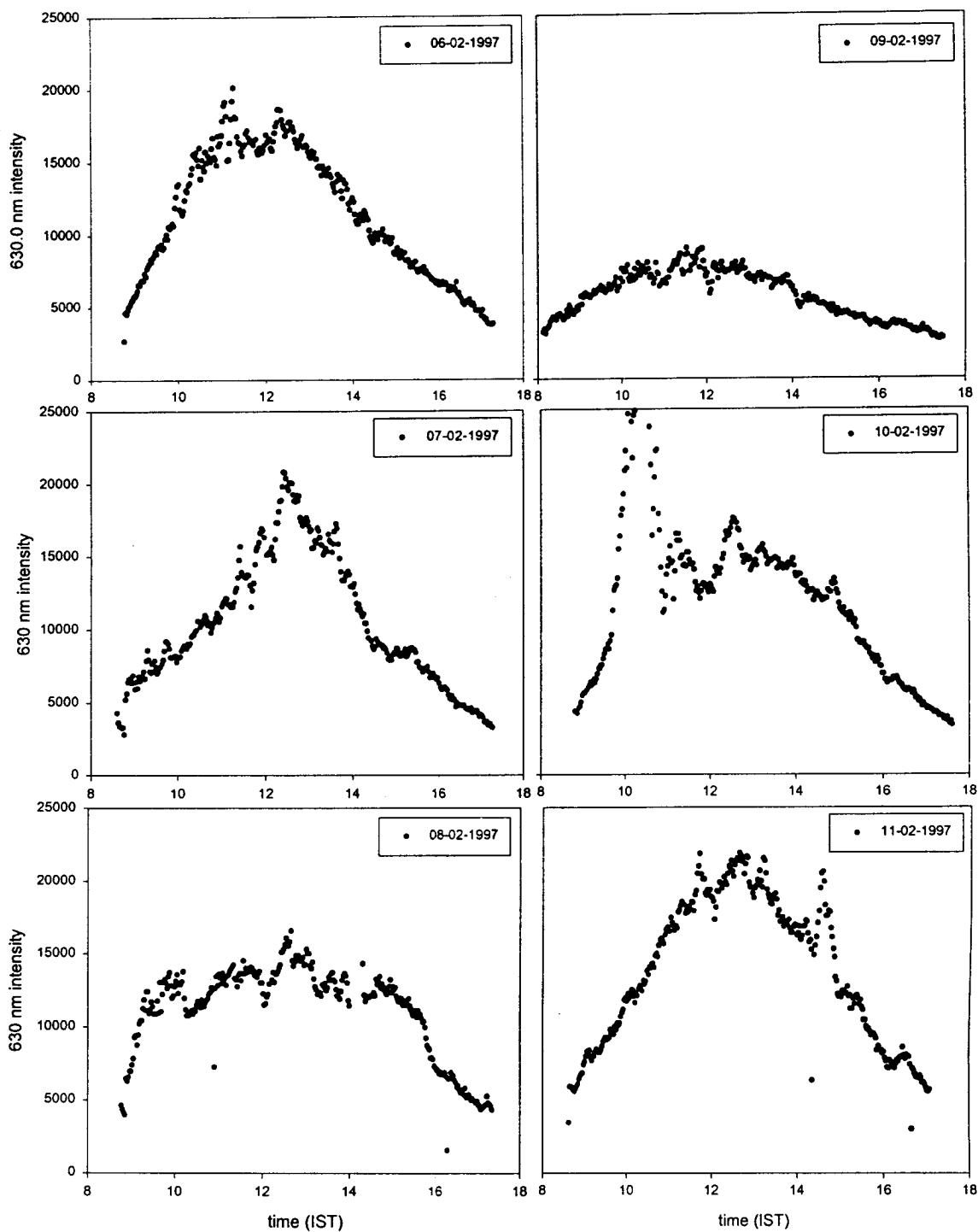
**Figure 7.13.** Intensity variabilities in the 630.0 nm dayglow during 6th-12th February 1997 space weather event.

During the February 1997 event, unfortunately the ionospheric parameters were not available, disabling the comparison between these events and so an appropriate judgement of the criticality of the position of the observational site for the response of the 630.0 nm dayglow emission to the space weather events. However, opposite nature of the 630.0 nm intensities suggest a process to be active which made the behaviour of these two locations different. It should be borne in mind that behaviour of turbopause height to these events is reported to be different in low/equatorial and mid/high latitudes. It can be suggested that it may be the variation of the turbopause height, which may play a crucial role in determining the redistribution of the atomic and molecular species during such space weather events, which ultimately affect the 630.0nm intensities on those occasions.

## 7.6# Conclusions:

Response of 630.0nm dayglow emission during space weather events presents a challenge for further study. It is shown by a model simulation that unusual changes in the turbopause height may change the 630.0 nm volume emission rates by a factor of 2-2.5. The suggestion of this process to be active, without having experimental verification looks speculative, but the opposite nature of the 630.0 nm intensities over Mt. Abu and Kolhapur suggests this process might play a crucial role in the thermosphere-ionosphere system.

# Scope for further work

Airglow monitoring is an important tool to study the atmospheric processes. They represent an average behavior of their peak height region of emission. Monitoring of multiple airglow emissions can provide a wealth of information regarding the dynamical features of the mesosphere - lower thermosphere - ionosphere system in addition to their mutual coupling. Until the present work, the simultaneous optical investigations in the mesosphere - lower thermosphere - ionosphere system were limited only to nighttime conditions. The investigation in the present thesis is one of the firsts few and is exploratory in nature. Therefore it provides clues for the future work. Some of the important aspects for future studies could be listed under following headings:

## 1# Mesospheric studies:

The MWDPM could be used to get temporal, day to day and seasonal behavior of variabilities in the daytime mesospheric temperatures, which is not yet known. These variabilities could provide the clues to the presence of waves and tidal modes, effects of which are of great importance in the coupling of atmospheric regions. Simultaneous neutral wind parameters could suggest about the dynamical processes occurring at those altitudes.

Round the clock variabilities in the mesospheric temperatures can provide important information regarding short as well as long period dynamical variations. Consistent presence of particular periods in the variabilities may indicate towards a preferable wave modes as agent for the lower and upper atmosphere coupling.

The mesopause, not being far from the dynamo region would have significant dynamical effects higher above. Temperature variations may alter the scale height distribution higher above changing the electron neutral and ion neutral collision frequencies resulting in changes in the conductivity profile and hence altering the electrodynamical parameters. These aspects are very important and may provide answers to many unexplained features in the electrodynamical processes like EEJ, over the equatorial latitudes.

## 2# Thermosphere – Ionosphere studies:

It is shown in the present work that Barbier type relation linking the ionospheric parameters with the dayglow 630.0 nm thermospheric emission intensity is valid over Waltair. Applicability of the same relation from other latitudes is an important aspect remaining for the future studies. Verification of the same for other latitudes may make the formula to be valid globally and would be crucial for the modeling studies.

Round the clock variabilities with all directional mirror scanning of the DNP may provide a clue about the persistent wave periods and their preferable direction from event to event.

Space weather related process and their effects over low and equatorial latitudes have been an open question so far, due to lack of a sufficient database. Differential behavior of 630.0nm dayglow during January 97 (from Mt. Abu) and February 1997 (from Kolhapur) space weather events demands simultaneous multi-instrument investigations and detailed verification. It also indicates the critical behavior of Mt. Abu as low latitude station from one event to other. A chain of photometers or ideally satellite borne photometer along with complementary ground based experiments is expected to provide important clues towards the response of the low and equatorial latitudes to space - weather events.

It has been shown that 630.0nm thermospheric emission is a good indicator of neutral and electrodynamical processes. Highly variable atmospheric conditions make these processes to vary with time. Effects of such varying geophysical processes, i.e. EIA, EEJ and CEJ on the 630.0 nm dayglow are yet to be investigated in detail in the future studies.

3# Simultaneous multiple airglow monitoring will provide important information on the propagation characteristics of waves and tides. These, along with the wind parameters and temperature would give a comprehensive picture of the large-scale dynamics of the mesosphere lower thermosphere.

4# Simultaneous investigation on 630.0nm and 557.7nm emissions revealed the significant thermospheric contributions in the latter. Occasional differential

behavior in both indicates towards a strong role of dynamics over the chemical processes. These aspects are not understood and call for a detailed study.

Apart from the above, response of dayglow emissions to the varying geophysical conditions is another challenge in near future that needs further investigations.

In short, the present investigation is believed to have opened up new horizons in the mesosphere – lower thermosphere – ionosphere coupling studies.

# References:

1) Aarons J., 'The longitudinal morphology of equatorial F layer irregularities relevant to their occurrence', Space Sci. Rev., 63, 209, 1993.

2) Abdu M.A., I. S. Batista, I. J. Kantor and J. H. A. Sobral, 'Gravity wave induced ionization layer in the night F region over Cachoera Paulista (22°S, 45°W)', J. Atmos. Terr. Phys., 44, 9, 759, 1982.

3) Abdu M. A., H. H. A. Sobaral, E. R. De Paula and I. S. Batista, 'Magnetospheric disturbance effects on the EIA: an overview', J. Atmos. Terr. Phys, 53, 757, 1991.

4) Abdu M. A., 'Major phenomena of the equatorial ionosphere – thermosphere system under disturbed conditions', J. Atmos. Sol. Terr. Phys., 59, 13, 1505, 1997.

5) Abdu, M.A., 'Coupling and energetics of the equatorial ionosphere - thermosphere system :advances during STEP period', J. Atmos. Sol. Terr. Phys., 61, 153, 1999.

6) Anandarao B. G., J. N. Desai, M. Giles, G. Martelli, R. Raghavarao and P. Rothwell, ' ' J. Atmos. Terr. Phys., 39, 927, 1977.

7) Anandarao B. G. and R. Raghavarao, ' Structural changes in the currents and fields of the equatorial electrojet due to zonal and meridional winds', J. Geophys. Res., 92, 2514, 1987.

8) Anderson D. N., 'A theoretical study of the ionospheric F region equatorial anomaly- II, results in the American and Asian sectors', Planet. Sp. Sci., 21, 421, 1973.

9) Anderson D. N., 'Modeling the ambient low latitude F region ionosphere', J. Atmos. Terr. Phys., 43, 753, 1981.

10) Appleton E. V., 1946, 'Two anomalies in the ionosphere', Nature, 157, 691.

11) Axford W. I. and Hines C. O., 'A unifying theory of high latitude geophysical phenomena and storms', Can. J. Phys., 39, 1433, 1963.

12) Baker D. N., 'Solar wind- magnetosphere drivers of space-weather', J. Atmos. Sol. Terr. Phys., 58, 14, 1509, 1996.

13) Barbier D., 'Recherches sur la raie 6300 de la luminescence atmospherique nocturne', Ann. Geophys., 15, 179, 1959.

14) Barmore F. E., ' High resolution observations of the 6300 $A^0$ oxygen line in the day airglow', Planet. Sp. Sci., 25, 185 , 1977.

15) Barth C. A. and Hilderbrandt A. F., 'The 5577 A airglow emission mechanism.', J. Geophys. Res.,66, 985 , 1961.

16) Barth C. A., 'three body reactions', Annales Geophysicae, 5, 329, 1964.

17) Bates D. R., 'The green light of the night sky', Panet. Sp. Sci., 29, 1061, 1981.

18) Bates D. R. and Dalgarno, J. Atmos. Terr. Phys., 26, 897, 1954.

19) Bates D. R. and Zipf E. C., 'The $O(^1S)$ quqntum yield from $O_2^+$ dissociative recombination', Planet. Sp. Sci., 28, 1081, 1980.

20) Behnke R. A. and R. M. Harper, 'Vector measurements of F region ion transport at Arecibo', J. Geophys. Res., 78, 8222, 1973.

21) Bens A. R., Cogger L. L., Shepherd G. G., 'Upper atmospheric temperatures from Doppler line widths', III, Planet. Sp. Sci., 13, 551 , 1965.

22) Blamont J. C., Donahue T. M., 'The dayglow of sodium D lines', J. Geophys. Res., 66, 1407, 1961.

23) Blamont J. C., Donahue T. M., 'Sodium dayglow: observation and interpretation of a large diurnal variation', J. Geophys. Res., 69, 4093, 1964.

24) Booker H. G., 'The role of acoustic gravity waves in the generation of spread and ionospheric scintillations', J. Atmos. Terr. Phys., 41, 501, 1979.

25) Brandt J. C., 'Oxygen red lined in the airglow III the dayglow', Astrophys. J., 128, 718, 1958.

26) Briggs B. H., 'The analysis of spaced sensor records by correlation technique', MAP Handbook, 13, 166, 1984.

27) Burrows K., T. S. G. Sastry, S. Sampath, J. D. Stolarik and M. J. Usher, 'The storm time equatorial electrojet', J. Atmos. Terr. Phys., 39, 125, 1977.

28) Cahill L. J. Jr., 'Investigation of the equatorial electrojet by rocket magnetometer', J. Geophys. Res., 64, 489, 1959.

29) Carlowicz M., 'Satellite scientists track storm from sun to surface', EOS, 78, 49 - 50, 1997.

30) Chandra S., E .I. Reed, B. E. Troy and J. E. Blamont, 'Equatorial airglow and ionospheric geomagnetic anomaly', J. Geophys. Res., 78, 4630, 1973.

31) Chandra S. and J. R. Herman, 'F region ionization and heating during magnetic storms', Planet. Sp. Sci., 17, 841, 1969.

32) Chanin M. L. and A. Hauchecorne, 'Lidar studies of the temperature and density using Rayleigh scattering', MAP Handbook, 13, 87, 1984.

33) Clemasha B.R., H. Takahashi and P.P. Batista, `Mesopause temperature at $23^0$ S', J. Geophys. Res., 95, D6, 7677, 1990.

34) Cocks T. D. and F. Jaka, `Daytime thermospheric temperatures, wind velocities and emission intensities derived from ground based observations of the OI 630.0 nm airglow line profile', J. Atmos. Terr. Phys., 41, 409, 1979.

35) Cogger L. L. and J. S. Murphee, ` The latitudinal and seasonal variation of atomic oxygen deduced from observations of E region OI 557.7 nm airglow', Space Research, XX, 115, 1980.

36) Cogger L. L., R. D. Elphinstone and J. S.Murphee, `Temporal and latitudinal 5577 A airglow variation', Can. J. Phys., 59, 1296, 1981.

37) Cogger L. L., R. D. Elphinstone and D. H. Giers.,`Wave characteristics obtained from OH rotational temperatures and 557.7 nm airglow intensities', J. Atmos. Terr. Phys., 50, 943 – 949, 1988.

38) Croom S., A. Robins and J. O. Thomas, `Two anomalies in the behaviour of the F2 layer of the ionosphere', Nature, 184, 2003, 1959.

39) Danilov A.D., U. A. Kalagin and A. Pokhunkov, `Variation of the turbopause level in the polar regions', Space Research, XIX, 173, 1979.

40) Davis T. N., K. Burrows and J. D. Stolarik, 'A latitudinal survey of the equatorial electrojet with rocket borne magnetometers', J. Geophys. Res., 72, 1845, 1967.

41) Desai J. N., B. G. Anandarao and R. Raghavarao, 'Photometer for detection of Lithium release in daytime', App. Opt., 18, 420, 1979.

42) Dewan E. M. and R. H. Picard, "Mesospheric Bores", J. Geophy. Res., 103, 6295, 1998.

43) Donahue T. M., R. Guenther and R. J. Thomas, `Distribution of atomic oxygen in the upper atmosphere deduced from OGO 6 airglow observations', J. Geophys. Res., 78, 6662, 1973.

44) Dungey J. W., 'Interplanetary magnetic field and the auroral zones', Phys. Rev. Lett., 6, 47, 1961.

45) Elphinstone R. D., L. L. Cogger, J. S. Murphee, G. S. N. Murty and J. W. Meriwether Jr.,` The analysis of hydroxyl rotational temperatures to characterize moving thermal structure near the mesopause', J. Atmos. Terr. Phys., 50, 657, 1988.

46) Farley D. T., E. Bonelli, B. G. Fejer and M. F. Larsen, 'The prereversal enhancement of the zonal electric fields in the equatorial ionosphere', J. Geophys. Res., 91, 13723, 1986.

47) Feldman P. D., J. P. Doering and E. C. Zipf, 'Excitation of O(1S) atoms in the day airglow', J. Geophys. Res., 76, 3087, 1971.

48) Fesen C. G., 'Simulation of the low latitude midnight temperature maximum', J. Geophys. Res., 101, 26063, 1996.

49) Forbes J. M., 'The equatorial electrojet', Rev. Geophys. And Sp. Phys., 19, 469, 1981.

50) Forbes J. M., D. Fritts, R. Garcia and A. Richmond, 'Lower thermosphere coupling', WITS Handbook, Ed. C. H. Liu and B. Edwards, 1, 154, 1988.

51) Fricke F. H. and U. Von Zahn, 'Mesopause temperatures derived from probing the hyperfine structure of the $D_2$ resonance line of Sodium by Lidar', J. Atmos. Sol. Terr. Phys., 47, 5, 499, 1985.

52) Fritts D. C., 'Gravity wave saturation in the middle atmosphere : A review of theory and observations', Rev. Geophys. Sp. Phys., 22, 3, 275, 1984.

53) Fukuyama K., 'Airglow variations and dynamics in the lower thermosphere and upper mesosphere – II. Seasonal and long term variations', J. Atmos. Terr. Phys., 39, 1, 1976.

54) Fukuyama K., ' Airglow variations and dynamics in the lower thermosphere and upper mesosphere – III. Variations during stratospheric warming events', J. Atmos. Terr. Phys., 39, 317, 1977.

55) Fuller – Rowell T. J. and D. Rees, 'A three dimensional time dependent global model of thermosphere', J. Atmos. Sci., 37, 2545, 1980.

56) Fuller – Rowell T. J., M. J. Codrescu, R. J. Moffet and S. Quegan, 'Response of the thermosphere and ionosphere to geomagnetic storms', J. Geophys. Res., 99, 3893, 1994.

57) Fuller - Rowell T. J., 'The dynamics of the lower thermosphere', The upper and lower thermosphere: A review of experiment and theory, Geophysical monograph –87, 23 – 36, 1995, edited by Johnson and Killeen.

58) Gadsden M., T. M. Donahue and J. C. Blamont, 'On the measurement of sodium dayglow emission by means of a Zeeman Photometer', J. Geophys. Res., 71, 5047, 1966.

59) Garcia, R.R. and S. Solomon, 'The effect of breaking gravity waves on the dynamics and chemical composition of the mesosphere and lower thermosphere', J. Geophys. Res., 90, 20, 3850, 1985.

60) Golden S. A., 'Kinetic parameters for OH nightglow modeling consistent with recent laboratory measurements', J. Geophys. Res., 78, 7023, 1997.

61) Goldberg R. A., C. H. Jackman, D. N. Baker and F. A. Herrero,'Change in the concentration of $O_3$ and OH during a high relativistic electron precipitation event',The upper mesosphere and lower thermosphere: A review of experiment and theory, Geophysical monograph – 87, ed. Johnson and Killeen, 215, 1995.

62) Gouin P. and P. N. Mayaud, 'A propos de l'existence possible d'un <<contre electrojet>> aux latitudes magnetiques equatoriales', Ann. Geophys., 23, 41,1967.

63) Greenspan J. A., 'Synoptic description of the 6300 A nightglow near $78^0$ West longitudes', J. Atmos. Terr. Phys., 28, 739, 1966.

64) Guberman S. L., ' The production of $O(^1S)$ from dissociative recombination of $O_2^+$', Nature, 327, 408, 1987.

65) Haerendel G., 'Theory of equatorial spread F', report: Max Planck Inst. Fur Phys. Und Astrophys., Garching, West Germany, 1974.

66) Hargreaves J. K., 'The Solar Terrestrial environment', Cambridge atmosphere and space Science series –5, 1995.

67) Hays P. B. and W. E. Sharp, 'Twilight airglow: photoelectrons and OI 5577 A radiation', J. Geophys. Res., 78, 1153, 1973.

68) Hays P. B., D. W. Rusch, R. G. Roble and J. C. G. Walker, 'The OI 6300 $A^0$ airglow', Rev. Geophys., 16, 225 , 1978.

69) Hecht J. H., S. K. Ramsay Howat, R. L. Walterscheid and J. R. Isler,'Observations of variations in airglow emissions during ALOHA –93', Geophys. Res. Lett., 22, 20, 2817, 1995.

70) Hedin A. E. and H. G. Mayr, 'Magnetic control of the near equatorial neutral atmosphere', J. Geophys. Res., 1669, 1973.

71) Hedin A. E., 'Empirical model of global thermospheric temperature and composition based on data from OGO 6 quadrupole mass spectrometer', J. Geophys. Res., 79, 215, 1974.

72) Hedin A. E., H. G. Mayr, C. A. Reber, N. W. Spencer and G. R. Carrignan, 'MSIS- 86 thermospheric model', J. Geophys. Res., 4649, 1987.

73) Hedin A. E., `Extention of the MSIS thermosphere model into the middle and lower atmosphere', J. Geophys. Res., 96, 1159, 1991.

74) Heelis R. A., P. C. Kendall, R. J. Moffett, D. W. Windle and H. Rishbeth, `Electrical coupling of the E and F regions and its effect on the F region drifts and winds', Planet. Sp. Sci., 22, 743, 1974.

75) Hernandez G., `The signature profiles of O($^1$S) in the airglow', Planet. Sp. Sci., 19, 1745, 1971.

76) Herraro F. A. and N. W. Spencer, 'On the horizontal distribution of the equatorial thermospheric midnight temperature maximum and its seasonal variation', Geophys. Res. Lett., 9, 1179, 1982.

77) Herraro F. A., H. G. Mayr and N. W. Spencer, 'Latitudinal (seasonal) variations in the thermospheric midnight temperature maximum: A tidal analysis', J. Geophys. Res., 88, 7255, 1983.

78) Hines, C.O., 'Internal atmospheric gravity waves at ionospheric heights', Can. J. Phys., 38, 1441, 1960.

79) Hocking W. K., `Dynamical coupling processes between the middle atmosphere and upper atmosphere', J. Atmos. Terr. Phys., 58, 6, 735, 1996.

80) Huang T. Y., H. Hur, T. F. Tuan, X. Li, E. M. Dewan and R. H. Picard, `Sudeen narrow temperature inversion layer formation in ALOHA -93, as a critical layer interaction phenomenon', J. Geophys. Res., 103, 27, 6323, 1998.

81) Huang, Y. N. and K. Cheng, 'Ionospheric disturbances at the Equatorial Anomaly crest region during the March 1989 magnetic storm, J. Geophys. Res., 96, A8, 13953, 1991.

82) Ishimoto M., C. J. Romick and C. I. Meng, `Energy distribution of energetic O+ precipitation into the atmosphere', J. Geophys. Res., 97, 8619, 1992.

83) Jarret A. H. and M. J. Hoey, 'A ground level photographic observation of the day airglow emission of atomic oxygen at 6300A', Planet Sp. Sci., II, 1251, 1963.

84) Kane R.P., `Geomagnetic field variations', Sp. Sci. Rev., 18, 413, 1976.

85) Kane R. P. and R. G. Rastogi, 'Some characteristics of the equatorial electrojet in Ethiopia (East Africa)', Ind. J. Radio Sp. Phys., 6, 85, 1977.

86) Kelley M. C., `The Earth's ionosphere: Plasma physics and electrodynamics', Academic Press Inc., 1989.

87) Killeen, T.L. and Johnson, R.M., 'Upper atmospheric waves, turbulence and winds: importance for mesospheric and thermospheric studies', Rev. Geophys. Sp. Phys., July, 737, 1995.

88) Krishnamurthy B. V. and K. Sengupta, 'Disappearance of $E_S$ associated with magnetic field depressions', Planet. Sp. Sci., 20, 371, 1972.

89) Kulkarni P. V., 'Rocket study of 5577 A OI emission at night over the magnetic equator', 81, 3740, 1976.

90) Lindzen, R.S., 'Turbulence and strees owing to gravity wave and tidal breakdown', J. Geophys. Res., 86, C10, 9707, 1981.

91) Liu C. H. and M. Hagan, 'Local heating'cooling of the mesosphere due to gravity wave and tidal coupling', Geophys. Res. Lett., 25, 15, 2941, 1998.

92) Llewellyn E. J., B. H. Long and B. H. Solheim, 'The quenching of OH* in the atmosphere', Planet. Sp. Sci., 26, 525, 1978.

93) Lopez - Moreno J.J., R. Rodrigo, F. Moreno, M. Lopez- Purtas and A. Molina, "distribution of vibrationally excited states of atmospheric hdroxyl at levels $v = 2$ to $v= 7$", Planet. Sp. Sci., 35, 1029, 1987.

94) Lowe R. P., C. M. LeBlanc and K. L. Gilbert, 'WINDII/ UARS observation of twilight behaviour of the hydroxyl airglow at mid latitude equinox', J. Atmos. Terr. Phys., 58, 10, 1863, 1996.

95) Lowrence G. M. and M. J. McEwan, 'Production of $O(^1S)$ from photodissociation of $O_2$', J. Geophys. Res., 78, 8314, 1973.

96) Luhman J., 'Space - Weather: physics and forcasts', Physics world, July, 31, 2000.

97) Lui A.T. Y., J. Williams, E. C. Roelof, R. W. McEntire, G. Mitchel, Geophys. Res. Lett., 23, 2641, 1996.

98) Lyons A. J. and L. Thomas, 'The $F_2$ region equatorial anomaly in the African, American and East Asian sectors during sunspot maximum', J. Atmos. Terr. Phys., 25, 373, 1963.

99) Martyn D. F., 'Atmospheric tides in the ionosphere, I. Solar tides in the $F_2$ region', Proc. Roy. Soc., London, A 189, 241, 1947.

100)   Maruyama T. and N. Matuura, 'Longitudinal variability of the annual changes in activity of equatorial spread F and plasma bubles', J. Geophys. Res., 89, 10903, 1984.

101) Mayaud P. N., 'The equatorial counter electrojet- A review of its geomagnetic aspects', J. Atmos. Terr. Phys., 39, 1055, 1977.

102) Maynard N. C., 'Measurements of ionospheric currents of the coast of Peru', J. Geophys. Res., 72, 1863, 1967.

103) Mayr H. G., I. Harris, N. W. Spencer, A. E. Hedin, L. E. Wharton, H. S. Portor, C. G. Walker and H. C. Carlson, 'Tides and midnight temperature anomaly in the thermosphere', Geophys. Res. Lett.,6, 447, 1979.

104) Mc Dade I.C., E. J. Llewellyn, D.P. Murtagh and R.G.H. Greer, 'ETON 5: Simultaneous rocket measurements of the OH meinel $\delta v = 2$ and (8,3) band emission profiles in the nightglow', Planet. Sp. Sci., 35, 1137, 1987.

105) McDade I. C., and E. J. Llewellyn, 'The excitation of $O(^1S)$ by O2 bands in the nightglow', Can. J. Phys., 64, 1626 , 1986.

106) McDade I. C., E. J. Llewellyn, R.G. H. Greer, G. Witt, ' Altitude dependence of the vibrational distribution of O2 in the nightglow and the possible effects of vibrational excitation in the formation of $O(^1S)$', Can. J. Phys., 62, 780, 1984.

107) McEwen D. J., D. P. Stelle, F. Crentzberg, D. D. Wallis, 'The ionospheric response to the CME event of 6 –11 January 1997', J. Atmos. Sol. Terr. Phys., 61, 223, 1999.

108) Majumdar Neeta and P. V. Kulkarni, 'Measurements of neutral temperature in 80 - 90 Km region with OH nightglow emission', Ind. J. Rad. Sp. Phys., 193, 1979.

109) Mendillo M. and J. Baumgardner, 'Airglow characteristics of equatorial plasma depletions', J. Geophys. Res., 87, 7641, 1982.

110) Mendillo M., J. Baumgardner, X. Pai and P. J. Sultan, 'Onset conditions for Equatorial spread F', J. Geophys. Res., 97, 13865, 1992.

111) Melo S., R. P. Lowe and J. P. Russell, 'Double peaked hydroxyl airglow profiles observed from WINDII/UARS', J. Geophys. Res., 105, 12397, 2000.

112) Meriwether J. W. Jr., 'High latitude airglow observations of correlated short term fluctuations in the hydroxyl meinel 8-3 band intensity and rotational temperature', Planet. Sp. Sci., 23, 1211, 1975.

113) Meriwether J. W., M. A. Biondi and D. N. Anderson, 'Equatorial airglow depletions induced by thermospheric winds', Geophys. Res. Lett., 12, 487, 1985.

114) Meriwether J. W., M. A. Biondi, F. A. Herrero, C. G. Fesen and D. C. Hallenback, 'Optical interferometric studies of the nighttime equatorial thermosphere: enhanced temperatures and zonal wind gradients', J. Geophys. Res., 102, A9, 20041, 1997.

115) Misawa K. and I. Takeuchi, 'Correlation among $O_2(0 -1)$ atmospheric band, OH( 8 -3) band and OI 5577 A line and among $P_1(2)$, $P_1(3)$ and $P_1(4)$ lines of OH $(8 - 3)$ band.', JATP, 40, 421 , 1978.

116) Mishin E. V., A. E. Epishova, L. M. Ishkova, E. F. Kozlov, L. E. Kolokolov, L. N. Rubtsov, N. I. Samorokin, L. N. Sidorova, V. M. Somsikov, V. A. Telegin and L. A. Yodovick, 'Disturbances of F region electron density following solar terminator during the WITS period of 16-20 March, 1988', J. Atmos. Terr. Phys., 53, 6/7, 643, 1991.

117) Mitra S. K., 'Geomagnetic control of $F_2$ region of the ionosphere', Nature, 158, 668 , 1946.

118) Moffet R. J., 'The equatorial anomaly in the electron distribution of the terrestrial F region', Fund. Cosmic. Phys., 4, 313, 1979.

119) Murata H., 'Wave motions in the atmosphere and relagted ionospheric phenomena', Space Sci. Rev., 16, 461, 1974.

120) Narayanan R., J. N. Desai, N. K. Modi, R. Raghavarao, R. Sridharan, 'Dayglow photometry: a new approach', Appl. Opt., 28, 2138, 1989.

121) Nelson G. J. and L. L. Cogger, 'Dynamical behavior of the nighttime ionosphere at Arecibo', J. Atmos. Terr. Phys., 33, 1711, 1971.

122) Nicolet M., 'The origin of the emission of oxygen green line in the airglow', Phys. Rev., 93, 633, 1954.

123) Noxon J. F., 'Day airglow', Space Sci. Rev., 8, 92, 1968.

124) Noxon J. F., R. M. Goody, 'Observations of day airglow emission', J. Atmos. Sci., 19, 342, 1962.

125) Onwumechilli A., 'Physics of geomagnetic phenomena vol.I, ed. Matshuhita S. and W. H. Campbell, Academic Press, New York, 1967.

126) Onwumechilli C. A., 'The equatorial electrojet', Gordon and Breach science, , 1997.

127) Ossakow S. L., 'Spread F theories – A review', J. Atmos. Terr. Phys., 43, 437, 1981.

128) Pallam Raju D., R. Sridharan, S. Gurubaran and R. Raghavarao, 'First results from ground-based daytime optical investigations of the development of equatorial ionization anomaly', Annales Geophysicae, 14, 238, 1996.

129) Pallam Raju D., R. Sridharan, R. Narayanan, N. K. Modi, R. Raghavarao and B. H. Subbraya, `Ground based optical observations of daytime auroral emissions from Antarctica', J. Atmos. Sol. Terr. Phys., 58, 13, 1591, 1995.

130) Pal S. R. and P.V. Kulkarni, 'Behaviour of oxygen 6300A emission in the night airglow and the dynamics of the ionosphere at low latitudes', Ann. Geophys., 24, 2, 1968.

131) Pallam Raju, D., and R. Sridharan, 'High resolution 2D maps of OI 630.0 nm thermospheric dayglow from equatorial latitudes', Ann. Geophysicae, 16, 996, 1998.

132) Pant Tarun Kumar, `Study of thermosphere ionosphere coupling under varying geophysical conditions', Ph.D. thesis, submitted to Gujrat University, India, 1998.

133) Pant T. K.and R. Sridharan, `A case study of the low latitude thermosphere during geomagnetic storms and its new representation by improved MSIS model', Annels Geophysicae, 16, 1513, 1998.

134) Petitdidier M. and H. Teitelbaum, `lower thermosphere emission and tides', Planet. Sp. Sci., 25, 711, 1977.

135) Prakash S., 'Generation of perturbation electric fields suitable for triggering of equatorial spread F by gravity waves in the E region and zonal winds in the F region', Ind. J. Radio Sp. Phys., 25, 211, 1996.

136) Queffelec J. C., B. R. Rowe, F. Vallee, J. C. Gomet, M. Moralais, `The yield of metastable atoms through dissociative recombination of $O_2^+$ ions with electrons', J. Chem. Phys., 91, 5335, 1989.

137) Raghavarao R. and B. G. Anandarao, 'Vertical winds as a plausible cause for equatorial counter electrojet', Geophys. Res. Lett., 7, 357, 1980.

138) Raghavarao R., P. Sharma and M. R. Sivaraman, `Correlation of ionization anomaly with the intensity of the electrojet', Space Res., XVIII, 277, 1978.

139) Raghavarao R., R. Sridharan, J. H. Sastri, V. V. Agashe, B. C. N. Rao, P. B. Rao and V. V. Somayajulu, 'The equatorial ionosphere', WITS Handbook, 48, 1988.

140) Raghavarao R., L. E. Wharton, N. W. Spencer, H. G. Mayr and L. H. Brace, `An equatorial temperature and wind anomaly (ETWA)', Geophys. Res. Lett., 18, 1193, 1991.

141) Raghavarao R., W. R. Hoegy, N. W. Spencer and L. E. Wharton, 'Neutral temperature anomaly in the equatorial thermosphere – A source of vertical winds', Geophys. Res. Lett., 20, 357, 1993.

142) Ranganath Rao H. N. and J. H. Sastri, Ann. Geophys., 12, 276, 1994.

143) Rajaram R. and S. Gurubaran, 'Seasonal variabilities of low latitude mesospheric winds', Ann. Geophysicae, 16, 197, 1998.

144) Rao C. S. R. and P. L. Malhotra, `A study of geomagnetic anomaly during I. G. Y.', J. Atmos. Terr. Phys., A26, 1075, 1964.

145) Rastogi R. G. and J. A. Klobuchar, 'Ionospheric electron content within the equatorial $F_2$ layer anomaly belt', J. Geophys. Res., 95, 19045, 1990.

146) Rastogi R. G. and Asha Patil, `Complex structure of equatorial electrojet current', Current Sci., 55, 433, 1986.

147) Rastogi R. G., `Counter equatorial electrojet currents in the indian zone', Planet. Sp. Sci., 21, 1355, 1973.

148) Rastogi R. G., 'Westward equatorial electrojet during daytime hours', J. Geophys. Res., 79, 1503, 1974.

149) Ratcliffe J. A., `Sun Earth and Radio: an introduction to the ionosphere and magnetosphere', World University press, 1970.

150) Reddy C. A., 'The equatorial electrojet: A review of the ionospheric and geomagnetic aspects', J. Atmos. Terr. Phys., 43, 557, 1981.

151) Reddy C. A. and C. V. Devasia, 'Height and latitude structure of electric fields and currents due to local East – West winds in the equatorial electrojet', J. Geophys. Res., 86, 5751, 1981.

152) Reddy C. A., 'The equatorial electrojet', Pure and App. Geophys., 131, 3, 485, 1989.

153) Richmond A. D., 'Equatorial electrojet- I. Development of a model including winds and instabilities', J. Atmos. Terr. Phys., 35, 1083, 1973a

154) Richmond A. D., 'Equatorial electrojet- II. Use of the model to study the equatorial ionosphere', J. Atmos. Terr. Phys., 35, 1105, 1973b.

155) Richmond A. D., 'Electron density profile changes associated with the equatorial electrojet', J. Atmos. Terr. Phys., 39, 157, 1977.

156) Roble R. G., 'Energetics of the mesosphere and Thermosphere', The uppper mesosphere and lower thermosphere: A review of experiment and theory, Geophysical monograph –87, 1, ed. Johnson and Killeen, 1995.

157) Rogers J. W., R. E. Murphy, A. T. Stair, J. C. Ulwik, K. D. Baker and L. L. Jensen, 'Rocket borne radiometric measurements of OH in the auroral zone', J. Geophys. Res., 78, 7023, 1973.

158) Rush C. M. and A. D. Richmond, 'The relationship between the equatorial anomaly and the strength of the equatorial electrojet', J. Atmos. Terr. Phys., 35, 1171, 1973.

159) Sampath S. and T. S. G. Sastri, 'Results from insitu measurements of ionospheric currents in the equatorial region- I', J. Geomag. Geoelectr., 31, 373, 1979.

160) Sastri J. H., 'Equatorial anomaly in F region – A review', Ind. J. Radio Sp. Phys., 19, 225, 1990.

161) Sastry T. S. G., 'Diurnal change in the parameters of the equatorial electrojet as observed by rocket borne magnetometers', Space Res., X, 778, 1970.

162) Scheer J., E.R. Reisin, J.P. Espy, M. Bittner, H.H. Graef, D. Offermann, P.P. Ammosov, V. M. Ignatyev, 'Large scale structures in hydroxyl rotational temperatures during DYANA', J. Atmos. Terr. Phys., 56, 13/14, 1701, 1994.

163) Schultz M. and Karl Stattegger K., 'Spectrum: spectral analysis of unevenly spaced paleoclimatic time series', Computers and Geosciences, 9, 929, 1997.

164) Sekar R. and R. Raghavarao, Role of vertical winds on the Rayleigh Taylor mode instabilities of the nighttime equatorial ionosphere', J. Atmos. Terr. Phys., 49, 981, 1987.

165) Sekar R. and R. Raghavarao, 'Critical role of the equatorial topside F region on the evolutionary characteristics of the plasma bubbles', Geophys. Res. Lett., 1995.

166) Sekar R., R. Suhasini and R. Raghavarao, 'Evolution of plasma bubble in the equatorial F region with different seeding conditions', Geophys. Res. lett., 22, 885, 1995.

167) Shepherd G. G., C. Mclandress and B. H. Solheim, 'Tidal influence on $O(^1S)$ airglow emission rate distributions at the geographic equator as observed as observed by WINDII', Geophys. Res. Letters, 22, 3, 275, 1995.

168)  Shepherd G. G., N. J. Siddiqi, R. H. Wiens and S. Zang, `Airglow measurements of possible changes in the ionosphere and middle atmosphere', Adv. Sp. Res., 20, 11, 2127, 1997a.

169)  Shepherd G. G., R.G. Rolble and W. E. Ward, `WINDII observations of the 558 nm emission in the lower thermosphere: the influence of dynamics on composition', J. Atmos. Sol. Terr. Phys., 59, 6, 655, 1997b.

170)  Shuman B. M., 'Rocket measurement of the equatorial electrojet', J. Geophys. Res., 75, 3889, 1970.

171)  Singh Vir et al., ` Study of O($^1$S) dayglow emission near equatorial latitudes', Ind. Journal of Radio and Space Phys., 26, 36, 1997.

172)  Sivaraman M. R., R. Suhasini and R. Raghavarao, 'Role of ambipolar diffusion in the development of equatorial anomaly in solar maximum and minuimum period', Ind. J. Radio and Sp. Phys., 5, 136, 1976.

173)  Sivjee G. G., `Airglow Hydroxyl emissions', Planet. Sp. Sci., 235, 1992.

174)  Sivjee G. G., K. A. Dick and P. D. Feldman, 'temporal variations in nighttime hydroxyl rotational temperatures', Planet. Sp. Sci., 20, 261, 1972.

175)  Slanger T. G. and G. Black, ` O($^1$S) in the lower thermosphere – Capman Vs Barth', Planet. Sp. Sci., 25, 79, 1977.

176)  Sobral J. H. A., G. L. Borba, M. A. Abdu, I. S. Batista, H. Sawant, C. J. Zamlutti, H. Takahashi and Y. Nakamura, 'Post-sunset wintertime 630.0 nm airglows perturbations associated with gravity waves at low latitudes in the South American sector', J. Atmos. Sol. Terr. Phys., 59, 13, 1611, 1997.

177)  Solomon S. C. and V. J. Abreu, `The OI 630 nm dayglow', J. Geophys. Res., 94, 6817, 1989.

178)  Somayajulu V. V., Ligi Cherian, K. Rajeev, Geetha Ramkumar and C. Raghava Reddi, 'Mean winds and tidal components during counter electrojet', Geophys. Res. Lett., 20, 1443, 1993.

179)  Spencer N. W., H. C. Brinton, H. G. Mayr and R. F. Theis, 'The midnight temperature anomaly', EOS Trans., 58, 990, 1977.

180)  Spencer N. W., G. R. Carignan, H. G. Mayr, H. B. Niemann, R. F. Theis and L. E. Wharton, 'The midnight temperature maximum in the earth's equatorial thermosphere', Geophys. Res. Lett., 6, 444, 1979.

181) Sridharan R. and R. Raghavarao, `Evidence for turbopause control on neutral density variations in the lower thermospehre, J. Atmos. Terr. Phys, 46, 10, 851, 1984.

182) Sridharan R., R. Raghavarao, S. Gurubaran and R. Narayanan, `First results of OI 630.0 nm dayglow measurements from equatorial latitudes, J. Atmos. Terr. Phys., 53, 521,1991.

183) Sridharan R., R. Narayanan R. and N. K. Modi, `An improved chopper mask design for the dayglow photometer', Applied Opt., 31, 425, 1992a.

184) Sridharan R., S. A. Haider, S. Gurubaran, R. Sekar and R. Narayanan, ` OI 630.0 nm dayglow in the region of equatorial ionization anomaly: temporal variability and its causative mechanism', J. Geophys. Res., 97, 13715, 1992b.

185) Sridharan R., R. Narayanan, N. K. Modi and D. P. Raju, `Novel mask design for multiwavelength dayglow photometry', Applied Opt., 32, 4178, 1993.

186) Sridharan R., D. Pallam Raju, R. Raghavarao and P. V. S. Ramarao, `Precursor to equatorial spread F in OI 630.0 nm dayglow', Geophys. Res. Lett., 21, 2797, 1994.

187) Sridharan R., N. K. Modi, D. Pallam Raju, R. Narayanan, Tarun Pant, Alok Taori and D. Chakrabarty, ` Multiwavelength daytime photometer – a new tool for the investigations of the atmospheric processes', Measurement Sci. and Tech., 9, 585, 1998.

188) Sridharan R., Alok Taori, D. Chakrabarty, H. Chandra, Som Sharma, R. Narayanan and N. K. Modi, 1999a, ` Effects of 6 January 1997 space weather related processes in the low latitude thermosphere ionosphere system', J. Atmos. Sol. Terr. Phys., 61, 13, 1001 – 1005.

189) Sridharan R., Alok Taori, S. Gurubaran, R. Rajaram and M. G. Shepherd, "First results on daytime mesopause OH rotational temperatures using ground based photmetry from equatorial latitudes", J. Atmos. Sol. Terr. Phys., 61, 15, 1331, 1999b.

190) Sridharan R., D. Pallam Raju, V. V. Somayajulu, Alok Taori, D. Chakrabarty and R. Raghavarao, 'Imprint of equatorial electrodynamical processes in the 630.0 nm dayglow', J. Atmos. Sol. Terr. Phys., 61, 15, 1143, 1999c.

191) Stenning R. J., 'A two layer ionospheric dynamo calculation', J. Geophys. Res., 86, 3543, 1981.

192) Stenning R. J., 1985, 'Modeling the equatorial electrojet', J. Geophys. Research, 90, 1705 – 1719, 1985.

193) Subbaraya B. H., "Mesosphere : coupling region between the upper atmosphere and middle atmosphere", Proc. Ind. Nat. Sci. Acad., 60, A, 1, 227 – 242, 1994.

194) Sultan P. J., 'Linear theory and modeling of the Rayleigh Taylor instability leading to the occurrence of equatorial spread F', J. Geophys. Res., 12, 26875, 1996.

195) Swenson G.R., S. B. Mende, S. P. Geller, 'Fabry - Perot Imaging observations of OH (8,3) rotational temperatures and Gravity waves', J. Geophy. Res.,95, 12251 – 12263, 1990.

196) Takahashi H., Y. Sahai, P. P. Batista, N. R. Teixeira, ` Diurnal and seasonal variations of the OH (8,3) airglow bands and its correlation with OI 5577 A', Planet. Sp. Sci., 25, 541, 1977.

197) Hakahashi H. and P. P. Batista, 'Simultaneous measurements of OH(9,4), (8,3), (7,2), (6,2) and (5,1) bands in the airglow', J. Geophys. Res., 86, 5632, 1981.

198) Takahashi H. et al, ` Tidal and solar effects on the 5577 A, NaD and OH (8, 3) airglow emission observed at $23^0$ S', Planet. Sp. Sci., 32, 897, 1984.

199) Takahashi H., P. P. Batista, Y. Sahai and B. R. Clemesha, `Atmospheric wave propagations in the mesopause region observed by the OH (8, 3) band, Na D, O2 A (8645 A) band and OI 5577 A nightglow emission', Planet. Sp. Sci., 33, 381, 1985.

200) Takahashi H., Y. Sahai, B. R. Chemasha, D. M. Simonich, N. R. Teixeira, R.M. Lobo and A. Eras, `Equatorial mesospheric and F – region airglow emissions observed from latitude $4^0$ S', Planet. Sp. Sci., 37, 6, 649, 1989.

201) Takahashi H., B. R. Clemesha, P. P. Batista, Y. Sahai, M. A. Abdu and P. Muralikrishna, ` Equatorial F region OI 6300 A and 5577 A. emission profiles observed by rocket borne airglow photometers', 32, 897, 1990.

202) Takahashi H., B. R. Clemesha, Y. Sahai and P. P. Batista, 'Seasonal variations of the mesopause temperature observed at equatorial ($4^0$S) and low ($23^0$S) latitude station', Adv. Sp. Res., 14, 9, 97, 1994.

203)   Taylor M. J., M. A. Hapgood and P. Rothwell, `Observations of gravity wave propagation in the OI(557.7 nm), NaD (589.2 nm) and the near infrared OH nightglow emission', Planet. Sp. Sci., 35, 413, 1987.

204)   Taylor M. J., P. J. Espy, D. J. Baker, R. J. Sica, P. C. Neal and W. R. Pendleton Jr., `Simultaneous intensity, temperature and imaging measurements of short period wave structure in the OH nightglow emission', Planet.Sp.Sci., 39, 8, 1171, 1991.

205)   Taylor M. J., D. N. Turnbull and R. P. Lowe, `Spectrometric and imaging measurements of a spectacular gravity wave event observed during the ALOHA - 93 ',Geophys. Res. Lett., 22, 20, 2849, 1995.

206)   Texier Le H., S. Solomon and R. R. Garcia, 'Seasonal variability of the OH Meinel bands', Planet. Sp. Sci., 35, 977, 1987.

207)   Tinsley B. A., `Neutral atom precipitation – a review', J. Atmos. Terr. Phys., 43, 617, 1981.

208)   Tinsley B. A., `Solar wind mechanism suggested for weather and climate change', EOS, 75, 32, 369, 1994.

209)   Tinsley B. A., R. Rohrbaugh, H. Rassoul, Y. Sahai, N. R. Teixeira and D. Slater, `Low latitude aurorae and storm time current system', J. Geophys. Res., 91, 11257, 1986.

210)   Tsunoda R. T., `Control of the seasonal and longitudinal occurrence of the equatorial scintillations by longitudinal gradient in integrated E region Pederson conductivity', J. Geophys. Res., 90, 447, 1985.

211)   Untiedt J., 'A model of the equatorial electrojet with a meridional current system', J. Geophys. Res., 72, 5799, 1979.

212)   Volland H., `Atmospheric electrodynamics', Springer Verlag, Berlin, 1984.

213)   Von Zahn U., J. Hoffner, V. Eska and M. Alpers, 'The mesopause altitude : Only two distinctive levels worldwide', Geophys. Res. Lett., 23, 22, 3231, 1996.

214)   Walker J. C. G., 'The green lone of atomic oxygen in the Day airglow', J. Atmos. Sci., 22, 361, 1965.

215)   Walker G. O., J. H. K. Ma, R. G. Rastogi, M. R. Deshpande and H. Chandra, 'Dissimilar forms of the ionospheric equatorial anomaly observed in East Asia and India', J. Atmos. Terr. Phys., 42, 629, 1980.

216)   Walker G. O., 'Longitudinal structure of the F region equatorial anomaly –a review', J. Atmos. Terr. Phys., 43, 589, 1981.

217) Walker G. O., J. H. K. Ma and E. Gotton, 'The equatorial ionosphere anomaly in electron content from solar minimum to solar maximum from South –East Asia', Ann. Geophysicae, 12, 195, 1994.

218) Wallace L. and M. B. McElroy, 'The visual dayglow', Planet. Sp. Sci., 14, 677, 1966.

219) Walterschid R. L., G. Schubert and J. M. Straus, 'A dynamical chemical model of wave driven fluctuations in the OH nightglow', J. Geophys. Res., 92, 1241, 1987.

220) Ward W. E., 'Tidal mechanisms of dynamical influence on oxygen recombination airglow in the mesosphere and lower thermosphere', Adv. Sp. Res., 21, 6, 795, 1998.

221) Whitehead J. D., 'Ionization disturbances caused by gravity waves in the presence of an electrostatic field and a background wind', J. Geophys. Res.,76, 238, 1971.

222) Wickwar, V.B. and H.C. Carlson, 'Ionospheric and thermospheric couplings: vertical, latitudinal and longitudinal', J. Atmos. Sol. Terr. Phys., 61, 141, 1999.

223) Yee J. H. and T. L. Killeen, 'Thermospheric production of $O(^1S)$ by dissociative recombination of vibrationally excited $O_2^+$', Planet. Sp. Sci., 34, 1101, 1986.

224) Yee J. H., and V. J. Abreu, ' Mesospheric 5577 A green line and atmospheric motion – atmospheric explorer satellite observations.', Planet. Sp. Sci., 35, 1389, 1987.

225) Zalesak S. T., S. L.Ossakow and P. K. Chaturvedi, 'Non linear equatorial spread F: The effect of neutral winds and background Pederson conductivity', J. Geophys. Res., 87, 151, 1982.

226) Zang S. P., G. G. Shepherd, 'The influence of the diurnal tide on the $O(^1S)$ and OH emission rates observed by WINDII on UARS', Geophys. Res. Lett., 26, 4, 529, 1999.

227) Zipf E. C., ' The excitation of $O(^1S)$ by the dissociative recombination of O2+ ions: electron temperature dependence', Planet. Sp. Sci., 36, 121, 1988.